ADAM MICKIEWICZ
UNIVERSITY
POZNAŃ

Doctoral thesis

Mateusz Zelent

Remagnetization and magnetization dynamics in complex magnetic textures, from antidots lattice to nanodots

Supervisor: **Prof. dr hab. Maciej Krawczyk**

Assistant supervisor: **Dr Michał Mruczkiewicz**

Faculty of Physics
Adam Mickiewicz University, Poznań

This dissertation is submitted for the degree of
Doctor of Physics

Poznań 2019

I would like to dedicate this thesis to o my lovely girlfriend **Weronika**
and my loving parents, **Grażyna** and **Zbigniew**…

Declaration

Declaration of the author of this dissertation:

I hereby declare that except where specific reference is made to the work of others, the contents of this dissertation are original and have not been submitted in whole or in part for consideration for any other degree or qualification in this, or any other university. This dissertation is my own work and all the contents of the dissertation have been obtained by legal means.

....
Mgr Mateusz Zelent

Declaration of the thesis Supervisor:

This dissertation is ready to be reviewed.

....
Prof. dr hab. Maciej Krawczyk

Acknowledgements

Throughout the work on this Thesis, I had the privilege to meet and collaborate with many people. I want to thank all of them for their valuable contributions and their support. In particular, I would like to thank the following people:

First, I would like to express my sincere gratitude to my supervisor, **prof. dr hab. Maciej Krawczyk**, as well as, to my assistant supervisor **dr Michał Mruczkiewicz** for their trust, patient, guidance, endless support (sometimes even after the midnight). Since my first day in the division, they taught me everything they know and gave me the freedom to realise my ideas. I enjoyed the scientific and private conversations with you. Michał was the first person I met at the plant when I came to apply for a position in MagnoWa grant. Thank you all for numerous fruitful discussions and for introducing me into the world of skyrmions. Without you, this thesis would never be completed.

I'm deeply indebted to **dr Paweł Gruszecki** and **mgr Szymon Mieszczak** for the enormous amount of work they put in developing our software for micromagnetic simulation post-processing tool, called MMPP (available on GitHub).

I want to thank all other members of the Nanomaterials Physics Division including **prof. UAM dr hab. Jarosław W. Kłos, prof. UAM dr hab. Sławomir Mamica, dr Andriy E. Serebryannikov, dr Piotr Graczyk, dr Justyna Rychły, mgr Vishal Vashistha and mgr Krzysztof Szulc** for their encouragement and accompanying me in my journey to complete this thesis.

Various parts of the presented thesis were supported by the Polish National Science Centre (NCN), Ministry of Science and Higher Education (MNiSW), and European Union Horizon 2020 and other:

1. NCN PRELUDIUM 14, Grant No. 2018/31/N/ST7/03918 **(PI)**,
2. NCN SONATA BIS 2 (2013-2018), Grant No. 2012/07/ST3/00538.
3. EU Horizon 2020 project MagIC Grant No. 644348,
4. Scholarship founded by Adam Mickiewicz University Foundation,
5. Scholarship founded by dr Jan Kulczyk Foundation,
6. OPUS11 (2017-2019), Grant No. 2016/21/B/ST3/00452,
7. OPUS9 (2016-2019), Grant No. 2015/17/B/ST3/00118,
8. "Premia na Horyzoncie" - MNiSW Grant No. 328712/PnH/2016,
9. National Scholarship Program of the Slovak Republic funded by the Ministry of Education, Science, Research, and Sport of the Slovak Republic (two scholarships in 2016/2017 and 2017/2018),
10. The simulations were partially performed at the Poznan Supercomputing and Networking Center (Grant No. 398).

Abstract

Bloch predicted a disturbance in the local magnetic order which can propagate in a magnetic material in a form of wave in 1929. It named as a spin wave since it is related to a collective excitation of the spins in ferromagnetic media. Magnonic crystals are artificial magnetic media with periodically modulated magnetic properties in space. Magnonic crystals are structures well known as a structure where spin waves band structure consists of intervals of allowed bands of SW frequencies and forbidden band gaps, making them structures with interesting properties. Magnetic skyrmions are solitonic magnetisation textures, whose stability is protected by their topology. The existence of magnetic skyrmions in both bulk and thin-film magnetic materials has been predicted by theory and observed experimentally. Due to their small size skyrmions can be used to develop extremely compact data storage devices, ushering in a new class of low-power devices.

In this thesis, the author presents the results of studying the static and dynamic properties of the complex ferromagnetic structures and unique skyrmions properties. The author studied magnetisation textures in patterned thin films during the remagnetisation process. In the next step, he studied the ferromagnetic resonance and characteristic of propagating spin-waves in the same structures. Then, he started investigations of skyrmion stabilisation in nanodisc and skyrmion nucleation process in antidot lattice during the remagnetisation process. Finally, he analysed the complex magnetic textures in patterned multilayers with perpendicular magnetic anisotropy and Dzyaloshinskii-Moriya interaction.

Abstrakt

Lokalne zaburzenie uporządkowania magnetycznego, które może rozprzestrzeniać się w postaci fali w materiale magnetycznym, zostało przewidziane przez Blocha w 1929 roku i nazwane falą spinową. Fale spinowe to kolektywne wzbudzenia spinów magnetycznych w materiałach ferromagnetycznych, w których pokładane są nadzieje, że w niedalekiej przyszłości staną się alternatywnym nośnikiem informacji, znacznie mniej energochłonnym od transportu elektronowego. Periodycznie strukturyzowane układy magnoniczne są sztucznymi ośrodkami o okresowo modulowanych właściwościach magnetycznych, zwane kryształami magnonicznymi. Kryształy magnoniczne uzyskały uznanie jako materiały, o bogatej strukturze pasmowej, co czyni je strukturami o bardzo interesujących właściwościach. W takich strukturach można znaleźć skomplikowane tekstury magnetyczne takie jak domeny magnetyczne, vortexy czy skyrmiony. Skyrmion jest kwazicząsteczką, charakteryzującą się tzw. ładunkiem topologicznym, będącą możliwie najmniejszym i jednocześnie stabilnym zakłóceniem jednorodnego namagnesowania. Istnienie skyrmionów magnetycznych zostało przewidziane teoretycznie i zaobserwowane w eksperymentalnie po raz pierwszy w 2009 roku. Ze względu na niewielkie rozmiary skyrmiony mogą być wykorzystywane do opracowywania wyjątkowo gęstych jednostek pamięci, wprowadzając nową klasę urządzeń o niskim poborze energii i wysokiej pojemności danych.

W pracy doktorskiej autor prezentuje wyniki badań właściwości statycznych i dynamicznych magnetyzacji w nanostrukturach magnetycznych. W pierwszych rozdziałach pracy doktorskiej znajduje się wprowadzenie do magnetyzmu, magnoniki i fal spinowych. W ramach pracy doktorskiej zostało zaprezentowane pięć publikacji naukowych zawierających wyniki badań: procesów przemagnesowania, rezonansu ferromagnetycznego, propagacji fal spinowych w strukturalizowanych materiałach ferromagnetycznych; stabilizacji skyrmionów w nanokropkach magnetycznych w których możliwe jest istnienie dwóch stanów skyrmionowych (skyrmionu o małej i dużej średnicy) o zbliżonych poziomach energetycznych; badania techniki formowania skyrmionów w sieci kwadratowej dziur w trakcie procesu przemagnesowania. W ostatniej pracy autor przedstawił wyniki badań właściwości sieci dziur w wielowarstwach ferromagnetycznych z prostopadłą anizotropią, w których zaobserwowano skomplikowaną teksturę magnetyczną. W ostatnim rozdziale doktoratu znajduje się podsumowanie, plany badawcze oraz krótkie zestawienie najważniejszych osiągnięć autora.

Short note about the author

The author graduated from Adam Mickiewicz University (UAM), Faculty of Physics in 2015, with M.Sc. degree in Medical Physics. He prepared his thesis as a PhD student in Nanomaterials Physics Division and under collaboration with Institute of Electrical Engineering, Slovak Academy of Sciences in Bratislava.

The author has been the principal investigator in the National Science Center (NCN) grant Preludium *Study of the bi-stable magnetic skyrmions in ultrathin nanodots* (NCN PRELUDIUM 14 (2017-2020), 2017/27/N/ST3/00419). He received two times the monthly internship scholarships from National Scholarship Program of the Slovak Republic funded by the Ministry of Education, Science, Research, and Sport of the Slovak Republic (in 2016/2017 and 2017/2018). He has also been an investigator in the seven other grants. The list of the grants and scholarships is as follows:

1. NCN SONATA BIS 2 (2013-2018), Grant No. 2012/07/ST3/00538.
2. EU Horizon 2020 project MagIC Grant No. 644348,
3. Scholarship founded by Adam Mickiewicz University Foundation,
4. Scholarship founded by dr Jan Kulczyk Foundation,
5. OPUS11 (2017-2019), Grant No. 2016/21/B/ST3/00452,
6. OPUS9 (2016-2019), Grant No. 2015/17/B/ST3/00118,
7. The simulations were partially performed at the Poznan Supercomputing and Networking Center (Grant No. 398).

The author has presented over twenty posters and over ten oral presentations at local and international conferences in Europe. Overall, he has contributed to fifteen scientific papers published in international journals from the JCR list. He has been the first, second or corresponding author in seven articles, which five of them are incorporated into this thesis and which have been published or under review in the following journals: Physical Review B, Physica Status Solidi: Rapid Research Letters, Journal of Physics D: Applied Physics. The full list of published papers is on page xxi.

The author has been an academic advisor of the three bachelor thesis and the two master thesis for students from physics, medical physics, computer technologies, and applications internet of things, where four students decided to write a dissertation based on the subjects proposed by the author.

The author was chosen twice by the editor of *Journal of Physics: Condensed Matter* as a reviewer of papers on skyrmions.

Author publication list

1. *Collective dynamical skyrmion excitations in a magnonic crystal*

   M. Mruczkiewicz, P. Gruszecki, **M. Zelent**, M. Krawczyk

   Physical Review B 93 (17), 174429, 2016

2. *Magnetization reversal mechanism in patterned (square to wave-like) Py antidot lattices*

   N. Tahir, **M. Zelent**, R. Gieniusz, M. Krawczyk, A. Maziewski, T. Wojciechowski, J. Ding, A.O. Adeyeye

   Journal of Physics D: Applied Physics 50 (2), 025004, 2016

3. *Geometrical complexity of the antidots unit cell effect on the spin wave excitations spectra*

   M. Zelent, N. Tahir, R. Gieniusz, J.W. Kłos, T. Wojciechowski, U. Guzowska, A. Maziewski, J. Ding, A.O. Adeyeye, M. Krawczyk

   Journal of Physics D: Applied Physics 50 (18), 185003, 2017

4. *Bi-stability of magnetic skyrmions in ultrathin multilayer nanodots induced by magnetostatic interaction*

   M. Zelent, J. Tobik, M. Krawczyk, K.Y. Guslienko, M. Mruczkiewicz

   Physica Status Solidi (RRL) – Rapid Research Letters 11 (10), 1700259, 2017

5. *The resonant dynamic magnetization distribution in ferromagnetic tin flm with the atidot*

   O. Busel, **M. Zelent**, O. Gorobets, Y. Gorobets, M. Krawczyk

   Acta Physica Polonica A 133 (3), 492-494, 2018

6. *Control of the spin wave phase in transmission through the ultrathin interface between exchange coupled ferromagnetic materials*

   M. Mailian, O.Y. Gorobets, Y.I. Gorobets, **M. Zelent**, M. Krawczyk

   Acta Physica Polonica A 133 (3), 480-482, 2018

7. *Co-and contra-directional vertical coupling between ferromagnetic layers with grating for short-wavelength spin wave generation*

   P. Graczyk, **M. Zelent**, M. Krawczyk

   New Journal of Physics 20 (5), 053021, 2018

8. *Driving magnetization dynamics in an on-demand magnonic crystal via the magnetoelastic interactions*

   C.L. Chang, S. Mieszczak, **M. Zelent**, V. Besse, U. Martens, R.R. Tamming, J. Janusonis, P. Graczyk, M. Münzenberg, J.W. Kłos, R.I. Tobey

   Physical Review Applied 10 (6), 064051, 2018

9. *Spin wave collimation using a flat metasurface*

   M. Zelent, M. Mailyan, V. Vashistha, P. Gruszecki, O.Y. Gorobets, Y.I. Gorobets, M. Krawczyk

   Nanoscale 11 (19), 9743-9748, 2019

10. *Spin-wave phase inverter upon a single nanodefect*

    O. V. Dobrovolskiy, R. Sachser, S. A. Bunyaev, D. Navas, V. Bevz, **M. Zelent**, W. Śmigaj, J. Rychły, M. Krawczyk, R. Vovk, M. Huth, G. Kakazei

    ACS Appl. Mater. Interfaces, 11, 17654-17662, 2019

11. *Remagnetization in arrays of ferromagnetic nanostripes with periodic and quasiperiodic order*

    K. Szulc, F. Lisiecki, A. Makarov, **M. Zelent**, P. Kuświk, H. Głowiński, J.W. Kłos, M. Münzenberg, R. Gieniusz, J. Dubowik, F. Stobiecki, M. Krawczyk

    Physical Review B 99 (6), 064412, 2019

12. *Reprogrammability and scalability of magnonic Fibonacci quasicrystals*

    F. Lisiecki, J. Rychły, P. Kuświk, H. Głowiński, J. W. Kłos, F. Groß, I. Bykova, M. Weigand, **M. Zelent**, E. J. Goering, G. Schütz, G. Gubbiotti, M. Krawczyk, F. Stobiecki, J. Dubowik, J. Gräfe

    Physical Review Applied 11 (5), 054061, 2019

13. *Magnons in a quasicrystal: propagation, extinction, and localization of spin waves in Fibonacci structures*

    F. Lisiecki, J. Rychły, P. Kuświk, H. Głowiński, J. W. Kłos, F. Groß, N. Träger, I. Bykova, M. Weigand, **M. Zelent**, E. J Goering, G. Schütz, M. Krawczyk, F. Stobiecki, J. Dubowik, J. Gräfe

    Physical Review Applied 11 (5), 054061

14. *Exchange spin waves transmission through the interface between two antiferromagnetically coupled ferromagnetic media*

    M. Mailian, O.Y. Gorobets, Y.I. Gorobets, **M. Zelent**, M. Krawczyk

    Journal of Magnetism and Magnetic Materials 484, 484-489, 2019

15. *Formation of Néel type skyrmions in an antidot Lattice with perpendicular magnetic anisotropy*

    S. Saha, **M. Zelent**, S. Finizio, M. Mruczkiewicz, S. Tacchi, A. K. Suszka, S. Wintz, N. S. Bingham, J. Raabe, M. Krawczyk, and L. J. Heyderman

    Phys. Rev. B, 100, 144435, 2019

Author publications included into thesis

1. *Magnetization reversal mechanism in patterned (square to wave-like) Py antidot lattices*

   N. Tahir, **M. Zelent**, R. Gieniusz, M. Krawczyk, A. Maziewski, T. Wojciechowski, J. Ding, A.O. Adeyeye

   Journal of Physics D: Applied Physics 50 (2), 025004, 2016

2. *Geometrical complexity of the antidots unit cell effect on the spin wave excitations spectra*

   M. Zelent, N. Tahir, R. Gieniusz, J.W. Kłos, T. Wojciechowski, U. Guzowska, A. Maziewski, J. Ding, A.O. Adeyeye, M. Krawczyk

   Journal of Physics D: Applied Physics, 50 (18), 185003, 2017

3. *Bi-stability of magnetic skyrmions in ultrathin multilayer nanodots induced by magnetostatic interaction*

   M. Zelent, J. Tobik, M. Krawczyk, K.Y. Guslienko, M. Mruczkiewicz

   Physica Status Solidi (RRL) – Rapid Research Letters 11 (10), 1700259, 2017

4. *Formation of Néel type skyrmions in an antidot lattice with perpendicular magnetic anisotropy*

   S. Saha, **M. Zelent**, S. Finizio, M. Mruczkiewicz, S. Tacchi, A. K. Suszka, S. Wintz, N. S. Bingham, J. Raabe, M. Krawczyk, and L. J. Heyderman

   Physical Review B, 100, 144435, 2019

5. *Edge localization of spin waves in antidot multilayers with perpendicular magnetic anisotropy*

   S. Pan, S. Mondal, **M. Zelent**, R. Szwierz, S. Pal, O. Hellwig, M. Krawczyk, A. Barman

   After second review (positive) in Physical Review B

Author publication in press list

1. Edge localization of spin waves in antidot multilayers with perpendicular magnetic anisotropy

   S. Pan, S. Mondal, **M. Zelent**, R. Szwierz, S. Pal, O. Hellwig, M. Krawczyk, A. Barman

   After second review (positive) in Physical Review B

2. *Controlled motion of Skyrmions in a magnetic antidot lattice*

   J. Feilhauer, S. Saha, J. Tobik, **M. Zelent**, K. Bublikov, L. J. Heyderman, and M. Mruczkiewicz

   Under review in Physical Review B

Introduction

Currently, computer technology is one of the fastest developing technologies, and the growing demand for computing power and data storage is crucial for the further development of the community. Nevertheless, the future of CMOS is not clear, since both the miniaturisation of single-element sizes and the operational speed will reach their ultimate limits soon. Therefore, one of the primary tasks facing modern science is the search for alternative concepts to CMOS, like **spin waves** and **skyrmions**. Spin waves are promising candidates for information carriers in advanced technology. **Magnonics**, alongside **spintronics**, opens the possibility to design devices even smaller, faster, and more energetically efficient than electronic ones. This concerns signal generation, transmission, amplification, and manipulation, as well as data storage. **Skyrmions** are magnetic textures, topologically protected spin configurations, which are of great interest for their unique physical properties. In particular, they represent the ultimate small achievable size for a nonvolatile magnetic memory element. From the beginning of my PhD study, my main goal was to connect knowledge about static and dynamic properties of complex ferromagnetic structures including unique skyrmions properties. To achieve this goal, I decided to answer the set of three questions:

1. How magnetisation texture in antidot lattices affects the ferromagnetic resonance spectrum?
2. How magnetostatic field influence on skyrmion stabilisation in nanodots?
3. Is it possible to nucleate skyrmion in antidot lattice during the remagnetization process?

Thus, the following thesis presents my research on static and dynamic properties of the magnetisation in complex nanostructures that I have conducted at the Faculty of Physics, Adam Mickiewicz University in Poznań, under the supervision of Professor Maciej Krawczyk and co-supervision of dr Michał Mruczkiewicz. My thesis covers a broad spectrum of topics related to magnetisation and spin waves in ferromagnets, which might be crucial for their future **spintronics** and **magnonic** applications. This thesis is divided into five main chapters, where the first three are an introduction. To begin with, I give the background for my research and describe the employed in my study theoretical and computational methods. The next chapter provides a brief introduction to key issues in micromagnetic simulation design and post-processing of micromagnetic simulation results. The main part of my thesis, chapter four, is divided into five subsections, related to my main research topics.

First two papers and last one, presents a systematic study of the magnetisation texture and spin waves properties in patterned magnetic films in the form of the antidot lattices. In this works, we have demonstrated the impact of the shape anisotropy and local effects originated by the antidots on the switching mechanism during the magnetisation reversal process, and their implications for standing and propagating spin waves. My third paper presents a study of the skyrmion stabilisation process in nanodots, where we found that the skyrmions can be stabilised due to two different mechanisms. The fourth paper presents a mechanism of skyrmion formation process in antidot lattice during the remagnetisation process. Furthermore, we proposed there, that by varying the lattice constant, we can modify the probability of skyrmion nucleation in different parts of a sample by proper patterning. Last paper presents the study of the complex magnetic texture, found in magnonic crystal with perpendicular magnetic anisotropy. In these samples, we found that the magnetisation near the edge of the holes was oriented perpendicular to the magnetisation in bulk material. The fifth chapter shortly presents the papers with my significant contribution, but not related to the main topic of my thesis. I believed, that based on my understanding of the static and dynamic properties of the magnonic crystals, as well as skyrmion properties, I would be able to use it someday, to propose new spintronic or magnonic logic devices.

....
Mateusz Zelent

Table of contents

Nomenclature

Roman Symbols

χ	Magnetic susceptibility
Δ_{DW}	Domain wall width
γ	Gyromagnetic ratio
$\mathbf{H}_0$	External magnetic field
$\mathcal{M}$	Magnetic moment
μ_{r}	Relative permeability
$\mathbf{B}$	Magnetic flux density
$\mathbf{D}_{\mathrm{DMI}}$	Dzyaloshinskii-Moriya vector
$\mathbf{N}$	Demagnetisation tensor
C	Curie constant
h	Skyrmion helicity
J_{ij}	Exchange constant between atomic site i and j
K_{ui}	Anisotropy constant
k_{B}	Boltzmann constant
K_{eff}	Effective anisotropy
p	Skyrmion polarity
Q	Skyrmion topological charge
$S_{i,j}$	Spin vector
T	Temperature
V	Volume
w_Z	Zeeman energy density
E_{anis}	Anisotropy energy
E_{demag}	Magnetostatic energy

E_{DMI}	Dzyaloshinskii-Moriya interaction
E_{ex}	Exchange energy
E_{total}	Total energy
E_{Z}	Zeeman energy
$\mathbf{H}$	Magnetic field
$\mathbf{M}$	Magnetisation

Chapter 1

Introduction to magnetism

1.1 Magnetism

Magnetic susceptibility χ is a dimensionless proportionality factor that indicates the degree of magnetisation of a material in response to an applied magnetic field. This dependence of magnetic susceptibility χ, on the magnetic field $\mathbf{H}$ is determined by the magnetic ordering type of the material. On the basis of this criteria, materials can be classified as *diamagnetic, paramagnetic, ferromagnetic, antiferromagnetic* or *ferrimagnetic* [1].

1.1.1 Paramagnetism

In paramagnetic materials we observe an increase of the net *magnetic moment* when subject to the external magnetic field. This effect is attributed to the fact, that atoms of the paramagnetic materials have non-compensated electron spins. Thus, each atom has a non-zero magnetic moment. In paramagnets, the interaction energy between the magnetic moments of different atoms is smaller than the thermal energy, which means that in the absence of an applied magnetic field, the orientation of the magnetic moments is highly disordered and the net magnetic moment vanishes. When a magnetic field is applied, the magnetic moments align along the direction of the applied field **H** due to the *Zeeman interaction* (see section 1.2.2) and the net magnetic moment becomes proportional to the field (see Fig. 1.1) [2].

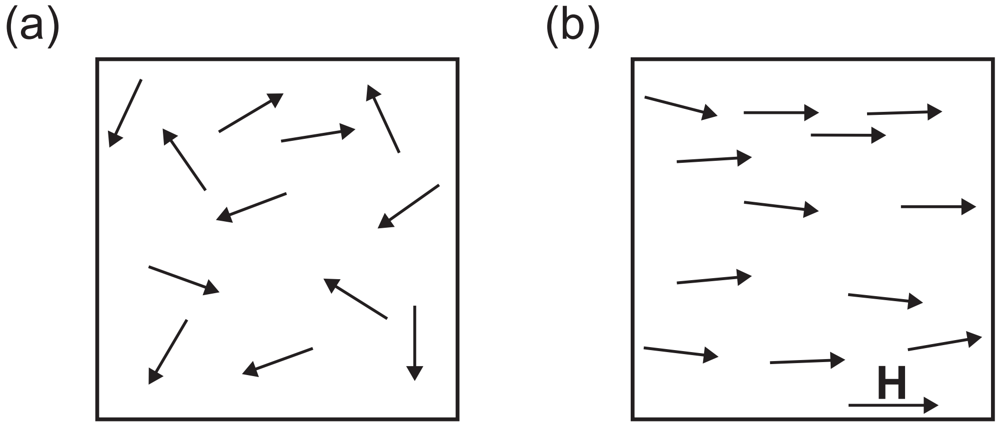

Fig. 1.1 Schematics of the magnetic moment order in paramagnets in the absence (a) and presence (b) of an applied magnetic field.

The magnetic moment of an atom can have three principal sources: The *spin* of the electrons, the *orbital angular momentum* of the electrons moving around the nucleus and the change in the orbital momentum induced by an applied magnetic field. The first two sources yield paramagnetic and the third diamagnetic contributions to the magnetisation. The *paramagnetic susceptibility* of paramagnets, χ, is inversely proportional to the temperature and is defined by *Curie's law* as [2]:

$$\chi = \frac{C}{T}, \tag{1.1}$$

where C is the *Curie constant*, characteristic for the material and can be expressed as:

$$C = \frac{N \cdot \mathcal{M}^2}{3 \cdot k_\mathrm{B}}, \tag{1.2}$$

for a two-level system with magnetic moment μ_m, where N is the number of magnetic particles per unit volume, and $\mathrm{k_B}$ is the *Boltzmann constant*. When subject to both a high magnetic field and a very low temperature, the magnetic moments within a paramagnetic substance align completely with the magnetic field. So the substance can be magnetically saturated. If the temperature is then raised, the thermal energy of the magnetic moments increases, which reduces the alignment of the moments. If the temperature is raised high enough, the thermal energy of the magnetic moments can dominate, destroying all net magnetisation [1].

1.1.2 Ferromagnetism

In contrast to paramagnetic materials, there is a class of materials, called ferromagnets, that can have a spontaneous magnetic moment – a magnetic moment even in zero applied magnetic field. The existence of spontaneous moment suggests that electron spins and, thus magnetic moments are arranged in regular order. It follows, that there is a magnetic interaction between the magnetic moments of the system that leads to the observed magnetic ordering. For ferromagnetic materials, the *magnetic susceptibility* $\chi \gg 0$ is defined as the ratio of magnetisation $\mathbf{M}$ (defined as $\mathbf{M} = \partial \mathbf{m}/\partial V$, magnetic moment over the volume) to the magnetic field $\mathbf{H}$:

$$\mathbf{M} = \chi \cdot \mathbf{H}, \tag{1.3}$$

where $\mathbf{H}$ is the magnetic field strength. In ferromagnets, the relationship between $\mathbf{M}$ and $\mathbf{H}$ is not linear and furthermore spontaneous magnetisation $\mathbf{M}$ can exist even in the absence of magnetic field. A typical feature of ferromagnetic materials is *hysteresis*, i.e., the magnetisation as function of the applied field follows a characteristic curve (see section 2.2.8). The value of the magnetisation for a given applied field, not only depends on the applied field, but also on the previous states of the system. The respond of the magnetic material can be defined also by the magnetic flux density $\mathbf{B}$ [2]:

$$\mathbf{B} = \mu_0 \cdot \mathbf{M} + \mu_0 \cdot \mathbf{H}, \tag{1.4}$$

where μ_0 is the vacuum permeability. The unit of $\mathbf{B}$ is Tesla (T) (1 T = 10^4 Gauss in CGS system of units). The relation between the magnetic field $\mathbf{B}$ and the magnetisation can be rewritten in the following form:

$$\mathbf{B} = \mu_0 \cdot \mathbf{H} \cdot (\chi + 1). \tag{1.5}$$

Introducing relative permeability $\mu_\mathrm{r} = 1 + \chi$, we can write:

$$\mathbf{B} = \mu_0 \cdot \mu_\mathrm{r} \cdot \mathbf{H} \equiv \mu \cdot \mathbf{H}. \tag{1.6}$$

Here, the μ is the *magnetic permeability*, which is a material parameter [2]. The units of μ is H/m^{-1} (Henry), which is the same unit as μ_0. The Heisenberg theory established, that this field forcing parallel alignment of the magnetic moments comes from the quantum mechanical *exchange interactions* (see sec. 1.2.1).

The Curie temperature separates the disordered paramagnetic phase at $T > T_C$ from the ordered ferromagnetic phase at $T < T_C$. This effect can be explained by the fact that the energy of the thermal motion of the magnetic moments overcomes that responsible for the ferromagnetic ordering. The different energy terms contributing to ferromagnetic order and their dependence on magnetisation $\mathbf{M}$ are discussed in the following subsections (1.2.1, 1.2.1, 1.2.2, 1.2.3, 1.2.4, 1.2.6).

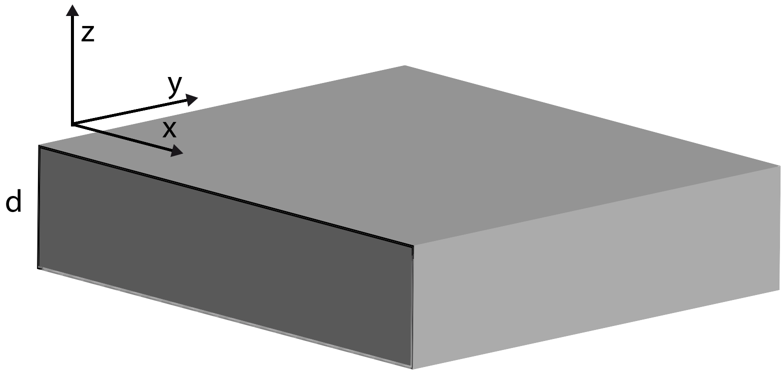

Fig. 1.2 Sketch of the ferromagnetic film with definition of the coordinate system. The grey is a film with a thickness d.

The magnetic state of a ferromagnetic material is described in the micromagnetic frameworks by a continuous vector field which is called the magnetisation density field $\mathbf{m}(\mathbf{r},t) = \mathbf{M}(\mathbf{r},t)/\mathrm{M_s}$, where $\mathrm{M_s}$ is the zero-temperature saturation magnetisation. The fundamental assumption is that the discrete distribution of the magnetic moments in a ferromagnetic material varies slowly over the lattice sites, and hence, it can be approximated accurately by a smooth magnetisation density field $\mathbf{M}(\mathbf{r},t)$. In micromagnetic approach we can assume a homogeneous magnetisation saturation as $\mathrm{M_s} = ||\mathbf{M}(\mathbf{r},t)||$, because each unit cell has the same number of magnetic moments. When the norm of the magnetisation density is fixed, only the magnetisation direction can change. Throughout this thesis, we use a left-handed Cartesian coordinate system with the film surface in the xy plane, as shown in Fig. 1.2. Consequently, the z axis is always parallel to the normal of the film.

1.2 Magnetic free energy terms

The *total magnetic free energy* depends on many physical interactions which influence the magnetisation field configuration $\mathbf{M}(\mathbf{r},t)$. Hence, the magnetic energy of the system E can be written down as a function of the magnetisation $\mathbf{M}$ and its spatial derivatives $\partial_{x,y,z}\mathbf{M}$. A total free energy in a ferromagnetic system can result from the following contributions: E_{ex} exchange energy, E_{demag} magnetostatic energy, E_{Z} Zeeman energy, E_{anis} anisotropy energy and E_{DMI} Dzyaloshinskii-Moriya interaction:

$$E_{\mathrm{total}} = E_{\mathrm{tx}} + E_{\mathrm{demag}} + E_{\mathrm{Z}} + E_{\mathrm{anis}} + E_{\mathrm{DMI}}. \tag{1.7}$$

In the following subsections, a short overview of the energy terms originating from the different physical interactions present in the chiral ferromagnetic films is discussed. Please note that, the thermal fluctuations are not taken into account.

1.2.1 Exchange energy

The exchange interaction was first treated by Heisenberg in 1928 to interpret magnetic order in ferromagnetic materials [2, 3]. This interaction is the cause of ferromagnetic order. The exchange interaction is of a quantum mechanical origin and is a result of the Pauli principle and Coulomb interactions [4]. It leads to the difference in energy between the parallel and antiparallel alignment of two coupled spins. In the simplest terms it can be described as a short-range interaction between only the nearest neighbouring spins on the atomic lattice. This exchange interaction is given by a Heisenberg Hamiltonian of the form:

$$\hat{\mathcal{H}}_{\mathrm{ex}} = -J_{ij} \cdot \sum_{ij} \mathbf{S}_i \cdot \mathbf{S}_j, \tag{1.8}$$

where J_{ij} is the exchange constant between atomic site i and j, $\mathbf{S}_i$ is a vector signifies the local spin at site i, and $\mathbf{S}_j$ is the neighbouring spin. In most cases J_{ij} is the isotropic and diagonal. A positive J_{ij} means parallel ferromagnetic spin coupling, whereas a negative J_{ij} means spins are antiparallel, i.e., antiferromagnetic in the ground state. So, the sign of J_{ij} defines the nature of the spin alignment.

We can conclude that the exchange interaction can favour parallel alignment of the magnetic moments and it leads to the existence of a spontaneous magnetisation $\mathrm{M_s}(T)$ in ferromagnets, furthermore far below from the Curie temperature, the temperature dependence of $\mathrm{M_s}(T)$ is negligible, and at certain temperature, the value of $\mathrm{M_s}(T) = |\mathbf{M}(\mathbf{r})|$ depends only on the dynamics of the elementary magnetic moments inside the elementary cell.

The exchange energy is, therefore, the energy required to rotate the spin magnetic moment with respect to its neighbours. From the Heisenberg exchange Hamiltonian describing this model, one obtains the expression for the exchange energy [4, 5]:

$$E_{\mathrm{ex}} = -2J \cdot \sum_{i \neq j} \mathbf{S}_i \cdot \mathbf{S}_j. \tag{1.9}$$

We can transform the summation with an integral, for the small deviation between neighbouring spins, introducing magnetisation and by neglecting all, except the nearest neighbours, exchange interactions. For a conscious geometry, the exchange energy depends on a kind of a lattice, for a simple cubic lattice of spins with a lattice parameter, a, can be expressed as:

$$E_{\text{ex}} = \frac{2J \cdot S^2}{a} \int_V \left[\nabla \mathbf{M(r)}\right]^2 dv, \tag{1.10}$$

where $2J \cdot S^2/a = A_{\text{ex}}$ is the exchange stiffness parameter, characteristic property of a ferromagnetic material. For the ferromagnetic materials the exchange stiffness constant is of the order of 10 pJ/m, V is the volume of ferromagnet, and dv an unit volume element. Exchange stiffness constant depends on the temperature and lattice structure, and it can be estimated employing relation:

$$A_{\text{ex}} \approx \frac{k_B \cdot T_C}{2a}, \tag{1.11}$$

where k_B is the Boltzmann constant, $k_B = 1.38065 \cdot 10^{-}23$ J/K, T_C is the Curie temperature of the material.

1.2.2 Zeeman energy

The *Zeeman energy* term describes the interaction between an external magnetic field and magnetic moments. Applying an external field force the magnetisation of a ferromagnetic system to align with the field direction. The energy density of the Zeeman interaction is given by:

$$w_Z = -\mu_0 \cdot \mathbf{H}_0 \cdot \mathbf{M}, \tag{1.12}$$

where $\mathbf{H}_0$ is the external magnetic field. This follows to the Zeeman energy:

$$E_Z = -\mu_0 \cdot \int_V \mathbf{H_0} \cdot \mathbf{M} \cdot dv. \tag{1.13}$$

The integration is performed over the volume of the magnetic sample.

1.2.3 Magnetostatic (demagnetisation) energy

The *demagnetisation energy* accounts for the *dipole–dipole interaction* in a magnetic system. This energy is also referred to as *magnetostatic energy* or *stray field* energy, owes its name to the fact that magnetic systems energetically favour macroscopically demagnetised states, if they are subject to dipole–dipole interaction only.

Dipolar interaction represents the interaction between a magnetic moment and the magnetic field generated by another magnetic moment. According to the classical treatment in electromagnetism, the two magnetic dipoles $\mathbf{M}_1$ and $\mathbf{M}_2$ separated by a distance $\mathbf{r}$, are treated as classical magnets and their dipolar interaction energy is equal to [6]:

$$E_{\text{demag}} = \frac{1}{4\pi \cdot \mu_0 \cdot r^3}\left[\mathcal{M}_1 \cdot \mathcal{M}_2 - \frac{3}{\mathbf{r}^2} \cdot (\mathcal{M}_1 \cdot \mathbf{r})(\mathcal{M}_2 \cdot \mathbf{r})\right]. \tag{1.14}$$

For typical values of magnetic moments, where $\mathcal{M}_1 = \mathcal{M}_2 = 1\mu_{\mathbf{b}}$, $\mathbf{r} = 2$Å, and we assume that $\mathcal{M}_1$ is $\perp$ to $\mathcal{M}_2$ and $\mathbf{r}$, the energy will be given as:

$$E_{\text{demag}} = \frac{\mu_B^2}{2\pi \cdot r^3} = 2.1 \cdot 10^{-24} J, \tag{1.15}$$

which is negligible value as compared to the thermal energy in room temperature. Therefore, it follows that the parallel ordering of the magnetic moments in the ferromagnetic material cannot be explained by the *dipole-dipole interactions*. However, this interaction is accountable for effects such as demagnetising field and spin waves especially in the long wave length regime. In this case, uniform magnetisation $\mathbf{M}$ generates *surface charges* which generate the dipole fields. These surface charges and the net volume charges create a demagnetisation field $\mathbf{H_d}$, pointing to the opposite direction of $\mathbf{M}$. The internal field experienced in the sample is the sum of the external and demagnetising field. $\mathbf{H_{int}} = \mathbf{H_0} - \mathbf{H_d}$. In the continuous limit, this demagnetisation energy is given by:

$$E_d = -\frac{\mu_0}{2} \int_V \mathbf{M} \cdot \mathbf{H}_d \cdot dv, \tag{1.16}$$

where factor $1/2$ must be included since each magnetic moment appears twice in the sum, $\mathbf{H}_d = -\bar{N} \cdot \mathbf{M}$, is the demagnetisation field, where $\bar{N}$ being a demagnetisation tensor which is dependent on the shape of sample:

$$\bar{N} = \begin{pmatrix} N_x & 0 & 0 \\ 0 & N_y & 0 \\ 0 & 0 & N_z \end{pmatrix}. \tag{1.17}$$

The demagnetising factors along each axis have a simple relationship $N_x + N_y + N_z = 1$. The calculation of the demagnetising tensor is not simple if the shape of the structure is irregular, because for complex geometries the demagnetising tensor varies from place to place in the structure. It should also be noticed that this treatment applies only to the case of an ellipsoid which is uniformly magnetised, and not to any other shapes or spatial distribution of the magnetisation. It is possible to compute the demagnetisation factors of a other shapes using the method introduced by A. Aharoni [7].

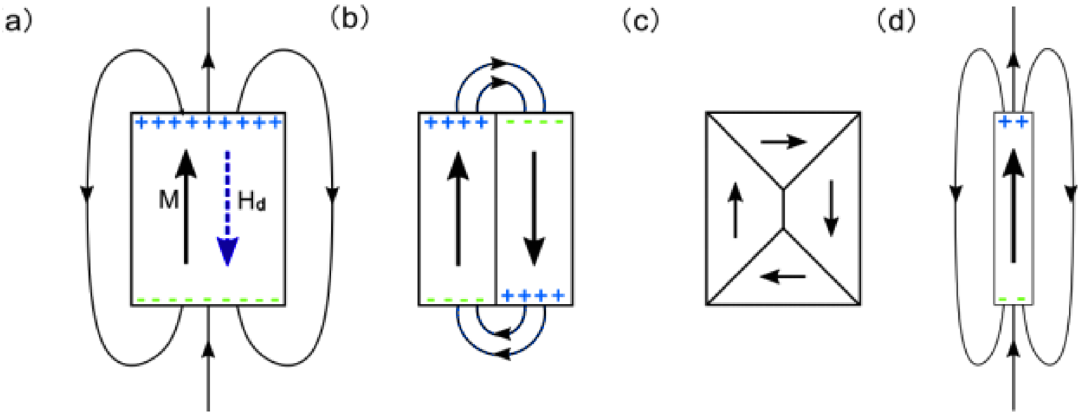

Fig. 1.3 : (a) Uniform magnetisation in a rectangular ferromagnetic object, in which the curved lines outside the object represent the magnetostatic fields and the blue (green) pluses (minus) represent the positive (negative) surface magnetic charges. Domain formation into (b) two domains and (c) a closure structure in order to minimised the magnetostatic energy for elements of same dimensions. (d) By decreasing the width of the object (a) creates a single-domain magnetic bar.

In ferromagnets the magnetostatic energy is responsible for the domains formation, which is formed to minimise the the total energy. The magnetic configuration in such domains can be uniform like in the the monodomain case shown in Fig. 1.3 (a). The demagnetisation energy is maximal in this case, so the total energy of the system is not minimised. Therefore, in cases, for instance where the demagnetising energy exceeds exchange energy, this single domain would be divided into two domains or more whose magnetisation orientations are aligned antiparallel to one another in order to reduce the demagnetisation energy, as shown in Fig. 1.3 (b). The size of the domains depends on the exchange and anisotropy, if present. The minimal demagnetisation energy can be obtained in certain cases, for instance, where a closure flux structure of magnetisation (also known as ’Landau domain’) is formed, as illustrated in Fig. 1.3 (c). The monodomain case has energy minimum, for very small structures as is presented in Fig 1.3 (d). Therefore the demagnetisation energy prefers the antipararel configuration of the magnetisation, contrary to the uniform magnetisation preferred by exchange interaction.

1.2.4 Magnetocrystalline energy

Another important contribution to the total free energy of a magnet is dependence of the magnetic energy on the magnetisation angle with respect to the crystallographic atomic lattice, and it is usually parameterised in terms of *anisotropy constants*. In this case, the energy of a magnet depends on the direction of the magnetisation with respect to the *crystal axes*. This important property, known as the *magnetic anisotropy*, contribute significantly to the *hysteresis* and *coercivity* [8]. It has been found that bulk magnetic materials can be relatively easily magnetised along certain direction, *easy axis*, while the biggest external field is required to saturate along direction, called the *hard axis*. In most magnetic materials, the main source of anisotropy is *magnetocrystalline anisotropy*, which involves electrostatic crystal-field interaction and relativistic spin-orbit coupling [9]. In other words, the origin of this energy lies in the spin–orbit coupling, either due to an anisotropic crystal structure or due to lattice deformation at material interfaces [10]. Depending on the symmetry of these anisotropies, the respective material will exhibit one or multiple easy axes. These axes are undirected and thus the energy does not depend on the sign of the magnetisation:

$$E_{\mathrm{anis}}(\mathbf{m}) = E_{\mathrm{anis}}(-\mathbf{m}). \tag{1.18}$$

The anisotropy field brings to the preferred direction the atomic moment, where the magnetisation tends to be aligned along a particular direction. Two common cases are: *crystalline anisotropy*, discussed above, and also the *shape anisotropy* having the origin in dipolar interaction.

The *uniaxial anisotropy* gives rise to one preferred direction. The energy density for the uniaxial anisotropy can be obtained starting from its effective field [5, 11]:

$$\mathbf{H}_{\mathrm{anis}}(K_{\mathrm{u1}}, K_{\mathrm{u2}}) = \frac{2K_{\mathrm{u1}}}{\mu_0 \cdot \mathrm{M_s}}(\mathbf{u} \cdot \mathbf{m}) \cdot \mathbf{u} + \frac{4K_{\mathrm{u2}}}{\mu_0 \cdot \mathrm{M_s}}(\mathbf{u} \cdot \mathbf{m})^3 \cdot \mathbf{u}, \tag{1.19}$$

where $\mathbf{u}$ is the unit vector pointing the direction of the easy axis, K_{u1} and K_{u2} are the first and second order uniaxial anisotropy constant. Thus it is given by [5, 11]:

$$w_{\mathrm{anis}} = -\frac{1}{2}\mathbf{H}_{\mathrm{anis}}(K_{\mathrm{u1}}) \cdot \mathbf{M} - \frac{1}{4}\mathbf{H}_{\mathrm{anis}}(K_{\mathrm{u2}}) \cdot \mathbf{M} \tag{1.20}$$

$$= -K_{\mathrm{u1}} \cdot (\mathbf{u} \cdot \mathbf{m})^2 - K_{\mathrm{u2}} \cdot (\mathbf{u} \cdot \mathbf{m})^4, \tag{1.21}$$

where $\mathbf{B}_{\mathrm{anis}}(K_{\mathrm{ui}})$ denotes the effective field term where only K_{ui} is taken into account. Anisotropy energy densities vary from less than 0.005 $\mathrm{MJ/m^3}$ in very soft magnets to more than 10 $\mathrm{MJ/m^3}$ in some rare-earth permanent magnets.

The simplest anisotropy-energy expression for a magnet of volume V is:

$$E_{\mathrm{anis}} = K_{\mathrm{u1}} \cdot \mathrm{V} \cdot \sin^2(\theta). \tag{1.22}$$

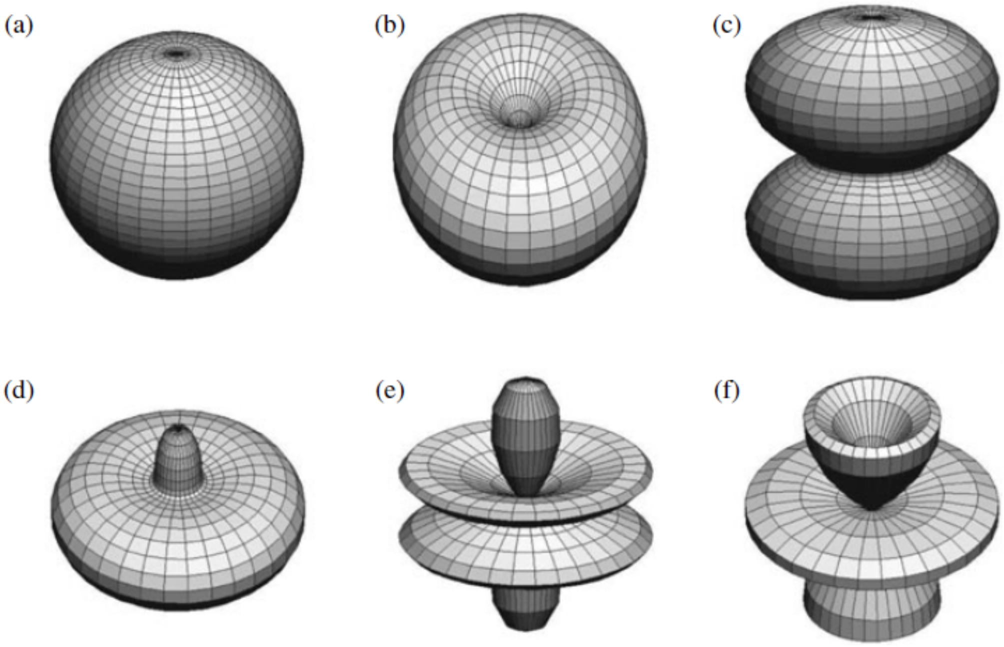

Fig. 1.4 Uniaxial anisotropy-energy landscapes: (a) isotropic, (b) easy axis, (c) easy plane, (d) easy cone, and (e–f) sixth-order landscapes. Reproduced with permission from Oxford University Press from [8].

Here θ represents polar coordinate of the magnetisation and K_{u1} is the first order uniaxial anisotropy constant. The uniaxial anisotropy constant K_{ui} (expressed in $\mathrm{J} \cdot \mathrm{m}^3$) can be either positive or negative. When it is positive, the energy is minimised when the magnetisation is aligned with the anisotropy direction $\mathbf{u}$, called an *easy axis* (1.4 (d)). When it is negative, the magnetisation tries to align in the plane perpendicular to the anisotropy axis to minimise the energy, which is then called a *hard axis* (1.4 (c)). Next to the uniaxial one, a second frequently used magnetocrystalline anisotropy is cubic anisotropy, but this one will be not used in this thesis.

The competition between magnetostatic and anisotropy interactions can be quantified by the dimensionless parameter Q defined as:

$$Q = \frac{2K_u}{\mu_0 \cdot \mathrm{M}_s^2} = \frac{\mathbf{H}_{\mathrm{anis}}}{\mathrm{M}_s}. \tag{1.23}$$

If $Q \geq 1$, the system is classified as a *hard magnet*, dominated by the anisotropy interaction, while if $Q \ll 1$ the system is classified as a *soft magnet*, dominated by magnetostatic interactions and shape anisotropy.

1.2.5 Shape anisotropy

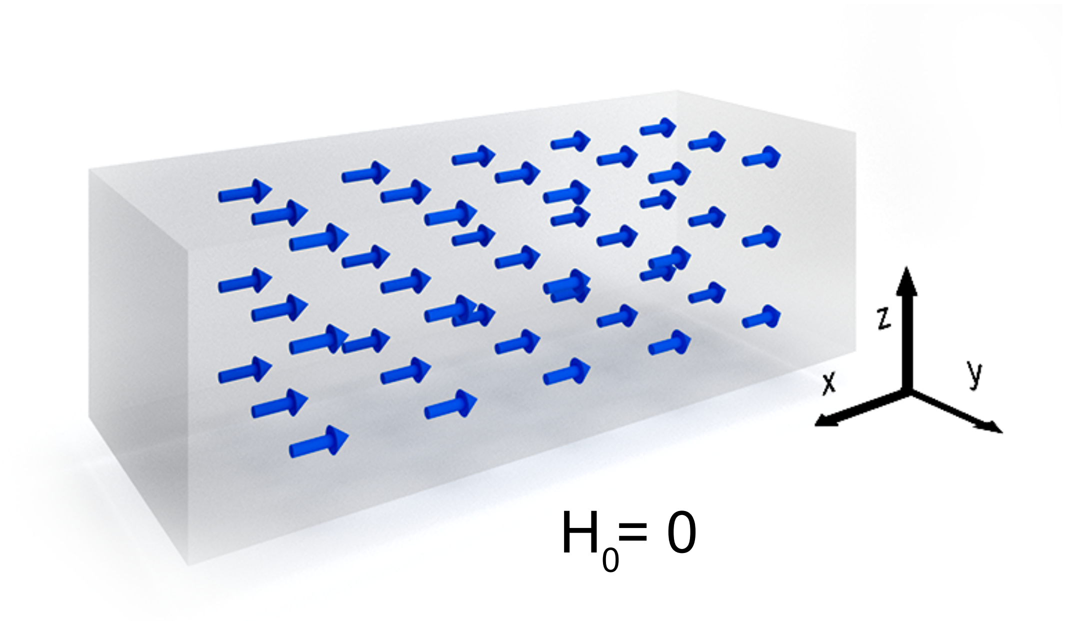

Fig. 1.5 Sketch of the ferromagnetic prism to describe the shape anisotropy. The magnetisation prefers to align along the axis parallel to the longer side of the sample since it will generates fewer magnetic surface charges.

In the absence of any external magnetic field the magnetisation tends to align itself parallel to the surfaces of ferromagnetic body. This phenomena originates from macroscopic magnetic charges at the magnet's surface and is a result of the minimisation of demagnetisation energy due to the shape of sample. More specifically, the magnetisation aligns preferably along directions that generates less magnetic charges which minimise the magnetostatic energy. The effect is called *shape anisotropy*, and is significantly pronounced in the case of nanoscale systems. For instance, for an elongated object as the one sketched in Fig.1.5 (a) the magnetisation prefers to be aligned along the x direction since it will generate fewer magnetic charges. However, within this configuration with uniform magnetisation in the bulk of the prism, the magnetic charges (at the surfaces along the x direction) are quite far from each other and this would also increase the magnetostatic energy. The value of the shape anisotropy can be calculated solving Eq. 1.16, assuming demagnetising tensor $\bar{N}$ related to the shape of structure. For instance, for a thin film with the diagonal components of the demagnetising tensor ($N_x = N_y, N_z = 1$), the shape anisotropy is:

$$K_{\text{shape}} = \mu_0 \frac{\mathrm{M}_\mathrm{s}^2}{2}. \tag{1.24}$$

1.2.6 Dzyaloshinskii-Moriya interaction

Another important contribution to the energy of the ferromagnet is the Dzyaloshinskii-Moriya interaction (DMI). Originally proposed as a phenomenological model by *Igor Dzyaloshinsky* [12], the antisymmetric exchange was also traced back to the spin-orbit coupling by *Toru Moriya* [13] in conjunction with a broken inversion symmetry. In fact it is included by the lack of inversion symmetry of the compound and a strong spin-orbit coupling. In other words, the electrons from two ferromagnetic atoms hybridise with electrons in an atom with high spin-orbit coupling. This has the effect of lowering the energy of their orthogonal spin state [14]. Similar to the exchange interaction, the DMI energy density can be written as the continuous function of the position, in analogy to approach to get exchange energy from the classical Heisenberg-like Hamiltonian. The DMI strength between two magnetic spins $\mathbf{S}_i$ and $\mathbf{S}_j$, can be expressed as:

$$\hat{\mathcal{H}}_{\mathrm{DMI},ij} = -\mathbf{D}_{\mathrm{DMI}} \cdot (\mathbf{S}_i \times \mathbf{S}_j), \tag{1.25}$$

where $\mathbf{D}_{\mathrm{DMI}}$ is the Dzyaloshinskii-Moriya vector. Due to the cross product between neighbouring spins, it favours orthogonal spin orientation, in contrast to the symmetric exchange coupling. When Dzyaloshinsky-Moriya interaction is strong enough, it cannot be neglected, and when the external magnetic field is weak enough, hence Zeeman term cannot dominate, the spins in a magnet align in a helical order.

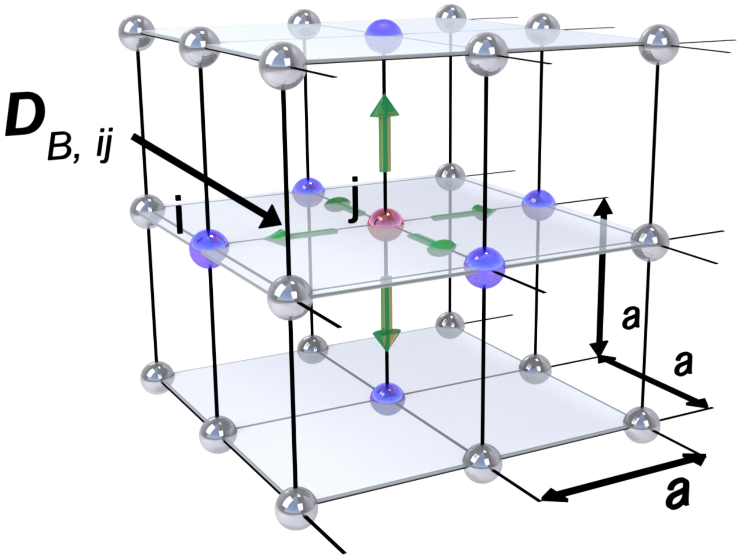

Fig. 1.6 Schematic of the bulk DMI in a cubic lattice. For visualisation a simple cubic lattice is assumed, with only nearest-neighbour interactions. Every atom (red) in the bulk of the simple cubic lattice has 6 nearest neighbours (blue). The bulk Dzyaloshinskii-Moriya interaction vectors are visualised in green, pointing along the connection $\mathbf{r}_{ij}$ to the nearest neighbours. Visualisation adapted from [15].

A broken inversion symmetry around midpoints between atoms is a first prerequisite to observe DMI. There are different classes of materials for which this prerequisite is satisfied and which exhibit DMI. We can distinguish two types of the DMI. The *bulk DMI* is found in materials with the non-centrosymmetric B20 crystal structure (see Fig. 1.6) in antiferromagnetic compounds such as: $\alpha - Fe_2O_3$ [12, 13], Heusler magnets such as Mn_2RhSn [16], and multiferroic perovskites such as $LaFeO_3$ [17]. The second type is a *interfacial DMI* found in ultra-thin films where asymmetry is induced at the interface between a ferromagnetic thin layer and a non-magnetic layer with a large spin-orbit coupling (see Fig. 1.7).

In general the direction of the DMI [18] vector is defined by the type of DMI in the material. A typical system that gives rise to interfacial DMI is a magnetic layer with an interface to a heavy-metal layer. Moriya showed [13] how to calculate the DMI vector D_{DMI} for localised moments. In 1980, Fert and Levy mentioned that doping FM samples with high spin-orbit materials, such as Pt or Au, could lead to the presence of a significant DMI due to the scattering of conduction electrons on the material impurities [19].

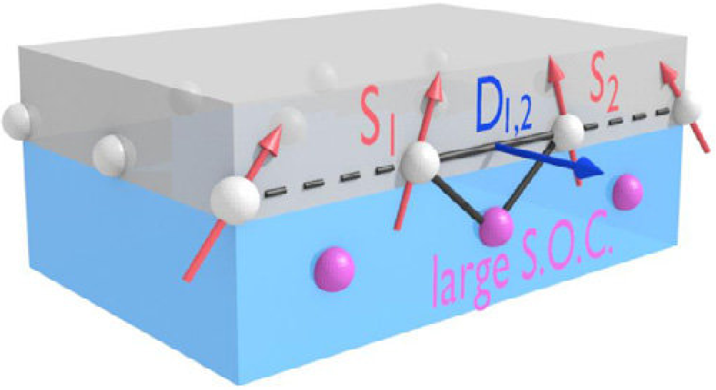

Fig. 1.7 A pair of atomic spins at the interface of a magnetic film with a metallic layer with large spin-orbit coupling in a noncentrosymmetric environment. Figure reproduced with permission from Springer Nature [20].

This antisymmetric exchange interaction is responsible for observation of *magnetic skyrmions* (see Chapter 2). For interfacial DMI, the orientation of the DM vector leads to the stabilisation of Néel-type magnetic skyrmions [21] whereas the lack of structural inversion symmetry in bulk materials [22, 23] (e.g. B20 materials like MnSi or FeGe) leads to the stabilisation of Bloch-type magnetic skyrmions [24]. In the micromagnetic framework, the continuous version of the DMI Hamiltonian [Eq. 1.25] yields, for its interfacial induced type, the following micromagnetic energy density [18]:

$$E_{\mathrm{DMI}}^{\mathrm{interfacial}} = D[\mathbf{m}_z(\nabla \cdot \mathbf{m}) - (\mathbf{m} \cdot \nabla)\mathbf{m}_z], \tag{1.26}$$

with DMI strength D. Note, that the energy depends only on the gradient of the magnetisation along the directions parallel to the interface. This equation reveals the chiral character of the DMI. The energy density:

$$w_{\mathrm{DMI}} = -\frac{1}{2}\mathbf{M} \cdot \mu_0 \cdot \mathbf{H}_{\mathrm{DMI}}, \tag{1.27}$$

can be calculated starting from the corresponding effective field term [25]:

$$\mathbf{H}_{\mathrm{DMI}} = -\frac{2D}{\mu_0 \cdot \mathrm{M_s}} \cdot (\nabla \times \mathbf{M}) \tag{1.28}$$

This expression of the interfacially-induced DMI energy density and DMI magnetic field is the one that will be used throughout this thesis in micromagnetic simulations.

References

[1] C. Kittel, *Introduction to Solid State Physics*, 8th ed. New York: Wiley, 2004.

[2] S. Chikazumi, *Physics of Ferromagnetism*. New York: Oxford University Press, 1997. DOI: 10.1007/978-3-642-25583-0.

[3] W. Heisenberg, “Zur Theorie des Ferromagnetismus,” *Zeitschrift für Physik*, vol. 49, no. 9-10, pp. 619–636, 1928. DOI: 10.1007/BF01328601.

[4] D. J. D. J. Griffiths, *Introduction to quantum mechanics*. Pearson Prentice Hall, 2005, p. 468.

[5] D. D. Stancil and A. Prabhakar, *Spin Waves*. Boston, MA: Springer US, 2009. DOI: 10.1007/978-0-387-77865-5.

[6] S. Blundell, *Magnetism in Condensed Matter*, ser. Oxford Master Series in Condensed Matter Physics. OUP Oxford, 2001, p. 238.

[7] A. Aharoni, *Introduction to the theory of ferromagnetism*. New York: Oxford University Press, 2000.

[8] R. Skomski, *Simple Models of Magnetism*. New York: Oxford University Press, 2008, vol. 9780198570. DOI: 10.1093/acprof:oso/9780198570752.001.0001.

[9] F. Bloch and G. Gentile, “Zur Anisotropie der Magnetisierung ferromagnetischer Einkristalle,” *Zeitschrift für Physik*, vol. 70, no. 5-6, pp. 395–408, 1931. DOI: 10.1007/BF01339586.

[10] W. Döring, *Ferromagnetism / Ferromagnetismus*, H. P. J. Wijn, Ed., ser. Encyclopedia of Physics / Handbuch der Physik. Berlin, Heidelberg: Springer Berlin Heidelberg, 1966, vol. 4 / 18 / 2, pp. 341–437. DOI: 10.1007/978-3-642-46035-7.

[11] J. Leliaert, M. Dvornik, J. Mulkers, *et al.*, “Fast micromagnetic simulations on GPU - Recent advances made with mumax3,” *Journal of Physics D: Applied Physics*, vol. 51, no. 12, p. 123 002, 2018. DOI: 10.1088/1361-6463/aaab1c.

[12] I. Dzyaloshinsky, “A thermodynamic theory of “weak” ferromagnetism of antiferromagnetics,” *Journal of Physics and Chemistry of Solids*, vol. 4, no. 4, pp. 241–255, 1958. DOI: 10.1016/0022-3697(58)90076-3.

[13] T. Moriya, “Anisotropic superexchange interaction and weak ferromagnetism,” *Physical Review*, vol. 120, no. 1, pp. 91–98, 1960. DOI: 10.1103/PhysRev.120.91.

[14] H. Yang, A. Thiaville, S. Rohart, *et al.*, "Anatomy of Dzyaloshinskii-Moriya Interaction at Co/Pt Interfaces," *Physical Review Letters*, vol. 115, no. 26, 2015. DOI: 10.1103/PhysRevLett.115.267210.

[15] G. Müller, "Exploration of skyrmion energy landscapes," PhD thesis, 2015.

[16] O. Meshcheriakova, S. Chadov, A. K. Nayak, *et al.*, "Large noncollinearity and spin reorientation in the novel Mn2RhSn Heusler magnet," *Physical Review Letters*, vol. 113, no. 8, p. 087 203, 2014. DOI: 10.1103/PhysRevLett.113.087203.

[17] C. Weingart, N. Spaldin, and E. Bousquet, "Noncollinear magnetism and single-ion anisotropy in multiferroic perovskites," *Physical Review B*, vol. 86, no. 9, p. 094 413, 2012. DOI: 10.1103/PhysRevB.86.094413.

[18] C. Abert, "Micromagnetics and spintronics: models and numerical methods," *The European Physical Journal B*, vol. 92, no. 6, p. 120, 2019. DOI: 10.1140/epjb/e2019-90599-6.

[19] A. Fert and P. M. Levy, "Role of anisotropic exchange interactions in determining the properties of spin-glasses," *Physical Review Letters*, vol. 44, no. 23, pp. 1538–1541, 1980. DOI: 10.1103/PhysRevLett.44.1538.

[20] A. Fert, V. Cros, and J. Sampaio, "Skyrmions on the track," *Nature Nanotechnology*, vol. 8, no. 3, pp. 152–156, 2013. DOI: 10.1038/nnano.2013.29.

[21] G. Chen, J. Zhu, A. Quesada, *et al.*, "Novel chiral magnetic domain wall structure in Fe/Ni/Cu(001) Films," *Physical Review Letters*, vol. 110, no. 17, p. 177 204, 2013. DOI: 10.1103/PhysRevLett.110.177204.

[22] N. Nagaosa and Y. Tokura, "Topological properties and dynamics of magnetic skyrmions," *Nature nanotechnology*, vol. 8, no. 12, pp. 899–911, 2013. DOI: 10.1038/nnano.2013.243.

[23] E. Turgut, H. Paik, K. Nguyen, *et al.*, "Engineering Dzyaloshinskii-Moriya interaction in B20 thin-film chiral magnets," *Physical Review Materials*, vol. 2, no. 7, p. 074 404, 2018. DOI: 10.1103/PhysRevMaterials.2.074404.

[24] A. Fert, N. Reyren, and V. Cros, "Magnetic skyrmions: Advances in physics and potential applications," *Nature Reviews Materials*, vol. 2, no. 7, p. 17 031, 2017. DOI: 10.1038/natrevmats.2017.31.

[25] Y. M. Luo, C. Zhou, C. Won, *et al.*, "Effect of Dzyaloshinskii-Moriya interaction on magnetic vortex," *AIP Advances*, vol. 4, no. 4, 2014. DOI: 10.1063/1.4874135.

Chapter 2

The development of magnetisation

During the last decades, magnetic materials have played a fundamental role in information technology, enabling the development and bringing to unprecedented levels our ability to share information, with an outstanding example of magnetic hard disk drivers. A common feature of the development of future devices, especially in spintronic and magnonics, is the drive towards smaller dimensions and lower power consumption. This ongoing trend of miniaturisation and optimisation has led to structure size in the nanometer regime, where the film thicknesses may be even as low as a few atomic layers [1].

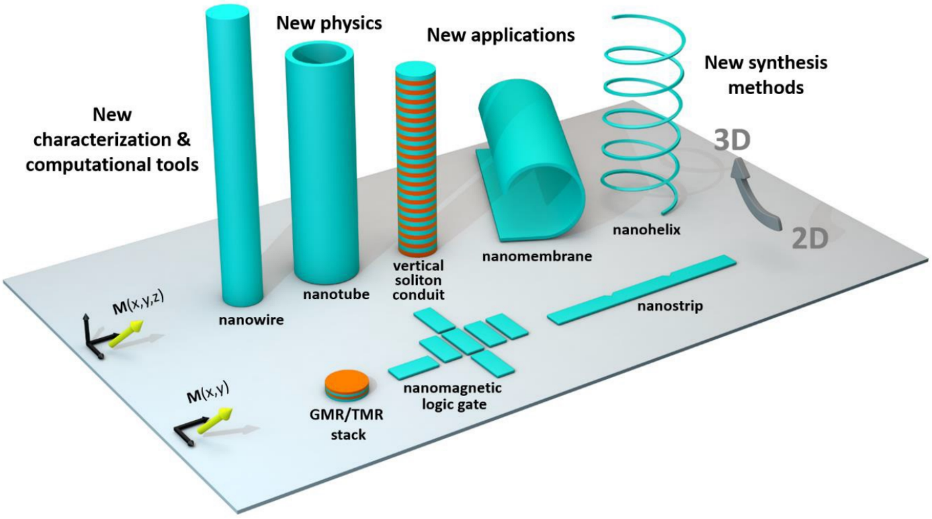

Fig. 2.1 Transitioning from two-dimensional (2D) to three-dimensional (3D) nanomagnetic systems requires new synthesis methods, new characterisation techniques, and new computational tools. This transition opens a new set of possible applications, as well as new physical phenomena arising from the interplay between 3D properties and magnetisation at the nanoscale. Reproduced from open access article distributed under the Creative Commons Attribution License [1].

Magnonics is an emerging field pretending to bring novel ideas for production ultralow power consumption logic circuits, in which the flow of *spin waves* (see section 2.2.4), rather than electric charges, transmits and processes information. Waves, including spin waves, excel at encoding information via their phase and interference. This enables a number of input signals to be processed in one unit, which offers the promise of multi-input multi-output logic gates [2, 3]. Today, going beyond hard disk media, magnetic nanodevices offer key advantages, such as non-volatility and low power consumption, with technologies such as Spin-Transfer Torque Magnetic Random-Access Memory (STT-MRAM) already close to large-scale production [1, 4]. Today, to find structures with more complex magnetic configurations and unprecedented properties scientist makes the expansion of nanomagnetism into three dimensions. (see Fig. 2.1). However, in the literature is a lack of theoretical and experimental works presenting the 3D properties of magnetic nanostructures due to both increased difficulty of their theoretical treatment and currently limited outlook for their fabrication and experimental investigation. In recent years, many new experimental techniques have been developed to raise hopes for new and promising experiments [5, 6]. The latest papers about the 2D and 3D magnonics nanostructures shows, that magnonic technology is not yet at such an advanced stage of development, but it raises hopes that it will bring new challenges, as well as promises for new magnetic configurations, physics, and higher areal density of unit elements in complex architectures [2].

2.1 Magnetisation configurations

Ferromagnetic materials belong to important class of solids which have played an indispensable role in data storage technologies. Their utility for technological applications stems from the basic physical property of ferromagnets, to exhibit spatially ordered magnetisation patterns under a variety of conditions. The physics of magnetic configurations have been studied for a long time in different 2D and 3D shapes. Usually only tiny nanomagnets, magnets subjected to a strong uniform external field or hard magnets are uniformly magnetised. Larger soft magnets are split into several magnetic domains, regions with uniform magnetisation, however, with different magnetisation direction in the neighbouring regions (*magnetic domains*). The mechanisms behind the magnetic domain formation can be quite complex, but usually domain patterns may be understood from the energetic considerations based on the micromagnetic modelling framework. The magnetic configuration in patterned films, like magnetic **antidots, nanodots, bi-layers, multilayers, nanostripes nanowires**, have shown interesting effects not present in homogeneous films. The studies of static and dynamic properties of the magnetisation have also been performed. Special attention is devoted to the application of magnonic crystals in data processing and information technologies. The therm, magnonic crystals, was introduced by Puszkarski and Krawczyk in 2001 [8] and independently by S. Nikitov et al. [9], and means an artificial magnetic media with properties characterised by periodic order, and are of interest in both basic physics and application magnonics devices. The spectra of spin-wave excitations in magnonic crystals are significantly different from spectra of uniform media and exhibit features such as *band gaps*, where spin waves are not allowed to propagate.

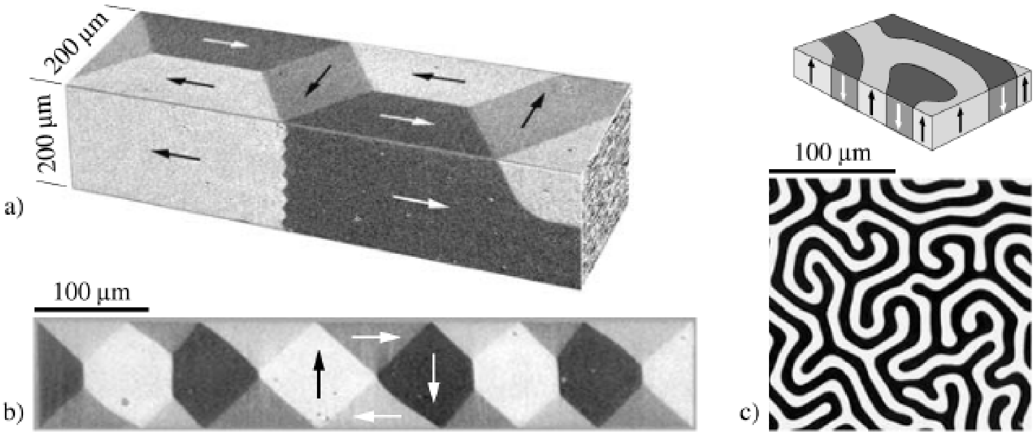

Fig. 2.2 Domains observed with the magnetooptical methods. (a) Image from two sides of an iron stripe. (b) Domains in an FeNi alloy. (c) Domains in a single-crystal garnet together with sketch of the domain structures. The direction of magnetisation in the domains are indicated by arrows. Reprinted by permission from Springer Nature, Domain Observation Techniques [7].

2.1.1 Magnetic domains

Figure 2.2 shows the magnetic microstructures in the absence of the external magnetic field observed using magnetooptical methods. In all cases, uniformly magnetised regions, so-called *magnetic domains*, are observed to appear spontaneously within otherwise unstructured samples. A simple picture of magnetic domain formation in a perpendicular magnetic system due to the interplay of magnetostatic, anisotropy and exchange energies is shown in Fig. 2.3. If we consider that initially the magnetic material consists of a single domain of uniform magnetisation (Fig. 2.3 (a)) pointing along the perpendicular to the film plane direction (due to the anisotropy) magnetic charges appear at two opposite edges creating a strong *demagnetising field* in the system and increasing the *magnetostatic energy* (see, Chapter 1.2.3). In order to minimise this energy, the magnetic structure gets divided into *magnetic domains* forming *domain walls* between them (Fig. 2.3 (b)).

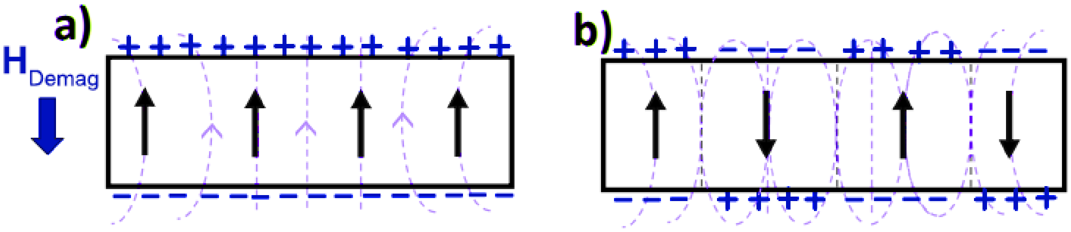

Fig. 2.3 The schematic diagrams of magnetic domain wall formation in a plane film. a) In a single domain case, the magnetisation aligns along one direction, creating magnetic charges at two opposite edges of the rectangular slab. These magnetic charges in turn create a strong demagnetisation field inside the magnetic material. b) To minimise its total energy, magnetic domains are formed, so that magnetic charges created by one magnetic domain get cancelled by the magnetic charges in the adjacent domains.

The formation of domains results from competition of various energy contributions, mainly *exchange*, *magnetostatic* (also called *shape anisotropy*), and *anisotropy energy*. In a ferromagnet the *anisotropy energy* and *exchange energy* is minimal when the magnet is magnetised homogeneously along the easy axis. The final structure minimises the total energy by reducing the dipolar energy of the system at the cost of domain wall energy (which increases *anisotropy* and *exchange*). It also depends on the magnetic history of the sample: during a hysteresis cycle, sample may display different amount, sizes and even types of domains. Usually larger number of domains can be obtained upon demagnetisation of a sufficiently large sample. Domain theory is very complex and there is no single and simple origin of domain formation [7].

2.1.2 Domain walls

A magnetic domain describes a region where the magnetisation is uniform and usually parallel to an easy magnetisation axis while the region separating the two domains is called a *domain wall*. Thus, the domain walls are regions of magnetisation where the magnetic moment or spin vector rotates as a function of position. Theoretical study of magnetic domain walls began with the work of Bloch [10], Landau and Lifshitz [11], and Néel [12], who first derived the basic static internal magnetisation structures.

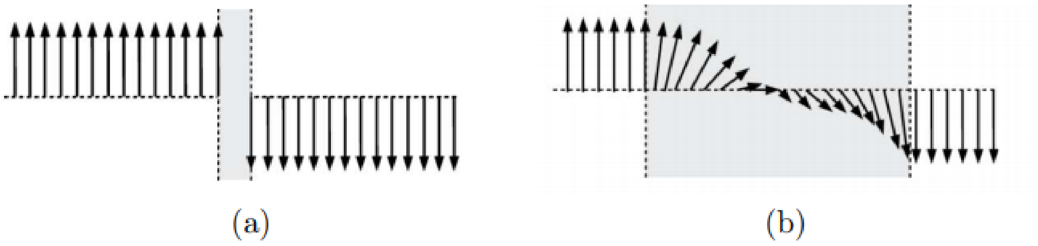
(a) (b)

Fig. 2.4 A narrow domain wall with an abrupt transition between the two neighbouring domains, (a) represents a high cost in exchange energy while a wide domain wall (b) represents a high cost in anisotropy energy. Figure reproduced base on the figure from Ref. [0].

Two domains separated by a narrow domain wall are shown in Fig. 2.4 (a) with the magnetisation along the easy anisotropy axis. Such an abrupt change of the magnetisation represents a high cost in exchange energy. In Fig. 2.4 (b) is shown a smooth angular dependence of the magnetisation between two oppositly orientated domains occurring in a wide domain wall. This configuration is reducing the exchange energy.

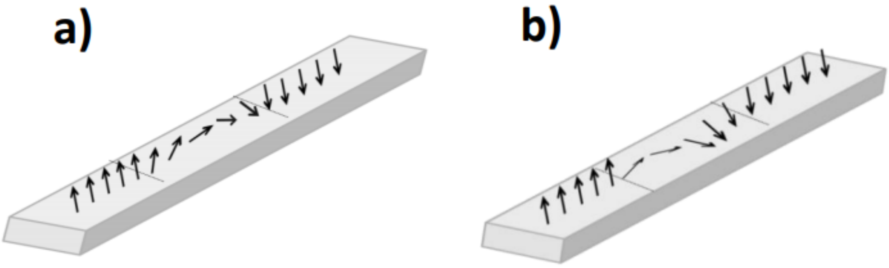

Fig. 2.5 The schematic diagrams of (a) Néel and (b) Bloch domain wall in a stripe with perpendicular magnetic anisotropy. a) In the Néel domain wall the magnetisation inside the domain wall varies its direction along the domain wall length. (b) Here, the magnetisation rotates out of plane to the domain wall length. Figure reproduced base on the figure from Ref. [0].

Two basic types of domain wall can be distinguished: *Bloch* and *Néel* domain wall. If the magnetisation rotates in the plane containing the magnetisation of the two domains, it is called a Néel domain wall. For a Bloch domain wall, the magnetisation rotates perpendicular to this plane. The domain wall type, depends mainly on the film thickness where Bloch walls are more common in bulk films, while Néel walls are often observed in thin films. In the case of magnetic thin films, the Bloch walls have an additional magnetostatic energy due to the surface magnetic charges, which increases with a decrease of film thickness. On the other hand, the magnetostatic energy of the Néel wall decreases with a decrease of film thickness [13].

Schematic diagram of these two domain walls is shown in Fig. 2.5. The domain wall structure and its dimensions result mainly from the two competing energy terms. The anisotropy try to minimise the dimensions of the domain wall, since the domain wall has components of its magnetisation perpendicular to the easy axis. The exchange interaction, the interaction that promotes the parallel alignment of the magnetisation, favours a wide domain wall. These opposing interactions lead to a characteristic domain wall width [13]:

$$\Delta_{\mathrm{DW}} = \sqrt{\frac{A_{\mathrm{ex}}}{K_{\mathrm{eff}}}}, \tag{2.1}$$

where:

$$K_{\mathrm{eff}} = K_{\mathrm{u}} + K_{\mathrm{shape}}, \tag{2.2}$$

and A_{ex} is the strength of the exchange interactions (Eq. 1.11). The total energy associated with the domain wall in this case is [13]:

$$E_{\mathrm{DW}} = 4\sqrt{A_{\mathrm{ex}} \cdot K_{\mathrm{eff}}}. \tag{2.3}$$

2.1.3 Magnonic crystals

Periodic modulation of the material properties is a well-known concept in photonics. This concept was proposed separately by Yablonovich [14] and John [15] in 1987 who considered the periodical variation of the dielectric constant. Furthermore, this idea was used by Puszkarski and Krawczyk [8, 16] to create similar crystals where instead of light (or electromagnetic waves) SWs were used as the carriers of information. They proposed magnonic crystals (whose name refers to the spin-wave quasiparticles, magnons), whose are materials with periodically modulated magnetic properties, where the SWs band structure [17–19] consists of intervals of allowed SW frequencies and forbidden gaps in which there are no allowed magnonic states [2, 9]. A large area of modern emerging spintronic fields deals with the data transfer and processing based on the magnon waves propagation [20]. In this case, magnonic crystals [21, 22] expected to be a the key elements of the magnonic spintronic devices including resonators, generators, filters, wave-guides [20, 21, 23]. The latter can be created by means of periodical arrangement of several different magnetic materials [21, 24, 25] or by using one material with periodically modulated geometrical parameters [21, 26, 27] including arrays of interacting magnetic strips [28, 29] or dots [23, 30]. The periodical magnetisation patterns can be also considered as a magnonic crystal, e.g. the DMI induced helical structure [30, 31] or skyrmion lattice [32–36].

2.1.4 Magnetic skyrmions

A rough categorisation of magnetisation configuration by the different possible orders of the magnetisation is the separation into collinear and non-collinear magnetism. Collinear magnetism refers to the magnetic order where the spins align in a common direction, as it is the case in typical ferromagnets under full saturation. The helimagnets, in that sense, are the prime example for noncollinear magnetism as the quantisation axis turns steadily from site to site. Helical magnets are currently of high interest[31, 37], because they serve as model systems for complex magnetic ordering, yielding interesting properties to observe whirling magnetic configurations like magnetic skyrmions [38–40].

Magnetic skyrmions (see Fig. from 2.6 to 2.9) are topologically non-trivial inhomogeneous magnetisation configurations. They possess a *topological charge* and they are the smallest as possible, but energetically stable, perturbation of a uniform magnetisation [41–43]. Such skyrmions are quasi-particles existing in magnetic materials and they give rise to emergent electrodynamics that cannot be described with standard Maxwell's equations [44–46]. Usually to stabilise a skyrmion, an additional to the isotropic Heisenberg exchange, an antisymmetric exchange term in the total energy (DMI, see chapter 1.2.6), is required.

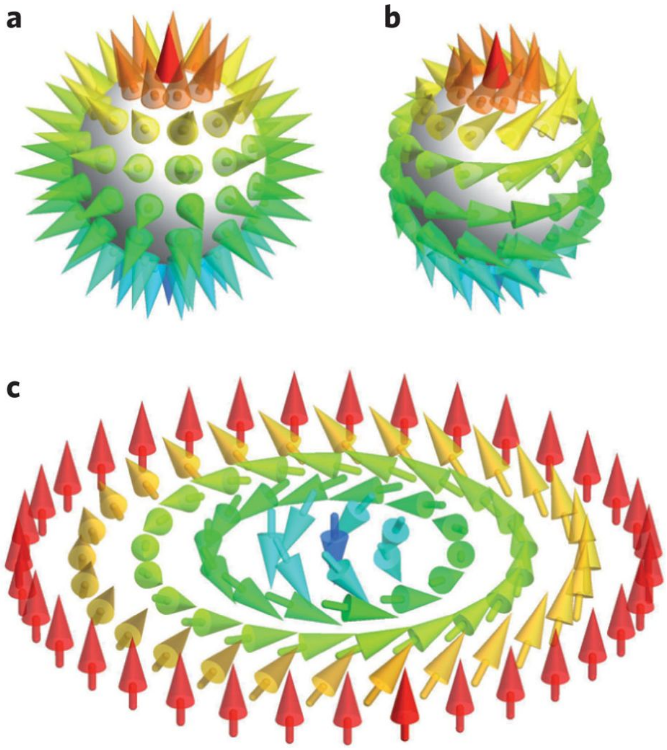

Fig. 2.6 Visualisations of skyrmions, (a) and (b) illustrate 3D skyrmions that can be found in bulk materials, (c) illustrates a 2D skyrmion in thin film. Figure reproduced with permission from: Ref. [47], K. Everschor, Univ. of Köln.

Skyrmion can be found in bulk helimagnetic materials with cubic B20 crystal lattice (bulk DMI), and ferromagnet/heavy metal multilayers with interfacial DMI [48, 49].

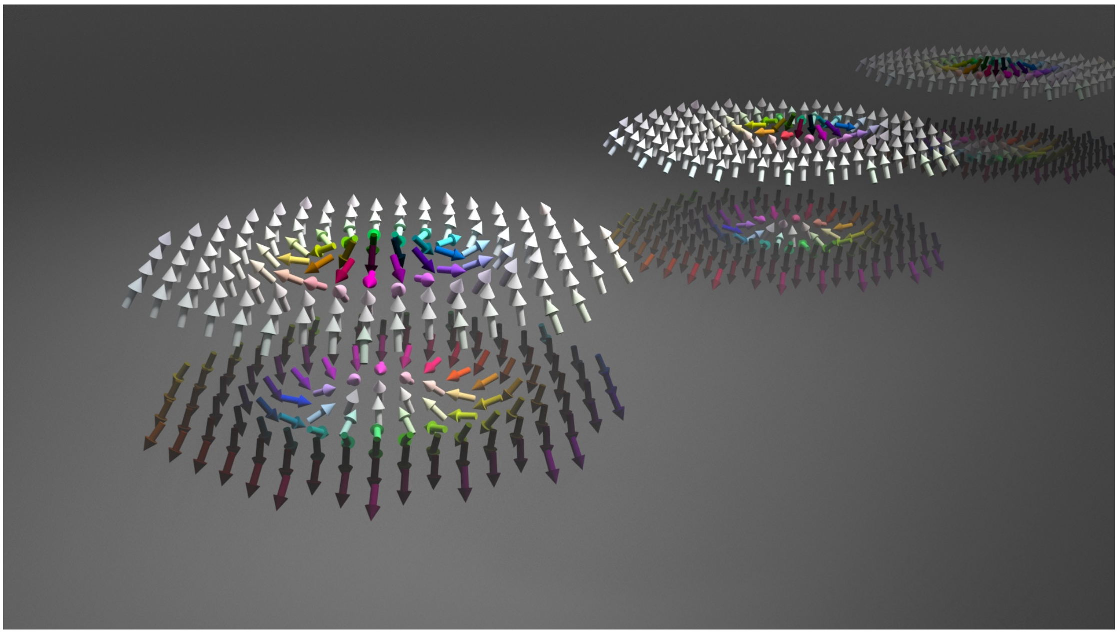

Fig. 2.7 Magnetic skyrmions are topologically-protected quasiparticle-like vortices of spins in chiral magnets, typically of a nanoscale size. On the figure: artistic visualisation of the individual antiferromagnetic skyrmions in nanodots are visible.

This interaction favours non-collinear alignment of the atomic spins with specific angle between them. In this sense, skyrmions are chiral spin structures with a whirling configuration [50]. Both types of DMI leads to favour more than the single domain state, the chiral skyrmion state, either in *ground state* or *metastable state* (a state in a local energy minimum). Their stability and dynamic properties strongly depend on

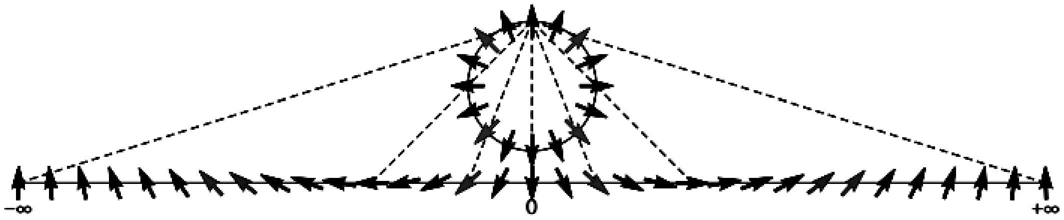

Fig. 2.8 Graphical representation of a spherical spin distribution relevant to the 2D Néel type skyrmion shape, and its stereographic projection.

their topological properties, thus called *topological protection* [51]. But why we are telling, they are a topologically protected? To answer to this question we can say, that it is impossible to create or destroy skyrmions, i.e., the magnetisation field can not be transformed in a continuous manner between the single domain state (uniformly magnetised) and a skyrmion state [52]. A topological transition requires the formation of a *Bloch point* [53] (the two points with opposite magnetisation infinitely close together, which seems to be a nonphysical process due to non-zero strength of the exchange interactions) [54, 55]. This claim is absolute within the limit of continuous field theory.

The atomistic nature of materials relaxes absolute prohibition of transformation to a energetically costly process. This is the reason for stability of the magnetic skyrmions.

Skyrmions are called *Néel-type* (Fig. 2.9 (a)) or *Bloch-type* (Fig. 2.9 (b)) with (Q = 1), in dependence on the orientation of the rotary plane of the magnetisation when going from the core to the outside rim. So far, various descriptions for magnetic skyrmions have been proposed, however, most of them include the notion of topology as defined in micromagnetics, where the continuous model is used. The magnetic skyrmions are characterised by a few topological invariants (also called as a *skyrmion numbers*), which are non-zero integer numbers relatively robust against moderate perturbations. The three main numbers define the skyrmions, they are the *topological charge Q* which define how many times magnetic moments wrap around a unit sphere (see Fig. 2.8), and the *helicity h*, which can be defined as the angle of the global rotation around the z-axis that relates various skyrmions (for the Néel skyrmion, helicity is zero), *polarity p* which describes whether the magnetisation points in the positive $(p = 1)$ or negative $(p = -1)$ z-direction at the centre of the skyrmion (but does not affect the topological charge). The difference in helicity distinguishes Bloch and Néel skyrmions from one another. Thus, in general magnetic skyrmions can be described with a non-zero integer value of the topological charge, expressed as [56]:

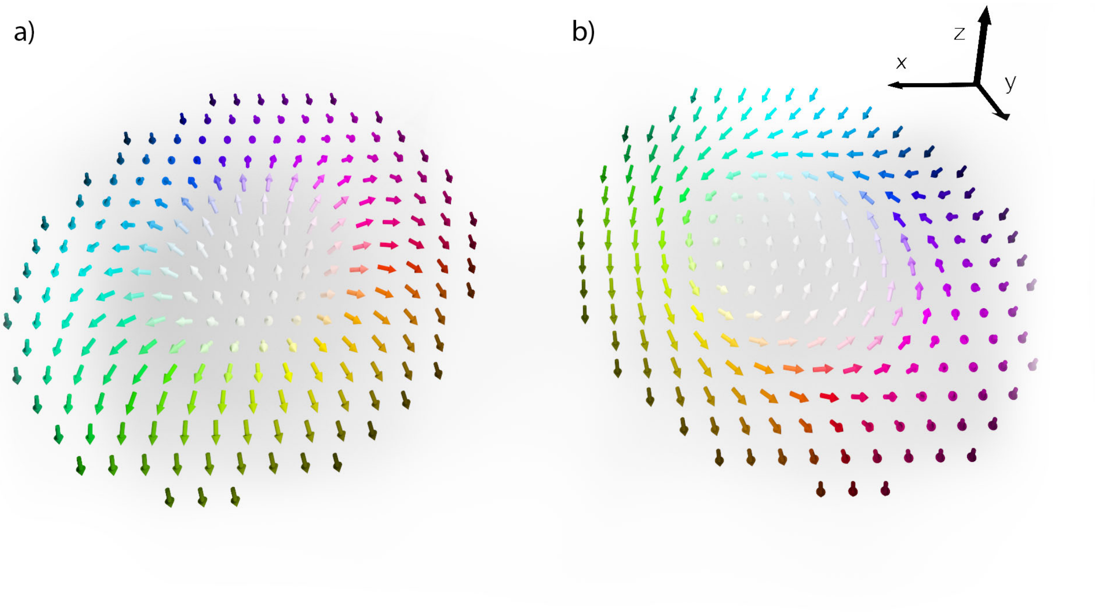

Fig. 2.9 Graphical representation of the isolated Néel (a), and Bloch (b) type skyrmion.

$$Q = \frac{1}{4\pi} \int \mathbf{m} \cdot \left(\frac{\partial \mathbf{m}}{\partial x} \times \frac{\partial \mathbf{m}}{\partial y} \right) dx\, dy. \tag{2.4}$$

By construction, the topological charge is an integer number, which for topologically nontrivial smoothly-varying field configurations attains values $0, \pm 1, \pm 2, \pm 3, \ldots$.

Among the several types of 2D skyrmions, the lowest-charged skyrmions observed in the bulk chiral magnets and thin magnetic films are the *Bloch-type* and *Néel-type*

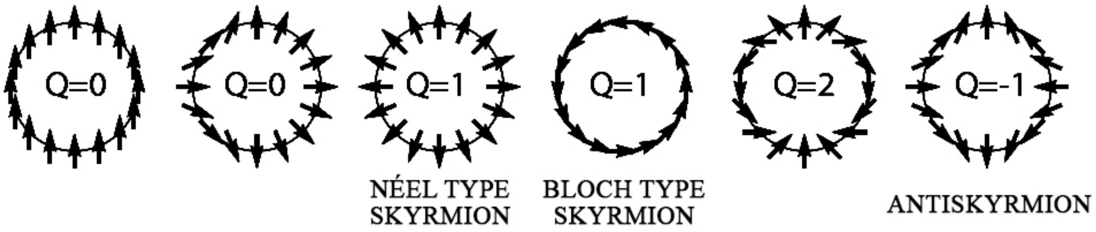

Fig. 2.10 Graphical representation of the magnetisation with different topological charge.

skyrmions, topologically equivalent (through a continuous mapping) to a hedgehog-like ”hairy sphere”. The bulk DMI typically leads to stability of a Bloch skyrmion, where magnetisation rotates perpendicular to the radial direction moving away from the centre of the skyrmion. Whereas, uniaxial interfacial DMI increases the stability of a Néel skyrmion, where magnetisation rotates in the plane parallel to radial direction.

The skyrmion number of each configuration also characterises the number of magnetic monopoles therein (see Fig. 2.10). The corresponding spin configuration on the unit sphere is similar to the magnetic vortex and therefore, this type of skyrmion in chiral B20 bulk magnets is also named a vortex-like skyrmion. As a matter of fact, magnetic vortices in magnetic nanostructures have half of the topological skyrmion number $Q = \pm\frac{1}{2}$. This can be determined again by projecting each individual spin of the magnetic vortex onto the unit sphere which occupies (upper/lower) half of the sphere, that correspondingly yields half of the skyrmion number. As a result, the skyrmion number can be used to identify the topological distinction of different types of the spin texture.

On the other hand, magnetic textures stabilised by DMI can also have opposite topological charge and polarity $(Q = -p)$. Such magnetic textures are referred to as *antiskyrmions* [57]. Antiskyrmions (see Fig. 2.10) can be stabilised by bulk DMI with lower symmetry, as was first predicted [44], and later realised experimentally at room temperatures in Heusler compounds with D2d symmetry [58].

2.2 Static and dynamic properties of the magnetisation

The experimental and theoretical studies of the patterned magnetic nanostructures have gained great interest in the scientific community, because of their potential applications in magnetic data storage, logic, sensors, microwave devices and various biomedical applications. Progress made during the last decade in handling and the analysis of matter leads to the elaboration of well-controlled artificial magnetic structures from micron to nanometer size [59–63]. These structures, which usually present arrays of separated magnetic items, are attracting increasing interest due to their potential applications [2, 17, 20, 62, 64–66].

2.2.1 The Landau-Lifshitz-Gilbert equation

In micromagnetics, the magnetisation dynamics is described by the *Landau-Lifshitz equation* (LL) that was originally proposed in [11]. This equation describes the spatially resolved precessional motion of the magnetisation in an effective field, where a magnetization vector $\mathbf{M}$ in a magnetic field $\mathbf{H}_{\text{eff}}$ is subjected to a torque $\mathbf{\Gamma} = -\gamma_e \cdot \mathbf{M} \times \mu_0 \cdot \mathbf{H}_{\text{eff}}$, where γ_e is the electron *gyromagnetic ratio*. Since the magnetic moment is proportional to an inherent angular momentum, the magnetic moment will change in time due to this exerted torque: $\partial_t \mathbf{M} \propto \mathbf{\Gamma}$. The equilibrium state is obtained when the torque is equal to 0, i.e., when the magnetic vector $\mathbf{M}$ is aligned along the effective field $\mathbf{H}_{\text{eff}}$ [59, 67].

Landau-Lifshitz assumed that the absolute value of the magnetisation is constant, so that the described dynamics of the magnetisation will have a precessional form. By analogy with the classical equation of precession of a moment in an external field, they derived the equation that includes contributions from all of the magnetic energies described above. This equation is called the Landau-Lifshitz equation and is given by:

$$\frac{\partial \mathbf{M}}{\partial t} = -\gamma_e \cdot \mathbf{M} \times \mu_0 \cdot \mathbf{H}_{\text{eff}} = -\gamma_G \cdot (\mathbf{M} \times \mathbf{H}_{\text{eff}}), \tag{2.5}$$

The constant γ_G is the *Gilbert gyromagnetic ratio*, a positive number, proportional to the electron gyromagnetic ratio γ_e. The later is give, in the SI system of units by $\gamma_e = 1.7595 \cdot 10^{11}$ rad/s^{-1}T^{-1}. The Gilbert gyromagnetic ratio is therefore [67]:

$$\gamma_G = \mu_0 \gamma_e = 2.2127606 \times 10^5 \text{mA}^{-1}\text{s}^{-1}. \tag{2.6}$$

A schematic representation of the magnetisation precession is shown in Fig. 2.11.

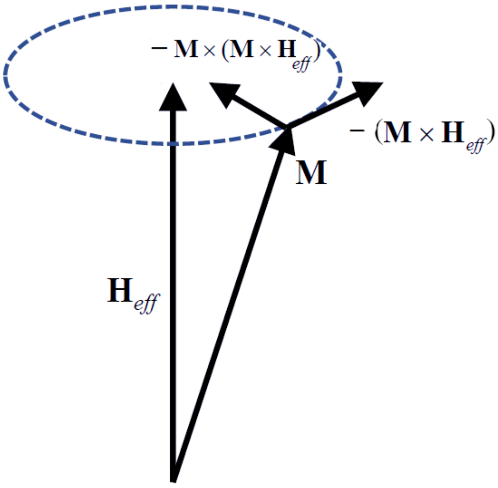

Fig. 2.11 Schematic precessional motion of the magnetisation $\mathbf{M}$ around the effective field $\mathbf{H}_{\text{eff}}$. $-\gamma(\mathbf{M} \times \mathbf{H}_{\text{eff}})$ is perpendicular to the field and the magnetisation, and describes the precession. If the motion is damped, the radius of precession is continuously decreased until the $\mathbf{M}$ and $\mathbf{H}_{\text{eff}}$ are aligned parallel.

Similar to the single magnetic moment, Eq. (2.5) predicts that the magnetisation **M** precesses indefinitely around the effective field without aligning. However, in real systems, such motion is not observed and the magnetisation does align along the effective field. This is due to *relaxation* process. To describe relaxation the damping term is added to the equation 2.5 to allow for a phenomenological description of the energy dissipation [67, 68]:

$$\frac{\partial \mathbf{M}}{\partial t} = -\gamma_{\mathrm{G}} \cdot (\mathbf{M} \times \mathbf{H}_{\mathrm{eff}}) + \frac{\alpha_{\mathrm{G}}}{\mathrm{M_s}} \cdot \left(\mathbf{M} \times \frac{\partial \mathbf{M}}{\partial t}\right), \tag{2.7}$$

where α_{G} is a phenomenological damping parameter. Equation 2.7 is alternative form of damping torque, formulated by Gilbert [69] and the torque equation is with this term called *Landau-Lifshitz-Gilbert equation* (**LLG**). Both forms of equations, Landau and Gilbert, are equivalent, thus we can transform the Landau formulation 2.7 to Gilbert form by replacing α by $\alpha = \frac{\alpha_{\mathrm{G}} \cdot \gamma_{\mathrm{G}}}{1+\alpha_{\mathrm{G}}^2}$ and renormalise the giromagnetic factor $\gamma = \frac{\gamma_{\mathrm{G}}}{1+\alpha_{\mathrm{G}}^2}$ [67]:

$$\frac{\partial \mathbf{M}}{\partial t} = -\gamma (\mathbf{M} \times \mathbf{H}_{\mathrm{eff}}) + \frac{\alpha}{\mathrm{M_s}} \cdot \Big(\mathbf{M} \times (\mathbf{M} \times \mathbf{H}_{\mathrm{eff}})\Big). \tag{2.8}$$

The first term on the right hand side of Eq. 2.8 corresponds to magnetic precession while the second term represents the transverse relaxation towards the effective field. The precessional torque is perpendicular to both $\mathbf{H}_{\mathrm{eff}}$ and **M**, while the damping torque has a component along the effective field, driving the magnetisation towards $\mathbf{H}_{\mathrm{eff}}$ as sketched in Fig. 2.11.

All numerical studies presented in this thesis have been performed using the LLG equation.

2.2.2 Length-scales

The *exchange length* l_{ex}, is a characteristic parameter of the ferromagnetic material and indicates the distance over which the parallel alignment of the spin magnetic moments is energetically favourable. This parameter has in literature two different meanings. In one, the l_{ex} depends on the saturation magnetisation of the material, $\mathrm{M_s}$ and the exchange stiffness constant, A_{ex} [7]:

$$l_{\mathrm{ex}} = \sqrt{\frac{2A_{\mathrm{ex}}}{\mu_0 M_s^2}}. \tag{2.9}$$

In the second it is defined as

$$l_{\mathrm{w}} = \sqrt{\frac{A_{\mathrm{ex}}}{K_{\mathrm{u}}}}. \tag{2.10}$$

The characteristic length l_{ex} defining the scale when the system is dominated by exchange interactions, i.e, when the length is smaller than l_{ex} , while l_{w} defines the characteristic length scale when magnetocrystalline anisotropy dominates. Objects smaller than the exchange length will be most probably uniformly magnetised since they cannot host a magnetic domain wall due to their dimensions.

2.2.3 Ferromagnetic resonance

In 1946, Griffiths [70] experimentally observed the *ferromagnetic resonance* (FMR) for the first time. In 1947, Kittel [71, 72] derived the formula for the FMR frequency in terms of external magnetic field and the internal magnetic parameters famously known as *Kittel formula*. Uniform precession is characterised by the in-phase motion of magnetic moments within whole a magnetic system. From this point of view it is possible to reduce the Landau-Lifshitz equation to the case where only magnetic moment precess in an internal field. Then the frequency of uniform precession for in plane magnetised thin film is given by:

$$f = \frac{\gamma}{2\pi} \cdot \sqrt{(H_0 + (N_x - N_z) \cdot \mathrm{M_s}) \cdot (H_0 + (N_y - N_z) \cdot \mathrm{M_s})}, \tag{2.11}$$

where N_x, N_y and N_z are the diagonal components of the demagnetising tensor in the x,y and z directions respectively. Here, magnetocrystalline or other forms of magnetic anisotropy are not considered, which may be present in the system. Thus, for the magnetic thin films the frequency of uniform precession depends upon the value of the saturation magnetisation $\mathrm{M_s}$. This property is widely used in experiments to determine the value of the magnetisation of saturation of the sample, just by measuring the frequency of uniform precession. Finally the frequency of the ferromagnetic resonance does not depend on the exchange stiffness, since all magnetic moments of the system are oriented along the same direction and precess in-phase. Thus the energy of the exchange interaction remains of zero value. Such an approximation is a widely used in analytical approach and is called the *macrospin approximation*.

2.2.4 Spin waves dispersion relation

Magnetic moments in a material can precess about their equilibrium direction in the presence of a magnetic field. They are coupled to each other through dipole-dipole and exchange interactions. The result of these interactions can be seen if one excites some magnetic moments locally, the precession motion of those moments can propagate spatially in the magnetic material like a wave. This wave is therefore a collective excitation of magnetic moments and is termed as a **spin wave** (SW). In the long-wavelength regime, the phase difference between consecutive spins is rather small, the spin-wave energy is primarily dominated by dipolar energy and the spin waves are referred to as dipolar-dominated or *magnetostatic spin waves*. In contrast, the short-wavelength spin waves are governed by exchange interaction and known as *exchange spin waves*. The properties of spin waves and their potential applications form emerging field of physics called magnonics. Spin waves have dispersive character and their dispersion characteristics $f(k)$, where k is a wavenumber depends strongly on the strength and direction of the applied magnetic field. The dispersion relations of dipolar modes can be calculated analytically by solving Landau–Lifshitz equation 2.8 together with Maxwell equations in magnetostatic approximation, which describe dipolar interactions. As mentioned in 1.1.2, the magnetisation can be written as:

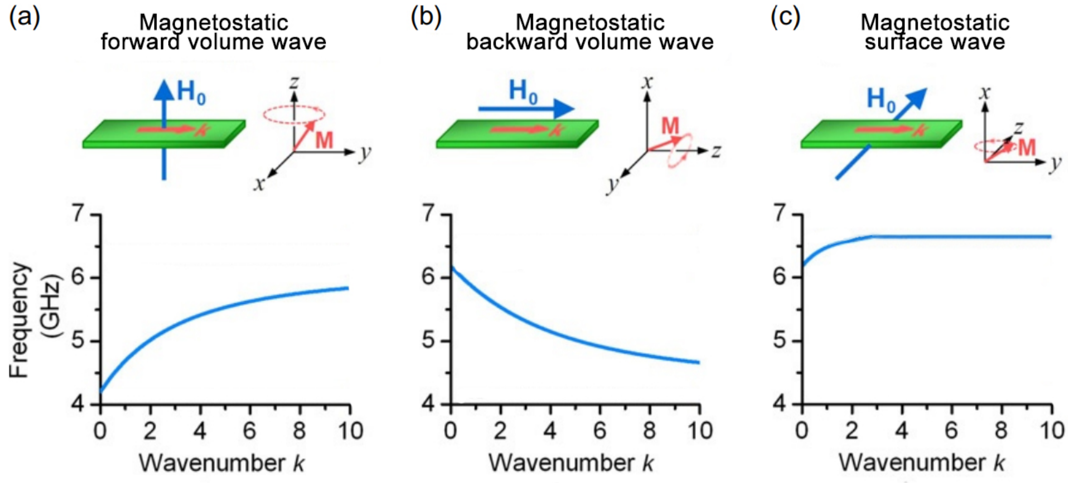

Fig. 2.12 Examples of the dispersion curves for: (a) magnetostatic forward volume waves; (b) magnetostatic backward volume waves; and (c) magnetostatic surface waves. Field and film configurations, magnetisation precession, and dispersion diagrams for three classes of spin waves in a long and narrow magnetic thin film strip. In each dispersion diagram, the curve shows the spin-wave frequency as a function of wavenumber k, and the horizontal dashed lines show three characteristic frequencies. Results are obtained for a magnetic film with following parameters: exchange stiffness $A_{ex} = 1e^{-11}$ J/m, magnetisation saturation $M_s = 1.4e6$ A/m, $\mathbf{H}_0 = 0.15$ T. Figure reproduced based on the figure from [73].

$$\mathbf{M}(\mathbf{r},t) = M_s + \mathbf{m}(\mathbf{r},t). \tag{2.12}$$

Here, for small angles of precesssion $\mathbf{M} \ll M_z$, $M_z \approx M_s$. Thus, $\mathbf{m}(\mathbf{r},t)$, having components only in the plane perpendicular to z, can be written as a sum of a series of plane waves:

$$\mathbf{m}(\mathbf{r},t) = \sum_k \mathbf{m} \cdot e^{i\cdot(2\pi\cdot f\cdot t - \mathbf{k}\cdot\mathbf{r})}. \tag{2.13}$$

Under these conditions the Landau–Lifshitz equation is linearised and solved to calculate analytically dispersion relation. In thin saturated ferromagnetic films we can distinguish three types of the magnetic field and film configurations which correspond to the three different classes of spin waves: magnetostatic forward volume waves, magnetostatic backward volume waves, and surface waves. The film and field configurations, magnetisation precessions, and dispersion diagrams for these three types of waves are shown in Fig. 2.12. In all discussions below, the external static magnetic field is applied along the z-axis (as indicated in Fig. 2.12) and the spin waves propagate in the film plane from left to right.

2.2.5 Magnetostatic forward volume wave

A magnetostatic wave, which propagates in the film plane ($\mathbf{k} \perp \mathbf{n}$) with the magnetisation perpendicular to the plane ($\mathbf{M} \parallel \mathbf{n}$), is called *magnetostatic forward volume wave* (MSFVW). For the lowest-order mode, a dispersion relation in absence of any exchange interactions and magnetic anisotropy [59]:

$$f_{\mathrm{MSFVW}}(k) = \frac{\gamma}{2\pi} \cdot \sqrt{\mathbf{H}_0 \cdot \left(\mathbf{H}_0 + \mathrm{M}_s \cdot \left(1 - \frac{1 - e^{-kd}}{kd}\right)\right)}. \tag{2.14}$$

Here k is the spin-wave wavenumber in the film plane and d is the thickness of the film. It depends on the magnitude of the wave vector and does not depend on its direction. The notation “forward” comes from the fact that the group velocity is in the same direction as the phase velocity. The group velocity can be calculated as:

$$\upsilon_g = \frac{\partial f}{\partial k}. \tag{2.15}$$

The tendency of group velocity can be seen directly from the positive slope of the dispersion curve (see, Fig. 2.12). “Volume” in the notation denotes that the spin-wave excitations are extended throughout the entire film thickness, as opposed to a surface wave discussed later [73, 74].

2.2.6 Backward volume magnetostatic waves

The other type of spin-wave excitation is called *magnetostatic backward volume wave* (MSBVW), it appears when waves propagate in a tangentially magnetised film, $\mathbf{M} \perp \mathbf{n}$, parallel to the magnetisation vector direction $\mathbf{k} \parallel \mathbf{M}$. The dispersion relation can be derived using a similar method described above for MSFVWs. An approximate dispersion relation in absence of any exchange interactions and magnetic anisotropy [59]:

$$f_{\mathrm{MSBVW}}(k) = \frac{\gamma}{2\pi} \cdot \sqrt{\mathbf{H}_0 \cdot \left(\mathbf{H}_0 + \mathrm{M_s} \cdot \frac{1-e^{-kd}}{kd}\right)}. \tag{2.16}$$

Contrary to MSFVW, the resonance frequency decreases when the wave vector increases. Here the negative group velocity points the direction opposite to the phase velocity ($\mathbf{k}$) indicating a backward wave character. In this case the magnetic field is applied tangentially, so the symmetry of wave propagation and spin orientation is broken and the dispersion relation is anisotropic, one needs to consider the angle between the magnetic field and the wave vector. Fig. 2.12 (b) shows an example of the MSBVW dispersion curve.

2.2.7 Magnetostatic surface waves

The third configuration (Fig. 2.12 (c)) represents the wave called *Magnetostatic Surface Wave* (MSSW) or *Damon-Eshbach* (DE) wave. It exists when the wave propagates in a tangentially magnetised film ($\mathbf{M} \perp \mathbf{n}$), but perpendicularly to the magnetisation vector direction $\mathbf{k} \perp \mathbf{M}$. This configuration is different from forward and backward volume waves, because the wavenumber of surface waves in out-of-plane direction is imaginary. The meaning of this imaginary wavenumber is that the wave amplitude exponentially decays in this direction. In the other words, for the film and field configuration showed in Fig. 2.12 (c), the waves with a wave vector pointing to the right propagate at the top surface of the film, while the waves with a wave vector pointing to the left propagate at the bottom surface of the film. Therefore, the surface waves are non-reciprocal waves [73]. Also, there is only a single propagating mode for surface waves instead of a series of modes with different thickness variations[59]. The dispersion relation for surface waves has been derived by Eshbach & Damon in 1960 [59, 75]:

$$f_{\mathrm{DE}}(k) = \frac{\gamma}{2\pi} \cdot \sqrt{\mathbf{H}_0 \cdot (\mathbf{H}_0 + \mathrm{M}_\mathrm{s}) + \frac{\mathrm{M}_\mathrm{s}^2}{4}(1 - e^{-2kd})}. \tag{2.17}$$

It is clear from Fig. 2.12 (c), that for the surface waves the group velocity and the phase velocity are in the same direction, the same as for forward volume waves. Furthermore, at $k = 0$, the frequency of MSSW as well as MSBVW mode becomes identical to the *Kittel formula* (Eq.: 2.11):

$$f_{\mathrm{DE}}(k = 0) = \frac{\gamma}{2\pi} \cdot \sqrt{\mathbf{H}_0 \cdot (\mathbf{H}_0 + \mathbf{M}_\mathrm{s})}. \tag{2.18}$$

Despite the fact that an analytical expression for the dispersion of magnetostatic spin waves can be derived for thin film geometry, it is not possible to derive such an expression for more complicated systems, such as unsaturated samples, samples of finite dimension, or with the exchange interactions included. The approximate dispersion relation for spin waves in extended thin film with the exchange effects included were obtained by Kalinikos and Slavin in 1986 [76].

2.2.8 Hysteresis loops

An important field of ferromagnetic materials study is the measurements and computations of the *hysteresis loops* [77]. From the definition, hysteresis is the dependence of the state of a system on its history. These experiments for magnetic materials can be perceived as dynamical problems with the external magnetic field changing over time [78, 79]. Although hysteresis in single-domain nanomagnets has been known for many decades [80], there is still much interest in looking a new effects and properties in this phenomenon. The retrieval of hysteresis properties is essential for many applications including the design and optimisation of permanent magnets [81] and giant magnetoresistance (GMR) sensors [82–85], but also formation regular domain patterns for magnonic applications. Hysteresis can be defined simply, as a relationship between the state of the system and the external parameters, where the state depends on the history of the external parameters, but not on their rate of variation.

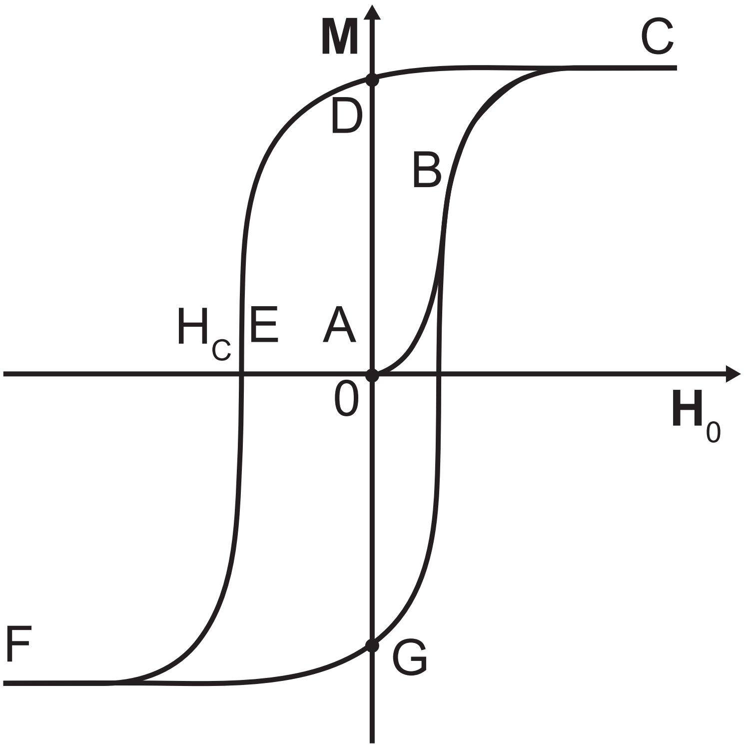

Fig. 2.13 An initial magnetisation curve (ABC) and a hysteresis loop (CDEFGBC) of a typical ferromagnet. Point A (at 0 **M** and 0 $\mathbf{H}_0$) denotes the initial unmagnetised state, C and F denote the saturated States, D corresponds to the saturation remanence, and E marks the coercive field H_c.

Hysteresis loops can have many different forms and by analysing them, information on the basic physical mechanisms controlling the observed magnetic phenomena can be gained. One of the first understanding of hysteresis loop is due to Weiss [86], who proposed the existence of the molecular field to account for spontaneous magnetisation, and also proposed the existence of domains within a magnetic material, which have since been observed directly. Hysteretic behaviour is presented graphically as a hysteresis loop in Fig. 2.13, where the component of the magnetisation, $\mathbf{M}$, along the direction of the applied magnetic field $\mathbf{H}_0$, is plotted as a function of $\mathbf{H}_0$.

For an initially unmagnetised material (A), the magnetisation increases with field to saturation, thus defining the initial magnetising curve (ABC). *A saturation state* (C) is reached when the applied field is sufficiently large to ensure that the material possesses a uniform magnetisation. For a hysteretic material, reducing the applied field (CD) to zero does not completely demagnetise the material and the residual magnetisation is called the *remanence* (D). The reverse field required to demagnetise the material, is named the *coercive* or *coercivity field*, H_c. The loop in Fig. 2.13 is completed by saturating the magnetisation in the reverse direction, then reducing the applied field to zero, and finally, increasing the field until positive saturation is once again established. This cycle defines the major hysteresis loop. *Minor loops* are produced when the maximum applied field is insufficient to saturate the magnetisation.

References

[1] D. Sanz-Hernández, R. F. Hamans, J. Osterrieth, *et al.*, "Fabrication of scaffold-based 3D magnetic nanowires for domain wall applications," *Nanomaterials*, vol. 8, no. 7, p. 483, 2018. DOI: 10.3390/nano8070483.

[2] A. V. Chumak, A. A. Serga, and B. Hillebrands, "Magnonic crystals for data processing," *Journal of Physics D: Applied Physics*, vol. 50, no. 24, p. 244 001, 2017. DOI: 10.1088/1361-6463/aa6a65.

[3] A. V. Chumak, "Fundamentals of magnon-based computing," *arXiv preprint arXiv:1901.08934*, 2019.

[4] D. Sander, S. O. Valenzuela, D. Makarov, *et al.*, "The 2017 Magnetism Roadmap," *Journal of Physics D: Applied Physics*, vol. 50, no. 36, p. 363 001, 2017. DOI: 10.1088/1361-6463/aa81a1.

[5] Gianluca Gubbiotti, *Three-Dimensional Magnonics*, G. Gubbiotti, Ed. Singapore: Jenny Stanford Publishing, 2019. DOI: 10.1201/9780429299155.

[6] A. Fernández-Pacheco, R. Streubel, O. Fruchart, *et al.*, "Three-dimensional nanomagnetism," *Nature Communications*, vol. 8, p. 15 756, 2017. DOI: 10.1038/ncomms15756.

[7] A. Hubert and R. Schafer, *Magnetic Domains: The Analysis of Magnetic Microstructures*. Berlin, Heidelberg: Springer Berlin Heidelberg, 1998. DOI: 10.1007/978-3-540-85054-0.

[8] H. Puszkarski and M. Krawczyk, "On the multiplicity of the surface boundary condition in composite materials," *Physics Letters A*, vol. 282, no. 1-2, pp. 106–112, 2001. DOI: 10.1016/S0375-9601(01)00163-3.

[9] S. A. Nikitov, P. Tailhades, and C. S. Tsai, "Spin waves in periodic magnetic structures - Magnonic crystals," *Journal of Magnetism and Magnetic Materials*, vol. 236, no. 3, pp. 320–330, 2001. DOI: 10.1016/S0304-8853(01)00470-X.

[10] F. Bloch, "Zur Theorie des Austauschproblems und der Remanenzerscheinung der Ferromagnetika," *Zeitschrift für Physik*, vol. 74, no. 5-6, pp. 295–335, 1932. DOI: 10.1007/BF01337791.

[11] L. D. Landau and E. M. Lifshitz, "Theory of the dispersion of magnetic permeability in ferromagnetic bodies," *Phys. Z. Sowietunion*, vol. 8, p. 153, 1935.

[12] L. Néel, "Effet des cavités et des inclusions sur le champ coercitif," *Cahiers de Physique*, vol. 25, no. 25, pp. 21–44, 1944.

[0] A. Hrabec, "Domain wall dynamics in magnetic nanostructures : Effect of magnetic field and electric current," PhD thesis, University of Grenoble, 2011.

[13] S. Chikazumi, *Physics of Ferromagnetism*. New York: Oxford University Press, 1997. DOI: 10.1007/978-3-642-25583-0.

[14] E. Yablonovitch and T. J. Gmitter, "Photonic band structure: The face-centered-cubic case," *Physical Review Letters*, vol. 63, no. 18, pp. 1950–1953, 1989. DOI: 10.1103/PhysRevLett.63.1950.

[15] S. John, “Strong localization of photons in certain disordered dielectric superlattices,” *Physical Review Letters*, vol. 58, no. 23, pp. 2486–2489, 1987. DOI: 10.1103/PhysRevLett.58.2486.

[16] M. Krawczyk and H. Puszkarski, “Magnonic spectra of ferromagnetic composites versus magnetization contrast,” *Acta Physica Polonica A*, vol. 93, no. 5-6, pp. 805–810, 1998. DOI: 10.12693/APhysPolA.93.805.

[17] M. Zelent, N. Tahir, R. Gieniusz, *et al.*, “Geometrical complexity of the antidots unit cell effect on the spin wave excitations spectra,” *Journal of Physics D: Applied Physics*, vol. 50, no. 18, p. 185 003, 2017. DOI: 10.1088/1361-6463/aa64ab.

[18] D. Kumar, P. Sabareesan, W. Wang, *et al.*, “Effect of hole shape on spin-wave band structure in one-dimensional magnonic antidot waveguide,” *Journal of Applied Physics*, vol. 114, no. 2, p. 023 910, 2013. DOI: 10.1063/1.4813228.

[19] S. Tacchi, G. Duerr, J. W. Klos, *et al.*, “Forbidden band gaps in the spin-wave spectrum of a two-dimensional bicomponent magnonic crystal,” *Physical Review Letters*, vol. 109, no. 13, p. 137 202, 2012. DOI: 10.1103/PhysRevLett.109.137202.

[20] A. V. Chumak, V. I. Vasyuchka, A. A. Serga, *et al.*, “Magnon spintronics,” *Nature Physics*, vol. 11, no. 6, pp. 453–461, 2015. DOI: 10.1038/nphys3347.

[21] M. Krawczyk and D. Grundler, “Review and prospects of magnonic crystals and devices with reprogrammable band structure,” *Journal of Physics: Condensed Matter*, vol. 26, no. 12, p. 123 202, 2014. DOI: 10.1088/0953-8984/26/12/123202.

[22] K. Di, V. L. Zhang, M. H. Kuok, *et al.*, “Band structure of magnonic crystals with defects: Brillouin spectroscopy and micromagnetic simulations,” *Physical Review B*, vol. 90, no. 6, p. 060 405, 2014. DOI: 10.1103/PhysRevB.90.060405.

[23] B Lenk, H Ulrichs, F Garbs, *et al.*, “The building blocks of magnonics,” *Physics Reports*, vol. 507, no. 4-5, pp. 107–136, 2011. DOI: 10.1016/j.physrep.2011.06.003.

[24] Z. K. Wang, V. L. Zhang, H. S. Lim, *et al.*, “Observation of frequency band gaps in a one-dimensional nanostructured magnonic crystal,” *Applied Physics Letters*, vol. 94, no. 8, p. 083 112, 2009. DOI: 10.1063/1.3089839.

[25] R. A. Gallardo, D. Cortés-Ortuño, T. Schneider, *et al.*, “Flat bands, indirect gaps, and unconventional spin-wave behavior induced by a periodic Dzyaloshinskii-Moriya Interaction,” *Physical Review Letters*, vol. 122, no. 6, p. 067 204, 2019. DOI: 10.1103/PhysRevLett.122.067204.

[26] E. N. Beginin, A. V. Sadovnikov, A. Y. Sharaevskaya, *et al.*, “Spin wave steering in three-dimensional magnonic networks,” *Applied Physics Letters*, vol. 112, no. 12, p. 122 404, 2018. DOI: 10.1063/1.5023138.

[27] A. V. Chumak, P Pirro, A. A. Serga, *et al.*, “Spin-wave propagation in a microstructured magnonic crystal,” *Applied Physics Letters*, vol. 95, no. 26, p. 262 508, 2009. DOI: 10.1063/1.3279138.

[28] G. Gubbiotti, S. Tacchi, M. Madami, *et al.*, “Brillouin light scattering studies of planar metallic magnonic crystals,” *Journal of Physics D: Applied Physics*, vol. 43, no. 26, p. 264 003, 2010. DOI: 10.1088/0022-3727/43/26/264003.

[29] J. Topp, D. Heitmann, M. P. Kostylev, *et al.*, “Making a reconfigurable artificial crystal by ordering bistable magnetic nanowires,” *Physical Review Letters*, vol. 104, no. 20, p. 207 205, 2010. DOI: 10.1103/PhysRevLett.104.207205.

[30] M. Mruczkiewicz, P. Gruszecki, M. Zelent, *et al.*, “Collective dynamical skyrmion excitations in a magnonic crystal,” *Physical Review B*, vol. 93, no. 17, p. 174 429, 2016. DOI: 10.1103/PhysRevB.93.174429.

[31] M. Garst, J. Waizner, and D. Grundler, “Collective spin excitations of helices and magnetic skyrmions: Review and perspectives of magnonics in non-centrosymmetric magnets,” *Journal of Physics D: Applied Physics*, vol. 50, no. 29, p. 293 002, 2017. DOI: 10.1088/1361-6463/aa7573.

[32] T. Okubo, S. Chung, and H. Kawamura, “Multiple-q states and the skyrmion lattice of the triangular-lattice heisenberg antiferromagnet under magnetic fields,” *Physical Review Letters*, vol. 108, no. 1, p. 17 206, 2012.

[33] I. Kezsmarki, S. Bordacs, P. Milde, *et al.*, “Neel-type skyrmion lattice with confined orientation in the polar magnetic semiconductor GaV4S8,” *Nature Materials*, vol. 14, no. 11, pp. 1116–1122, 2015. DOI: 10.1038/nmat4402.

[34] H. S. Park, X. Yu, S. Aizawa, *et al.*, “Observation of the magnetic flux and three-dimensional structure of skyrmion lattices by electron holography,” *Nature Nanotechnology*, vol. 9, no. 5, pp. 337–342, 2014. DOI: 10.1038/nnano.2014.52.

[35] D. A. Gilbert, B. B. Maranville, A. L. Balk, *et al.*, “Realization of ground-state artificial skyrmion lattices at room temperature,” *Nature Communications*, vol. 6, no. 1, p. 8462, 2015. DOI: 10.1038/ncomms9462.

[36] T. Okubo, S. Chung, and H. Kawamura, “Multiple-q states and the Skyrmion lattice of the triangular-lattice Heisenberg antiferromagnet under magnetic fields,” *Physical Review Letters*, vol. 108, no. 1, 2012. DOI: 10.1103/PhysRevLett.108.017206.

[37] R. Georgii and T. Weber, “The helical magnet MnSi: skyrmions and magnons,” *Quantum Beam Science*, vol. 3, no. 1, p. 4, 2019. DOI: 10.3390/qubs3010004.

[38] X. Z. Yu, N. Kanazawa, Y. Onose, *et al.*, “Near room-temperature formation of a skyrmion crystal in thin-films of the helimagnet FeGe,” *Nature Materials*, vol. 10, no. 2, pp. 106–109, 2011. DOI: 10.1038/nmat2916.

[39] X. Zhang, Y. Zhou, K. M. Song, *et al.*, “Skyrmion-electronics: Writing, deleting, reading and processing magnetic skyrmions toward spintronic applications,” *Journal of Physics: Condensed Matter*, 2019. DOI: 10.1088/1361-648X/ab5488.

[40] K. Everschor-Sitte, J. Masell, R. M. Reeve, *et al.*, “Perspective: Magnetic skyrmions - Overview of recent progress in an active research field,” *Journal of Applied Physics*, vol. 124, no. 24, 2018. DOI: 10.1063/1.5048972.

[41] N. Romming, A. Kubetzka, C. Hanneken, *et al.*, “Field-dependent size and shape of single magnetic Skyrmions,” *Physical Review Letters*, vol. 114, no. 17, p. 177 203, 2015. DOI: 10.1103/PhysRevLett.114.177203.

[42] N. Nagaosa and Y. Tokura, “Topological properties and dynamics of magnetic skyrmions,” *Nature nanotechnology*, vol. 8, no. 12, pp. 899–911, 2013. DOI: 10.1038/nnano.2013.243.

[43] C. Moreau-Luchaire, C. Moutafis, N. Reyren, *et al.*, “Additive interfacial chiral interaction in multilayers for stabilization of small individual skyrmions at room temperature,” *Nature Nanotechnology*, vol. 11, no. 5, pp. 444–448, 2016. DOI: 10.1038/nnano.2015.313.

[44] A. Bogdanov and A. Hubert, “Thermodynamically stable magnetic vortex states in magnetic crystals,” *Journal of Magnetism and Magnetic Materials*, vol. 138, no. 3, pp. 255–269, 1994. DOI: 10.1016/0304-8853(94)90046-9.

[45] O. Boulle, J. Vogel, H. Yang, *et al.*, “Room-temperature chiral magnetic skyrmions in ultrathin magnetic nanostructures,” *Nature Nanotechnology*, vol. 11, no. 5, pp. 449–454, 2016. DOI: 10.1038/nnano.2015.315.

[46] C. Marrows, “An inside view of magnetic skyrmions,” *Physics*, vol. 8, p. 40, 2015. DOI: 10.1103/Physics.8.40.

[47] K. Everschor, “Current-induced dynamics of chiral magnetic structures,” PhD thesis, University of Cologne, 2012.

[48] A. Fert and P. M. Levy, “Role of anisotropic exchange interactions in determining the properties of spin-glasses,” *Physical Review Letters*, vol. 44, no. 23, pp. 1538–1541, 1980. DOI: 10.1103/PhysRevLett.44.1538.

[49] A. Crépieux and C. Lacroix, “Dzyaloshinsky–Moriya interactions induced by symmetry breaking at a surface,” *Journal of Magnetism and Magnetic Materials*, vol. 182, no. 3, pp. 341–349, 1998. DOI: 10.1016/S0304-8853(97)01044-5.

[50] O. Boulle, J. Vogel, H. Yang, *et al.*, “Room-temperature chiral magnetic skyrmions in ultrathin magnetic nanostructures,” *Nature Nanotechnology*, vol. 11, no. 5, pp. 449–454, 2016. DOI: 10.1038/nnano.2015.315.

[51] A. O. Leonov, T. L. Monchesky, N. Romming, *et al.*, “The properties of isolated chiral skyrmions in thin magnetic films,” *New Journal of Physics*, vol. 18, no. 6, pp. 1–16, 2016. DOI: 10.1088/1367-2630/18/6/065003.

[52] S. Rohart, J. Miltat, and A. Thiaville, “Path to collapse for an isolated Néel skyrmion,” *Physical Review B*, vol. 93, no. 21, p. 214 412, 2016. DOI: 10.1103/PhysRevB.93.214412.

[53] C. Andreas, A. Kákay, and R. Hertel, “Multiscale and multimodel simulation of Bloch-point dynamics,” *Physical Review B*, vol. 89, no. 13, p. 134 403, 2014. DOI: 10.1103/PhysRevB.89.134403.

[54] G. Henkelman and H. Jónsson, “Improved tangent estimate in the nudged elastic band method for finding minimum energy paths and saddle points,” *The Journal of Chemical Physics*, vol. 113, no. 22, pp. 9978–9985, 2000. DOI: 10.1063/1.1323224.

[55] R. Dittrich, T. Schrefl, D. Suess, *et al.*, “A path method for finding energy barriers and minimum energy paths in complex micromagnetic systems,” *Journal of Magnetism and Magnetic Materials*, vol. 250, pp. 12–19, 2002. DOI: 10.1016/S0304-8853(02)00388-8.

[56] S. L. Zhang, G. Van Der Laan, and T. Hesjedal, “Direct experimental determination of the topological winding number of skyrmions in Cu2OSeO3,” *Nature Communications*, vol. 8, 2017. DOI: 10.1038/ncomms14619.

[57] A. A. Kovalev and S. Sandhoefner, “Skyrmions and Antiskyrmions in Quasi-Two-Dimensional Magnets,” *Frontiers in Physics*, vol. 6, no. SEP, 2018. DOI: 10.3389/fphy.2018.00098.

[58] A. K. Nayak, V. Kumar, T. Ma, *et al.*, “Magnetic antiskyrmions above room temperature in tetragonal Heusler materials,” *Nature*, vol. 548, no. 7669, pp. 561–566, 2017. DOI: 10.1038/nature23466.

[59] D. D. Stancil and A. Prabhakar, *Spin Waves*. Boston, MA: Springer US, 2009. DOI: 10.1007/978-0-387-77865-5.

[60] M. Jamali, J. H. Kwon, S. M. Seo, *et al.*, “Spin wave nonreciprocity for logic device applications,” *Scientific Reports*, vol. 3, p. 3160, 2013. DOI: 10.1038/srep03160.

[61] F. Ciubotaru, O. Zografos, G. Talmelli, *et al.*, “Spin waves for interconnect applications,” in *2017 IEEE International Interconnect Technology Conference (IITC)*, vol. 1, IEEE, 2017, pp. 1–4. DOI: 10.1109/IITC-AMC.2017.7968984.

[62] P. Talbot, A. Fessant, and J. Gieraltowski, “Electromagnetic sensors based on magnonic crystals for applications in the fields of biomedical and NDT,” *Procedia Engineering*, vol. 120, pp. 1241–1244, 2015. DOI: 10.1016/j.proeng.2015.08.839.

[63] H. Yu, O. D’Allivy Kelly, V. Cros, *et al.*, “Approaching soft X-ray wavelengths in nanomagnet-based microwave technology,” *Nature Communications*, vol. 7, p. 11 255, 2016. DOI: 10.1038/ncomms11255.

[64] J. M. De Teresa, A. Fernández-Pacheco, R. Córdoba, *et al.*, “Review of magnetic nanostructures grown by focused electron beam induced deposition (FEBID),” *Journal of Physics D: Applied Physics*, vol. 49, no. 24, 2016. DOI: 10.1088/0022-3727/49/24/243003.

[65] N. Tahir, M. Zelent, R. Gieniusz, *et al.*, “Magnetization reversal mechanism in patterned (square to wave-like) Py antidot lattices,” *Journal of Physics D: Applied Physics*, vol. 50, no. 2, p. 025 004, 2017. DOI: 10.1088/1361-6463/50/2/025004.

[66] M. Zelent, M. Mailyan, V. Vashistha, *et al.*, “Spin wave collimation using a flat metasurface,” *Nanoscale*, vol. 11, no. 19, pp. 9743–9748, 2019. DOI: 10.1039/C8NR10484K.

[67] A. P. Guimarães, *Principles of Nanomagnetism*, ser. NanoScience and Technology. Berlin, Heidelberg: Springer Berlin Heidelberg, 2009, 1–20. DOI: 10.1007/978-3-642-01482-6.

[68] M. Getzlaff, *Fundamentals of magnetism*. Berlin, Heidelberg: Springer, 2008. DOI: 10.1007/978-3-540-31152-2.

[69] T. L. Gilbert, “A phenomenological theory of damping in ferromagnetic materials,” *IEEE Transactions on Magnetics*, vol. 40, no. 6, pp. 3443–3449, 2004. DOI: 10.1109/TMAG.2004.836740.

[70] J. H. Griffiths, “Anomalous high-frequency resistance of ferromagnetic metals,” *Nature*, vol. 158, no. 4019, pp. 670–671, 1946. DOI: 10.1038/158670a0.

[71] C. Kittel, “Interpretation of Anomalous Larmor Frequencies in Ferromagnetic Resonance,” *Physical Review*, vol. 71, no. 4, pp. 270–271, 1947. DOI: 10.1103/PhysRev.71.270.2.

[72] C. Kittel, “On the theory of ferromagnetic resonance absorption,” *Physical Review*, vol. 73, no. 2, pp. 155–161, 1948. DOI: 10.1103/PhysRev.73.155.

[73] M. Wu, “Nonlinear Spin Waves in Magnetic Film Feedback Rings,” in *Solid State Physics*, vol. 62, Academic Press, 2010, pp. 163–224. DOI: 10.1016/B978-0-12-374293-3.00003-1.

[74] D. D. Stancil, "Introduction to Magnetism," in *Theory of Magnetostatic Waves*, New York, NY: Springer New York, 1993, pp. 1–19. DOI: 10.1007/978-1-4613-9338-2.

[75] J. R. Eshbach and R. W. Damon, "Surface magnetostatic modes and surface spin waves," *Physical Review*, vol. 118, no. 5, pp. 1208–1210, 1960. DOI: 10.1103/PhysRev.118.1208.

[76] B. A. Kalinikos and A. N. Slavin, "Theory of dipole-exchange spin wave spectrum for ferromagnetic films with mixed exchange boundary conditions," *Journal of Physics C: Solid State Physics*, vol. 19, no. 35, pp. 7013–7033, 1986. DOI: 10.1088/0022-3719/19/35/014.

[77] R. H. Victora, "Quantitative theory for hysteretic phenomena in CoNi magnetic thin films," *Physical Review Letters*, vol. 58, no. 17, pp. 1788–1791, 1987. DOI: 10.1103/PhysRevLett.58.1788.

[78] M. E. Schabes and H. N. Bertram, "Magnetization processes in ferromagnetic cubes," *Journal of Applied Physics*, vol. 64, no. 3, pp. 1347–1357, 1988. DOI: 10.1063/1.341858.

[79] A. Manzin and O. Bottauscio, "Connections between numerical behavior and physical parameters in the micromagnetic computation of static hysteresis loops," *Journal of Applied Physics*, vol. 108, no. 9, p. 093 917, 2010. DOI: 10.1063/1.3503873.

[80] E. C. Stoner and E. P. Wohlfarth, "A Mechanism of Magnetic Hysteresis in Heterogeneous Alloys," *Phil. Trans. R. Soc. Lond. A.*, vol. 240, p. 599, 1948.

[81] R. Hertel, "Micromagnetic simulations of magnetostatically coupled Nickel nanowires," *Journal of Applied Physics*, vol. 90, no. 11, pp. 5752–5758, 2001. DOI: 10.1063/1.1412275.

[82] R. Skomski, P. Manchanda, P. K. Kumar, *et al.*, "Predicting the Future of Permanent-Magnet Materials," *IEEE Transactions on Magnetics*, vol. 49, no. 7, pp. 3215–3220, 2013. DOI: 10.1109/TMAG.2013.2248139.

[83] C. Treutler, "Magnetic sensors for automotive applications," *Sensors and Actuators A: Physical*, vol. 91, no. 1-2, pp. 2–6, 2001. DOI: 10.1016/S0924-4247(01)00621-5.

[84] D. Suess, J. Fidler, K. Porath, *et al.*, "Micromagnetic study of pinning behavior in percolated media," *Journal of Applied Physics*, vol. 99, no. 8, 08G905, 2006. DOI: 10.1063/1.2164437.

[85] J. Fischbacher, A. Kovacs, H. Oezelt, *et al.*, "Nonlinear conjugate gradient methods in micromagnetics," *AIP Advances*, vol. 7, no. 4, p. 045 310, 2017. DOI: 10.1063/1.4981902.

[86] P. Weiss, "L'hypothèse du champ moléculaire et la propriété ferromagnétique," *Journal de Physique Théorique et Appliquée*, vol. 6, no. 1, pp. 661–690, 1907. DOI: 10.1051/jphystap:019070060066100.

Chapter 3

Micromagnetic simulations

In this chapter the most important advantages and difficulties of the micromangetic simulations which are related to the thesis are discussed. The main part of the study is based on the numerical solution of the Landau-Lifshitz-Gilbert equation adopted in **Mumax3** software. In particular, the numerical approach of magnetisation relaxation, calculation of the ferromagnetic resonance spectrum, dispersion relation of spin waves and extracting iso-frequency contours from simulations for ferromagnetic nanostructures are discussed.

3.1 Introduction to computational micromagnetism

Due to the achievements in science and technology toward miniaturisation of devices into the nanometer-length scale, within the last decades the physics of nanostructures, interfaces and surfaces became a central area of research. New experimental and theoretical challenges are imposed because the objects of the study are in the range or even smaller than the characteristic length scales of the system, including the carrier mean free path, spin diffusion length, magnetic exchange length, or excitation wavelength. To support experimental studies, to predict the functionality of the nanostructures and design nanoscale devices, the numerical tools have also been developed. Thus, computational micromagnetics has been developed, that sees widespread use in both modern physics and magnetic device engineering communities [1–3]. With the advancement of micromagnetic models, simulation techniques, and processing power, the list of phenomena that can be studied has grown substantially and includes such diverse fields, as the spin transfer torque [1, 4], and spin-wave properties, including dispersion relation in magnonic crystals [5–7].

To investigate magnetic properties of micro and nanoscale materials we have to deal with an extremely high numbers of magnetic moments, and the description of the magnetisation within atomistic approach is complicated and it requires a considerable computational effort. The much more efficient approach to describe the magnetisation at computational reliable scales relies on considering the magnetisation, a continuous function of space $\mathbf{M}(\mathbf{r})$, instead of a magnetic moment. The magnetisation at each point represents an average over a certain elementary volume ΔV, where ΔV must be small enough, such that the magnetisation can be considered uniform within ΔV, and it must be large enough in order to contain a significant number of atomic magnetic moments. The dynamics of the elementary moments inside each cell is much faster than the dynamics of the average magnetisation. This theory was introduced by W.

F. Brown [8, 9] and it is known as **micromagnetic theory** or *continuum theory* of magnetically ordered materials, and is based on solution of the LL equation (2.7, 2.8). However, to solve the LL equation numerically, one has to approximate the continuum theory as a discrete problem.

3.2 Computational micromagnetics

An essential equation in most of the micromagnetic models [1, 8] is the LLG equation 2.8, which is a differential equation governing the magnetisation dynamics. This equation can be analytically solved only under specific assumptions and in general for a very limited number of systems [10–12]. Because of the complexity of the problem the solution requires the use of *micromagnetic simulation* (MS) software. Numerical micromagnetic modelling plays a very important part in understanding and analysing experimental results, allowing reproduction of magnetisation dynamics observed in real samples. MS is a valuable tool to increase our understanding of nanomagnetic systems and to guide experiments through parameter spaces that would otherwise be difficult and expensive to navigate. The most common approach used in numerical micromagnetism is to perform the spatial discretisation to approximate the continuous field **M**. In general two methods are possible for discretising the simulated sample (see Fig. 3.1): the *finite element method* (**FEM**) and *finite difference method* (**FDM**).

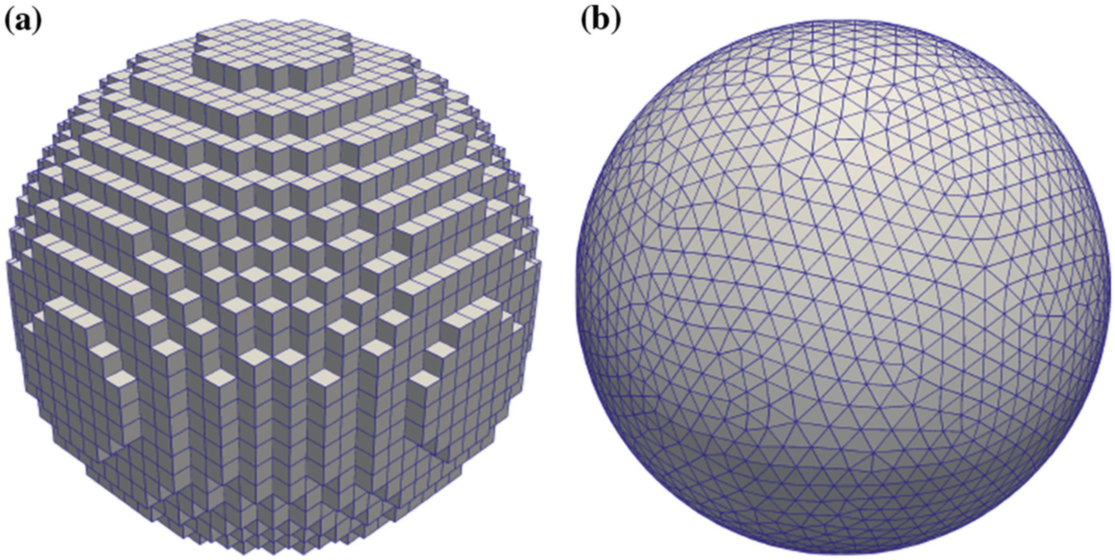

Fig. 3.1 Generated spatial mesh of sphere for different numerical methods. (a) Regular cuboid grid with 8217 cells as required for **FDM**. (b) Tetrahedral grid with 7149 vertices as required for **FEM**. (Reprinted by permission from Springer Nature, Spintronics in Micromagnetics in Springer Handbook of Materials Modeling, Vol. 1 Methods: Theory and Modeling, https://doi.org/doi:10.1007/978-3-319-42913-7 76-1, @ 2019.)

The finite element method (**FEM**) is a numerical technique for finding approximate solutions to boundary value problem for partial differential equations. It uses subdivision of a computational domain into smaller parts, called finite elements. Depending upon the dimension of the problem, these can be triangles, squares, or rectangles in two dimensions or tetrahedrons, cubes, or hexahedra for three-dimensional problems. The numerical implementation of this method is a challenging task, since it involves the nontrivial generation of meshes, the numerical computation of integrals for the system-matrix assembly and the solution of large linear systems. However, it is easier to construct complex geometries using this method.

In **FDM** the continuous space domain is replaced by a discrete set of lattice points, usually on the rectangular or cubic lattice in two- and three-dimensions, respectively. Each differential operator is replaced by the finite difference operator on the lattice points, and the boundary conditions on the surfaces of the domain are replaced by their discrete counterparts. This method is considered to be relatively fast, yet with low memory consumption, since only the magnetisation, the right-hand side of the Landau-Lifshitz equation and, the Fourier image of the convolution kernel need to be stored. The main downsides of the FDM are the inability to adequately approximate curved geometries (e.g. a sphere, where a staircase effect appear, see Fig. 3.1a) and reduced efficiency for sparse problems, as time-consuming calculations (e.g. fast Fourier transformation [FFT]) have to be performed on empty cells. However, recently Serban Lepadatu in ref. [13] published the multilayered convolution method to compute demagnetising fields in a single magnetic body which is able to handle layers with arbitrary spacing, arbitrary thicknesses, and arbitrary relative positioning between them without impacting the computational performance.

After discretisation, the continuous partial differential equation is replaced with a system of first-order ordinary differential equations with n unknown that can subsequently solved using a variety of standard time integration algorithms (like Runge-Kutta, Multistep, BDF or Heuen) [14–16].

Typically, these methods introduce distinct discretisations for space and time. For both methods the magnetic region is subdivided into simulation cells resulting in a simulations mesh. However, the requirements for the mesh differ significantly for both methods. Independent from the discretisation method, the cell size has to be chosen sufficiently small in order to accurately resolve the structure of domain walls. The characteristic length for the domain-wall width is the exchange length, which is dependent on the saturation magnetisation of the material, M_s and the exchange stiffness constant, A_{ex} (See section 2.2.2).

To compare such distinct numerical solvers, as well as to evaluate their validity and reliability, NIST's Micromagnetic Modelling Activity Group (μMag) publishes standard micromagnetic problems [30]. Recent additions have included the spin transfer torque [31], the calculations of the spin-wave dispersion relation[32], ferromagnetic resonance [33] and for materials with Dzyaloshinskii–Moriya interaction [34]. These tests are used to validate the numerical implementation of the micromagnetic model.

Name	Release	FEM/FDM	GPU	Free	Supported	Reference
Boris	2019	FDM	Yes	Yes	Yes	[17]
Commics	2018	FEM	No	Yes	Yes	[18, 19]
Fidimag	2018	FDM	No	Yes	Yes	[20, 21]
OOMMF (with GPU support)	2016	FDM	Yes	Yes	Yes	[22]
Grace	2015	FDM	Yes	Yes	Yes	[23]
LLG micromagnetics simulator	2015	FDM	Yes	No	–	[24]
Mumax3	2014	FDM	Yes	Yes	Yes	[14, 25]
Magnum.fd	2014	FDM	Yes	Yes	Yes	[26]
Magnum.fe	2013	FEM	No	No	Yes	[27, 28]
Micromagnum	2012	FDM	Yes	Yes	No	[29]

Table 3.1 List of general-purpose micromagnetic codes. The largest distinction between these packages is how they discretize space, which is either using an **FDM** or **FEM** approach. Next, we indicate whether they run exclusively on CPU, or are capable of using graphics cards (GPUs). Finally, it is indicated whether the codes are commercial or free software, and if they are still developed.

3.3 Micromagnetic applications

The simulation of magnetic materials falls into several paradigms, depending on the length scales, materials and phenomena of interest. The magnetisation of a magnetic material is described by a continuous vector field **M**. Usually, it is when temperature effects are neglected, the norm of the magnetisation vector at each point is assumed to be constant and equal to the saturation magnetisation, M_s. Conventional MS softwares provide only the space-time data by solving the LLG equation and thus conversions of the data into the frequency and wavevector domain are left to the post-processing tools, which is important step for a deep understanding of the obtained results, especially in magnonics applications. The FMR spectra, modes visualisation and the dispersion relation provide valuable insight into the characteristics of magnetisation oscillations and propagating spin waves which is important for both fundamental and applied researches.

In this chapter we will present a micromagnetic approach based on the solutions adopted in the **Mumax3** software. The open-source software, written in C++ and Golang programming language **Mumax3** [14, 35], solves the time and space dependent magnetisation evolution in nano- and micro-scale magnets using a finite-difference discretisation.

3.3.1 Relaxation processes

In order to compute the stable static magnetisation configurations or to calculate the hysteresis properties of the ferromagnetic materials, the algorithm which minimise total energy or torque is required. The micromagnetic solvers integrate the LLG equation of motion in time. However, the accessible time scale of micromagnetics simulations is in the range of nanoseconds. The measurement time for hysteresis loops of permanent magnets is in the range of seconds. Therefore, micromagnetic solvers that minimise the energy directly instead of solving a time dependent equation might be more suitable for the analysis for magnetisation reversal processes.

The stable magnetisation configurations of a system corresponds to local minima in the energy landscape and are given by the competition between different energy terms. The nonlinear nature of the energy contributions leads to a complex energy landscape, which makes difficult to efficiently seek for energy minima. A complexity increases the risk to miss a local minimum, and calls for a thoughtful choice of minimisation algorithm (see, Fig. 3.2). Furthermore, system can have several energy local minima (metastable states), which satisfy the relaxation condition $\Delta E(\Delta \mathbf{M} = 0)$. This fact makes the relaxation process difficult especially in complex or high symmetry structures. It may result in incorrect results, therefore, it is important to carefully verify the stability of the system.

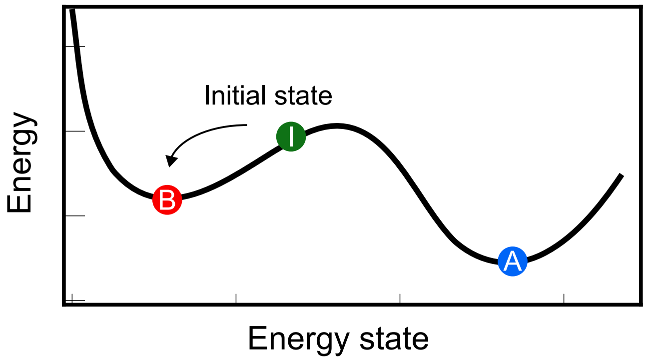

Fig. 3.2 Sketch of the energy landscape between the ”flower” state B and the domains state A. Despite the total energy is lower in the domains state, the system can collapse in a local minimum.

The local minima, stable equilibrium state of the magnetisation can be found by minimising an expression for the total free energy (see section 1.2). It is possible to minimise the free magnetic energy analytically by using variational calculus, but mostly only in a few simple cases. In most cases however, one has to resort to numerical approaches to minimise the total energy. Various tailored approaches for micromagnetic energy minimisation including optimised steepest descend methods and variants of the conjugate gradient method have been proposed in order to achieve high performance and reduce the risk to miss local minima [36–40].

In **Mumax3** the two numeric relaxation methods are implemented. In general, by solving LLG equation, the free magnetic energy decreases in time if the damping parameter is positive ($\alpha > 0$). Consequently, one can relax a magnetic state by solving the LLG equation until the energy is converged to a local minimum. Mumax3 to reduce the computation time, the *relax* function used to find the system energy minimum, disables the precession term in LLG equation, so that the effective field points towards decreasing energy.

Second function available in **Mumax3** is *minmizer*. Its implementation is based on the steepest gradient energy minimisation scheme for micromagnetics derived by *Exl, et al.* [39]. The algorithm uses a *Barzilai-Borwein* adaptive step size [41]. Conjugate gradient method considers the gradient of energy on each cell, and calculates the steepest trajectory. It then changes the magnetisation direction along the steepest decent direction to reduce the energy in an iterative fashion. The method searches on a curve that lies on the sphere, which keeps the magnitude of the magnetisation vector constant. The step size is selected according to a modified *Barzilai-Borwein* method. For the computation of static hysteresis loops the steepest descent minimiser is much faster than a Landau-Lifshitz micromagnetic solver. the minimise function is very well suited for calculation of the hysteresis loop, where system is never far away from the ground state.

3.3.2 Ferromagnetic resonances

Ferromagnetic resonance (FMR) is a powerful experimental method of probing the dynamics of magnetisation in ferromagnetic films. In the presence of an external magnetic field $\mathbf{H}_0$, the magnetisation $\mathbf{M}$ of a ferromagnet precesses according to the Landau-Lifshitz equation. Radio frequency (RF) magnetic field $\mathbf{H}_0$ at this resonant frequency applied perpendicular to $\mathbf{H}_0$ will couple to a uniform precession of $\mathbf{M}$ about the direction of $\mathbf{H}_0$, resulting in absorption of energy from the RF field. In addition to the uniform mode, the external RF field may also couple to nonuniform or directly to the spin-wave modes, depending on the symmetries, inhomogeneities and deformity of the structure and the magnetisation configuration. Contributions to the energy of these modes arise from a combination of exchange and dipolar interactions. In terms of computational micromagnetics, there are at least five approaches that can be used to simulate the FMR:

1. Method one: the system is perturbed from its equilibrium state by applying a short-lived and sufficiently weak excitation (to avoid remagnetisation), followed by simulation and recording of the magnetisation dynamics. Resonance frequencies and corresponding modes are extracted by performing the Fourier transform of the recorded data in time, into the frequency domain. This is an efficient way to determine the eigenmodes of the system.

2. Method two: This method is related to the resonance magnetic field spectra collected in well known experimental FMR cavity or Vector Network Analyzer - Ferromagnetic Resonance (VNA-FMR) techniques, and it is difficult to obtain in standard micromagnetic software. Here, the time-dependent periodic sinusoidal magnetic microwave field of fixed frequency f is used to determine the magnetisation precession amplitude in response to the system. The ferromagnetic response

for any frequency is proportional to the power absorption of the microwave field, and can be expressed in the value of the magnetisation excitation. This method is conceptually simple, but computationally very demanding, as for every frequency f, the MS needs to compute the time evolution of the system.

3. Method three: In this method to excite SW precession we have to use a microwave external magnetic field. The suitable way is to use the field in the form of the *sinc* function in the time domain and spatially homogeneous in the whole sample:

$$H_0(t) = \frac{1}{\mu_0} \cdot AmpRF \cdot \mathrm{sinc}(2\pi \cdot f_{\mathrm{cut}} \cdot (t - t_0)). \tag{3.1}$$

Here, $AmpRF$ is an amplitude of the external RF magnetic field and f_{cut} is its cut-off frequency. The amplitude of RF field should be sufficient to excite precession above numerical noise, and small enough to keep static magnetic configuration unchanged. In most cases, it is good to use 10-50 times smaller than $\mu_0 \cdot M_s$, than the static magnetic field. In this method we will obtain the FMR spectra in corresponding frequency range from 0 to f_{cut}. Resonance frequencies and corresponding modes are extracted by performing the Fourier transform on the recorded data. t_0 corresponds to the time, which is needed to obtain the symmetrical character of the excitation of the sinc function. Furthermore, this shift prevent system against sudden excitation.

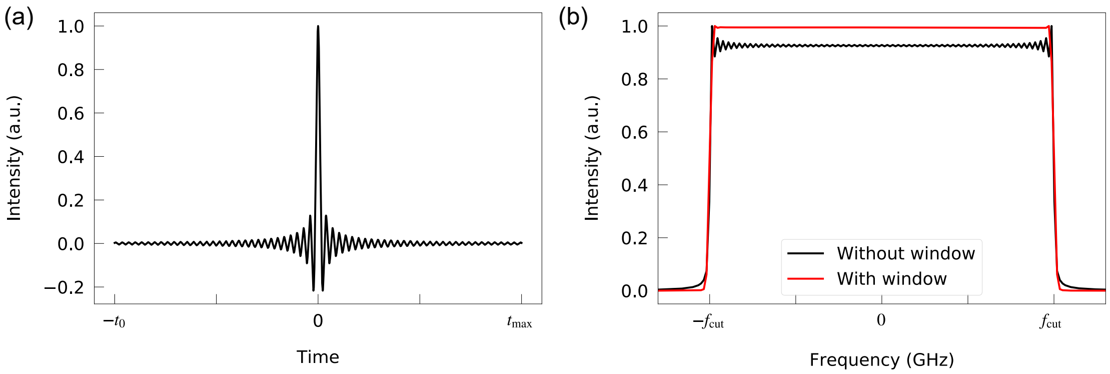

Fig. 3.3 (a) The sinc function sinc(x), also called the "sampling function," is a function that arises frequently in signal processing and the theory of Fourier transforms. The full name of the function is "sine cardinal," but it is commonly referred to by its abbreviation, "sinc." (b) A Fourier transform showing a rectangular distribution of frequencies between $\pm f_{\mathrm{cut}}$.

4. Method four: This method is called as "*eigenvalue method*", where instead of simulating the time evolution of the system's magnetisation, as in the methods above. The task here is represented as an eigenvalue problem, whose solutions provide the frequencies (eigenvalues) and mode shapes (*eigenvectors*) of the system. This method requires software to solve *eigenproblem* in real space or reciprocal space, with the use Comsol Multiphyscisc and FEM or Plane Wave Method, for instance.

To calculate the FMR spectra using time dependent methods we need to keep in mind the *Nyquist–Shannon sampling theorem*, where simulation data saving time sampling (and also indirectly time step) should be sufficient for f_{cut}. To receive the eigenmodes frequencies we need to collect data through some time, and perform fast Fourier transform of the signal. Please not, that the FMR spectrum resolution is proportional to the total collecting time with relation $df = N/2+1$, where N is a number of collected steps.

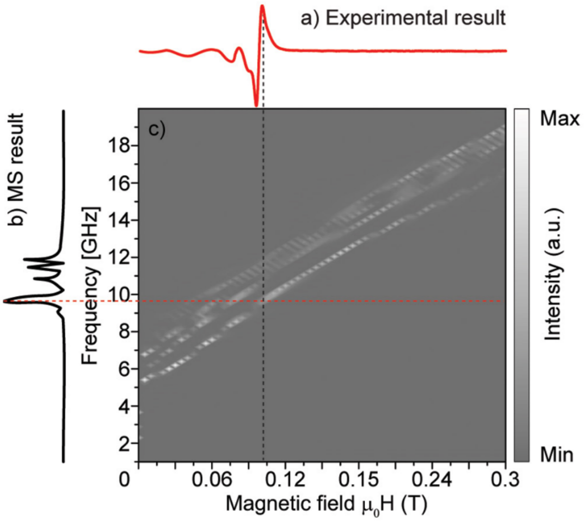

Fig. 3.4 (a) Experimental magnetic field dependent FMR spectra at 9.4 GHz for $\phi(\mathbf{H}_0) = 0^\circ$ and (b) frequency dependent FMR spectra obtained from MSs for $\phi(\mathbf{H}_0) = 0^\circ$ in static external magnetic field 0.1 T. (c) Gray scale map showing intensity spectra of the SWs in the wave-like ADL obtained from MSs in dependence on frequency and magnetic field amplitude for $\phi\mathbf{H} = 0^\circ$. Cutting of this plot along vertical line (black dashed) gives frequency dependent FMR spectra in (a), cutting along horizontal line (dashed red) gives magnetic field dependent spectra directly related to the measured spectra in (b). (Reproduced with permission of IOP Publishing in the format Book via Copyright Clearance Center, Geometrical complexity of the antidots unit cell effect on the spin-wave excitations spectra, https://doi.org/10.1088/1361-6463/aa64ab, @ 2017.)

Fig. 3.4 (c) presents the relationship between the method two and method three of obtaining the ferromagnetic resonance spectra. The methods are similar to the experimental technique and simulations, respectively. This figure shows the FMR intensity spectra of SWs in 10 nm thin film of Py with antidot lattice pattern in dependence on the magnetic field and frequency obtained from MSs.

Typically to perform MSs for different values of the magnetic field, simulations have to be performed separately for each value of the magnetic field. Experimental results are obtained in the opposite way. For a constant frequency (characteristic for a resonance cavity), the answer of the system expressed by the absorption spectra is collected depending on the value of the magnetic field. This relation is shown in Fig. 3.4 (a-c), where the measurements are performed in dependence on the magnetic field magnitude at fixed frequency 9.4 GHz. These are marked with a horizontal red dashed line. The MSs are performed in dependence on frequency at fixed magnetic field magnitude 0.1 T, they are marked by the vertical black-dashed line. Thus, the spectra related to the experimental and MSs spectra can be obtained by taking cuts of the grey scale map along the horizontal and vertical lines shown in Fig. 3.4 (c), respectively.

3.3.3 Miccromagnetic approach for calculation of the dispersion relation

SWs have a complex *dispersion relation* (DR) even in a homogeneous thin film which is substantially different from the dispersion of SWs in a bulk material. The dispersion depends on the direction and the magnitude of the wave vector, the relative strength of short-range exchange interactions with respect to the strength of long-range dipolar interaction and anisotropy, the external shape of the sample, the magnitude of the applied static magnetic field and its orientation in relation to the direction of SWs propagation. Also the antisymmetric exchange interactions (Dzyaloshinskii-Moriya interactions), magnetocrystalline anisotropy and magnetostatic effects a contribute to the SWs dynamics. The spectrum of spin waves propagating in magnetic systems is important from both fundamental and application points of view. The knowledge of the dispersion relation of spin waves is necessary to understand its propagation and transmission characteristics. For materials like magnonic crystals with discrete periodicity, the DR is a periodic function with a period equal to the reciprocal lattice vector $G = 2\pi/a$, a being a lattice constant. As only limited analytical methods are available, the use of the full LLG equation in time domain and the spatial Fourier transformations of the results to obtain the dispersion relation, are rarely seen [42]. This is because, the analysis of the SW dynamics in time domain is very complex and time consuming task. The ideal situation is a single run of simulation which gives the full information about SW dynamics and can be used to generate dispersion relation. However, in many cases, the results of several MSs are needed to obtain the dispersion relation of sufficiently fine resolution in frequency and wave vector domain, containing as many as possible branches of SW modes [42]. In this section, the procedure for generation of the dispersion relation, based on MSs, will be described.

To calculate the dispersion of spin waves one should transform the real space time domain data into the reciprocal space frequency domain. Micromagnetic solvers, like Mumax3, produce the output data in multiple files where each file corresponds to a particular instance of simulation time and contains the information about magnetisation distribution over the entire magnetic object. To calculate dispersion relation numerically based on the Fourier transformation, the Nyquist's law must be preserved in regime of time sampling and space size discretisation. To calculate SW dispersion relation in one direction several conditions must be fulfilled due to reduction cost of the Fourier transformation:

1. the cell size have to be enough small to satisfy exchange length limit and to measure small k-vectors,

2. the simulated structure should be enough big to satisfy required k-vector resolution,
3. the rate of sampling of magnetisation in time should be high enough to capture the precessional motion correctly.

Satisfying the above conditions for dispersion calculations provides a lot of information within one simulation run. However, it requires large computational resources, especially in patterned samples. Where the region of space, where no magnetic material is present, is assumed to have zero saturation magnetisation, but despite this, in formations about their existence are saved in the output files, significantly increasing the size of the files.

Another important element is the way of the wave excitation. As it was mentioned in the previous chapter, the form of the dynamic magnetic field determines character of the excited SWs. There are many ways for spin wave excitation dedicated to the dispersion calculations, such as excitation of the entire sample volume with oscillations of different phase and amplitude, point excitation and many others. However, we will focus on the technique, that allows isotropic and uniform excitation of the full range of the wave vectors. It is important to use dynamic field which will excite as many SW modes of different symmetries as possible, to collect information about full spectra of the SW excitation. Very useful for that purpose are excitations in form of the sinc function. Here, we demonstrate the dynamic magnetic field in the form of product of two sinc functions, in the two-dimensional space and time domain:

$$H_0(t,x,y) = \frac{1}{\mu_0} \cdot w(x,y,t) \cdot AmpRF \cdot \mathrm{sinc}(2\pi \cdot k_{\mathrm{cut}} \cdot \rho(x,y)) \cdot \mathrm{sinc}(2\pi \cdot f_{\mathrm{cut}} \cdot (t - t_0)), \quad (3.2)$$

where

$$\rho(x,y) = \sqrt{(x - x_0^2) + (y - y_0^2)}. \quad (3.3)$$

The $\rho(x,y)$ is a function, that builds the distribution of the magnetic field as a function of in two-dimensional space. The w is the Fast Fourier Transformation (FFT) window function to control the spectral leakage and aliasing effects:

$$w(x,y,t) = \mathrm{window}(x) \cdot \mathrm{window}(y) \cdot \mathrm{window}(t). \quad (3.4)$$

The w is a space and time domain function, which effectively reduce the spectral leakage and the scalloping loss. Therefore, a three-dimensional (for example Hanning or Chebyshev) window function is suggested (but not mandatory) method for improving the readability of the Fourier transformation results. It can be found, that once the 2D space and 1D time window functions are applied, the power distribution becomes more concentrated in comparison to the case without window function. Therefore, three dimensional (3D) character of this window equalises the efficiency the of wave vectors excitation [43] (see, Fig. 3.3). A dynamic component of the magnetisation (in our case orthogonal to the external bias field as we consider fully saturated samples) should be selected for the purpose of the dispersion analysis.

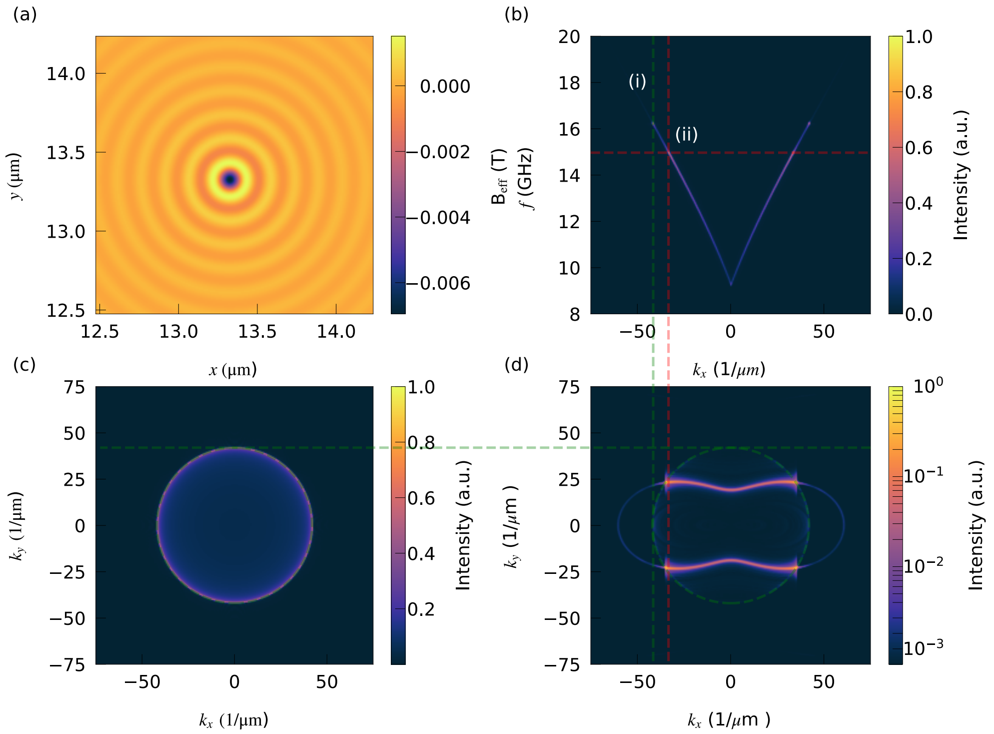

Fig. 3.5 The magnetic field distribution and result of the 2D and 3D FFT transformation of the MS results, performed for standard 10 nm Py thin film with 0.1 T applied in the film plane magnetic field. (a) The colormap that shows the spatial distribution of the magnetic field obtained according to Eq. 3.2 without a window function (in order to obtain visible k_{cut} wave vectors). (b) The dispersion relation of 10 nm Py thin film for the bias field of AmpRF = 0.1 T. The green and red dashed lines, marked by symbol i and ii, indicate the k_{cut} wave vector and f_{cut} frequency, respectively. (c) The results of the 2D FFT of the magnetic field distribution from (a) used in MSs to obtain a dispersion relation. The colormap amplitude represents the excitation strength of the wave vector in dependence on the direction. (d) The isofrequency contours presented for f_{cut} frequency, with visible circular countour of k_{cut} wave vectors. The figure indicates, that the used antenna was not able to excite waves equally in all directions. Waves shorter than 24 nm (42·1/μm) were excited with much lower energy.

Propagating spin waves in continuous magnetic media show continuous dispersion of frequency as a function of wavevector. To visualise the dispersion of spin waves propagating in one direction, the 2D FFT have to be calculated. To do it, we performed MSs of 20 μm x 20 μm uniform thin film of Py. The excitation field described by Eq. 3.2 have been used. Fig. 3.5 presents the dispersion relation for 0.1 T in Py film with thickness of 10 nm where the magnetic field is parallel to the magnetisation. To highlight the k_{cut} and f_{cut} thresholds, the windowing functions were neglected, and are indicated by (i) and (ii) dashed lines, respectively.

The isofrequency contours are the curves of the constant frequency plotted in the wavevector space (see Fig. 3.5 (d)). They are wave counterparts of the Fermi surfaces known from the theory of the solid state physics. The isofrequency contours are very important tool for the analysis of the wave propagation phenomena, giving a deep insight into direction and velocity of propagating, reflected and refracted waves in homogeneous media and also in artificial crystals. In micromagnetic approach to calculate such dependency, the three fold (one in time and two in space) Fourier transforms are needed. The intensity and contrast of this type of calculation depends on the previously defined excitation field. In logarithmic scale it is possible to see a whole isofrequency contour, including shadow of the maximum wave vector k_{cut}.

Based on the isofrequency contours analysis, the direction of propagation can be found. The wavefronts of propagating waves are related to the direction of the energy transfer, i.e., the direction of the group velocity vector [$\mathbf{v}_g = 2\pi \cdot \nabla_{\mathbf{k}} f(\mathbf{k})$, where $f(\mathbf{k}) = f(\mathbf{k}_x, \mathbf{k}_y)$ is a 2D dispersion relation]. In the case of isotropic dispersion, the isofrequency contours are circular and the direction of the group velocity are equal to the direction of propagation.

In the case of magnonic crystals one of the most important advantages of the dispersion relation is a possibility to observe the band-gaps. The width of the band-gap gives insight into the depth of the periodic modulation of said parameters. In addition the dispersion calculations can be used to detect localised modes, since they have no spatial dispersion. Furthermore, the second advantage of this technique is, that the amplitude of the spin waves can be always extracted in addition to the values for their wave vectors and frequencies. This amplitude can be used to study scattering processes in the magnetic system. Therefore, in order to investigate spin waves in magnetic systems it is essential to be able to extract the full magnonic dispersion relation, in particular, from MSs.

References

[1] D. V. Berkov, C. T. Boone, and I. N. Krivorotov, “Micromagnetic simulations of magnetization dynamics in a nanowire induced by a spin-polarized current injected via a point contact,” *Physical Review B*, vol. 83, no. 5, p. 054 420, 2011. DOI: 10.1103/PhysRevB.83.054420.

[2] S. Erokhin, D. Berkov, N. Gorn, *et al.*, “Micromagnetic modeling and small-angle neutron scattering characterization of magnetic nanocomposites,” *Physical Review B*, vol. 85, no. 2, p. 024 410, 2012. DOI: 10.1103/PhysRevB.85.024410.

[3] G. Finocchio, I. N. Krivorotov, X. Cheng, *et al.*, “Micromagnetic understanding of stochastic resonance driven by spin-transfer-torque,” *Physical Review B*, vol. 83, no. 13, p. 134 402, 2011. DOI: 10.1103/PhysRevB.83.134402.

[4] M Najafi, B Kruger, S Bohlens, *et al.*, “Proposal for a standard problem for micromagnetic simulations including spin-transfer torque,” *Journal of Applied Physics*, vol. 105, no. 11, p. 113 914, 2009.

[5] M. Mruczkiewicz, P. Gruszecki, M. Zelent, *et al.*, “Collective dynamical skyrmion excitations in a magnonic crystal,” *Physical Review B*, vol. 93, no. 17, p. 174 429, 2016. DOI: 10.1103/PhysRevB.93.174429.

[6] S Tacchi, P Gruszecki, M Madami, *et al.*, “Universal dependence of the spin wave band structure on the geometrical characteristics of two- dimensional magnonic crystals,” *Nature Publishing Group*, no. June, 2015. DOI: 10.1038/srep10367.

[7] F. B. Mushenok, R. Dost, C. S. Davies, *et al.*, “Broadband conversion of microwaves into propagating spin waves in patterned magnetic structures,” *Applied Physics Letters*, vol. 111, no. 4, pp. 1–18, 2017. DOI: 10.1063/1.4995991.

[8] W. F. Brown, *Micromagnetics*, J. Wiley, Ed., ser. Interscience tracts on physics and astronomy. J. Wiley, 1963.

[9] W. F. Brown, “Micromagnetics, Domains, and Resonance,” *Journal of Applied Physics*, vol. 30, no. 4, S62–S69, 1959. DOI: 10.1063/1.2185970.

[10] R. Zivieri, A. Giordano, R. Verba, *et al.*, “Theory of nonreciprocal spin-wave excitations in spin Hall oscillators with Dzyaloshinskii-Moriya interaction,” *Physical Review B*, vol. 97, no. 13, p. 134 416, 2018. DOI: 10.1103/PhysRevB.97.134416.

[11] J. Burgess, J. Losby, and M. Freeman, “An analytical model for vortex core pinning in a micromagnetic disk,” *Journal of Magnetism and Magnetic Materials*, vol. 361, pp. 140–149, 2014. DOI: 10.1016/J.JMMM.2014.02.078.

[12] F. Tejo, A. Riveros, J. Escrig, *et al.*, “Distinct magnetic field dependence of Néel skyrmion sizes in ultrathin nanodots,” *Scientific Reports*, vol. 8, no. 1, p. 6280, 2018. DOI: 10.1038/s41598-018-24582-x.

[13] S. Lepadatu, “Efficient computation of demagnetizing fields for magnetic multilayers using multilayered convolution,” *Journal of Applied Physics*, vol. 126, no. 10, p. 103 903, 2019. DOI: 10.1063/1.5116754.

[14] J. Leliaert, M. Dvornik, J. Mulkers, *et al.*, “Fast micromagnetic simulations on GPU - Recent advances made with mumax3,” *Journal of Physics D: Applied Physics*, vol. 51, no. 12, p. 123 002, 2018. DOI: 10.1088/1361-6463/aaab1c.

[15] A. Rahim, C. Ragusa, B. Jan, *et al.*, “A mixed mid-point Runge-Kutta like scheme for the integration of Landau-Lifshitz equation,” *Journal of Applied Physics*, vol. 115, no. 17, 2014. DOI: 10.1063/1.4852118.

[16] O. Vacus and N. Vukadinovic, “Dynamic susceptibility computations for thin magnetic films,” *Journal of Computational and Applied Mathematics*, vol. 176, no. 2, pp. 263–281, 2005. DOI: 10.1016/j.cam.2004.07.016.

[17] *Boris Computational Spintronics – Boris Micromagnetics*, URL: https://www.boris-spintronics.uk.

[18] *Carl-Martin Pfeiler / commics · GitLab*, URL: https://geras.asc.tuwien.ac.at/cpfeiler/commics.

[19] P. Carl-Martin, R. Michele, S. Bernhard, *et al.*, “Computational micromagnetics with Commics,” Institute for Analysis and Scientific Computing, Vienna University of Technology, Wien, Tech. Rep., 2018.

[20] *Fidimag*, URL: https://computationalmodelling.github.io/fidimag/.

[21] *Welcome to Fidimag’s documentation! — Fidimag 0.1 documentation*, URL: https://fidimag.readthedocs.io/en/latest/?badge=latest.

[22] *OOMMF Project at NIST*, URL: https://math.nist.gov/oommf.

[23] R. Zhu, "Grace: A cross-platform micromagnetic simulator on graphics processing units," *SoftwareX*, vol. 3-4, pp. 27–31, 2015. DOI: 10.1016/j.softx.2015.11.001.

[24] *LLG Micromagnetics Simulator (Micromagnetics analysis) - Planet Technology International (Hong Kong) Co., Ltd.* URL: http://planet-tech.com.hk/product/soft/llg.html.

[25] A. Vansteenkiste, J. Leliaert, M. Dvornik, *et al.*, "The design and verification of MuMax3," *AIP Advances*, vol. 4, no. 10, p. 107 133, 2014. DOI: 10.1063/1.4899186.

[26] *Welcome to magnum.fd's documentation! — magnum.fd 0.2 documentation*, URL: http://micromagnetics.org/magnum.fd/.

[27] *Introduction — magnum.fe 2.2.2 documentation*, URL: http://micromagnetics.org/magnum.fe/.

[28] C. Abert, L. Exl, F. Bruckner, *et al.*, "magnum.fe: A micromagnetic finite-element simulation code based on FEniCS," *Journal of Magnetism and Magnetic Materials*, vol. 345, pp. 29–35, 2013. DOI: 10.1016/J.JMMM.2013.05.051.

[29] *MicroMagnum*, URL: http://micromagnum.informatik.uni-hamburg.de/.

[30] NIST, *MuMag standard problems*, URL: https://www.ctcms.nist.gov/mumag/mumag.org.html, 1998.

[31] M. Najafi, B. Krüger, S. Bohlens, *et al.*, "Proposal for a standard problem for micromagnetic simulations including spin-transfer torque," *Journal of Applied Physics*, vol. 105, no. 11, p. 113 914, 2009. DOI: 10.1063/1.3126702.

[32] G. Venkat, D. Kumar, M. Franchin, *et al.*, "Proposal for a standard micromagnetic problem: Spin wave dispersion in a magnonic waveguide," *IEEE Transactions on Magnetics*, vol. 49, no. 1, pp. 524–529, 2013. DOI: 10.1109/TMAG.2012.2206820.

[33] A. Baker, M. Beg, G. Ashton, *et al.*, "Proposal of a micromagnetic standard problem for ferromagnetic resonance simulations," *Journal of Magnetism and Magnetic Materials*, vol. 421, pp. 428–439, 2017. DOI: 10.1016/J.JMMM.2016.08.009.

[34] D. Cortés-Ortuño, M. Beg, V. Nehruji, *et al.*, "Proposal for a micromagnetic standard problem for materials with Dzyaloshinskii–Moriya interaction," *New Journal of Physics*, vol. 20, no. 11, p. 113 015, 2018. DOI: 10.1088/1367-2630/aaea1c.

[35] A. Vansteenkiste, J. Leliaert, M. Dvornik, *et al.*, "The design and verification of MuMax3," *AIP Advances*, vol. 4, no. 10, p. 107 133, 2014. DOI: 10.1063/1.4899186.

[36] C. Abert, "Micromagnetics and spintronics: models and numerical methods," *The European Physical Journal B*, vol. 92, no. 6, p. 120, 2019. DOI: 10.1140/epjb/e2019-90599-6.

[37] R. Hertel, "Micromagnetic simulations of magnetostatically coupled Nickel nanowires," *Journal of Applied Physics*, vol. 90, no. 11, pp. 5752–5758, 2001. DOI: 10.1063/1.1412275.

[38] J. Fischbacher, A. Kovacs, H. Oezelt, *et al.*, "Nonlinear conjugate gradient methods in micromagnetics," *AIP Advances*, vol. 7, no. 4, p. 045 310, 2017. DOI: 10.1063/1.4981902.

[39] L. Exl, S. Bance, F. Reichel, *et al.*, "LaBonte's method revisited: An effective steepest descent method for micromagnetic energy minimization," *Journal of Applied Physics*, vol. 115, no. 17, p. 17D118, 2014. DOI: 10.1063/1.4862839.

[40] W. Scholz, J. Fidler, T. Schrefl, *et al.*, “Scalable parallel micromagnetic solvers for magnetic nanostructures,” *Computational Materials Science*, vol. 28, no. 2, pp. 366–383, 2003.

[41] J. Barzilai and J. M. Borwein, “Two-point step size gradient methods,” *IMA Journal of Numerical Analysis*, vol. 8, no. 1, pp. 141–148, 1988. DOI: 10.1093/imanum/8.1.141.

[42] D. Kumar, J. W. Kłos, M. Krawczyk, *et al.*, “Magnonic band structure, complete bandgap, and collective spin wave excitation in nanoscale two-dimensional magnonic crystals,” *Journal of Applied Physics*, vol. 115, no. 4, p. 043 917, 2014. DOI: 10.1063/1.4862911.

[43] D. Kumar, O. Dmytriiev, S. Ponraj, *et al.*, “Numerical calculation of spin wave dispersions in magnetic nanostructures,” *Journal of Physics D: Applied Physics*, vol. 45, no. 1, p. 015 001, 2012. DOI: 10.1088/0022-3727/45/1/015001.

Chapter 4

Main research topics

4.1 Co-authorship statements

Author presents statements on the co-authorship of the attached papers, four co-authors on each paper. In the introduction before each paper, the author briefly summarised the research and specified his contribution to the work. The author points out that most of the manuscripts were made in collaboration with experimental groups, where his contribution does not include sample preparation and measurement.

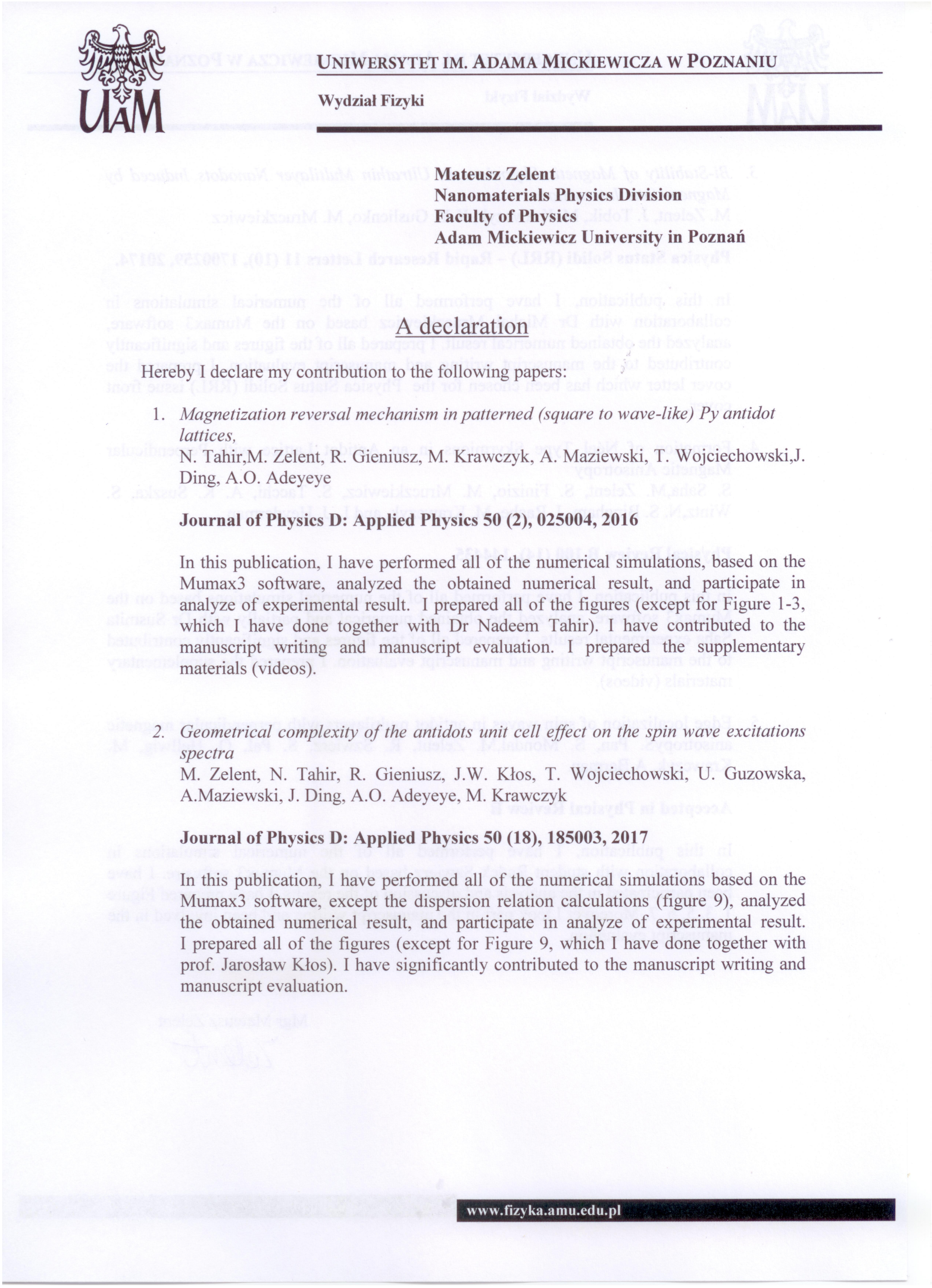

UNIWERSYTET IM. ADAMA MICKIEWICZA W POZNANIU
Wydział Fizyki

Mateusz Zelent
Nanomaterials Physics Division
Faculty of Physics
Adam Mickiewicz University in Poznań

A declaration

Hereby I declare my contribution to the following papers:

1. *Magnetization reversal mechanism in patterned (square to wave-like) Py antidot lattices,*
   N. Tahir,M. Zelent, R. Gieniusz, M. Krawczyk, A. Maziewski, T. Wojciechowski,J. Ding, A.O. Adeyeye

   Journal of Physics D: Applied Physics 50 (2), 025004, 2016

   In this publication, I have performed all of the numerical simulations, based on the Mumax3 software, analyzed the obtained numerical result, and participate in analyze of experimental result. I prepared all of the figures (except for Figure 1-3, which I have done together with Dr Nadeem Tahir). I have contributed to the manuscript writing and manuscript evaluation. I prepared the supplementary materials (videos).

2. *Geometrical complexity of the antidots unit cell effect on the spin wave excitations spectra*
   M. Zelent, N. Tahir, R. Gieniusz, J.W. Kłos, T. Wojciechowski, U. Guzowska, A.Maziewski, J. Ding, A.O. Adeyeye, M. Krawczyk

   Journal of Physics D: Applied Physics 50 (18), 185003, 2017

   In this publication, I have performed all of the numerical simulations based on the Mumax3 software, except the dispersion relation calculations (figure 9), analyzed the obtained numerical result, and participate in analyze of experimental result. I prepared all of the figures (except for Figure 9, which I have done together with prof. Jarosław Kłos). I have significantly contributed to the manuscript writing and manuscript evaluation.

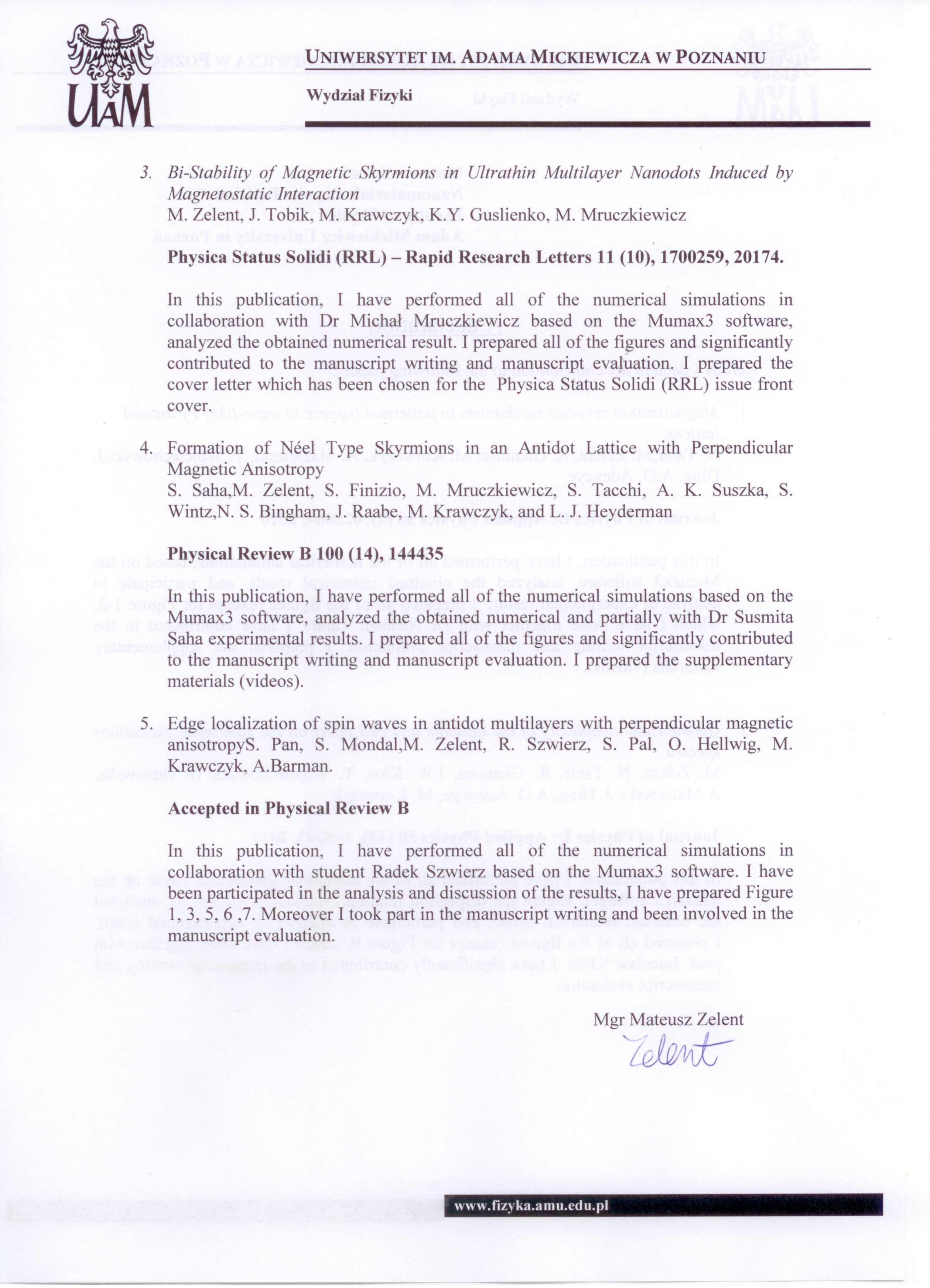

3. *Bi-Stability of Magnetic Skyrmions in Ultrathin Multilayer Nanodots Induced by Magnetostatic Interaction*
   M. Zelent, J. Tobik, M. Krawczyk, K.Y. Guslienko, M. Mruczkiewicz

   Physica Status Solidi (RRL) – Rapid Research Letters 11 (10), 1700259, 20174.

   In this publication, I have performed all of the numerical simulations in collaboration with Dr Michał Mruczkiewicz based on the Mumax3 software, analyzed the obtained numerical result. I prepared all of the figures and significantly contributed to the manuscript writing and manuscript evaluation. I prepared the cover letter which has been chosen for the Physica Status Solidi (RRL) issue front cover.

4. Formation of Néel Type Skyrmions in an Antidot Lattice with Perpendicular Magnetic Anisotropy
   S. Saha,M. Zelent, S. Finizio, M. Mruczkiewicz, S. Tacchi, A. K. Suszka, S. Wintz,N. S. Bingham, J. Raabe, M. Krawczyk, and L. J. Heyderman

   Physical Review B 100 (14), 144435

   In this publication, I have performed all of the numerical simulations based on the Mumax3 software, analyzed the obtained numerical and partially with Dr Susmita Saha experimental results. I prepared all of the figures and significantly contributed to the manuscript writing and manuscript evaluation. I prepared the supplementary materials (videos).

5. Edge localization of spin waves in antidot multilayers with perpendicular magnetic anisotropyS. Pan, S. Mondal,M. Zelent, R. Szwierz, S. Pal, O. Hellwig, M. Krawczyk, A.Barman.

   Accepted in Physical Review B

   In this publication, I have performed all of the numerical simulations in collaboration with student Radek Szwierz based on the Mumax3 software. I have been participated in the analysis and discussion of the results, I have prepared Figure 1, 3, 5, 6 ,7. Moreover I took part in the manuscript writing and been involved in the manuscript evaluation.

Mgr Mateusz Zelent
Zelent

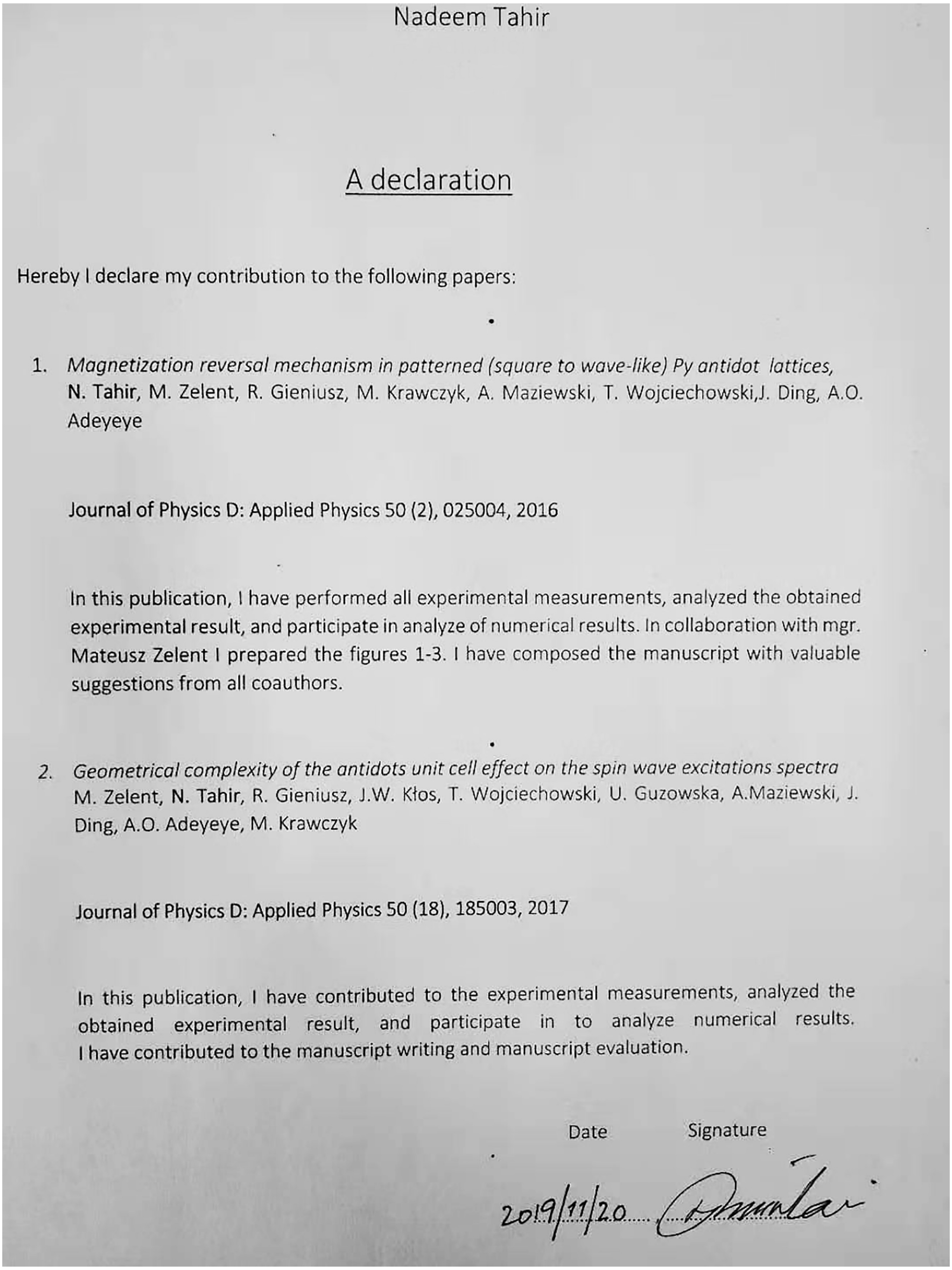

Nadeem Tahir

A declaration

Hereby I declare my contribution to the following papers:

1. *Magnetization reversal mechanism in patterned (square to wave-like) Py antidot lattices,*
   N. Tahir, M. Zelent, R. Gieniusz, M. Krawczyk, A. Maziewski, T. Wojciechowski,J. Ding, A.O. Adeyeye

   Journal of Physics D: Applied Physics 50 (2), 025004, 2016

   In this publication, I have performed all experimental measurements, analyzed the obtained experimental result, and participate in analyze of numerical results. In collaboration with mgr. Mateusz Zelent I prepared the figures 1-3. I have composed the manuscript with valuable suggestions from all coauthors.

2. *Geometrical complexity of the antidots unit cell effect on the spin wave excitations spectra*
   M. Zelent, **N. Tahir**, R. Gieniusz, J.W. Kłos, T. Wojciechowski, U. Guzowska, A.Maziewski, J. Ding, A.O. Adeyeye, M. Krawczyk

   Journal of Physics D: Applied Physics 50 (18), 185003, 2017

   In this publication, I have contributed to the experimental measurements, analyzed the obtained experimental result, and participate in to analyze numerical results. I have contributed to the manuscript writing and manuscript evaluation.

Date Signature

2019/11/20.........

dr hab. Ryszard Gieniusz , prof. UwB

University of Bialystok

A declaration

Hereby I declare my contribution to the following papers:

1. *Magnetization reversal mechanism in patterned (square to wave-like) Py antidot lattices,*
   N. Tahir, M. Zelent, **R. Gieniusz**, M. Krawczyk, A. Maziewski, T. Wojciechowski, J. Ding, A.O. Adeyeye

   Journal of Physics D: Applied Physics 50 (2), 025004, 2016

   In this publication, I was involved in the experimental measurements and discussion concerning obtained results. I have been involved in manuscript writing and evaluation.

2. *Geometrical complexity of the antidots unit cell effect on the spin wave excitations spectra*
   M. Zelent, N. Tahir, **R. Gieniusz**, J.W. Kłos, T. Wojciechowski, U. Guzowska, A. Maziewski, J. Ding, A.O. Adeyeye, M. Krawczyk

   Journal of Physics D: Applied Physics 50 (18), 185003, 2017

   In this publication, I was involved in the experimental measurements and discussion concerning obtained results. I have been involved in manuscript writing and evaluation.

Date Signature

20.11.2019, R. Gieniusz

Prof. dr hab. Andrzej Maziewski

Department of Physics of Magnetism

University of Bialystok

A declaration

Hereby I declare my contribution to the following papers:

1. *Magnetization reversal mechanism in patterned (square to wave-like) Py antidot lattices,* N. Tahir, M. Zelent, R. Gieniusz, M. Krawczyk, **A. Maziewski**, T. Wojciechowski, J. Ding, A.O. Adeyeye

   Journal of Physics D: Applied Physics 50 (2), 025004, 2016

   In this publication, I have contributed to the problem definition experimental measurements, I was involved in the discussion concerning obtained results, manuscript writing and its evaluation.

2. *Geometrical complexity of the antidots unit cell effect on the spin wave excitations spectra,* M. Zelent, N. Tahir, R. Gieniusz, J.W. Kłos, T. Wojciechowski, U. Guzowska, **A. Maziewski,** J. Ding, A.O. Adeyeye, M. Krawczyk

   Journal of Physics D: Applied Physics 50 (18), 185003, 2017

   In this publication, I have contributed to the problem definition experimental measurements, I was involved in the discussion concerning obtained results, manuscript writing and its evaluation.

Date Signature

2019.11.22 ……………………, ……………………… A Maziewski

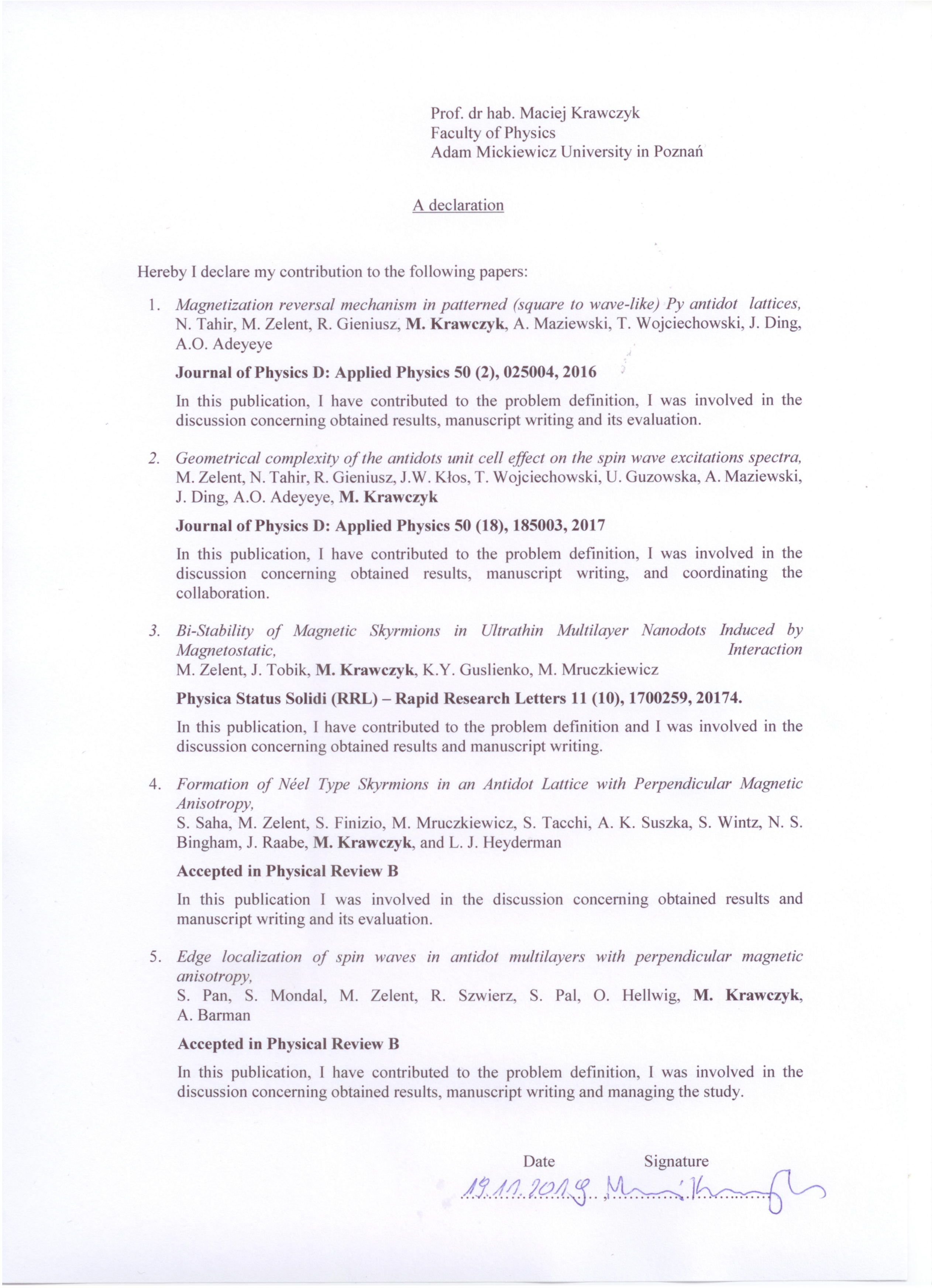

Prof. dr hab. Maciej Krawczyk
Faculty of Physics
Adam Mickiewicz University in Poznań

A declaration

Hereby I declare my contribution to the following papers:

1. *Magnetization reversal mechanism in patterned (square to wave-like) Py antidot lattices,* N. Tahir, M. Zelent, R. Gieniusz, **M. Krawczyk**, A. Maziewski, T. Wojciechowski, J. Ding, A.O. Adeyeye

   Journal of Physics D: Applied Physics 50 (2), 025004, 2016

   In this publication, I have contributed to the problem definition, I was involved in the discussion concerning obtained results, manuscript writing and its evaluation.

2. *Geometrical complexity of the antidots unit cell effect on the spin wave excitations spectra,* M. Zelent, N. Tahir, R. Gieniusz, J.W. Kłos, T. Wojciechowski, U. Guzowska, A. Maziewski, J. Ding, A.O. Adeyeye, **M. Krawczyk**

   Journal of Physics D: Applied Physics 50 (18), 185003, 2017

   In this publication, I have contributed to the problem definition, I was involved in the discussion concerning obtained results, manuscript writing, and coordinating the collaboration.

3. *Bi-Stability of Magnetic Skyrmions in Ultrathin Multilayer Nanodots Induced by Magnetostatic, Interaction*
   M. Zelent, J. Tobik, **M. Krawczyk**, K.Y. Guslienko, M. Mruczkiewicz

   Physica Status Solidi (RRL) – Rapid Research Letters 11 (10), 1700259, 20174.

   In this publication, I have contributed to the problem definition and I was involved in the discussion concerning obtained results and manuscript writing.

4. *Formation of Néel Type Skyrmions in an Antidot Lattice with Perpendicular Magnetic Anisotropy,*
   S. Saha, M. Zelent, S. Finizio, M. Mruczkiewicz, S. Tacchi, A. K. Suszka, S. Wintz, N. S. Bingham, J. Raabe, **M. Krawczyk**, and L. J. Heyderman

   Accepted in Physical Review B

   In this publication I was involved in the discussion concerning obtained results and manuscript writing and its evaluation.

5. *Edge localization of spin waves in antidot multilayers with perpendicular magnetic anisotropy,*
   S. Pan, S. Mondal, M. Zelent, R. Szwierz, S. Pal, O. Hellwig, **M. Krawczyk**, A. Barman

   Accepted in Physical Review B

   In this publication, I have contributed to the problem definition, I was involved in the discussion concerning obtained results, manuscript writing and managing the study.

Date Signature

19.11.2019

Dr Michał Mruczkiewicz
Institute of Electrical Engineering
Slovak Academy of Sciences

A declaration

Hereby I declare my contribution to the following papers:

1. *Bi-Stability of Magnetic Skyrmions in Ultrathin Multilayer Nanodots Induced by Magnetostatic Interaction*
M. Zelent, J. Tobik, M. Krawczyk, K.Y. Guslienko, **M. Mruczkiewicz**
Physica Status Solidi (RRL) – Rapid Research Letters 11 (10), 1700259, 20174.
In this publication, I have contributed to problem definition, performing numerical simulations, and discussion concerning obtained results. I have been involved in manuscript writing and its evaluation.

2. *Formation of Néel Type Skyrmions in an Antidot Lattice with Perpendicular Magnetic Anisotropy*
S. Saha, M. Zelent, S. Finizio, **M. Mruczkiewicz**, S. Tacchi, A. K. Suszka, S. Wintz, N. S. Bingham, J. Raabe, M. Krawczyk, and L. J. Heyderman
Accepted in Physical Review B

In this publication, I have contributed to discussion concerning obtained results. I have been involved in manuscript writing.

Date Signature
01/10/2019.......,......................

Dr. Sebastian Wintz
Paul Scherrer Institut
Forschungsstrasse 111
5232 Villigen PSI
Switzerland

Declaration

Hereby I declare my contribution to the following paper:

"Formation of Néel Type Skyrmions in an Antidot Lattice with Perpendicular Magnetic Anisotropy"

by S. Saha, M. Zelent, S. Finizio, M. Mruczkiewicz, S. Tacchi, A. K. Suszka, **S. Wintz**, N. S. Bingham, J. Raabe, M. Krawczyk, and L. J. Heyderman,

which was accepted for publication in Physical Review B.

In this publication I have contributed to the measurements. I was involved in both the discussion of the obtained results and in writing manuscript writing.

Baden, 07.10.2019

Sebastian Wintz

PAUL SCHERRER INSTITUT

ETH
Eidgenössische Technische Hochschule Zürich
Swiss Federal Institute of Technology Zurich

Dr. Susmita Saha

ETH-Zurich - Paul Scherrer Institut
5232 Villigen PSI
Switzerland
Tel: +41 56/ 310 20 81
E-mail:susmita.saha@psi.ch

Villigen,
24th Sep, 2019

Hereby I declare my contribution to the following papers:

Formation of Néel Type Skyrmions in an Antidot Lattice with Perpendicular Magnetic Anisotropy,

S. Saha, M. Zelent, S. Finizio, M. Mruczkiewicz, S. Tacchi, A. K. Suszka, S. Wintz, N. S. Bingham, J. Raabe, M. Krawczyk, and L. J. Heyderman

In this publication I have contributed to the sample design, preparation and measurements. I was involved in the discussions concerning obtained results and manuscript writing and its evaluation.

Yours Sincerely,

Susmita Saha

(Susmita Saha)

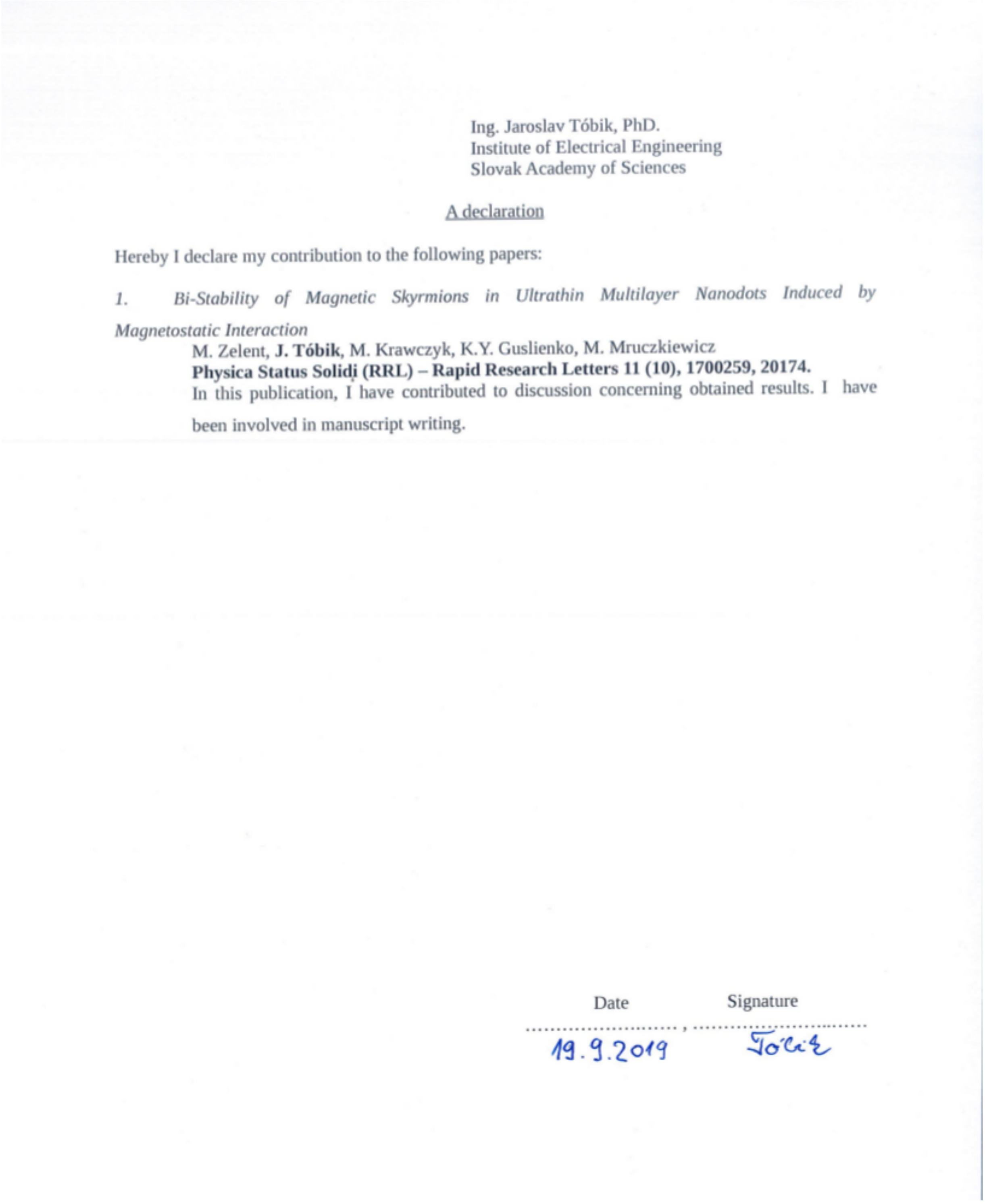

Ing. Jaroslav Tóbik, PhD.
Institute of Electrical Engineering
Slovak Academy of Sciences

A declaration

Hereby I declare my contribution to the following papers:

1. *Bi-Stability of Magnetic Skyrmions in Ultrathin Multilayer Nanodots Induced by Magnetostatic Interaction*
M. Zelent, **J. Tóbik**, M. Krawczyk, K.Y. Guslienko, M. Mruczkiewicz
Physica Status Solidi (RRL) – Rapid Research Letters 11 (10), 1700259, 20174.
In this publication, I have contributed to discussion concerning obtained results. I have been involved in manuscript writing.

Date Signature
……………………, ……………………
19.9.2019

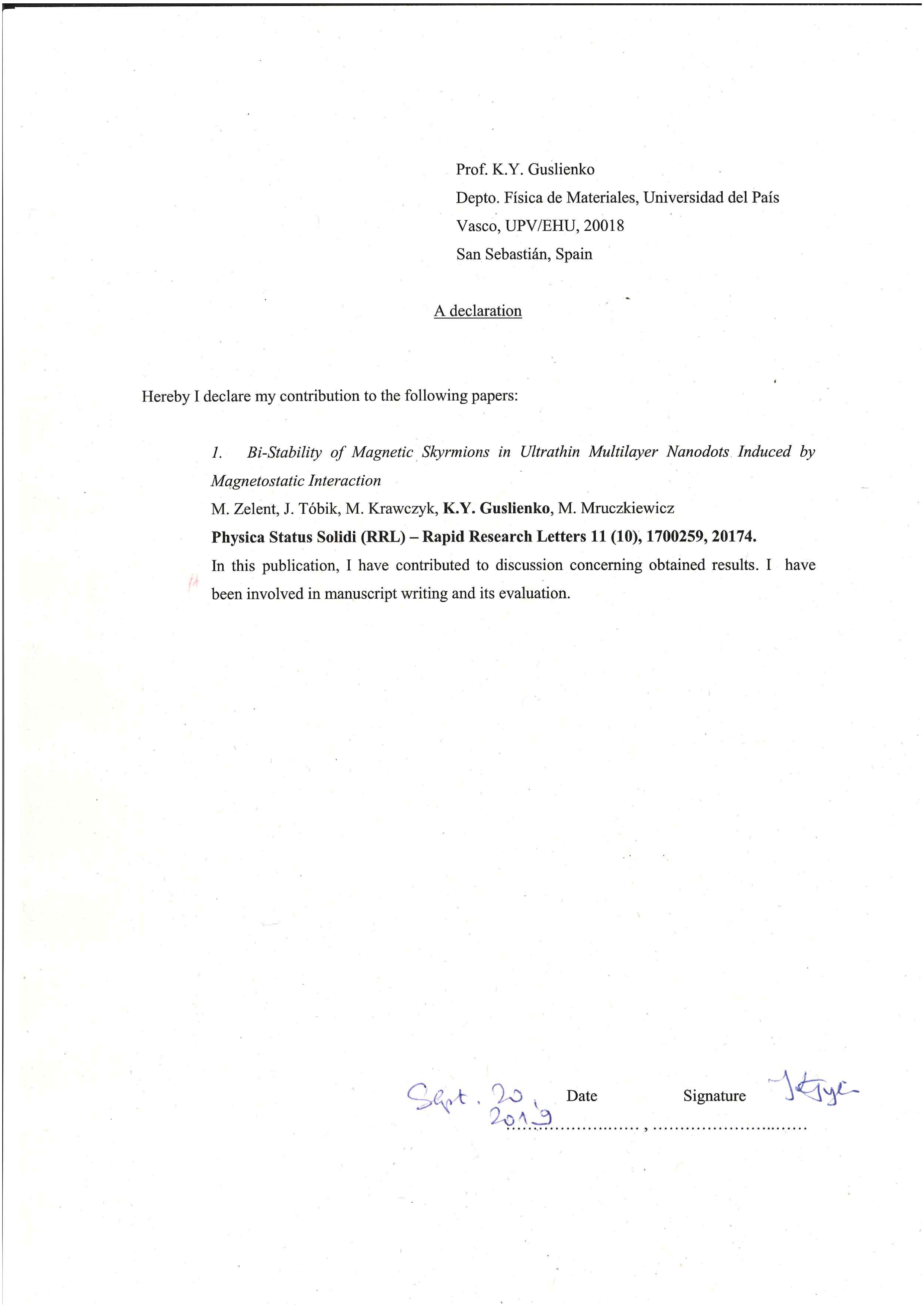

Prof. K.Y. Guslienko
Depto. Física de Materiales, Universidad del País
Vasco, UPV/EHU, 20018
San Sebastián, Spain

A declaration

Hereby I declare my contribution to the following papers:

1. *Bi-Stability of Magnetic Skyrmions in Ultrathin Multilayer Nanodots Induced by Magnetostatic Interaction*
   M. Zelent, J. Tóbik, M. Krawczyk, **K.Y. Guslienko**, M. Mruczkiewicz
   Physica Status Solidi (RRL) – Rapid Research Letters 11 (10), 1700259, 20174.
   In this publication, I have contributed to discussion concerning obtained results. I have been involved in manuscript writing and its evaluation.

Sept. 20, 2019 Date Signature
……………………, ……………………

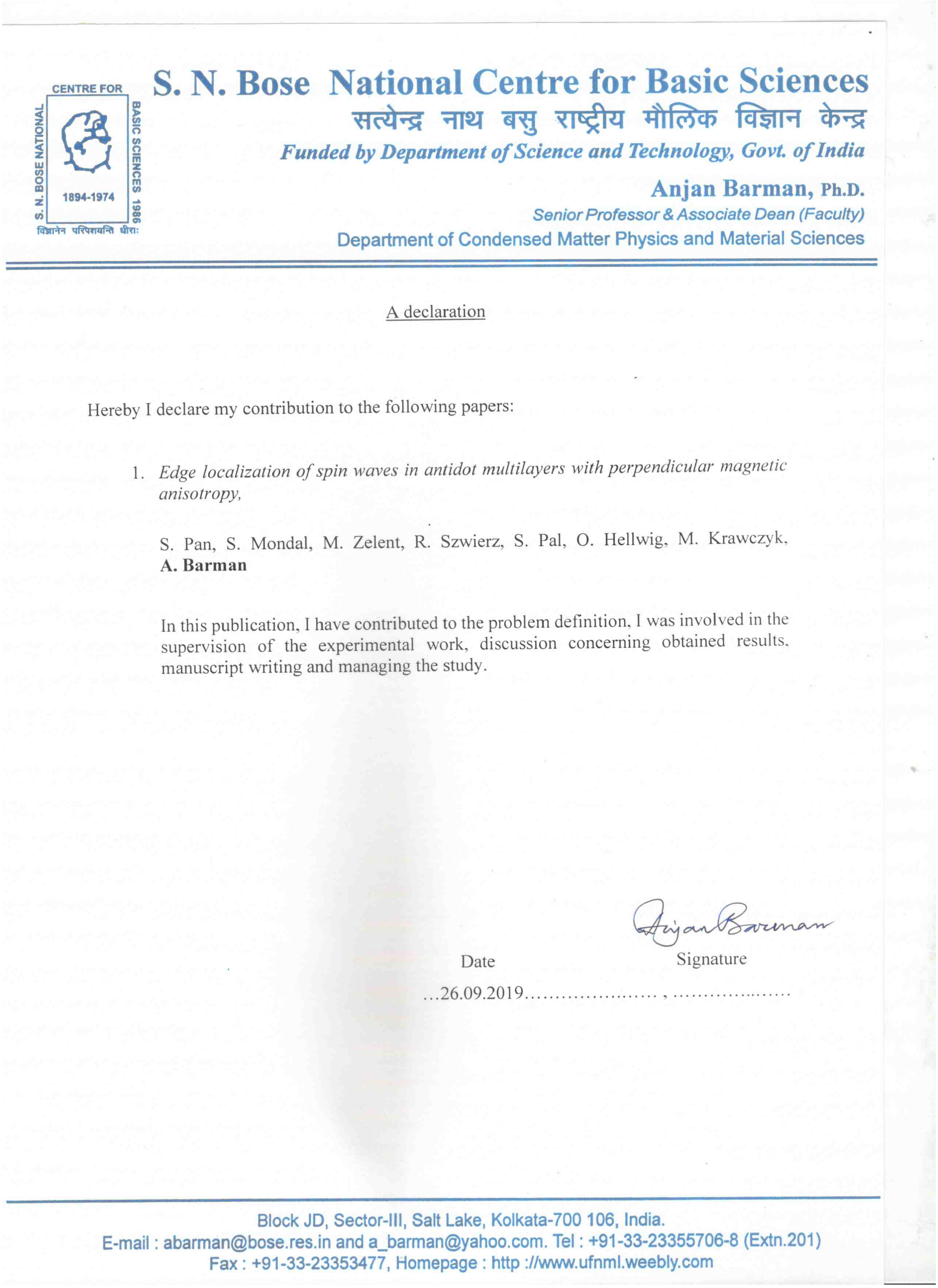

S. N. Bose National Centre for Basic Sciences
सत्येन्द्र नाथ बसु राष्ट्रीय मौलिक विज्ञान केन्द्र
Funded by Department of Science and Technology, Govt. of India
Anjan Barman, Ph.D.
Senior Professor & Associate Dean (Faculty)
Department of Condensed Matter Physics and Material Sciences

A declaration

Hereby I declare my contribution to the following papers:

1. *Edge localization of spin waves in antidot multilayers with perpendicular magnetic anisotropy,*

   S. Pan, S. Mondal, M. Zelent, R. Szwierz, S. Pal, O. Hellwig, M. Krawczyk, **A. Barman**

   In this publication, I have contributed to the problem definition, I was involved in the supervision of the experimental work, discussion concerning obtained results, manuscript writing and managing the study.

Anjan Barman

Date Signature

…26.09.2019……………..……, …………..……

Block JD, Sector-III, Salt Lake, Kolkata-700 106, India.
E-mail : abarman@bose.res.in and a_barman@yahoo.com. Tel : +91-33-23355706-8 (Extn.201)
Fax : +91-33-23353477, Homepage : http ://www.ufnml.weebly.com

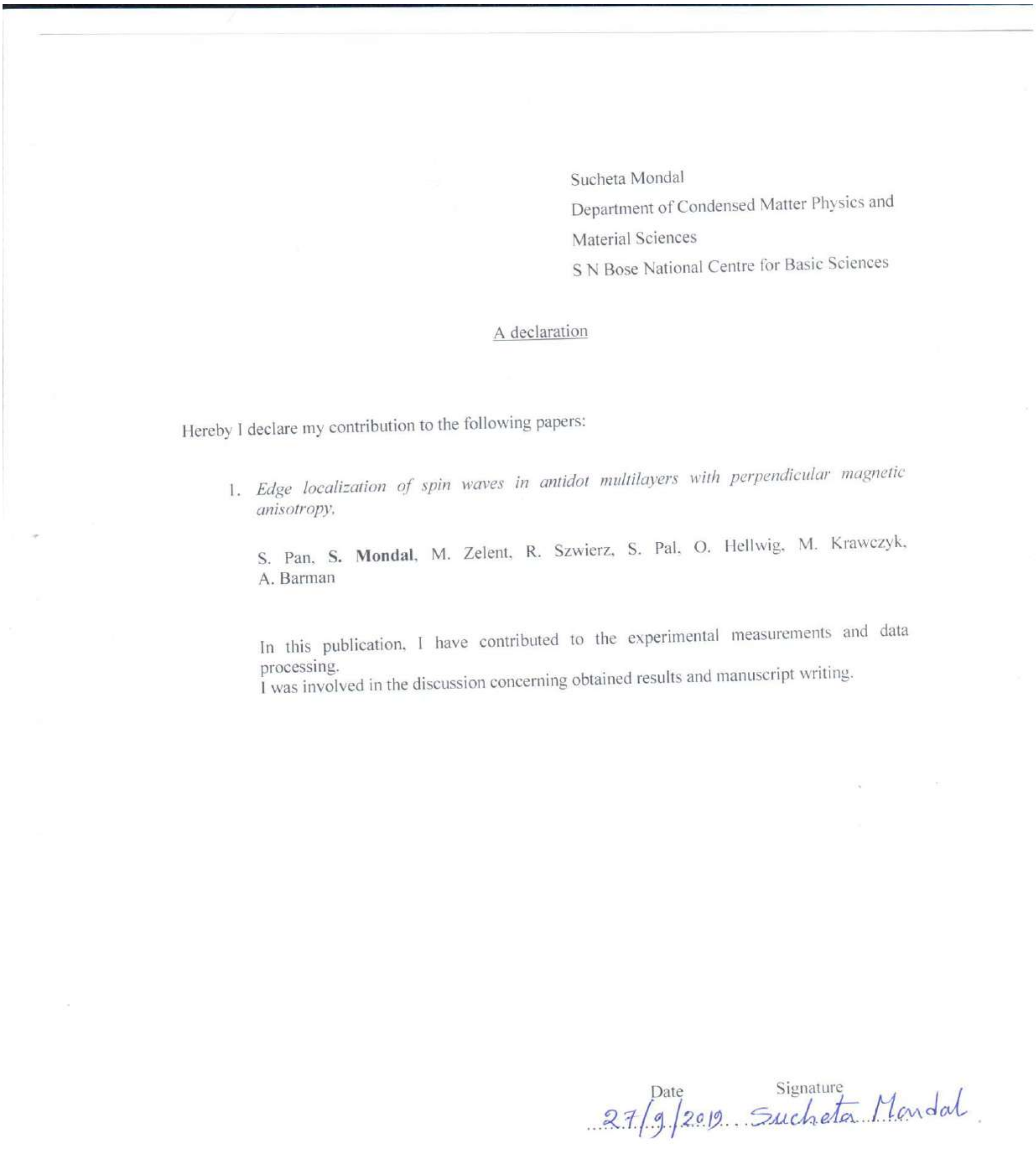

Sucheta Mondal
Department of Condensed Matter Physics and
Material Sciences
S N Bose National Centre for Basic Sciences

A declaration

Hereby I declare my contribution to the following papers:

1. *Edge localization of spin waves in antidot multilayers with perpendicular magnetic anisotropy,*

   S. Pan, **S. Mondal**, M. Zelent, R. Szwierz, S. Pal, O. Hellwig, M. Krawczyk, A. Barman

   In this publication, I have contributed to the experimental measurements and data processing.
   I was involved in the discussion concerning obtained results and manuscript writing.

Date Signature
27/9/2019 Sucheta Mondal

Santanu Pan
Department of Condensed Matter Physics and
Material Sciences
S N Bose National Centre for Basic Sciences

A declaration

Hereby I declare my contribution to the following papers:

1. *Edge localization of spin waves in antidot multilayers with perpendicular magnetic anisotropy,*

   S. Pan, S. Mondal, M. Zelent, R. Szwierz, S. Pal, O. Hellwig, M. Krawczyk, A. Barman

   In this publication, I have contributed to experimental measurements and data processing.

   I was also involved in the discussion concerning obtained results and manuscript writing.

Date Signature
27/09/2019 Santanu Pan

4.2 Magnetization reversal mechanism in patterned (square to wave-like) Py antidot lattices

4.2.1 Introduction

Antidot lattices (ADLs), a regular array of antidots in a continuous film, have attracted much interest due to their technological applications and fundamental research. The competition between the intrinsic and shape anisotropy, together with local effects originated by the antidots, establish new scenario for engineering the magnetic properties of the thin film by tailoring the geometric parameters. Our interest was in the studies on the equilibrium magnetic states and magnetization reversal processes, which are governed by the interplay between anisotropy, shape of antidots and lattice symmetry. In collaboration with group from Białystok and Singapore we have investigated the magnetic anisotropies and magnetization reversal mechanisms in systematically engineered ADLs (from square to wave-like, via bi-component ADLs) by longitudinal magneto-optical Kerr effect (LMOKE) microscopy. Experimental results were interpreted and reproduced by micromagnetic simulations.

In this publication, the Author has performed all of the numerical simulations based on the Mumax3 software. He has analysed the obtained numerical results and participated in analyse of the experimental results. He has prepared all the figures (except Figure 1-3, which he has done together with Dr Nadeem Tahir). He has contributed to the manuscript writing and manuscript evaluation. He has prepared the supplementary materials (videos).

Number of Ministerial points: 70.
Impact Factor: 2.829

J. Phys. D: Appl. Phys. **50** (2017) 025004 (9pp)
doi:10.1088/1361-6463/50/2/025004

Magnetization reversal mechanism in patterned (square to wave-like) Py antidot lattices

N Tahir[1,5,6], **M Zelent**[2], **R Gieniusz**[1], **M Krawczyk**[2], **A Maziewski**[1], **T Wojciechowski**[3], **J Ding**[4] **and A O Adeyeye**[4]

[1] Faculty of Physics, University of Bialystok, ul. Konstantego Ciołkowskiego 1L, Bialystok 15-245, Poland
[2] Faculty of Physics, Adam Mickiewicz University in Poznan, Umultowska 85, 61-614 Poznan, Poland
[3] Institute of Physics, Polish Academy of Sciences, al. Lotnikow 32/46, PL-02-668 Warsaw, Poland
[4] Department of Electrical and Computer Engineering, National University of Singapore, Singapore
[5] Division of Science and Technology, University of Education, Lahore, Pakistan

E-mail: ntahir@uwb.edu.pl

Received 22 June 2016, revised 4 October 2016
Accepted for publication 2 November 2016
Published 1 December 2016

Abstract

The effects of shape and geometry of antidot (square, bi-component, and wave-like) lattices (ADLs) on the magnetization reversal processes and magnetic anisotropy has been systematically investigated by magneto-optical Kerr effect based microscopy. Our experimental results were reproduced by micromagnetic simulations, which highlight the qualitative agreement with the experimental results. We have demonstrated that a small antidot in the center of a unit cell in the square ADL is sufficient to induce additional easy axes with large coercive fields. In wave-like patterns, narrow channels connecting smaller and larger antidots (bi-component ADL) further drastically change the anisotropy map, creating the high coercive fields along a wide angular range (90°) of directions parallel to the channels. In simulated results, we have observed formation of periodic domain structures in all ADLs, however, in the case of a wave-like pattern it is most regular and moreover two different periodic patterns are stabilized at different applied magnetic field values. The formation of 360° domain walls were also observed in wave-like ADL where these domains are formed along the lines connecting adjacent larger and smaller antidots, perpendicular to the channels. These findings point out the possibility of exploiting ADLs with complex unit cells in magnonic or spintronic applications.

Keywords: magnetic anisotropy, reversal mechanism, micromagnetic simulations, magnetic domains

S Online supplementary data available from stacks.iop.org/JPhysD/50/025004/mmedia

(Some figures may appear in colour only in the online journal)

1. Introduction

Nanoscale patterned magnetic films are envisaged for technological purposes profiting from the possibilities of tailoring the local distribution of magnetization in a controlled manner.The magnetic nanodots [1–5] and nanowires [6] have shown interesting results where the study of statics and dynamics of magnetization have been well studied. Antidot lattices (ADLs), a regular array of antidots in a continuous film, have attracted much interest here, due to their technological applications and

---

[6] Author to whom any correspondence should be addressed.

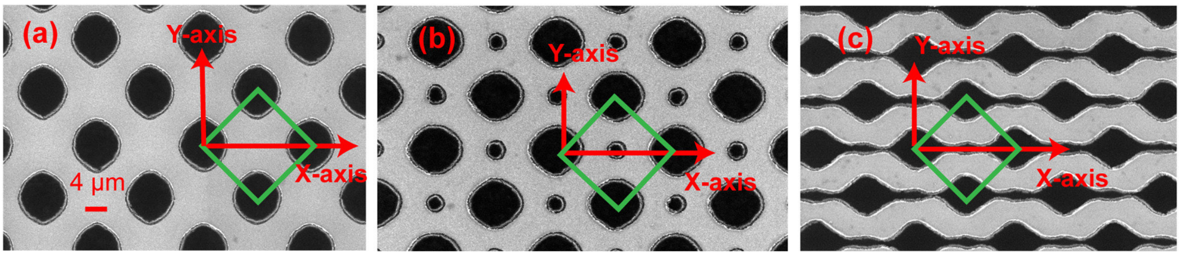

Figure 1. SEM images of the three investigated samples, (a) square antidot lattice, (b) bi-component antidot lattice and (c) wave-like pattern.

fundamental research [7]. They have emerged as strong candidates for magneto-photonic crystals [8], sensors of magnetic nanoparticles [9], waveguides for spin waves [10, 11] or magneto-logic devices may also be realized by antidots [12, 13]. The competition between the intrinsic and shape anisotropy, together with local effects originated by the antidots, establish new scenario for engineering the magnetic properties of the thin film by tailoring the geometric parameters. The interest is in the studies on the equilibrium magnetic states and magnetization reversal processes, which are governed by the interplay between anisotropy, size, shape, the distance between antidots and lattice symmetry [14]. Moreover, the ADLs are also used to fabricate magnonic crystals (MCs), i.e. magnonic metamaterials with periodic modulation of their magnetic properties for tailoring spin wave dynamics [15–17]. With the change of the size, shape and density of the antidots, the coercive field can be systematically engineered [18, 19]. From the fundamental point of view, the antidots affect the switching mechanism during the magnetization reversal process, which still is not fully understood in the nanoscale regime. The basic models of the inclusions [20] or nearest-neighbor rule [21] are used to describe the remagnetization process in different lattices and volume densities [18, 19]. The modification of magnetization reversal in bi-component (with alternating diameters) ADLs as compared to a homogeneous array of antidots magnetization reversal was investigated [22, 23], however only along one direction of the applied magnetic field, connecting larger and smaller antidots.

In the present study we have investigated the magnetic anisotropies and magnetization reversal mechanisms in systematically engineered ADLs (from square to wave-like, via bi-component ADLs) by longitudinal magneto-optical Kerr effect (LMOKE) microscopy. Experimental results were reproduced by micromagnetic simulations performed with MuMax [24]. We demonstrated how one can tune the magnetic anisotropy and magnetization reversal in a controlled way through appropriate nanopatterning and application of an in-plane static magnetic field. For an angle of 45° (with respect to the diagonal of the square lattice) several processes are identified: local rotation of the magnetization between antidots, formation of the global boundaries and domain chains [25]. At this direction of the magnetic field, the easy axis is formed in bi-component ADL, which is absent in the square ADL. Furthermore, in micromagnetic simulation results we have identified regular domain structures, with especially interesting 360° domain walls found. These domain walls stabilize in the wave-like ADL for magnetic field reversal along the direction parallel to the channels.

2. Experimental methods

Large area ($4 \times 4\,\text{mm}^2$) $Ni_{80}Fe_{20}$ (Permalloy (Py)) antidot nanostructures were patterned on commercially available silicon (Si) substrates by employing DUV lithography at 248 nm exposing wavelength. In order to create patterns in the resist, the substrate was spin coated with 60 nm thick bottom anti-reflecting coating (BARC) followed by a 480 nm positive deep UV-photoresist which is four to five times thicker than those typically used for e-beam lithography. Thicker resist helps to achieve high aspect ratio and additionally makes the lift-off process easier. A Nikon lithographic scanner with KrF excimer laser radiation was used to expose the resist. In order to transfer resist patterns into antidots, 10 nm thick Py was deposited at room temperature by e-beam evaporation technique at a rate of $0.2\,\text{Å}\,\text{s}^{-1}$ while the pressure in the chamber was maintained at 2×10^{-6} Torr [26]. The samples with various geometries starting from basic (unit) structure, antidots in square lattice (figure 1(a)), to more complex systems (wave-like pattern, figure 1(c)) by systematically inclusion of additional smaller antidots (bi-component antidots with alternating diameters, figure 1(b)) were fabricated through the above discussed procedure. In order to keep the edges of the structures sharp, the last step of the sample fabrication process (lift-off of BARC) was not carried out so BARC is present inside the antidots' lattice which is confirmed from scanning electron microscopy (SEM) and atomic force microscopy (AFM) analysis. The antidots are close to the circular shape. In square ADL, the diameter D is 405 nm and period $a = 650$ nm, in bi-component ADL the diameters of larger and smaller antidots are 410 and 140 nm, respectively, and $a = 650$ nm. In the wave-like structure larger and smaller antidots are 350 and 130 nm, and the period is 580 nm.

Structural analysis was carried out by ZEISS EVO scanning electron microscopy. Magnetization reversal mechanism was studied through Kerr microscopy in longitudinal (LMOKE) configuration where applied external field was along the sample plane. The region of interest was selected approximately of the order of a few hundred microns whereas the antidot structures are of the order of a few hundred nanometers. Although there are some inhomogenities in the samples observed by the scanning electron microscope (see figure 1), the signal obtained by LMOKE is aggregate from the homogenous as well as from the inhomogeneous part of the sample.

3. Experimental results

It has been observed that the reference sample (10 nm thick Py film) possesses very small in-plane anisotropy with small change in the coercive field H_c (<1 Oe) states that continuous films (reference samples) have weak uniaxial anisotropy due to the polycrystalline nature of the film and the absence of field induced anisotropy [18, 27].

Square ADL (figure 2(a)) shows a remarkable increase in H_c in comparison to the reference sample. The increase in H_c after patterning could be related to the non-magnetic vacancies, which hinder the domain wall movement [28]. For $\phi_H = 0°$ almost square-like hysteresis loop (with $H_c = 110$ Oe) suggests easy axis for this direction, while for $\phi_H = 45°$ decrease in the H_c to ~50 Oe (and shape of the hysteresis loop shown for $\phi_H = 40°$) confirms the hard axis. Furthermore from the observation of LMOKE hysteresis, figure 2(a) one can see that for in-plane angles of 0° and 90° magnetization in remanences are larger as compared to 40° which is a hard axis (being closest neighbors). The difference in magnetization in remanences for 0° and 90° could be related to the lack of perfect circular shape (see figure 1(a)). Magnetization hysteresis loop for 40° shows that magnetization reverses smoother, characteristic for the hard axis. For an ADL with a square lattice, a four-fold magnetic anisotropy with alternating hard and easy axis after every 45° was observed. The hard axes along the edges of the square ADL and easy axis along the diagonal direction can be seen from the polar plot of the coercive field shown in figure 3(a), which is related to the symmetry of the ADL.

Figure 2(b) shows the exemplary LMOKE hysteresis for bi-component ADL. From the LMOKE hysteresis loops it is clear that magnetization reversal goes through two step reversal mechanisms. In the case of field applied along *X* and *Y*-axes as defined in figure 1(b), the larger antidots are connected through smaller antidots, whereas in the square lattice those were easy axes. These axes remain still easy axis with large H_c as can be seen in figure 3(b). These axes remain still easy axis with large H_c as can be seen in figure 3(b). A similar scenario for the magnetization reversal can be expected also for the magnetic field directed along 45° as along both directions the magnetization remanence and coercive fields have similar values (see, table 1). In the present situation the direction of the magnetic field is parallel to the rows of larger (smaller) holes. The change of the lattice from the basic square ADL lattice to bi-component (with alternating diameters) ADL introduces eight-fold anisotropy, figure 3(b), although the symmetry of the lattice has not been changed. This shows that the magnetization reversal process depends not only on the lattice symmetry but also on the composition of the unit cell, in this case on the number and size of the antidots in the unit cell. The remanent magnetization state of the ADL is not only a result of the minimization of the magnetostatic energy of each antidot itself but also the magnetostatic interactions among the antidots.

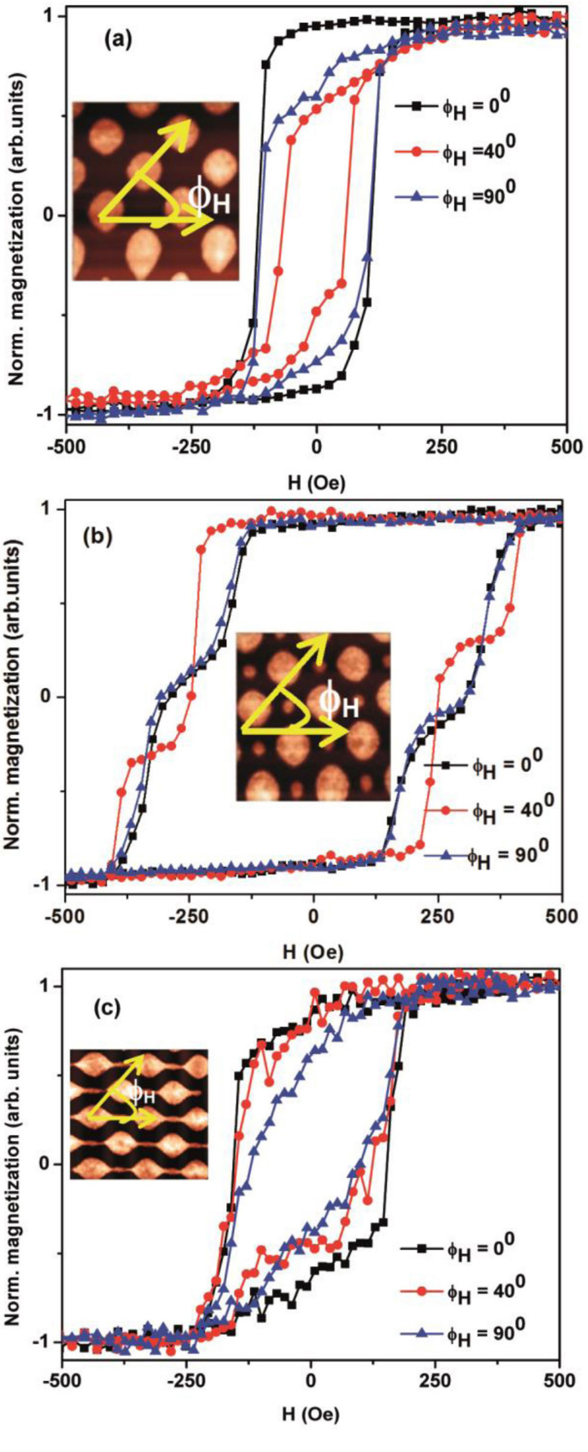

Figure 2. LMOKE hysteresis loops for in-plane magnetic field under angles of 0, 40, and 90° with respect to the main direction of the square lattice for (a) square ADL, (b) bi-component ADL and (c) wave-like structure. The arrangement for the measurements is shown in inset of figures 1(a)–(c).

In the third case, when larger and smaller antidots are connected to make the wave-like pattern, the exemplary hysteresis loops for certain in-plane angles are shown in figure 2(c). It can be seen from LMOKE hysteresis and H_c polar dependence (figure 3(c)) that easy (hard) axis can be observed when the field is along (perpendicular) to the direction of the wave-like patterns, which is along $X(Y)$-axes. Clearly two fold symmetry has been observed in figure 3(c).

The differences of the magnetic properties between the continuous and antidot films can be explained by a change in the mechanism of magnetization reversal originated from a different effective magnetic anisotropy. Here, we point out the contribution of the configurational anisotropy [29, 30] having origin in the variations of the magnetization pattern at different ADLs and dependent on the magnetic field orientation. In the continuous and ADL films, the reversal is preceded through the propagation of domain wall (DW) after the nucleation barriers are overcome at low coordination sites, such as defects or grain boundaries. The DW pinning strength and the local symmetry of the anisotropy determine both coercivity and density (size) of the magnetic domains during reversal. In the continuous thin film well-defined uniaxial anisotropy systems with low energy pinning centres, a fast DW propagation with very large magnetic domains are expected. In the antidot film, the antidots act as strong pinning centres for the DW and additional to domain wall propagation also magnetization rotation can contribute to the magnetization reversal, especially in ADLs with small thicknesses [31]. At the macroscopic scale, the magnetic behavior from different arrangements is averaged with the MOKE measurements.

The configurational anisotropy is induced due to the antidot lattice (ADL) pattern and can be explained through the considerations of the surface magnetic 'charges' that appear at the interface between magnetic material and the antidots [18, 32]. Through the demagnetizing field they facilitate the formation of the magnetic configurations lowering magnetic energy and formation of the domains as the external magnetic field is progressively lowered from the saturation state. More detailed analysis can be performed through micromagnetic simulations in the next coming paragraphs.

4. Micromagnetic simulations

In order to explain the magnetic anisotropy behavior in the structures under investigation obtained in LMOKE measurements (figures 2 and 3), an understanding of the distribution of the microscopic spin orientation in such structures is needed. This was achieved through performing micromagnetic simulations of the remagnetization processes using MuMax simulations (version 3.8) [24]. The simulation structures for three studied geometries are shown in figures 5–7. Simulations are performed for ideal structures, preserving a circular shape of antidots (in square ADL and bi-component ADL) and circular holes connected with narrow channels for a wave-like structure. The larger antidots of 400 nm and smaller antidots of 140 nm diameter were used in all cases.

The magnetic parameters used for simulations are standard values of the Py: saturation magnetization $M_s = 800$ kA m^{-1}, exchange constant $A = 13 \times 10^{-12}$ J m^{-1}, and anisotropy constant $K_u = 0$ [18]. For square ADL and bi-component ADL the mesh of size 2.4 nm × 2.4 nm × 10 nm, and 3.3 nm × 3.3 nm × 10 nm for wave-like structures was used along the X-, Y- and Z-axis respectively. Periodic boundary conditions for each of the in-plane directions with eight repetitions

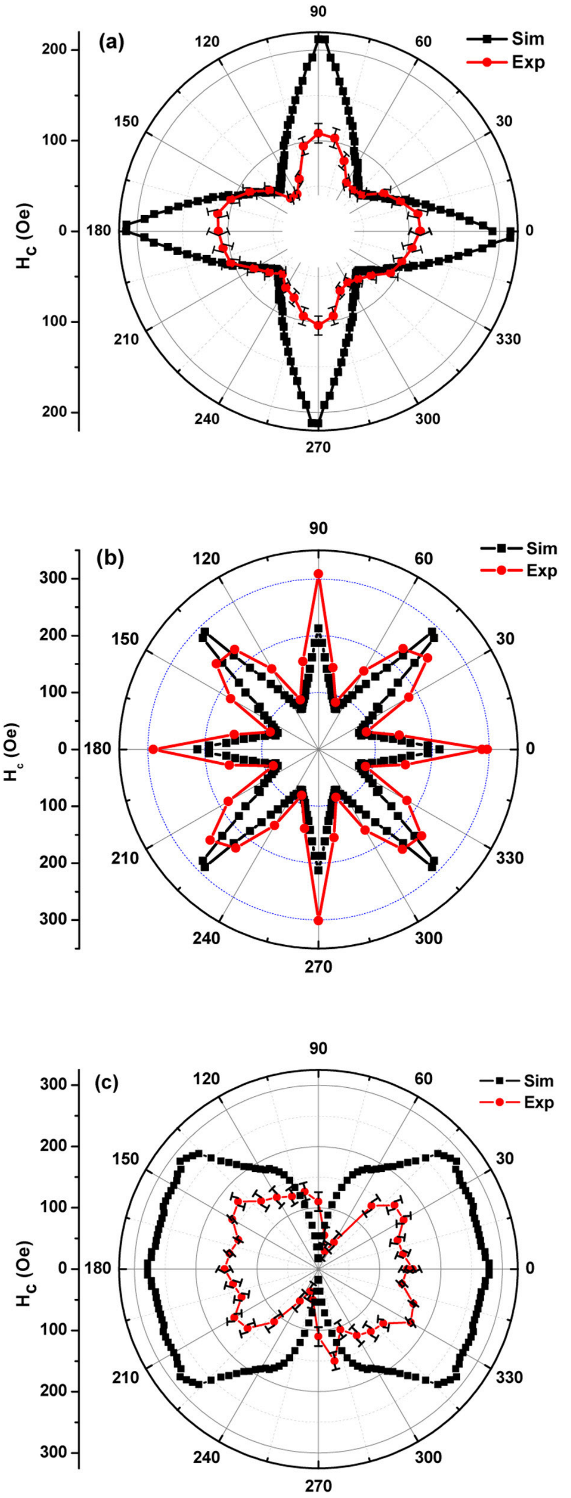

Figure 3. Polar plot showing comparison of simulated (black) and experimental (from LMOKE, red) H_c field for (a) square ADL, (b) bi-component ADL and (c) wave-like structure.

Table 1. The values of the coercive field (H_c) and magnetization in remanence (M_{rem}) in three samples: square ADL, bi-component ADL and wave-like structure. These values were taken at orientations of the magnetic field pointed out in second column (in parenthesis ϕ_H is used in micromagnetic simulations).

		H_c (Oe) Experiment	M_{rem} (arb.units.) Experiment	H_c (Oe) Simulation	M_{rem} (arb. units.) Simulation
Square ADL	Easy axis, 0°(1°)	110	0.92	177.5	0.88
	Hard axis, 40°(44°)	50	0.52	62.5	0.63
Bi-component ADL	Easy axis, 0°(1°)	297	0.91	182.5	0.86
	Easy axis, 40°(44°)	248	0.94	267.5	0.89
	Hard axis, 20°(22°)	88.5	0.86	77.5	0.80
Wave-like	Easy axis, 0°(1°)	155	0.78	307.5	0.89
	Hard axis, 90°(88°)	109	0.48	31	0.03

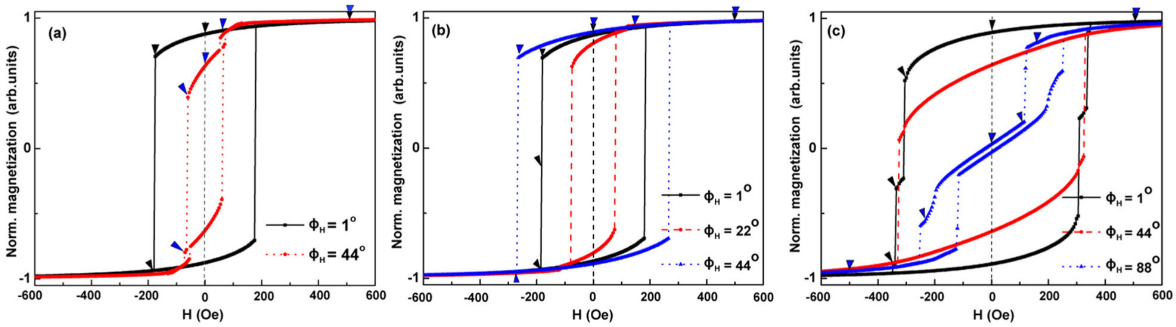

Figure 4. Hysteresis loops obtained from micromagnetic simulations at different in-plane angles ϕ_H for (a) square ADL, (b) bi-component ADL and (c) wave-like ADL. The inverted triangles mark the magnetic field magnitude at which the magnetization distributions are presented in figures 5–7.

of the supercells shown in figures 5–7 (all figures should be read from left to right) along the in-plane directions are used to reduce the influence of the external ends of the structure [33]. We verified that changes of the size of the supercell as well as the number of repetitions do not introduce valuable changes in the magnetization reversal process. Built-in function, edge smoothing to overcome staircase effects at the antidots edges was employed. The external magnetic field in all simulations of hysteresis loops was started from the 3 kOe and decreased up to the full reversal of the magnetization with steps of 5 Oe. For each step of decreasing external field, we used the Mumax [24] *relax*() function, to find the system's energy minimum. To protect finding the metastable state we also used short impulse of homogeneous excitation of small amplitude for every field value.

Figure 4(a) shows the in-plane magnetization curves for the field applied along the X-axis of the square ADL for $\phi_H = 1°$, and 44° obtained from simulations. Note, in order to prevent the effects of ideal symmetry in simulation from the high symmetry directions, we used slightly deviated ϕ_H values, i.e. at 1° and 44° instead 0° and 45°, respectively. The polar plot of the angular dependence of the coercive field obtained from simulations is shown in figure 3(a) with a black line. Simulations show good agreement with the experimental data, demonstrating a hard axis along the direction connecting the nearest neighbors' antidots, and easy axes along the directions connecting the next-neighbor antidots of the square lattice, however with overestimation of the H_c (see table 1). This overestimation can be attributed to the ideal circular shape of antidots and defect free structure used in simulations [34]. The remagnetization process in square ADL can be explained with the maps of the magnetization at different parts of the hysteresis loops shown in figure 5. After reducing the field progressively from saturation, the surface charges at the boundaries between antidots and magnetic layer lead to the formation of the domains through demagnetizing field. At $\phi_H = 1°$ the domains with magnetization reaching ±45° with respect to the X-axis (wedge shape domains) are located at areas between the nearest antidots, the large domains with magnetization along magnetic field are located in the central area of the unit cell (diamond shape domains) (see figure 5(b) at 0 field) [18]. When the field is increased in the opposite direction, the increase (of the wedge domains supplemented with gradual rotation towards the ±45°) or decrease (these along field direction) of the individual domain areas continues until the critical field of about −177.5 Oe at which magnetization switching is activated (see figure 5(b) at −180 Oe). All domains are switched by 180°. The diamond shaped domains reach already final orientation along the Y-direction, while the wedge shaped domains change orientation from ±45° to ∓135° (figure 5(b), 200 Oe).When the external field is applied along the direction connecting nearest antidots, these domains may coalesce more easily, resulting with decreased magnetization at remanence and coercive field with respect to the easy axis direction. The remagnetization process is shown in figure 5(c) for $\phi_H = 44°$. The results for square ADL are in

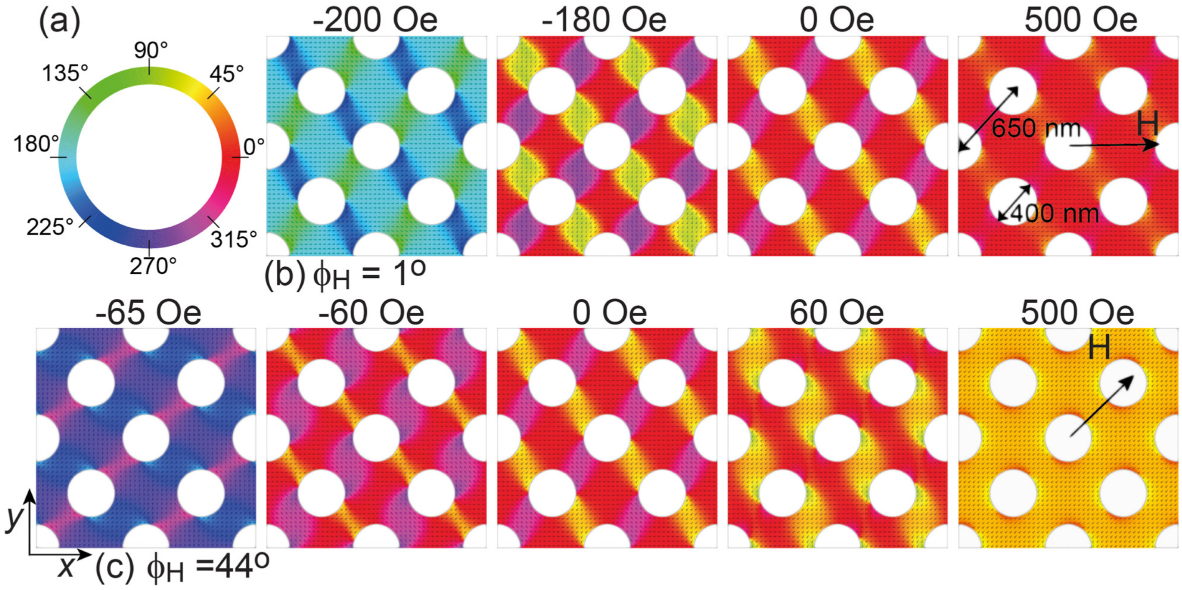

Figure 5. (a) Map of colors used to indicate the direction of the magnetization in the ADL plane. Magnetization distribution obtained from micromagnetic simulations for different magnetic field values at angles (b) $\phi_H = 1°$ and (c) $\phi_H = 44°$ for the square ADL. Switching of the magnetization happens between −180 and 200 Oe, and between −60 and −65 Oe in (a) and (b), respectively.

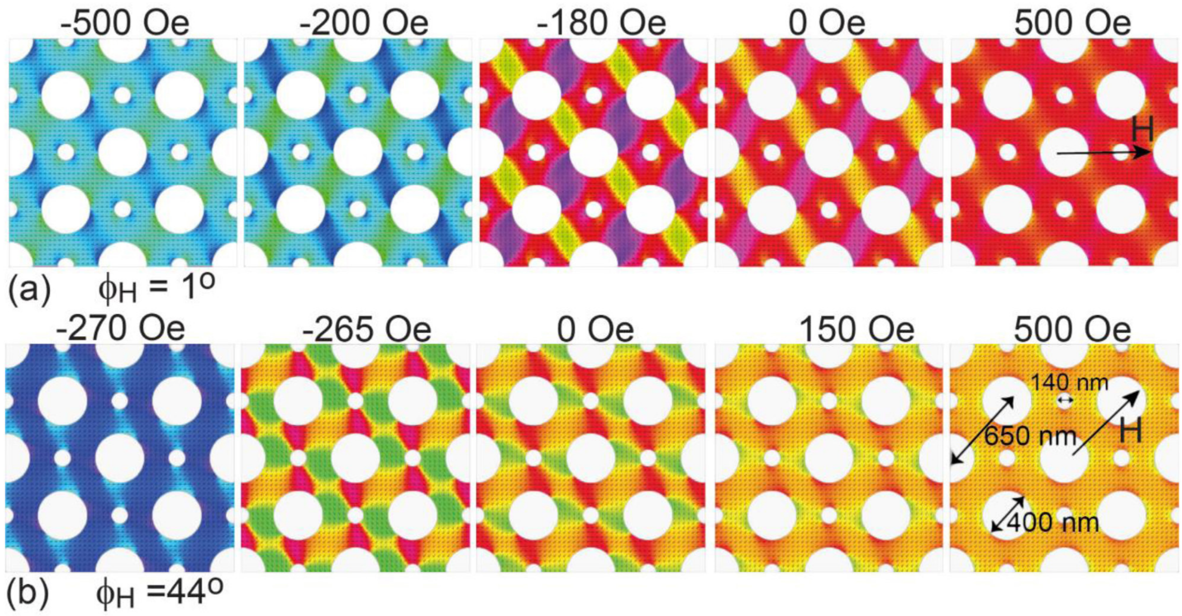

Figure 6. Magnetization distribution obtained from micromagnetic simulations inbi-component ADL for various external magnetic field values during magnetization reversal with the magnetic field at angles (a) $\phi_H = 1°$ and (b) $\phi_H = 44°$.

agreement with the literature [35], where such domains are resulted due to the smooth decrease of the component of magnetization parallel to the applied field.

Experimentally, the magnetization reversal mechanism in bi-component ADL is markedly modified as compared to the square ADL. In simulations we modified the square ADL by adding smaller antidots (70 nm of radius) in the center of the unit cell (figure 6) which increased the filling fraction of the square ADL (a ratio of the antidots area to the area of the unit cell) 0.036 to the value of 0.349. The small modification of the pattern introduces two new easy axes around ±45 ° directions with respect to the *X*-axis, which is in agreement with LMOKE measurements, figure 3(b). The hard axis direction in the bi-component ADL can be ascribed to $\phi_H = 22.5°$ and its odd integer multiples. Along these directions the coercive field has lowest magnitude of 70 Oe. The magnetization reversal along $\phi_H = 1°$ and 44° is explained through simulations results shown in figure 6.

The two step-hysteresis loop from LMOKE measurements (figure 2(b)) suggested the reversal process at two different

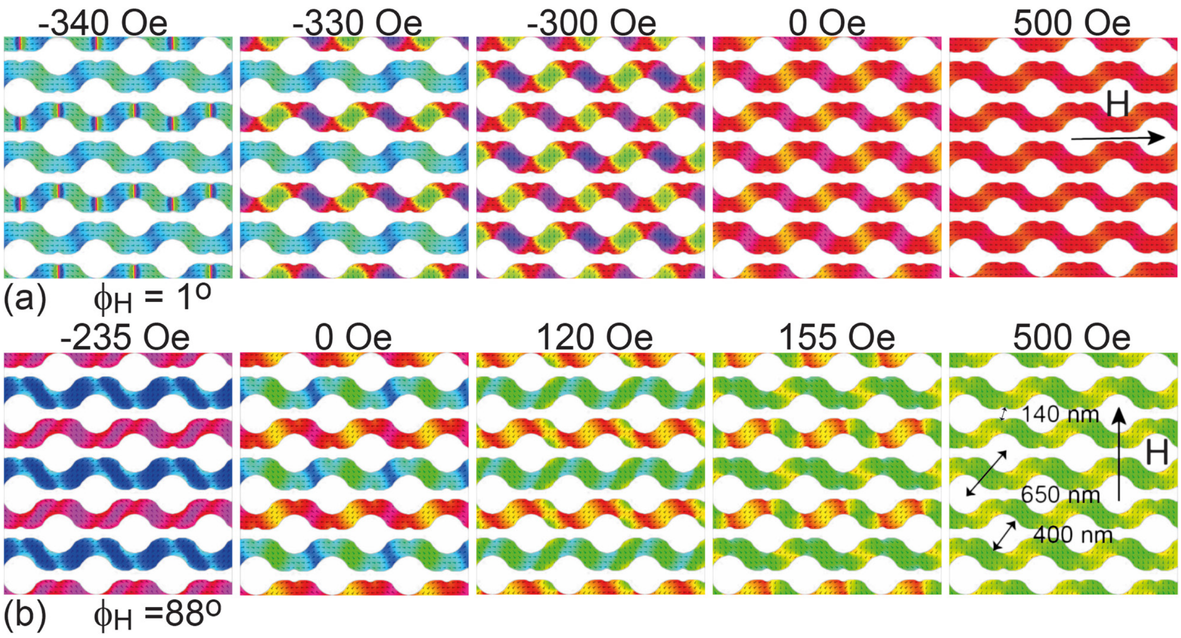

Figure 7. Magnetization distribution obtained from micromagnetic simulations in the wave-like ADL for various external magnetic field values during magnetization reversal with the magnetic field at angles (a) for $\phi_H = 1°$, (b) $\phi_H = 88°$.

switching fields. However, in micromagnetic simulations at $\phi_H = 1°$ (figure 4(b)) there is only a single switch in the hysteresis loop, which is similar to the loop for square ADL [16]. At positive saturation field all the spins in the bi-component ADL are aligned along the field direction (figure 6(a) at 500 Oe). As in the case of square ADL, similar domain formation has been observed due to the demagnetizing field created around the boundary between larger antidots and magnetic film with decreasing magnetic field (compare figures 5(b) and 6(a)). The wedge shaped domains with magnetization oriented at ±45° to the field direction are formed between the closest larger antidots. The results are comparable to the literature [22]. The nucleation of domains around small antidots is suppressed and rather rotation of the magnetization according to the demagnetization field is observed. As the field is increased in the reverse direction, the magnetization starts decreasing due to the rotation of the wedge domains until the critical switching field is reached (−182.5 Oe). The coercive field is only slightly higher than for the square ADL (see, table 1), thus the significantly smaller H_c in square ADL (figure 2(a)) as compared to bi-component ADL (figure 2(b)) can be attributed to the deformed shape of the antidots in the square ADL (see figure 1(a)).

The magnetization reversal at the angle $\phi_H = 44°$ demonstrates the qualitative difference in behavior as compared to the square ADL, although in both cases this direction is along the line connecting neighboring holes of the same size. In bi-component ADL this is an easy axis direction (figure 3(b)) while in square ADL it was a hard axis (figure 3(a)) with coercive fields 267.5 and 62.5 Oe, respectively. This difference, presented also in experimental results, is well reconstructed with micromagnetic simulations (figure 4(b)), however we did not find two step reversal of magnetization in bi-component ADL, which is present in LMOKE results (figure 2(b)). This can be attributed to the ideal circular shape of the holes in simulations and to the array without any defects. The maps of the magnetization configuration during the process of the remagnetization for $\phi_H = 44°$ is shown in figure 6(b). We see that in this process the smaller antidots play a crucial role because the remagnetization starts from the formation of domains connecting nearest larger and smaller antidots, i.e. along lines under ±45° to the direction of the magnetic field, which are wider near the larger antidots. In the domains aligned along the *Y*-axis, the magnetization is oriented along the *X*-axis and whereas in horizontal domains magnetization is oriented along the *Y*-axis, see figure 6(b) at −265 Oe, just before switching.

The simulated hysteresis loops for wave-like patterns are shown in figure 4(c) whereas the angular dependence of the coercive field is shown in figure 3(c). An agreement with the measured data of uniaxial anisotropy is found, with the hard axis along the *Y*-axis, and easy axis along the *X* direction. A broad angular range of ϕ_H (from −45° to 45°) with almost the same value of the coercive field around 310 Oe is found. The experimental results agree qualitatively with the simulated results. The overestimated values of the coercive field obtained in micromagnetic simulations (see, table 1) can be related to irregularities and defects in the fabricated sample, and the larger antidot size used in simulations. Indeed, in figure 1(c) we can see bridges connecting nearest Py wave-like channels which change locally demagnetizing fields and can influence the coercive fields and magnetization at remanence, decreasing and increasing it at $\phi_H = 90°$ and 0° respectively. Overall from the polar plot of the coercive field (figure 3(c)) the wave-like structure is found to be between ADLs and a lattice of stripes. Uniaxial anisotropy is characteristic for an array of stripes [36, 37] and for zigzag nanocolumns [38] while the reversal process still follows the trend observed in the square and bi-component ADL and can be described as below.

The magnetization reversal mechanism at $\phi_H = 1°$ follows the similar trend as observed for square ADL (figure 6(b)) and bi-component ADL (figure 7(a)) up to the switching field, as one can see in the remanent state images in figure 7(a). The magnetization is pinned along the X-axis around the smaller antidots. During the reversing of the applied field, the magnetization in the wave-like stripes at first switches the magnetization in every alternative stripe (figure 7(a) at −330 Oe). While in the rest of the stripes, the magnetization extension of domains and magnetization rotation follow the increase in amplitude of the magnetic field. After second switching we found a regular array of 360° domain walls along the vertical lines connecting larger and smaller antidots (figure 7(a) at −340 Oe) [39, 40]. These domain walls are formed near the leavings existing in the structure after smaller holes. Because in the vicinity of these smaller holes the magnetization is pinned along the field direction (see the red areas in figure 7(a) at −300 and −330 Oe, and the movie in the supplementary material for visualization of the domain wall formation (stacks.iop.org/JPhysD/50/025004/mmedia)). After applying sufficient reversal field all the domains are aligned parallel to the applied field direction.

The reversal along the hard axis (perpendicular to the wavelike stripes) is intriguing because the coercive field drops to small values (close to 0) around this direction. (Note that due to ideal symmetry in the simulated structure exactly at 90°, the reversal process is quantitatively different from the loops at nearest angles, showing valuable H_c. Thus we decide to discuss the close orientation here). In square and bi-component ADLs this direction was equivalent to 0°, however here in wave-like structure the easy and hard axis are along 0° and 90°. The magnetization configuration at various stages of the magnetization reversal process for the $\phi_H = 88°$ is shown in figure 7(b). The ramagnetization starts from rotating magnetization along the waveguide at parts of the waveguides oriented at 45° to the X-axis (see 155 Oe image). With decreasing magnetic field these domains extend in every second stripe up to switching at 115 Oe, while in the rest of the stripes the magnetization rotates in the opposite direction. Between 155 Oe and −235 Oe the magnetization is generally antiparallel in adjacent waveguides, which with decreasing magnetic field results in small coercive field and remanent magnetization, a similar effect to the formation of the vortices. Indeed the semi-vortex alignment of the magnetization can be found around the larger antidots in figure 7(b) at 0 Oe and –235 Oe. Although in experiment the coercive field does not drop to so small values as in simulations (the smallest H_c found in LMOKE is 39 Oe at $\phi_H = 250°$, see figure 3(c)), we believe that this is due to defects (i.e. bridges connecting adjacent waveguides as discussed above) and irregularities in the shape of the antidots seen in figure 1(c). After an increase of the magnetic field in the opposite direction, the magnetization switches in the remaining stripes.

5. Conclusions

The effects of shape and geometry of the ADLs on magnetic properties of the thin film, such as coercivity, anisotropy and magnetization reversal has been systematically investigated experimentally and numerically. Different magnetic anisotropies, four fold symmetry (square ADL), eight fold symmetry (bi-component ADL), and in ADL with a wave-like pattern the magnetic anisotropy drastically changes into two fold symmetry, which is substantially different from square and bi-component ADLs. We showed that a smaller antidot covering only about 3% of the square ADL's unit cell is already sufficient to introduce additional easy axes (with high coercive field) found in bi-component ADL. In the wave-like pattern, which can be regarded as originating in bi-component ADL, the coercive field is found to remain almost on the same values around the direction parallel to the channels. Moreover, results of the micromagnetic simulations suggest that this effect can be induced by very narrow channels connecting larger and smaller antidots. In simulated results we have observed the formation of periodic domain structures in all ADLs, however in the case of the wave-like pattern it is most regular and moreover two different periodic patterns are stabilized at different applied magnetic field values. Numerically we have also found the formation of regular 360° domain walls during the magnetization reversal process, which in wave-like ADL are created along lines connecting adjacent larger and smaller antidots for magnetic fields oriented along the channels. These domains remain stable with the rotation of the magnetic field from the high symmetry direction, which justify the simulation results, apart from the lack of experimental validation of this finding due to the limitation of the available aperture. We believe that the presented results can stimulate further research to design and tailor patterned magnetic films with desired in-plane anisotropies unavailable for homogeneous films. Moreover, the soft magnetic films with regular pattern and tailored anisotropy—reprogrammable MCs can be used to exploit the magnetization dynamics for microwave applications.

Acknowledgment

This research is supported by the SYMPHONY project operated within the Foundation for Polish Science within the Team Programme co-financed by the EU European Regional Development Fund, Grant No. OPIE 2007-2013, and partially received funding from Polish National Science Centre Project No. UMO-2012/07/E/ST3/00538. The simulations were partially performed at Poznan Supercomputing and Networking Center (grant No 209).

References

[1] Novosad V, Grimsditch M, Darrouzet J, Pearson J, Bader S D, Guslienko K, Otani Y, Shima H and Fukamichi K 2003 *Appl. Phys. Lett.* **82** 3716

[2] Novosad V, Guslienko K Yu, Shima H, Otani Y, Kim S G, Fukamichi K, Kikuchi N, Kitakami O and Shimada Y 2002 *Phys. Rev.* B **65** 060402

[3] Van de Wiele B, Fin S, Pancaldi M, Vavassori P, Sarella A and Bisero D 2016 *J. Appl. Phys.* **119** 203901

[4] Jorzick J, Demokritov S O, Hillebrands B, Bailleul M, Fermon C, Guslienko K Y, Slavin A N, Berkov D V and Gorn N L 2002 *Phys. Rev. Lett.* **88** 047204

[5] Zivieri R, Santoro G and Franchini A 2007 *J. Phys.: Condens. Matter* **19** 305012

[6] Agramunt-Puig S, Del-Valle N, Pellicer E, Zhang J, Nogués J, Navau C, Sanchez A and Sort J 2016 *New J. Phys.* **18** 013026

[7] Zivieri R, Malagò P, Giovannini L, Tacchi S, Gubbiotti G and Adeyeye A O 2013 *J. Phys.: Condens. Matter* **25** 336002

[8] Ctistis G, Papaioannou E, Patoka P, Gutek J, Fumagalli P and Giersig M 2009 *Nano. Lett.* **9** 1

[9] Sushruth M, Ding J, Duczynski J, Woodward R C, Begley R A, Fangohr H, Fuller R O, Adeyeye A O, Kostylev M and Metaxas P J 2016 *Phys. Rev. Appl.* **6** 044005

[10] Shwarze T and Grundler D 2013 *Appl. Phys. Lett.* **102** 222412

[11] Madami M, Gubbiotti G, Tacchi S, Carlotti G and Jain S 2014 *Physica* B **435** 152

[12] Chumak A V, Vasyuchka V I, Serga A A and Hillebrands B 2015 *Nat. Phys.* **11** 453

[13] Torresa L, Diaz L L, Alejos O and Inigues J 1999 *J. Appl. Phys.* **85** 6208

[14] Haering F *et al* 2013 *Nanotechnology* **24** 465709

[15] Krawczyk M and Grundler D 2014 *J. Phys.: Condens. Matter* **26** 123202

[16] Zivieri R and Giovannini L 2013 *Phot. Nanostruct. Fundam. Appl.* **11** 191

[17] Mruczkiewicz M, Krawczyk M, Mikhaylovskiy R V and Kruglyak V V 2012 *Phys. Rev.* B **86** 024425

[18] Wang C C, Adeyeye A O and Singh N 2006 *Nanotechnology* **17** 1629

[19] Deshpande N G, Seo M S, Jin X R, Lee S J, Lee Y P, Rhee J Y and Kim K W 2010 *Appl. Phys. Lett.* **96** 122503

[20] Hilzinger H R and Kronmüller H 1976 *J. Magn. Magn. Mater.* **2** 11

[21] Tse D H Y, Steinmuller S J, Trypiniotis T, Anderson D, Jones G A C, Bland J A C and Barnes C H W 2009 *Phys. Rev.* B **79** 054426

[22] Tripathy D, Vavassori P, Porro J M, Adeyeye A O and Singh N 2010 *Appl. Phys. Lett.* **97** 042512

[23] Tripathy D, Vavassori P and Adeyeye A O 2011 *J. Appl. Phys.* **109** 07B902

[24] Vansteenkiste A and B. V. DWiele B V D 2011 *J. Magn. Magn. Mater.* **323** 2585

[25] Mengotti E *et al* 2008 *J. Appl. Phys.* **103** 07D509

[26] Sing N, Goolaup S and Adeyeye A O 2004 *Nanotechnology* **15** 1539

[27] Adeyeye A O, Goolaup S, Singh N, Jun W, Wang C C, Jain S and Tripathy D 2008 *IEEE. Trans. Magn.* **44** 1935

[28] Vavassori P, Gubbiotti G, Zangari G, Yu C T, Yin H, Jiang H and Mankey G J 2002 *J. Appl. Phys.* **10** 7992

[29] Cowburn R P, Adeyeye A O and Welland M E 1998 *Phys. Rev. Lett.* **81** 5414

[30] Mahato B K, Choudhury S, Mandal R, Barman S, Otani Y and Barman A 2015 *J. Appl. Phys.* **117** 213909

[31] Merazzo K J, Leitao D C, Jimenez E, Araujo J P, Camarero J, del Real R P, Asenjo A and Vazquez M 2011 *J. Phys. D: Appl. Phys.* **44** 505001

[32] Krivoruchko V N and Marchenko A I 2011 *J. Appl. Phys.* **109** 083912

[33] Van de Wiele B, Manzin A, Vansteenkiste A, Bottauscio O, Dupre L and De Zutter D 2012 *J. Appl. Phys.* **111** 053915

[34] Michea S, Palma J L, Lavın R, Briones J, Escrig J, Denardin J C and Rodrıguez-Suarez R L 2014 *J. Phys. D: Appl. Phys.* **47** 335001

[35] Yu C T, Jiang H, Shen L, Flanders P J and Mankey G J 2000 *J. Appl. Phys.* **87** 6322

[36] Han G C, Zong B Y, Luo P and Wu Y H 2003 *J. Appl. Phys.* **93** 9202

[37] Goolaup S, Singh N, Adeyeye A O, Ng V and Jalil M B A 2005 *Eur. Phys. J.* B **44** 259

[38] Buchta K, Lewandowski M, Bischoff L, Synoradzki K, Błaszyk M, Toliński T and Luciński T 2014 *Thin Solid Films* **568** 13

[39] Muratov C B and Osipov V V 2008 *J. Appl. Phys.* **104** 053908

[40] Gonzalez Oyarce A L, Llandro J and Barnes C H W 2013 *Appl. Phys. Lett.* **103** 222404

4.3 Geometrical complexity of the antidots unit cell effect on the spin wave excitations spectra

4.3.1 Introduction

This paper presents analysis and interpretation of experimental data and numerical calculations concerning spin wave dynamics in three types of ADLs based on permalloy thin films with increased complexity of the unit cell: simple square ADL, bi-component ADL and wave-like ADL (formed by introducing the air gaps between smaller and larger antidots) investigated already in the previous paper (Ch. 4.2). Here, we are interested in studies of ferromagnetic resonances spectra (FMR) and dispersion relations obtained by Brillouin light scattering (BLS) giving detailed information about dynamical properties of the magnonic system. The results of the measurements were interpreted with the aid of micromagnetic simulations and plane wave method calculations.

In this publication, the Author has performed all of the numerical simulations based on the Mumax3 software, except the dispersion relation calculations (figure 9). He analysed the obtained numerical results and participate in analyse of experimental results. He has prepared all the figures (except for Figure 9, which he has done together with prof. Jarosław Kłos). He has significantly contributed to the manuscript writing and manuscript evaluation.

Number of Ministerial points: 70.
Impact Factor: 2.829

J. Phys. D: Appl. Phys. **50** (2017) 185003 (13pp) https://doi.org/10.1088/1361-6463/aa64ab

Geometrical complexity of the antidots unit cell effect on the spin wave excitations spectra

M Zelent[1,7], N Tahir[2,3], R Gieniusz[2], J W Kłos[1], T Wojciechowski[4,5], U Guzowska[2], A Maziewski[2], J Ding[6], A O Adeyeye[6] and M Krawczyk[1,7]

[1] Faculty of Physics, Adam Mickiewicz University in Poznan, Umultowska 85, 61-614 Poznań, Poland
[2] Faculty of Physics, University of Bialystok, ul. Konstantego Ciołkowskiego 1L, Białystok 15-245, Poland
[3] Division of Science and Technology, University of education, Lahore, Pakistan
[4] Institute of Physics, Polish Academy of Sciences, al. Lotnikow 32/46, PL-02-668 Warsaw, Poland
[5] International Research Centre MagTop al. Lotnikow 32/46 PL 02-668 Warszawa, Poland
[6] Department of Electrical and Computer Engineering, National University of Singapore, Singapore

E-mail: mateusz.zelent@amu.edu.pl and krawczyk@amu.edu.pl

Received 15 October 2016, revised 27 February 2017
Accepted for publication 6 March 2017
Published 10 April 2017

Abstract

Three types of antidot lattices (ADLs) based on a permalloy thin film, with increasing complexity of the unit cell: simple square, bi-component square, and wave-like ADLs were studied experimentally using both ferromagnetic resonance and Brillouin light scattering spectroscopy techniques. An additional small antidot placed in the center of the square unit cell induces significant modification of the ADL spin-wave spectrum and changes its dependence on the orientation of the in-plane applied magnetic field. The introduction of air-gaps connecting small and large antidots transforms the system into the wave-like ADL and results in further changes in the spin-wave spectrum, including a strong discrimination between two mutually orthogonal principal directions of the ADL in terms of spin-wave propagation. We also point out the impact of defected holes on the obtained spectra. The micromagnetic simulations and the calculation based on the plane wave method satisfactorily confirmed the experimental results.

Keywords: spin waves, magnetism, micromagnetic modeling, Brillouin scattering, ferromagnetic resonance, magnonic crystals

(Some figures may appear in colour only in the online journal)

1. Introduction

Recent studies have shown that spin waves (SWs) in nanopatterned magnetic media can be of use in various applications, including signal transmission, signal processing, communication and sensing [1–5]. The short wavelengths of SWs, as compared to the electromagnetic waves of the same frequencies, provide an opportunity for significant miniaturization of microwave devices. In electronic and signal processing devices, elements based on SWs could operate on much higher frequencies and consume even two orders of magnitude less energy. Moreover, an SW spectrum can be tuned with the magnitude and orientation of the magnetic field; different magnetization configurations realizable in the same structure correspond to different SW spectra. The inherent nonreciprocity of magnetic materials and of SW propagation in magnetic materials gives an additional advantage to SW devices in these applications [6]. These prospects stimulate the research in magnonics [7–9].

An important class of magnonic structures, patterned thin films include magnonic crystals (MCs), a subclass of special interest, with periodic artificial patterning [10, 11]. The SW

---

[7] Authors to whom any correspondence should be addressed.

spectrum of an MC has frequency bands separated by band gaps; these are frequency ranges allowed and disallowed to propagating SWs, respectively. As in other types of artificial crystals, the bands and gaps in the SW spectrum of an MC can be modeled by changing the size, shape and symmetry of the pattern [12, 13]. However, it can be also controlled by changing the magnitude or orientation of the magnetic field [13, 14]. The SW dispersion can be changed by switching between stable magnetic configurations, a property known as reprogrammability [15, 16]. Finally, an overlayer or substrate can be added to the MC to significantly modify its magnonic spectrum by inducing: surface anisotropy [17], the Dzyaloshinskii–Moriya interaction [18] or nonreciprocity [19–22]. Because of these unique features, MCs, besides being an intriguing subject of fundamental research, are of much interest from the point of view of the above-mentioned applications.

There is particular interest in MCs in the form of a 2D antidot lattice (ADL) [23], with a periodic array of holes (antidots) drilled in a ferromagnetic film. The interest in such structures is due to the relative simplicity of their fabrication, especially in the case of ADLs based on metallic ferromagnetic films, which offer downscaling of the MC to the nanometer size range required for applications [24–27]. The magnonic spectrum of an ADL strongly depends on the shape of the antidots and the lattice type [28–30], but is also influenced by the magnetic properties at the antidot edges [31]. An SW spectrum can be further modified by filling the antidots with a ferromagnetic material in direct contact with or separated from the host material [32–35]. This great variety of ADLs has led to the observation of an abundance of their SW spectra. The most intensive modes observed in ferromagnetic resonance (MR) and Brillouin light scattering (BLS) studies are the fundamental mode (FM), which shows in-phase oscillations of the magnetization in a major part of the ADL, and edge modes (EMs) with an amplitude concentrated near the edges of the antidots. [23] Despite numerous studies, the relationship between the geometry of the unit cell and the SW dynamics in MCs, especially ADLs, remains to be elucidated.

In the present work, we investigated the square array of cylindrical holes (square ADL—figure 1(a)) in thin Py film as a base structure. Then we complicated the structure by placing an additional smaller hole at the center of the unit cell (bi-component ADL—figure 1(b)). The results from these two reference structures are used to interpret the spectrum obtained for the wave-like ADL. The wave-like ADL structure is derived from the bi-component ADL by drilling the narrow channels between nearest larger and smaller holes along the one principal direction of the ADL–horizontal axis in figure 1(c). The square ADLs were broadly investigated in the past, also with the various shapes of the antidots [36]. However, there are few research papers reporting investigations of the SW dynamics in thin film bi-component ADLs [37–39], moreover, for wave-like structures the detailed scientific reports are still missing. From our previous studies [40], we knew that these modifications of the square unit cell introduce significant changes in the magnetization reversal anisotropy map, making them interesting for exploring the SW dynamics. We use FMR and BLS techniques to study the standing and the propagating SWs in this set of ADLs. We found that the sensitivity of the FMR spectra on orientation of the magnetic field is strongly dependent on the minor changes of the antidot pattern in the unit cell, even if the unit cell preserves the same symmetry. The strongest angular dependence of the FMR spectra has been found for the wave-like pattern. For this structure, the changes of the demagnetizing field modifies the SWs spectrum. Here, the rotation of magnetic field transforms FM into the EMs which leads to losses of their intensity in BLS spectra. We found that the dispersion relations of SWs are significantly affected by the modification of the antidot pattern in the unit cell, even if this modification covers less than a few percent of the unit cell area. Our experimental results are successfully interpreted on the basis of calculations performed with the plane wave method (PWM) [41] and micromagnetic simulations (MS). Moreover, the comparison of experimental and numerical results allows us also to identify the influence of distortions of the antidots' shape on the FMR spectra, which can result in decreasing angular dependence of the FM. Thus, a general view that governs the SW characteristics in square lattice ADLs with a complex unit cell has been presented. The presented results can be useful for the design of magnonic devices operating in the microwave frequency range.

The paper is organized as follows. In section 2, we present the fabrication process of the ADLs and experimental methods used in our investigations of the SW dynamics. In section 3, we present the results of the FMR measurements, which have been interpreted with the results from the MSs. The propagative properties of SWs are discussed in section 4, where the results of BLS measurements are explained by PWM calculations. In the last section, we summarize our results.

2. Fabrication and experimental methods

Large area ($4 \times 4\,\mathrm{mm}^2$) of $\mathrm{Ni}_{80}\mathrm{Fe}_{20}$ (Py) antidot nanostructures were patterned on commercially available silicon (Si) substrates by employing deep ultraviolet lithography at 248 nm exposing wavelength. To deposit the Py layer, we used electron beam deposition from $\mathrm{Ni}_{80}\mathrm{Fe}_{20}$ alloy materials. In order to create patterns in the resist, the substrate was spin coated with 60 nm thick, bottom anti-reflecting coating (BARC), followed by a 480 nm positive deep UV-photoresist, which is four to five times thicker than those typically used for e-beam lithography. Thickness was monitored using standard quartz crystal control during deposition. Further details about the fabrication procedure can be found elsewhere [42]. After fabrication, the thickness was confirmed using atomic force microscopy. Thicker resist helps to achieve a high aspect ratio and additionally makes the lift-off process easier. A Nikon lithographic scanner with KrF excimer laser radiation was used to expose the resist. In order to transfer resist patterns into antidots, 10 nm thick Py was deposited at room temperature by e-beam evaporation technique at a rate of 0.2 Å s^{-1}, while the pressure in the chamber was maintained at 2×10^{-6} Torr.

As shown in figure 1, the samples with various geometries, starting from basic square ADL (a), to the most complex system (wave-like pattern, (c)) by the systematic inclusion of additional antidots (bi-component ADL with alternating diameters of circular antidots (b)) were fabricated by the procedure discussed above. In order to keep the edges of the structures sharp, the last

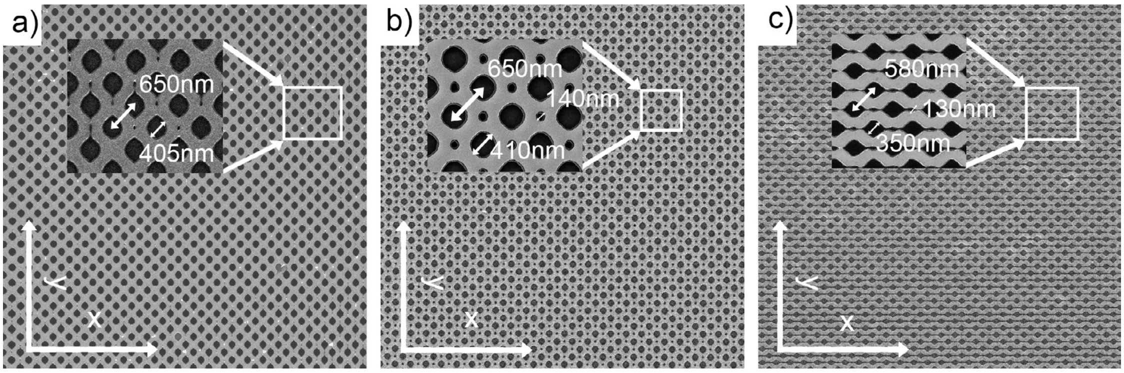

Figure 1. SEM images of the three samples based on Py film investigated in the paper: (a) square ADL, (b) bi-component ADL—composed of two kinds of antidots and (c) wave-like ALD, where lager and smaller antidots are connected by the air tranches. The thickness of Py layer is 10 nm.

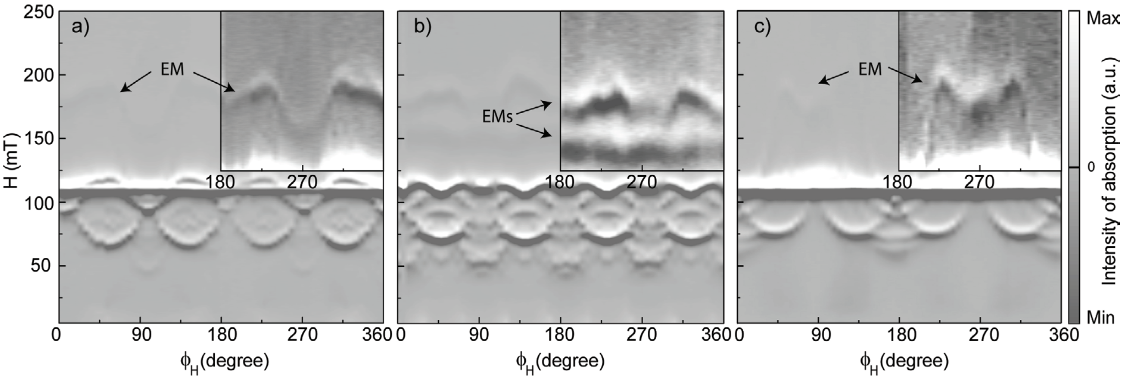

Figure 2. FMR spectra in dependence on the in-plane angle of the magnetic field with respect to the *x*-axis for the ADL samples presented in figure 1: (a) square ADL, (b) bi-component ADL and (c) wave-like ADL. The FMR signal is shown with a greyscale. The value zero on the intensity scale marks the FMR resonance field. The labels EM point weakly visible EMs. To enhance their visibility at the top-right corners (inset) the grey scale has been shown with increased contrast.

step of the sample fabrication process (lift-off of the BARC) was not carried out, so the BARC is present inside the antidots lattice, which is confirmed by scanning electron microscope (SEM). The antidots are close to the circular shape in (b), however the larger deformations are visible for square and wave-like ADLs (see insets in figures 1(a) and (c)). In square ADL, the diameter of antidots D is 405 nm and period 650 nm (nearest distance between centers of larger antidots). In bi-component ADL the diameter of larger and smaller antidots is 410 and 140 nm, respectively. For bi-componet ADL, we assumed the same period (650 nm), as for square ADL. In the wave-like structure the sizes of larger and smaller antidots are 350 and 130 nm, respectively, and the period is 580 nm. We introduce a coordinating system with the x-axis along the horizontal direction in figure 1, connecting next-nearest larger antidots.

The dynamics of the magnetization (standing SWs) was studied through conventional X-band FMR at constant frequency 9.4 GHz in dependence on the static magnetic field H orientation in the film plane. The orientation of the H field is described by the angle ϕ_H, where $\phi_H = 0$ is a direction along the x-axis. The SW dispersion relations were measured with BLS spectrometry. In these measurements, we limit our studies to the Damon–Eshbach geometry (propagation of SWs perpendicular to the direction of the external magnetic field). In this configuration, the larger group velocity of SWs is expected. All BLS measurements were performed at room temperature in backscattering geometry using a Sandercock (3 + 3)-pass tandem Fabry–Perot interferometer to analyze the frequency shift of light from a single-mode solid state laser with $\lambda = 532$ nm [43, 44]. The measurements were performed for different angles of incidence of the probing light beam, i.e. the angle between the direction of the incident laser beam and the film normal θ. The amplitude of the SW in-plane wave vector q is related to the angle of incidence by the relation $q = (4\pi/\lambda)\sin\theta$. By changing θ in the range of 10°–80°, it is possible to change q in the range of $0.41–2.3 \times 10^5$ cm^{-1}.

3. The angular dependence of the FMR spectra

3.1. Measurements

The FMR spectra in dependence on the static magnetic field orientation are shown in figure 2. The results for the patterned samples can be compared with the data obtained from the uniform Py film of 10 nm thickness, being a reference sample. In the FMR spectra of the reference sample, a single resonance line of constant position (i.e. independent of the angle ϕ_H) was observed at 102 mT. This line corresponds to the resonance of a uniform mode. The lack of any angular dependence for this resonance confirms that the reference sample has negligible in-plane anisotropy [40, 42].

In every FMR spectrum, we observed the line with very high intensity, whose resonant magnetic field is close to the FMR field of the reference sample. We correlate this line with an excitation of the FM. Apart from the FM line, there are lines with the lower resonance fields, which we attribute to the bulk modes (BMs), with oscillating amplitude of the SW in the bulk regions of ADL. The lines with the resonance field higher than the FM field are the EMs. Deeper insights into the above discussed modes will be presented later with the aid results obtained with MS. Now, we will discuss the angular variation of FMR lines.

Figure 2(a) shows a 2D gray scale map of the FMR spectra collected at different magnetic field orientations in the square ADL. The presence of a four-fold symmetry in the spectra can be recognized [29, 45, 46]. However, there are also some noticeable details (at low magnetic fields) which discriminate 0° and 90° field directions, nominally equivalent orientations. We attribute these features of the FMR spectrum to the deviation of the antidots from a circular shape seen in the SEM image in figure 1(a). For various in-plane angles, we can separate two clear resonances of the BMs, one around 93 mT at smaller angles ($\phi_H < 20°$) and for larger angles another BM becomes intensive with resonant field decreasing to 69 mT at $\phi_H = 45°$. For both of them, the variation of magnetic field position with change of the magnetic field orientation is observed.

We also notice, that the most intensive resonance line related to the FM mode (around 110 mT) almost does not depend on the magnetic field orientation, which is an unexpected result for ADLs [29, 47]. A similar effect was already observed for the ferromagnetic dots, where asymmetric deformation led to a decrease of the resonance frequency variation in dependence on the in-plane magnetic field orientation [48]. In ADL, we also attribute this insensitivity to the specific deformation of antidots from the ideal circular shape (see figure 1(a)). As shown in appendix A, the elliptical deformation can lead to significant decrease of the FM resonance frequency variation in dependence on the orientation of H. We find, that a change of the antidots' shape modifies the demagnetizing field in areas of the FM localization. The changes of the demagnetizing field, combined with the confinement of the FM, compensate the influence of the lattice. Nevertheless, more detailed studies are required to elucidate the effect, which are beyond scope of this paper. Similar defects can be seen also in figure 1(c) for wave-like ADL and similar values of the FM resonance field which is independent of magnetic field orientation. We note, the variation of the BMs and EMs resonance fields with ϕ_H are still observable in figures 1(a) and (c).

Only a single EM is found in the square ADL (figure 2(a)). With a change of the in-plane angle ϕ_H from 0 to 45° its resonance field increases. A further increase of the angle to 90° decreases its resonance field. When we compare the spectra taken at 90° and 0°, we note differences—the EM for 90° (at 162 mT) is observed at a significantly lower resonance field than for 0° (at 182 mT) and it has a much smaller intensity. This again points at a non-circular shape of the antidots with different curvature of their edges along orthogonal directions (see figure 1(a)) [48].

Figure 2(b) presents the FMR results for the bi-component ADL. The slight oscillation of the FM resonant field with an angle ϕ_H is clear while the FMR spectrum at $\phi_H = 90°$ is almost the same as at $\phi_H = 0°$. The FMR spectrum fully preserves the four-fold symmetry of the considered square ADL. Numbers of BMs excited at intermediated angles are also found, with the most pronounced line around $\phi_H = 45°$ at field 73 mT. For this angle, the applied field is parallel to the side of the square lattice of antidots and this intensive excitation is close to the BM measured in the square ADL (figure 2(a)), although the signal is more intensive in the bi-component ADL (comparable to the intensity of the FM). This points at the excitation having its origin at the larger antidots. Additional BM resonances of low intensities, not found in the square ADL, could be attributed to the presence of smaller antidots. For $\phi_H = 0°$ the three lines are clearly observed at fields 42, 51, and 78 mT, while in the case of square ADL the only one resonance line apart from FM was observed. At the angle $\phi_H = 18°$ the most reach spectra for bi-component ADL are detected with several resonance peaks below the FM line (72, 75, 83 and 96 mT). Overall, the spectra of square and bi-component ADL are qualitatively different for other angles.

There are two EMs in the bi-component ADL (figure 2(b)). The resonance at higher field (varied from 181 to 186 mT for ϕ_H changed from 0° to 44°, respectively), we attribute to the EM at the larger antidots, because at similar fields EM was observed for the square ADL (figure 2(a), with resonance line varied from 182 to 191 mT for respective field orientations). The resonance line at the lower field (around 158 mT), which is weakly dependent on the field orientation, can be connected with EM localized at smaller antidots. There is a good match between spectra at $\phi_H = 0$ and 90°, which suggests that the shape of the antidots is close to circular (figure 1(b)).

Figure 2(c) presents the results of the FMR measurements for the wave-like ADL. We found the two-fold symmetry axis according with the symmetry of the structure. For small ϕ_H resonance lines of small intensity are observed only below the FM field. At $\phi_H = 0°$ multiple BM resonances are found with the most intensive at 60, 70 and 90 mT. Around $\phi_H = 45°$ one additional resonance peak with significant intensity appears at 74 mT. This peak is very similar to that previously observed for square and bi-component ADLs (figures 2(a) and (b)). At $\phi_H = 90°$ the BMs are not detected. The most intensive resonance field, FM does not change with the rotation of the external magnetic field, like in the square ADL. This is also unexpected result. We attribute this effect to the shape of the antidots, being quite similar to antidots in the square ADL.

For wave-like ADL, we did not observe the EM at $\phi_H = 0°$ (figure 2(c)). The EM detaches from the FM only at $\phi_H \cong 18°$ and increases the resonance field with increasing ϕ_H. The maximal resonance field is reached at $\phi_H = 45°$ (197 mT), with further increase of ϕ_H the resonance field of this mode slightly decreases. The most intensive signal

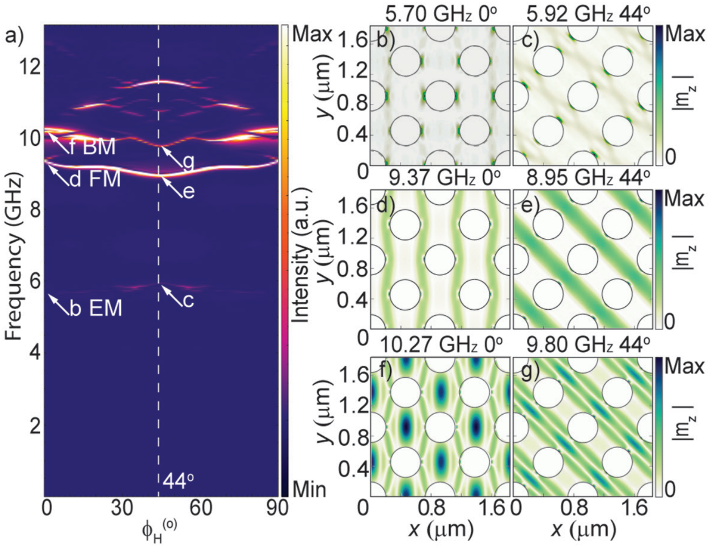

Figure 3. (a) FMR frequency spectra of the square ADL obtained from MSs in dependence on the in-plane angle of the external magnetic field with respect to the x-axis ($\mu_0 H = 0.1$ T). (b)–(g) Amplitude of the SWs marked with arrows (b), (d) and (f) for $\phi_H = 0°$ and (c), (e) and (g) for $\phi_H = 44°$ in (a).

from the EM is detected at H oriented along the y-axis ($\phi_H = 90°$).

3.2. Micromagnetic simulations (MS)

The experimental results of the FMR measurements are further analyzed through the MS with the MuMax3 environment [49]. The Landau–Lifshitz equation, including exchange and dipolar fields and small damping, is solved with the finite difference method in time and real space domain. MSs were performed for the following structural parameters, while keeping fixed for investigated structures: the thickness—10 nm, the diameter of the larger antidots—400 nm and the lattice constant 650 nm. The diameter of smaller antidots in bi-component and wave-like ADLs was assumed to be 140 nm. For wave-like ADL, the width of the smallest air-gaps between wave-like channels is around 90 nm. The assumed lattice constant and the size of larger antidots are only slightly different as compared to the square and bi-component samples (see figure 1). However, the diameter of larger antidots assumed in MS is larger than the diameter of the antidot from the experimental wave-like sample. We decided to keep the same size of the unit cell and the geometrical features common for all ADLs to clearly elucidate the role of complexities of the unit cell. The magnetic parameters used for MSs are standard values of the Py: saturation magnetization $M_s = 800$ kAm^{-1}, exchange constant $A = 13 \times 10^{-12}$ Jm^{-1}. A magnetocrystalline anisotropy is neglected in our calculations and a small damping constant was assumed $\alpha = 0.001$. For all the structures the mesh of size $2 \times 2 \times 10$ nm was used along the x, y and z-axis, respectively. Periodic boundary conditions along the x- and y-direction (with 16 repetitions of square cells in the supercell) are used to reduce the influence of the external ends of the structure. We employed the built-in function for edge smoothing to overcome staircase effects at the antidots edges. For excitation of the SW precession, we used a microwave external magnetic field in the form of the *sinc* function in the time domain and spatially homogeneous in the whole sample with maximal amplitude of 5.413×10^{-2} T and cutoff frequency $f = 45$ GHz. After collecting data through 30 ns, we performed a fast Fourier transform of the signal to get the frequency spectra of SW excitations, which are related to the resonance magnetic field spectra collected in FMR measurements: a part of the experimental spectrum at low values of the magnetic resonance field corresponds to the high frequency part of the simulated spectrum. The relation between ferromagnetic resonance frequencies and ferromagnetic resonance fields is discussed in appendix B.

Figures 3–5 show in panels (a) the calculated maps of the FMR frequency spectra in dependence on ϕ_H (the magnetic field magnitude was fixed to $\mu_0 H = 0.1$ T in these simulations) for square ADL, bi-component ADL and wave-like ADL, respectively. For all structures the satellite peaks are observed on both sides of the most intensive line which corresponds to FM, similar to the experimental data. To identify SW excitations, we show (in parts (b)–(g) of figures 3–5) the spatial distributions of SWs amplitude related to the most intensive lines in the calculated spectra. These spatial profiles of SWs were plotted in two orientations of the magnetic fields, ϕ_H equals to 0 and 44° in square and bi-component ADL. For wave-like ADL we analyzed the profiles of SWs for a few other angles ϕ_H. Overall, the calculated spectra in angular dependence are qualitatively in good agreement with the experimental results presented in figure 2 when we refer the FMR fields to FMR frequencies (see appendix B for clarification).

In the square ADL, a single low frequency mode is recognized as an EM with in-phase oscillations on both sides of the antidots (see figures 3(b) and (c)). Its frequency slightly varies from 5.7 to 5.92 GHz in the range of ϕ_H from 0 to 44°. This frequency variation of the EM is solely due

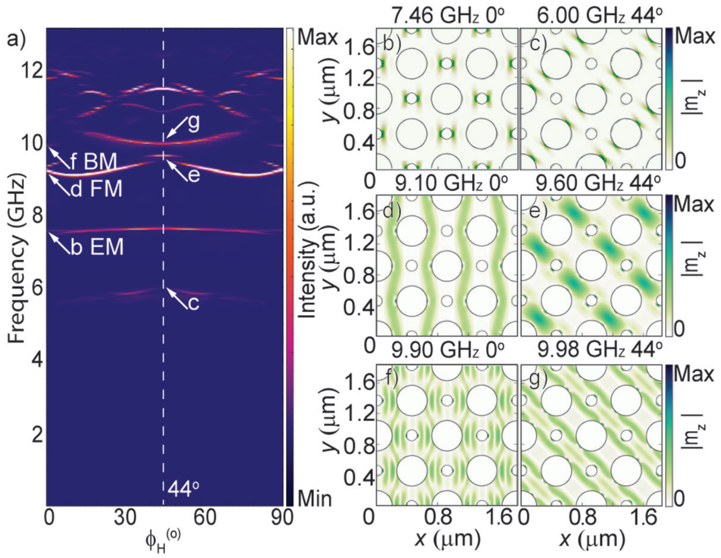

Figure 4. (a) Calculated FMR frequency spectra of the bi-component ADL in dependence on the in-plane angle of the magnetic field ($\mu_0 H = 0.1$ T). Visualization of the SW modes amplitude distribution with the most intensive resonances is shown in (b), (d) and (f) for $\phi_H = 0$ and (c), (e) and (g) $\phi_H = 44°$ for modes marked with arrows in (a).

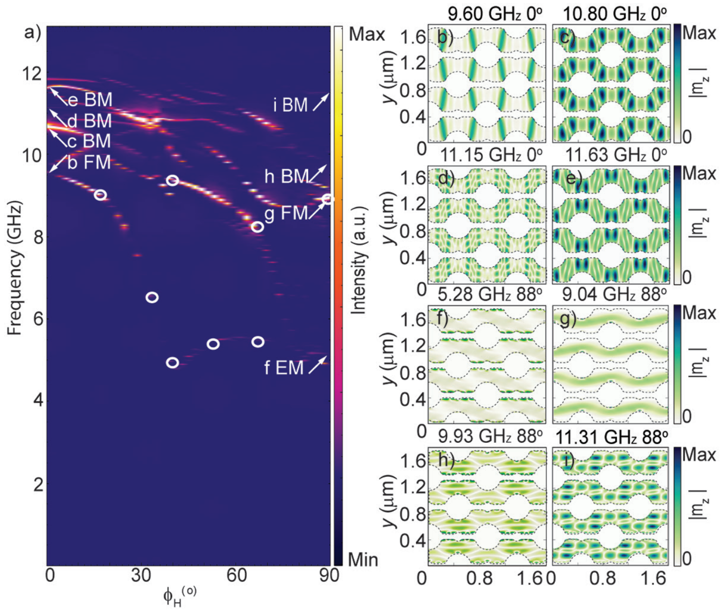

Figure 5. (a) Calculated FMR frequency spectra in dependence on the angle of the in-plane magnetic field ($\mu_0 H = 0.1$ T) for wave-like ADL. Visualization of the SW modes related to the most intensive resonances in FMR spectra for $\phi_H = 0°$ (b)–(e) and $\phi_H = 88°$ (f)–(i). White circles in (a) mark frequencies of the FM and EMs for which the profiles for oblique orientation of the external magnetic field are presented in figure 6.

to the demagnetizing field which depends on ϕ_H. Angular dependence of the demagnetizing field results from the anisotropy induced by the lattice. In figures 3(d) and (e) we show the spatial profile of the FM. The change of frequencies of the FM in dependence on ϕ_H corresponds to the most intensive line which decreases from 9.37 GHz at $\phi_H = 0$ to 8.95 GHz at $\phi_H = 45°$. This confirms the independence of the resonance magnetic field on ϕ_H, found in experimental results (figure 2(a)) does not exist in an ideal structure investigated in MSs. Therefore, we can conclude again that the experimental result is an effect of the irregularities in the sample (already discussed in the experimental part and in appendix A). Also, plenty of high frequency BMs are recognized in MS spectra, with the most intensive at 10.27 GHz ($\phi_H = 0$, figure 3(f)) and 9.80 GHz ($\phi_H = 44°$, figure 3(g)), which have maximal amplitude concentrated between antidots along the direction perpendicular to H and two nodal lines in the unit cell along the same direction. Its position is

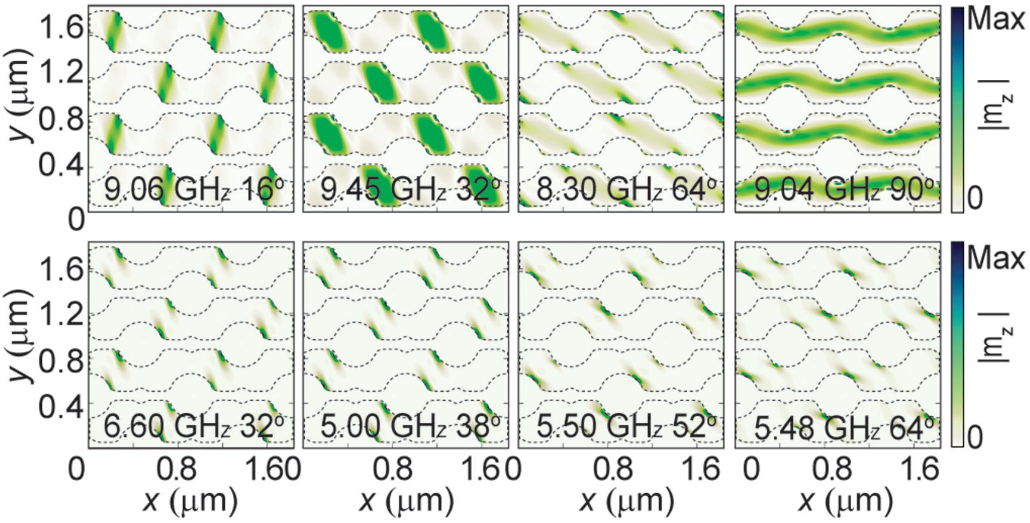

Figure 6. Visualization of the SW's FM (top row) and EM (bottom row) for oblique directions of the external magnetic field in the wave-like ADL. The frequencies of these modes are marked in figure 5 by white circles.

shifted by half of the ADL period, as compared to the FM. We can link this mode with the line at 93 mT in the measurements shown in figure 2(a).

In figure 4, the results of MSs for bi-component ADL are shown. Comparing figures 3(a) and 4(a), one can see that the additional small antidot inside the square unit cell leads to changes in the calculated spectra which overall agree with the measurements (figures 2(a) and (b)). The EM found in the square ADL (figure 3(c)) remains almost on the same frequency level in the bi-component ADL (figure 4(c)) and its amplitude distribution is also similar. There is also additional resonance line above this EM and below FM. That new EM mode observed at frequency 7.46 GHz ($\phi_H = 0°$) has amplitude oscillating in-phase located near small antidots—see figure 4(b). The frequency of FM in bi-component ADL at $\phi_H = 0°$ is 9.1 GHz, which is 320 MHz lower than for the square ADL. Moreover, opposite to square ADL, the FM frequency increases to 9.60 GHz (after slight decrease) with increasing ϕ_H for the field directed alongside the square unit cell. The small holes at 0° (figure 4(d)) introduce an additional demagnetizing field in the area of the FM confinement, while at 44° (figure 4(e)) they introduce quantization of the FM along the direction perpendicular to H. FMR frequency spectra show also several excitations above the FM frequency with comparable intensity. These BMs show quantization along or perpendicular to the field direction. Their profiles are modified by the presence of the small antidots as compared to the square ADL and their frequencies are changed as well.

For the wave-like ADL, the calculated FMR frequency spectrum along with the amplitude of exemplary SW excitations are collected in figure 5. We can observe a drastic difference between this spectrum and the spectra of the square and bi-component ADLs with interesting dependences of SWs frequencies on ϕ_H found. For $\phi_H = 0°$, the magnetic field and static magnetization are oriented along the wave-like channels, parallel to the x-axis. Even in a saturation state, a demagnetizing field is too weak to catch EMs, and this mode has not been found either in MSs or FMR measurements. The FM frequency (9.6 GHz) in wave-like ADL is higher than in the square and bi-component ADL, as well as in homogeneous Py film (9.3 GHz at the same field 0.1 T). Such behavior confirms that the wells of the demagnetizing field, located close to the interfaces, cannot shift down the FMR frequencies and be competitive to confinement effect. The amplitude of the FM mode is concentrated in the parts of the wave-like structure rotated by ±45° to the x-axis and oscillate in the same phase. Nevertheless, this mode (figure 5(b)) still slightly reminds of FM modes from figures 3(d) and 4(d), although it is formed in wave-like channels separated by air gaps, thus the SW excitations in neighboring wave-like channels are coupled by dipolar interactions only.

During the rotation of the magnetic field from 0° to 45°, the demagnetizing field decreases in the parts of the wave-like structure rotated by −45°, confining the SW amplitude in those areas and continuously transforming FM into EM. The EM observed for larger values of ϕ_H are concentrated at the edges of the big antidots (see figures 5 and 6 starting from (b) through points marked by white circles). This mode reaches minimal frequency (~5 GHz) at $\phi_H = 45°$. This scenario is consistent with the experimental observations (figure 2(c)), where EM was observed only for $\phi_H > 18°$ and took the maximal values of the resonant field at $\phi_H = 45°$ and 135°. In measurements, the transformation of the FM is not clear, because the intensive and independent on ϕ_H was observed there (figure 2(c)). Close to $\phi_H = 30°$, when the FM mode transforms into the EM and loses its intensity, another mode appears around 9 GHz and acquires a large intensity. The profile of this new FM is shown in the top row in figure 6 (9.45 GHz at $\phi_H = 32°$) and its amplitude distribution is very close to the profile of the FM in the bi-component ADL (figure 4(e)). However, the frequency of this mode in the wave-like ADL decreases (well below 7 GHz) with further increase of ϕ_H and its profile transforms continuously from like an FM (at 64°, 8.30 GHz in figure 6) into the EM with amplitude

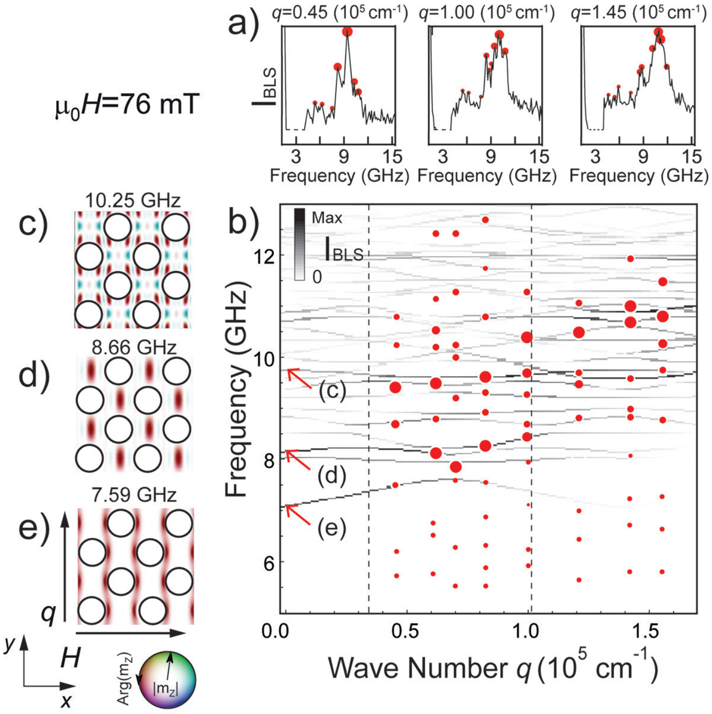

Figure 7. (a) Representative experimental BLS spectra of scattering intensity I_{BLS} in frequency domain for different values of the q vector, $q = (0.45, 1.00, 1.45) \times 10^5\ \mathrm{cm}^{-1}$ in square ADL. (b) BLS intensity map calculated with PWM (gray scale map) and from BLS measurements (filled circles) for Damon–Eshbach configuration in dependence on the wave vector. The size of the filled circles and the intensity of the dark colors denotes the BLS intensity. The thin vertical lines denote the borders of the BZs. The red arrows point at the most intensive modes in a center of the BZ for which the profiles of the out-of-plane component of the dynamical magnetization were plotted in (c)–(e). The color in profiles refers to the phase of dynamical magnetization and the intensity of the color denotes the magnitude of the SW amplitude.

concentrated at the edges of narrow air gaps (see also figure 5(f) the EM at $\phi_H = 88°$). With increase of the ϕ_H the intensity of the new FM decreases and around 65° another one mode has higher intensity (see the profile at 88° shown in figure 5(g)). The profile of this mode is very close to the FM found in the square and bi-component ADL (see figures 3(d) and 4(d)). The described scenario points out the possibility of designing a structure in which clockwise and counter-clockwise rotation of the external magnetic field will give a different microwave frequency response. This can be achieved for instance by changing the thickness or width of the wave-like parts oriented at +45 ° and −45 °, with respect to the *x*-axis.

We note also that at $\phi_H = 0°$ a few BMs of high intensity are found in wave-like ADL. Their intensity decreases with rotation of the magnetic field, according with the measurements. From the profiles shown in figures 5(c)–(e) and (h)–(i), we can relate them to the BMs, which are quantized along the field direction and concentrated in different parts of the structure.

4. BLS spectroscopy measured and PWM modelled SWs dispersion relation

In order to study the influence of increased complexity of the unit cell on properties of propagating SWs, we measured dispersion relation with the aid of BLS spectroscopy. To interpret experimental data, the BLS cross-section, the dispersion relation and the spatial distribution of the out-of-plane dynamical component of the magnetization, for the most intensive modes, were computed with PWM. The PWM is a useful method for calculation of the SW spectra in MCs [52], enabling calculation of the dispersion relation and profiles for MCs of any lattice type and for arbitrary shapes of the elements. We used the same sizes of antidots and lattice periods for square and bi-component ADLs as assumed for MS. However, for wave-like ADL, we took slightly different values of lattice constant (548 nm), because we read out, from STM images (figure 1), the periods 775 nm in the x- or y-direction (see figure 9). Due to the distortion of circular shape of antidots in wave-like ADL, we approximate then by diamond shaped antidots for PWM calculations. In the PWM the Landau–Lifshitz equation is linearized, then it is transformed into the algebraic eigen problem in the frequency domain and reciprocal space, which is solved numerically. Experimental samples. The details of the PWM can be found elsewhere [50, 51].

For the square ADL in MS and FMR measurements, we found the mode of frequency slightly below FM to be the EM (see figure 3). However, in PWM calculations (see figure 7(b)) the first SW excitation is at 7.59 GHz (at Brillouin zone (BZ) center) with amplitude distribution presented in figure 7(e). In PWM this mode has mixed character, combining FM (amplitude concentrated in the channels perpendicular to *H*) and EM (strong amplitude at the edges of antidots) both oscillating in-phase. This is a result of the assumptions made in PWM. In the PWM the artificial material is introduced instead

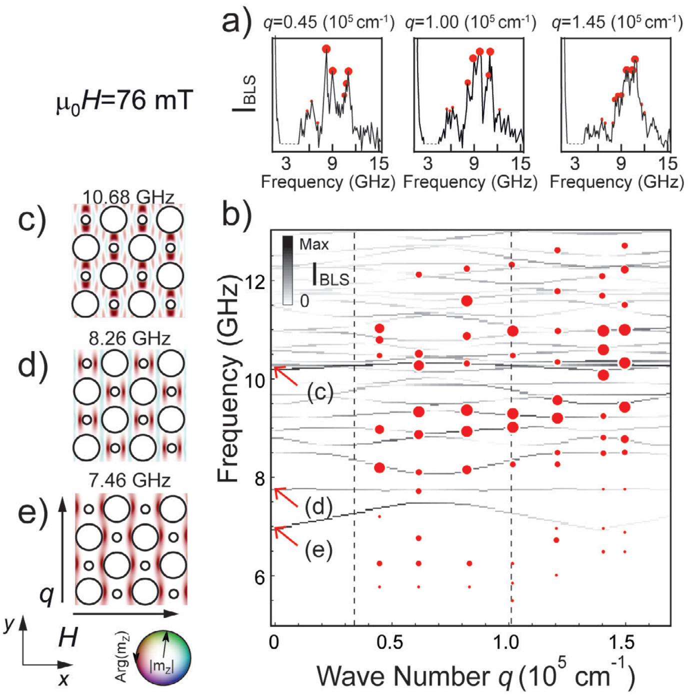

Figure 8. (a) Representative experimental BLS spectra of scattering intensity I_{BLS} in frequency domain for different values of the q wave vector $q = (0.45, 1.00, 1.45) \times 10^5\ \mathrm{cm}^{-1}$ in bi-component ADL. (b) BLS cross-section calculated using PWM (gray scale map), with BLS experimental points (filled circles) in Damon–Eshbach configuration where magnetic field was applied in one of the principal directions of the ADL ($\phi = 0°$). The meaning of the dots size and intensity of color map is the same as in figure 7. The thin vertical lines denote the borders of BZs. The red arrows show the most intensive modes in center of the BZ for which the profiles of the out-of-plane component of dynamical magnetization are plotted in (c)–(e). The color in profiles refers to the phase of the SW amplitude and the intensity of color denotes the amplitude.

of the non-magnetic, which results in strong artificial pinning of the magnetization at the antidot edges. This shifts up the frequency of the EM, while the other modes are almost unaffected [52]. For a small ratio of antidots' separation to thickness of the ADL, like in the samples considered in this paper, the FM and EM merge to form collective excitation shown in figure 7(e). Below, we will consider only FM and BMs in the square ADL.

The modes found in PWM at 7.59 and 8.66 GHz at 76 mT (figures 7(d) and (e), respectively) are the same as modes obtained in MS, shown in figures 3(f) and (d), respectively. These modes have the largest BLS intensity at small wavenumbers (see figure 7(a)). The SW amplitude distribution of the FM mode suggests that this mode will be able to propagate with noticeable group velocity. Indeed, the slope of its dispersion branch (i.e. group velocity) is largest in these spectra. Two modes of higher frequency and large (calculated) BLS intensity have the amplitudes quite concentrated in the areas between next-neighbor antidots. Therefore, their dispersion branches are flat, which is equivalent to the small values of group velocity for these modes. The measured BLS spectra starts at the wave numbers exceeding the first BZ boundary, thus the part of the spectra with valuable slope is out of the experimental range. Overall, there is noticeable agreement with the PWM results, for the most intensive parts of the spectra. The results confirm also the properties known from the previous studies [52].

The measured and calculated SW dispersion relation of the bi-component ADL is presented in figure 8(b), jointly with the SW profiles obtained from PWM at the center of the first BZ shown in figures 8(c)–(e) and the exemplary BLS intensity spectra in figure 8(a). Using MS, we found two kinds of EMs in this system (see figure 4). The PWM overestimates again the frequency of these EMs. The wells of demagnetizing field around the larger antidots are deeper and wider than for the smaller ones. Therefore, we see in PWM calculations the modes which are a mixture of the EM of larger antidots and FM (figure 8(e)), further on called FM for simplicity. This mode has similar spatial distribution to the corresponding FM mode in the square ADL (figure 7(e)) and similar slope in the first BZ. The frequency of the FM in bi-component ADL is slightly lowered in comparison to the frequency of the FM mode in square ADL. It can be understood if we consider that this mode is concentrated near the wells of demagnetizing field. This lowering is larger for bi-component ADL where two kinds of such wells exist.

The next intensive mode is concentrated mostly around smaller antidots, in the wells of the demagnetizing field and therefore we cannot find its counterpart in the square ADL. Due to such localization, this mode is weakly dispersive. The high intensity at 10.86 GHz (figure 8(c)) is similar in its spatial amplitude distribution to the mode of the square ADL lattice at 8.66 GHz (figure 7(d)). Both modes have the amplitude concentrated in the areas between

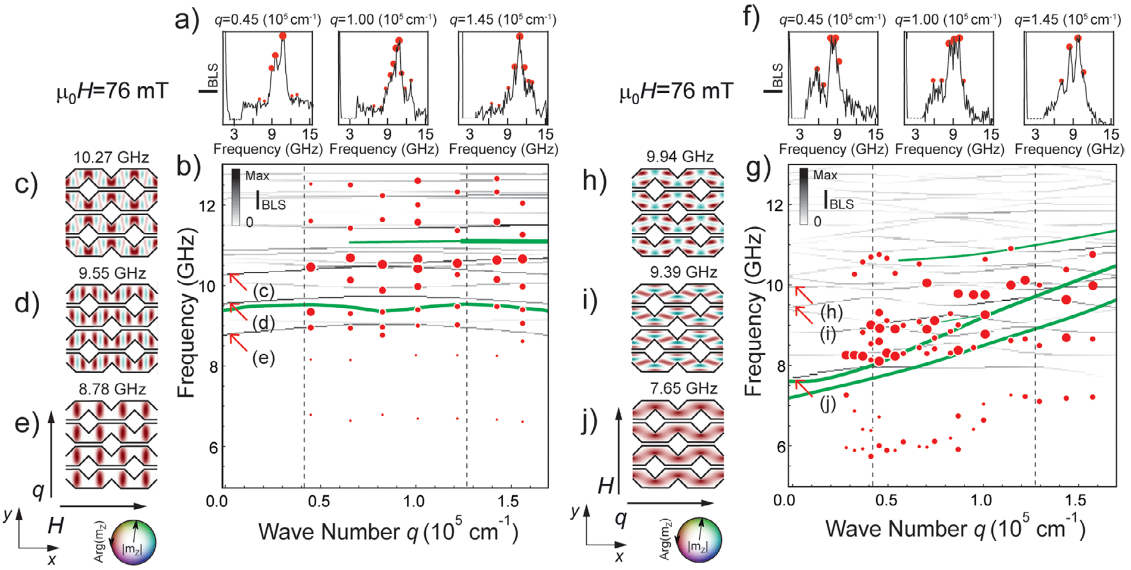

Figure 9. (a) and (f) Representative experimental BLS spectra of scattering intensity I_{BLS} in frequency domain for different values of q wave vector $q = (0.45, 1.00, 1.45) \times 10^5\ \mathrm{cm}^{-1}$ in wave-like structure. BLS cross-section calculated using PWM (gray scale map) with BLS experimental points (filled circles) for wave-like ADL in Damon–Eshbach configuration for the in-plane magnetic field oriented at (b) $\phi_H = 0°$ and (g) $\phi_H = 90°$. The size of the filled circles and the intensity of the dark colors denotes the BLS intensity. The green lines mark the most intensive SW excitations in the array of straight stripes (width 425 nm and periodicity 775 nm) for comparison. The thin vertical lines denote the borders of the BZs. The red arrows show the most intensive modes in center of the BZ for which the profiles of the out-of-plane component of dynamical magnetization vector are plotted in (c)–(e) and (h)–(j). The color in profiles refers to the phase of the SW amplitude and the intensity of color denotes the amplitude.

larger antidots along the y-axis, but for bi-component ADL the smaller antidot is placed in the center of this region. This makes the area of confinement for the mode smaller in bi-component ADL and shifts up its frequency relative to the frequency of the corresponding mode in the square ADL. This mode is also nondispersive. Overall, for FM and BM good agreement between BLS and PWM results is obtained.

The wave-like structure in PWM calculations (figure 9) was simplified as compared to the experimental sample (figure 1(c)) and used in MSs. We omitted the small deformation remaining from small antidots and approximated the larger antidots with diamond-like shape (with 275 nm long sides) which is far from the circular antidots used in MSs, but is close to the shapes of the antidots in the sample (see figure 1(c)). The width of the air-gaps separating the waveguides was assumed to be 57 nm. These modifications were introduced to use analytical formulas for Fourier coefficients describing spatial distribution material parameters in periodic structure composed of elementary shapes: rectangles and diamonds. We consider two orthogonal directions of H (along the x and y-axis) and the SW propagation always perpendicular to H.

For the magnetic field applied along the x-axis (figures 9 (a)–(e)) the static demagnetizing field is weak and does not affect significantly the internal magnetic field. The air-gaps break the exchange interaction between the wave-like channels weakening the strength of coupling for SWs. For this configuration, the propagation of SWs is ineffective, and all modes have flat bands with low group velocities, nicely confirmed in BLS measurements. In the considered frequency range we plotted profiles of three SW modes of significant BLS cross-sections for the wave number $q = 0$. The amplitude of the FM (of lowest frequency shown in figure 9(e)) is concentrated in the tilted sections of the wave-like channels, where the width of the wave-like channel is maximal. Its profile is close to the FM found in MS (figure 5(b)). The other mode of high BLS intensity (in a whole considered values of q) has an amplitude concentrated in the narrower parts of the channels (figures 5(e) and 9(c)).

For the magnetic field oriented perpendicular to the wave-like channels (figures 9(f)–(j)), the strong demagnetizing field shifts down the frequencies of SWs and creates suitable conditions for the EMs (see also figure 5). These EMs are observed in outcomes of PWM only being mixed with FM—see figure 9(j), where the intensity of the SW amplitude is increased in the vicinity of the flat sides of the waveguides and has a continuous amplitude distribution along the channels. As expected, the SWs can more easily propagate through continuous magnetic material (i.e. along the waveguide). Indeed, this is observed in the calculated and measured dispersion relations shown in figure 9(g). The group velocity of FM is 0.12 km s^{-1} at $q = 0$ (for the propagation across the wave-like channels (figure 9(b)) it is 0.05 km s^{-1}). The BLS intensities move to higher frequencies with increasing q and follow the dispersion relation calculated for the array of the straight stripes shown in figure 9 with solid green lines.

5. Conclusions

Using FMR and BLS spectroscopies we investigated Py-based thin planar periodic structures with three following geometries of the unit cell: simple square, bi-component and wave-like. The results of the measurements were interpreted with the aid of the MS and the PWM calculations. Good agreement between numerical and experimental results was achieved. We have found that a small additional antidot in the center of the square unit cell covering only 5% of the area is sufficient to valuably modify the FMR spectra. This small antidot introduces additional edge mode (with amplitude concentrated at the edges of the small antidots) and significantly changes the FM dependence on the orientation of the static magnetic field. The maximum (minimum) of the resonance frequency occurs at $\phi_H = 0°$ (45°) in square ADL. In bi-component ADL the maxima and minima resonance frequencies are at 45° and 0°, respectively, thus opposite to square ADL. We have also shown that irregular shape of antidots in square ADL can modify noticeably the angular dependence of the SW spectra. The shape distortion from the circular introduces non-equivalence of two perpendicular orientations of the magnetic field and introduces independence of the FM resonance position on the magnetic field orientation.

Adding air-gaps along parallel lines connecting large and small antidots introduces further interesting changes in dependence of the FMR spectra on the magnetic field orientation. Here, the FM continuously transforms into the edge mode when the external magnetic field rotates from the direction parallel to the wave-like channels ($\phi_H = 0°$) to the direction perpendicular to that line. At 30° this mode becomes localized near the edges of the channels but at the same angle the other SW mode becomes most intensive in the FMR spectra. The frequency of this other intensive mode also decreases with further rotation of the magnetic field direction.

The propagation properties of SWs were investigated in the Damon–Eshbach configuration. For in-plane applied magnetic field four-fold symmetry in the SWs excitation spectra was observed for both the square and bi-component ADLs. We demonstrated that introducing small air-gaps in the wave-like ADL decreased this symmetry to two-fold (SWs excitation at two perpendicular orientations of applied magnetic field are not equivalent). When the magnetic field is perpendicular to the wave-like channel the group velocity at the BZ center is high, in the perpendicular orientation it drops to the small value.

The information acquired in this paper about SW dynamics in ADLs shall be interesting for the magnonics and applications of the MCs in microwave technology, in processing information and especially in sensing applications pointed out recently for the ADLs [5, 53].

Acknowledgments

This research is supported by the SYMPHONY project operated within the Foundation for Polish Science within the Team Programme co-financed by the EU European Regional Development Fund, Grant No. OPIE 2007–2013, and partially received funding from the Polish National Science Centre Project No. UMO-2012/07/E/ST3/00538 and from the European Union Horizon 2020 research and innovation programme under the Marie Sklodowska-Curie grant agreement No. 644348 (MagIC). The simulations were partially performed at Poznan Supercomputing and Networking Center (grant No. 209).

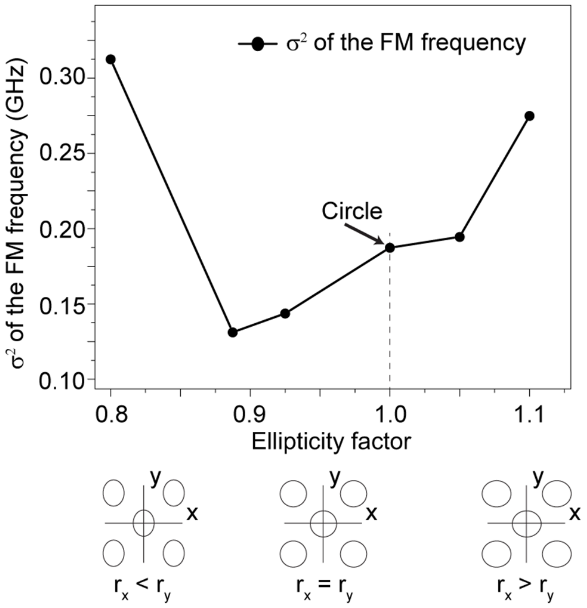

Figure A1. Variance σ^2 of the FM frequency obtained from MSs for different orientations of the external magnetic field ($\phi_{H,i} = 0°$, 45°, 90°, 135° and 180°) in dependence on the ellipticity factor (r_x/r_y) of the antidots shape. At the bottom schematic pictures of the square lattice with the deformed antidots shape are shown.

Appendix A

We found a significant correlation between deformation of the antidot shape and frequency of the FM in the ADL. To describe FM frequency dependence on the direction of the magnetic field we calculated variance σ^2:

$$\sigma^2 = \frac{\sum_{i=1}^{n}\left(f_i - \overline{f}\right)^2}{(n-1)}, \tag{A.1}$$

of the FM frequency for circular and ellipsoidal antidots, where f_i represents FM frequency for the $\phi_{H,i}$ angle of the external magnetic field, $\overline{f}$ their average value and n is the number of different angles extracted from simulations. The MSs were performed for 0, 45, 90, 135 and 180°. The variance used to estimate how far simulated frequencies, for different angles of the magnetic field orientation, are spread out from their mean, are calculated in dependence on the ellipticity factor and shown in figure A1. We observe a notable reduction of the variance only for the FM frequency during changing the shape of the antidots from the ideal circle to the elongated ellipses along the direction of the further neighbors. The strongest reduction was found when the ellipticity factor is close to 0.9 (axes of the ellipse are $r_x = 360$ and $r_y = 400$ nm, along the x and y axes, respectively), thus reducing the width of the ferromagnetic material disparities along the axis connecting further and closer neighbors. These results suggest that even small deformation of the antidots shape (the same for every antidot in ADL) can change the FMR spectra. This results in flattening of the angular dependence of the FM resonance field. We believe that this effect, giving very similar results known from

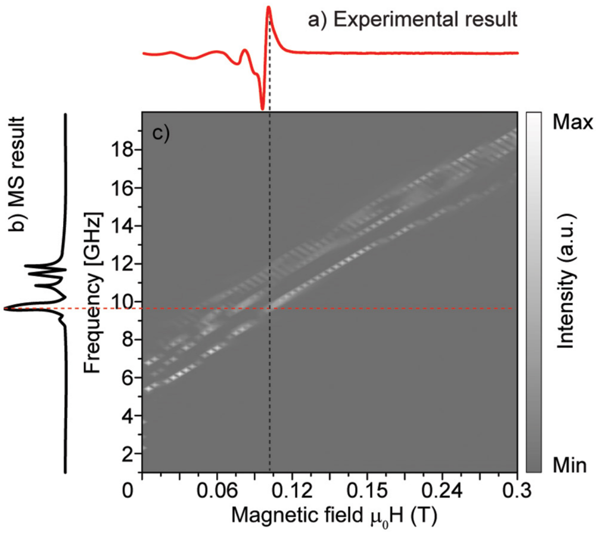

Figure B1. (a) Experimental magnetic field dependent FMR spectra at 9.4 GHz for $\phi_H = 0°$ and (b) frequency dependent FMR spectra obtained from MSs for $\phi_H = 0°$ in static external magnetic field 0.1 T. (c) Gray scale map showing intensity spectra of the SWs in the wave-like ADL obtained from MSs in dependence on frequency and magnetic field amplitude for $\phi_H = 0°$. Cutting of this plot along vertical line (black dashed) gives frequency dependent FMR spectra in (a), cutting along horizontal line (dashed red) gives magnetic field dependent spectra directly related to the measured spectra in (b).

the literature for Py dots [48], in combination with a large number of defects (for square ADL and wave-like structure) is a major cause of the FM FMR frequency independence of the external magnetic field orientation observed in measurements in the square and wave-like ADLs shown in figures 2(a) and (c).

Appendix B. Resonance frequency versus resonant magnetic field

In figure B1(c) we show the FMR intensity spectra of SWs in the wave-like ADL in dependence on frequency and magnetic field amplitude oriented at $\phi_H = 0°$ obtained from MSs. This result allows to explain the relation between the experimental results obtained in FMR measurements shown in figure 2 and MSs results shown in figures 3–5. The measurements are performed in dependence on the magnetic field magnitude at fixed frequency 9.4 GHz, marked in figure B1(c) with a horizontal red-dashed line. The MSs are performed in dependence on frequency at fixed magnetic field magnitude 0.1 T, marked by the vertical black-dashed line in figure B1(c). Thus, the spectra related to the experimental (figure B1(a)) and MSs spectra (figure B1(b)) can be obtained by taking cuts of the gray scale map shown in figure B1(c) along the horizontal and vertical line, respectively. We see, that FM in measured FMR spectra has a larger magnetic field (along red-dashed line), while in MSs it has a lower frequency (along the black-dashed line) as compared to BM modes. The EMs do not exist here.

References

[1] Chumak A V, Serga A A and Hillebrands B 2014 Magnon transistor for all-magnon data processing *Nat. Commun.* **5** 4700

[2] Stamps R L *et al* 2014 2014 Magnetism roadmap *J. Phys. D: Appl. Phys.* **47** 333001

[3] Zhu Y, Chi K H and Tsai C S 2014 Magnonic crystals-based tunable microwave phase shifters *Appl. Phys. Lett.* **105** 022411

[4] Metaxas P J *et al* 2015 Sensing magnetic nanoparticles using nano-confined ferromagnetic resonances in a magnonic crystal *Appl. Phys. Lett.* **106** 232406

[5] Sushruth M *et al* 2016 Resonance-based detection of magnetic nanoparticles and microbeads using nanopatterned ferromagnets *Phys. Rev. Appl* **6** 044005

[6] Gurevich A G and Melkov G A 1996 *Magnetization Oscillations and Waves* (Boca Ration, FL: CRC Press)

[7] Kruglyak V V, Demokritov S O and Grundler D 2010 Magnonics *J. Phys. D: Appl. Phys.* **43** 26

[8] Lenk B, Ulrichs H, Garbs F and Münzenberg M 2011 The building blocks of magnonics *Phys. Rep.* **507** 107

[9] Nikitov S A *et al* 2015 Magnonics: a new research area in spintronics and spin wave electronics *Phys.—Usp.* **58** 1002

[10] Puszkarski H and Krawczyk M 2003 Magnonic crystals—the magnetic counterpart of photonic crystals *Solid State Phenom.* **94** 125

[11] Nikitov S A, Tailhades Ph and Tsai C S 2001 Spin waves in periodic magnetic structures—magnonic crystals *J. Magn. Magn. Mater.* **236** 320

[12] Manda R, Barman S, Saha S, Otani O and Barman A 2015 Tunable spin wave spectra in two-dimensional $Ni_{80}Fe_{20}$ antidot lattices with varying lattice symmetry *J. Appl. Phys.* **118** 053910

[13] Krawczyk M and Grundler D 2014 Review and prospects of magnonic crystals and devices with programmable band structure *J. Phys.: Condens. Matter* **26** 123202

[14] Gubbiotti G *et al* 2010 Brillouin light scattering studies of planar metallic magnonic crystals *J. Phys. D: Appl. Phys.* **43** 264003

[15] Topp J, Heitmann D, Kostylev M P and Grundler D 2010 Making a reconfigurable artificial crystal by ordering bistable magnetic nanowires *Phys. Rev. Lett.* **104** 207205

[16] Tacchi S *et al* 2010 Analysis of collective spin-wave modes at different points within the hysteresis loop of a one-dimensional magnonic crystal comprising alternative-width nanostripes *Phys. Rev.* B **82** 184408

[17] Tripathy D and Adeyeye A O 2011 Perpendicular anisotropy and out-of-plane exchange bias in nanoscale antidot arrays *New J. Phys.* **13** 023035

[18] Mruczkiewicz M and Krawczyk M 2016 Influence of the Dzyaloshinskii–Moriya interaction on the FMR spectrum of magnonic crystals and confined structures *Phys. Rev.* B **94** 024434

[19] Sokolovskyy M L, Klos J W, Mamica S and Krawczyk M 2012 Calculation of the spin-wave spectra in planar magnonic crystals with metallic overlayers *J. Appl. Phys.* **111** 07C515

[20] Verba R *et al* 2013 Conditions for the spin wave nonreciprocity in an array of dipolarly coupled magnetic nanopillars *Appl. Phys. Lett.* **103** 082407

[21] Mruczkiewicz M *et al* 2013 Nonreciprocity of spin waves in metallized magnonic crystal *New J. Phys.* **15** 113023

[22] Jamali M *et al* 2013 Spin wave nonreciprocity for logic device applications *Sci. Rep.* **3** 3160

[23] Tacchi S, Gruszecki P, Madami M, Carlotti G, Klos J W, Krawczyk M, Adeyeye A and Gubbiotti G 2015 Universal dependence of the spin wave band structure on the

geometrical characteristics of two-dimensional magnonic crystals *Sci. Rep.* **5** 10367

[24] Yu H, d'Allivy Kelly O, Cros V, Bernard R, Bortolotti P, Anane A, Brandl F, Heimbach F and Grundler D 2016 Approaching soft x-ray wavelengths in nanomagnet-based microwave technology *Nat. Commun.* **7** 11255

[25] Yu H *et al* 2013 Omnidirectional spin-wave nanograting coupler *Nat. Commun.* **4** 2702

[26] Gulyaev Y V *et al* 2003 Ferromagnetic films with magnon bandgap periodic structures: magnon crystals *J. Exp. Theor. Phys. Lett.* **77** 567

[27] Semenova E K and Berkov D V 2013 Spin wave propagation through an antidot lattice and a concept of a tunable magnonic filter *J. Appl. Phys.* **114** 013905

[28] Hu C-L *et al* 2011 Field tunable localization of spin waves in antidot arrays *Appl. Phys. Lett.* **98** 262508

[29] Neusser S *et al* 2010 Anisotropic propagation and damping of spin waves in a nanopatterned antidot lattice *Phys. Rev. Lett.* **105** 067208

[30] Kostylev M P *et al* 2008 Propagating volume and localized spin wave modes on a lattice of circular magnetic antidots *J. Appl. Phys.* **103** 07C507

[31] Kłos J W, Kumar D, Krawczyk M and Barman A 2014 Influence of structural changes in a periodic antidot waveguide on the spin-wave spectra *Phys. Rev.* B **89** 014406

[32] Tacchi S *et al* 2011 Band diagram of spin waves in a two-dimensional magnonic crystal *Phys. Rev. Lett.* **107** 127204

[33] Kłos J W *et al* 2012 The impact of the lattice symmetry and the inclusion shape on the spectrum of 2D magnonic crystals *J. Appl. Phys.* **111** 123910

[34] Malago P *et al* 2015 Spin-wave dynamics in permalloy/cobalt magnonic crystals in the presence of a nonmagnetic spacer *Phys. Rev.* B **92** 064416

[35] Krawczyk M *et al* 2013 Magnonic band structures in two-dimensional bi-component magnonic crystals with in-plane magnetization *J. Phys. D: Appl. Phys.* **46** 495003

[36] Mandal R *et al* 2013 Effects of antidot shape on the spin wave spectra of two-dimensional $Ni_{80}Fe_{20}$ antidot lattices *Appl. Phys. Lett.* **103** 262410

[37] Madami M *et al* 2013 Spin wave dispersion in permalloy antidot array with alternating holes diameter *IEEE Trans. Magn.* **49** 3093

[38] Ding J, Tripathy D and Adeyeye A O 2012 Dynamic response of antidot nanostructures with alternating hole diameters *Europhys. Lett.* **98** 16004

[39] Wang Q *et al* 2012 Dynamic response of antidot nanostructures with alternating hole diameters *IEEE Trans. Magn.* **48** 3246

[40] Tahir N, Zelent M, Gieniusz R, Krawczyk M, Maziewski A, Wociechowski T, Ding J and Adeyeye A O 2017 Magnetization reversal mechanism in patterned (square to wave-like) Py antidot lattices *J. Phys. D: Appl. Phys.* **50** 025004

[41] Krawczyk M and Puszkarski H 2008 Plane-wave theory of three-dimensional magnonic crystals *Phys. Rev.* B **77** 054437

[42] Adeyeye A O and Singh J 2008 Large area patterned magnetic nanostructures *J. Phys. D: Appl. Phys.* **41** 153001

[43] Cottam M G and Lockwood D J 1986 *Light Scattering in Magnetic Solids* (New York: Wiley)

[44] Carlotti C and Gubbiotti G 1999 Brillouin scattering and magnetic excitations in layered structures *Riv. Nuovo Cimento* **33** 1

[45] Neusser S, Botters B and Grundler D 2008 Localization, confinement, and field-controlled propagation of spin waves in $Ni_{80}Fe_{20}$ antidot lattices *Phys. Rev.* B **78** 054406

[46] Gubbiotti G *et al* 2015 Angle-resolved spin wave band diagrams of square antidot lattices studied by Brillouin light scattering *Appl. Phys. Lett.* **106** 262406

[47] Tacchi S *et al* 2012 Mode conversion from quantized to propagating spin waves in a rhombic antidot lattice supporting spin wave nanochannels *Phys. Rev.* B **86** 014417

[48] Nembach H T *et al* 2011 Effects of shape distortions and imperfections on mode frequencies and collective linewidths in nanomagnets *Phys. Rev.* B **83** 094427

[49] Vansteenkiste A *et al* 2014 The design and verification of MuMax_3 *AIP Adv.* **4** 107133

[50] Sokolovskyy M L and Krawczyk M 2011 The magnetostatic modes in planar one-dimensional magnonic crystals with nanoscale sizes *J. Nanopart. Res.* **13** 6085

[51] Krawczyk M, Sokolovskyy M L, Klos J W and Mamica S 2012 On the formulation of the exchange field in the Landau–Lifshitz equation for spin-wave calculation in magnonic crystals *Adv. Condens. Matter Phys.* **2012** 764783

[52] Neusser S *et al* 2011 Magnonic minibands in antidot lattices with large spin-wave propagation velocities *Phys. Rev.* B **84** 094454

[53] Metaxas P J *et al* 2015 Sensing magnetic nanoparticles using nano-confined ferromagnetic resonances in a magnonic crystal *Appl. Phys. Lett.* **106** 232406

4.4 Bi-Stability of magnetic skyrmions in ultrathin multilayer nanodots induced by magnetostatic interaction

4.4.1 Introduction

The magnetic skyrmions are topologically stable spin configurations, which usually originate from chiral interactions known as Dzyaloshinskii-Moriya exchange interaction. Typically, confined ultrathin ferromagnetic multilayer structures are considered for hosting the skyrmions. However, the influence of magnetostatic interactions on skyrmion stability is not well understood. We report the results of numerical calculations of magnetic skyrmion stability in ultrathin magnetic multilayer nanodots with interfacial Dzyaloshinskii-Moriya exchange interaction. We found that in presence of the lateral confinement the magnetostatic energy significantly influences the skyrmion stability and leads to stabilisation of large skyrmion even at low values of the DMI strength, in addition to small skyrmion stabilised by presence of strong DMI. The bi-stability of skyrmion with different radii is investigated in detail using as an example dipolarly-coupled Pt/Co/Ir multilayer nanodots. The main outcomes of this article are: (i) skyrmions can be stabilised due to two different mechanisms, primary DMI or primary magnetostatic interaction leading to small and large size skyrmions, respectively, (ii) individual bi-stable skyrmions can be obtained in confined geometry with realistic values of the dot sizes, the DMI, exchange and anisotropy parameters, (iii) numerical technique able to estimate the minimum energy path for any skyrmion diameter in finite nanodot.

In this publication, Author has performed all of the numerical simulations in collaboration with Dr Michał Mruczkiewicz based on the Mumax3 software, he analysed the obtained numerical results and prepared all the figures. He significantly contributed to the manuscript writing and manuscript evaluation. **Author has prepared the front cover which has been chosen by editor for the issue front cover**.

Number of Ministerial points: 100.
Impact Factor: 3.721

RAPID RESEARCH LETTER

Skyrmion Stabilization

physica status solidi pss rrl
www.pss-rapid.com

Bi-Stability of Magnetic Skyrmions in Ultrathin Multilayer Nanodots Induced by Magnetostatic Interaction

M. Zelent, J. Tóbik, M. Krawczyk, K. Y. Guslienko, and M. Mruczkiewicz**

We report the results of simulations of magnetic skyrmion stability in ultrathin magnetic multilayer nanodots with interfacial Dzyaloshinskii–Moriya exchange interaction (DMI). We found that in presence of the lateral confinement the magnetostatic energy significantly influences the skyrmion stability and leads to stabilization of large-radius skyrmion even at low values of the DMI strength, in addition to small-radius skyrmion stabilized by DMI. In particular, stabilization of the skyrmion state with two different radii (bi-stability) is found in dipolarly-coupled $(Pt/Co/Ir)_n$ circular nanodots with the number of repeats of the unit cell $n = 3$ and 5. The bi-stability range is located at the DMI strength of 0.9–1.1 mJ m^{-2} or at the total Co-layer thickness of 2.2–2.6 nm.

Magnetic skyrmions are topologically non-trivial inhomogeneous magnetization configurations that can be stabilized in thin ferromagnetic films or non-centrosymmetric bulk magnetic crystals. The strong spin–orbit coupling and lack of the inversion symmetry give rise to the chiral Dzyaloshinskii–Moriya exchange interaction (DMI),[1,2] such as in bulk helimagnetic materials with cubic B20 crystal lattice (bulk DMI), or at the interface between two dissimilar materials, ferromagnet/heavy metal (interfacial DMI).[3,4] Both types of DMI are considered to be favoring the chiral skyrmion stabilization, either in ground state (the lowest energy state) or metastable state (a higher energy local energy minimum). The skyrmion classification in uniaxial magnets according to the crystal symmetry was suggested on the base of Lifshitz invariants, see Ref. [5] and references therein. The cubic DMI typically leads to stability of a Bloch skyrmion, where magnetization rotates perpendicular to radial direction moving away from the center of the skyrmion. Whereas, uniaxial interfacial DMI increases the stability of a Néel skyrmion (**Figure 1**a), where magnetization rotates in the plane parallel to radial direction. Nanosize skyrmions have a potential to provide useful solutions for cheap low-power, high-density data storage, and processing.[6–10] The discovery of strong interfacial DMI in ultrathin Co/Pt, Co/Pd, and Co/Pt/Ir multilayer films and dots expanded the possibilities for individual skyrmion stabilization in nanostructures.[11,12]

Moreau-Luchaire et al.[11] observed by scanning transmission X-ray microscopy stable sub-100nm magnetic skyrmions in dipolarly-coupled Pt/Co/Ir multilayers. Boulle et al. observed the Néel skyrmions in Pt/Co/MgO dots by photoemission electron microscopy combined with X-ray magnetic circular dichroism. [13] Recently, Pollard et al.[12] reported on Lorentz microscopy imaging of less than 100nm stable skyrmions in exchange-coupled Co/Pd multilayers at room temperature. The stability of an isolated skyrmion in infinite film applying perpendicular magnetic field was discussed in Refs. [5,9]. Very recently two types of skyrmions or bubbles with different radii were found to be stable in some cases in infinite ferromagnetic film.[14] Starting from Ref. [15], the skyrmion triangular lattices in bulk ferromagnets and infinite films were intensively investigated.[16] It was shown that lateral confinement modifies the conditions for the skyrmion stability significantly in ultrathin films,[10,13,17–23] as well as in the case of the B20 compounds.[17,18,24]

Recent studies demonstrated that the magnetic skyrmions are promising candidates for solving problems with unstable data storage, when size of the memory unit cells is decreasing below a critical size resulting in data loss.[25,26] It was shown that the skyrmions with opposite core polarities reveal hysteresis behavior when external magnetic field is varied.[6] This feature is of interest to design a new generation of data storage devices. In Ref. [19] the stability of a Néel skyrmion in circular nanodot was studied, and it was shown that due to the dot edge presence, the skyrmions with the sizes R_s/R (R_s is a skyrmion radius) between 0.50 and 0.78 are stable above critical value of DMI, D_c, for the dot radii $R = 25$–100 nm. In this study, the magnetostatic interaction was accounted as an effective uniaxial magnetic anisotropy.

However, increasing the dot thickness the magnetostatic energy is expected to play an important role in skyrmion stabilization even in ultrathin films/dots and should be taken into account.[13,21,27] It might even lead to stabilization of antiskyrmions with no DMI.[28]

M. Zelent, Prof. M. Krawczyk
Faculty of Physics, Adam Mickiewicz University in Poznan, 61-614 Poznań, Poland
E-mail: mateusz.zelent@amu.edu.pl

Dr. J. Tóbik, Dr. M. Mruczkiewicz
Institute of Electrical Engineering, Slovak Academy of Sciences, 841 04 Bratislava, Slovakia
E-mail: m.mru@amu.edu.pl

Prof. K.Y. Guslienko
Depto. Fisica de Materiales, Universidad del País Vasco, UPV/EHU, 20018 San Sebastian, Spain

Prof. K.Y. Guslienko
IKERBASQUE, the Basque Foundation for Science, 48013 Bilbao, Spain

DOI: 10.1002/pssr.201700259

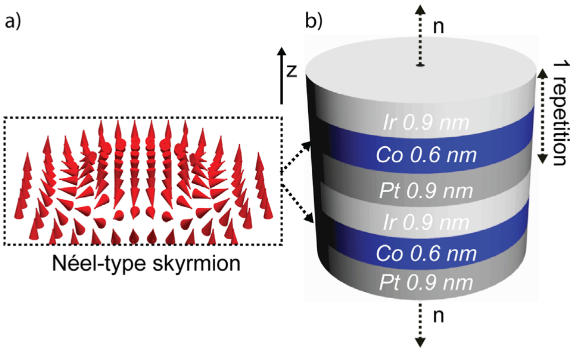

Figure 1. a) Magnetization configuration of the ferromagnetic layers in the circular layered dot (Néel-type skyrmion). b) Sketch of the multilayer nanodot based on dipolarly coupled ultrathin Co layers with varied number of repeats, *n*, of the Ir/Co/Pt unit cell.

The present paper is aiming at the following main points: Firstly, we show how the lateral confinement and corresponding magnetostatic energy lead to stabilization of the large-radius skyrmions, if DMI strength is weak. Secondly, we show that due to the lateral confinement and strong magnetostatic interactions, the skyrmions can be bi-stable in multilayer circular dots even at zero magnetic field.

A Néel skyrmion can be stabilized in a ultrathin dot within a finite range of interfacial DMI values, *D*. This range depends on competition of the DMI, exchange, anisotropy and magnetostatic interactions. The control of the magnetostatic interaction is realized by changing the number of repeats, *n*, of the Co layers in the stack (Figure 1). For a description of the skyrmion we use the reduced magnetization components $\boldsymbol{m} = \boldsymbol{M}/M_s = (m_r, m_\phi, m_z)$ in the cylindrical coordinate system with the *z* axis directed along the dot thickness.

Figure 2 shows the normalized skyrmion radii R_s/R for $n = 1$–9 repeats of the ferromagnetic layer of thickness $t_{\mathrm{Co}} = 0.6$ nm, with Co–Co separation 1.8 nm, dot radius $R = 250$ nm and magnetic parameters corresponding to Pt/Co/Ir dot as given in Computational Details. The static skyrmion configurations were simulated with the procedure described in Computational Details. All considered skyrmions possess the same core polarity, m_z at the center of the dot, it is -1.

We can distinguish two types of skyrmions, small size and large size or bubble skyrmions, depending on DMI strength *D* (Figure 2a). The clear border between the skyrmions cannot be defined and in some cases there is continuous transition between these two types of the skyrmions when DMI strength is varied, for example $n = 1$ (red line in Figure 2a). We note that there is strong influence of the number of ferromagnetic layer repeats on the large radius skyrmion stability and size, evidencing that the magnetostatic interaction plays an important role in stabilization of this skyrmion. The smaller skyrmion can nucleate at the DMI strength above 0.92 mJ m^{-2} and the range where it can exist decreases as the number of repeats increases. The points marked as D_{Cn} indicate the edges of stability of the small radius skyrmions and inflation points for rapid grow of skyrmion size with increase of the DMI strength for each number *n* of ferromagnetic layers in the stack. Increasing number of repeats decreases the critical DMI value where stable small radius skyrmion starts to grow. Thus, we conclude that the increase of magnetostatic interaction strength leads to decreasing the stability range of the small radius skyrmion.

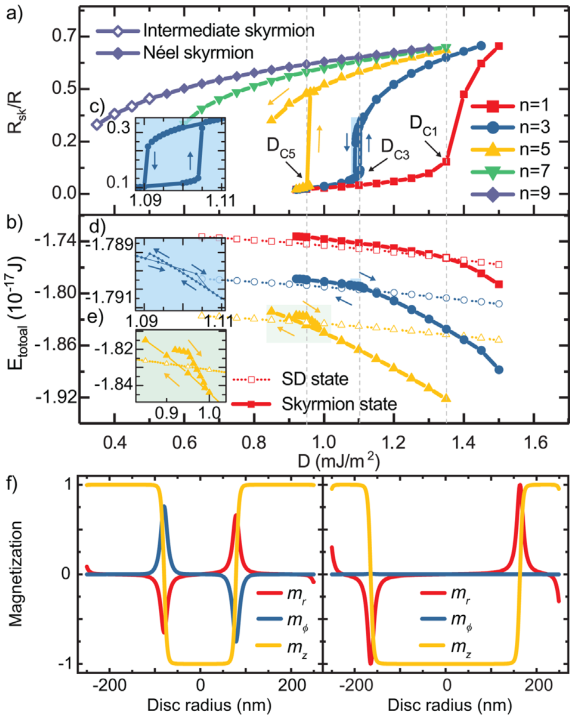

Figure 2. a) Normalized skyrmion radius, R_s/R, as a function of DMI strength *D* for different number of the ferromagnetic layers in the stack. D_{Cn} represents the edge of stability of the small radius skyrmion and inflection point for rapid grow of skyrmion size with increase of DMI. b) Total magnetic energy (including the DMI, exchange, anisotropy, and magnetostatic energies) for an isolated skyrmion (solid line), and for perpendicular single domain (SD) states as a function of DMI strength *D* for different numbers of the ferromagnetic layers. c) Inset: enlarged dependence of the skyrmion radius for $n = 3$. d,e) Inset: enlarged dependence of the total magnetic energy for $n = 5$ and 3 respectively. f) Profiles of the skyrmion magnetization components for $n = 9$ layers, at $D = 0.35$ mJ m^{-2} (on the left) and $D = 1.3$ mJ m^{-2} (on the right), plotted along the radial *x* direction.

Increasing number of repeats extends the range of DMI where large radius skyrmions can be nucleated. However, the large DMI strength supports Néel-like skyrmion stabilization. Skyrmions with weak DMI strength lose the Néel-like character (the considerable m_r magnetization component resulting in extra magnetostatic energy[29] cannot be compensated by DMI), intermediate states between Bloch- and Néel-like skyrmions appear (Figure 2f), indicated by open dots in Figure 2a.[10] Therefore, the hysteresis is a competition between small radius Néel-like skyrmions and large radius skyrmions having non-zero m_ϕ magnetization component (intermediate Bloch/Néel skyrmions[10]). Further increase of the number of ferromagnetic layer repeats and magnetostatic interaction strength in the layered stack leads to stabilization of the Bloch-like skyrmions even at zero DMI.[21]

It was simulated (see Figure 2a) that in some range of DMI and for certain number of the layer repeats, there is bi-stability of skyrmion with the same core polarity, but different sizes. For single layer ($n=1$) the bi-stability was not observed, however, it is present for 3 and 5 layers ($n=3$, 5). The difference between the large and small skyrmion radii, at the same DMI value, is relatively small for 3 layers (for $D=1.1\,\mathrm{mJ\,m^{-2}}$), but it increases for 5 layers (for $D=0.95\,\mathrm{mJ\,m^{-2}}$), and is 75.5 and 114.3 nm, respectively. Further increasing the number of repeats leads to destroying of small-radius Néel skyrmion stability. Therefore, the bi-stability can be observed only if magnetostatic interaction has intermediate strength competing with DMI. For three layers ($n=3$) we performed additional simulations, varying the dot radius R between 100 and 1000 nm. We found that there is a critical value of R that can support the skyrmion bi-stability and it is enhanced for large R. The range of D where bi-stable skyrmions can exist expands with increasing the dot radius.

As shown in Figure 2b the total magnetic energy (including the DMI, exchange, anisotropy, and magnetostatic energies) drawn as a solid line is higher than the single domain state energy for smaller skyrmion for each case. At higher values of D, the single domain state is no longer ground state, whereas the large radius skyrmion is. It is consistent with the previous observations.[30] For the cases $n=7$ and $n=9$ the energy of the large skyrmion is still lower than the SD energy.

Stable skyrmions with different equilibrium radii can be characterized by their relative energies and energy barrier separating them, see **Figure 3**a. To investigate the origin of two minima in the energy profile, we have analyzed the total energy and forces (and their components) acting on the skyrmion when the radius is varied at fixed DMI, $D=0.95\,\mathrm{mJ\,m^{-2}}$. In order to plot the energy profile as a function of skyrmion radius $E(R_s)$, we use the frozen spins technique (see Computational Details). Since the DMI is strong enough to ensure the Néel type magnetization twisting, we assume that the frozen spins $m_z = 0$, $m_r = 1$ correspond to the lowest energy state at each radius of the ring, so the change of radius crosses a saddle point in the energy function and allows us to estimate the minimum energy path and height of the energy barrier for bi-stable skyrmions.

We replace multilayer dot with simplified system, a single-layer circular dot with effective Co thickness, t_{Co}. That allows to continuously change the magnetostatic contribution to the total energy and study its influence on the skyrmion stabilization. Specific t_{Co} could be also reproduced by a multilayer system with fitted t_{Co} and Co–Co layer separation[1]. Figure 3c presents simulated sizes of stable skyrmion states in the nanodot as a function of the layer thickness, t_{Co}. Simulations showed that bi-stability exists and two possible skyrmion states are stable within the range of Co thickness 2.2–2.6 nm.

When the energy profile is calculated at $t_{\mathrm{Co}} = 0.6$ nm, a single minimum is present around $R_s = 12$ nm ($R_s/R = 0.048$), see Figure 3d-e, and position of this minimum agrees with skyrmion stabilized without the use of frozen spins. The stabilization of this skyrmion is possible due to canceling of contributing forces: magnetostatic, exchange and anisotropy.[13] These forces are calculated from derivatives of contributions to the total energy with respect to the skyrmion radius R_s and are presented in Figure 3d as F_{mag} for magnetostatic force and F_σ for remaining forces. The sum of all forces ΣF presented in Figure 3e is zero at the energy minimum. The effect of the dot edge plays minor role on stabilization and this skyrmion state is also expected to exist in infinite film.[19] The skyrmion stabilization is realized due to the nonlinear change in the magnetic energy as function of skyrmion radius induced when the skyrmion diameter is in order of domain wall (DW) width.[14][2]

When the Co thickness is increased to $t_{\mathrm{Co}} = 2.4$ nm, the skyrmions with two different sizes can be stable. The energy profile as function of the skyrmion radius is presented in Figure 3a. The energy minima correspond to skyrmion sizes found in Figure 3a at this value of t_{Co}. Analyzing the force F_{mag} (Figure 3f) one can observe significant curvature of the function at high values of R_s. The curvature increases with thickness (or M_s) increasing (Figure 3i) and appears due to presence of the nanodot edge. The edge changes the F_{mag} function and leads to stabilization of large radius skyrmion. Thus, presence of the lateral confinement modifies the magnetostatic energy introducing nonlinearity in the magnetostatic force F_{mag} as function of the skyrmion radius (see Figure 3f, i), and results in stabilization of skyrmion with size that is not related to the dot radius and DW width. The size of large skyrmion is not fixed to $R_s/R = 0.7$–0.8 as in Ref. [19], but is proportional to the magnetostatic interaction strength. The Co thickness 6.6 nm ($n=11$) and $D=1.4$–$1.6\,\mathrm{mJ\,m^{-2}}$ [11] correspond according to Figure 2a and c to the stable Néel skyrmion with the radius $R_s/R = 0.6$.

We distinguish two mechanisms of the skyrmion stabilization in nanodots: i) small radius Néel skyrmion is stabilized by DMI when R_s is in range of the DW width; and ii) large radius skyrmion is stabilized by nonlinear increase of the magnetostatic interaction with skyrmion radius increasing. The latter is solely present in confined geometries. The stabilization of these skyrmions is independent and a bifurcation can be present in some cases, leading to the skyrmion bi-stability in nanodots.

Further increase of t_{Co} leads to increase of curvature of the dependence $F_{\mathrm{mag}}(R_s)$, crossing at small values of R_s is not possible and small radius skyrmion becomes unstable (Figure 3i). The effect of the nonlinearity in the magnetostatic energy is very pronounced and large radius skyrmion is still stable.

An example shown in Figure 3a for particular set of parameters exhibits a double well potential separated by small energy barrier, $\Delta E = 2.33 \times 10^{-20}$ J. The energy barrier height

---

[1] We assume that the the dot radius is much larger than the separation between the ferromagnetic layers $t_{\mathrm{sep}} \ll R$ leading to uniform magnetic field across the thickness. We assume also that the effective dot thickness should be much smaller than the cycloid period, $t_{\mathrm{eff}} \ll L$, where $L = 4\pi A/D$ and A being the micromagnetic exchange constant.[19]

[2] In nanodot, this nonlinearity in the energy as function of the skyrmion radius is also present when the difference between dot radius and skyrmion radius is in the range of domain wall width (or slightly higher due to spin canting at the dot boundaries). Thus, the stable skyrmions in nanodot can be classified as small or large size even when the magnetostatic interaction is taken into account as an effective easy-plane anisotropy.[19]

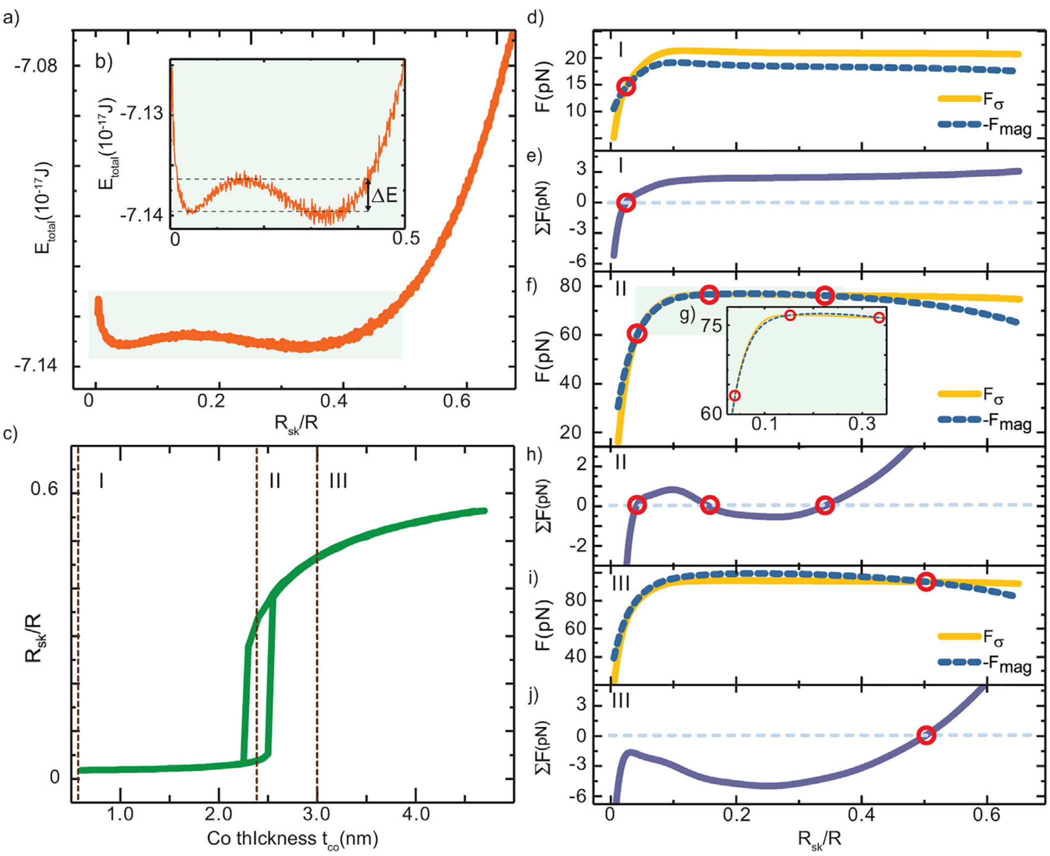

Figure 3. The energy profile of skyrmion state as function of normalized skyrmion radius R_s/R in 250nm radius dot ($t_{Co} = 2.4$ nm and $D = 0.95$ mJ m^{-2}). b) Inset: enlarged energy profile with the indicated scale of the total energy. c) Small and large skyrmion size as function of the thickness of Co layer. Dashed lines marked as I, II, III correspond to the force analysis presented in the panels (d-j). d,f,i) present the forces corresponding to the dot with different Co thicknesses, 0.6 nm (I), 2.4 nm (II), and 3.0 nm (III), respectively. F_{mag} is a magnetostatic force, and remaining forces are presented by F_σ. e,h,j) The sum of all forces is presented for I, II, and III cases, respectively, where zero value corresponds to the energy minimum. Red circles indicate energy minimum expressed as a crossing of the curves of partial forces. g) Inset: enlarged forces for (II).

can be enhanced and optimized via control of the magnetic parameters, geometry or external magnetic field. The switching between two skyrmion states can be realized, for example, by sweeping external magnetic field or applying a field pulse. Therefore, the skyrmion size hysteresis behavior can be realized without presence of a Bloch point as in switching between the skyrmions with opposite polarities.[6] The calculated skyrmion bi-stability is principally different from one calculated accounting DMI for magnetic vortices[31] because the latter is realized for different signs of D.

In conclusion, we analyzed influence of the magnetostatic interaction in circular multilayer nanodots on stability of the skyrmion magnetization configurations in ferromagnetic layers. We found that the skyrmions can be stabilized due to two different mechanisms, primary DMI or primary magnetostatic interaction leading to small and large size skyrmions, respectively. We found that these two kinds of the skyrmions can be stable simultaneously in the same nanodot. Thus, we demonstrated bi-stability of the skyrmion configurations with the same core polarities, but different sizes. The bi-stable skyrmions can be obtained in dots with realistic values of the dot sizes and the DMI strength, exchange and anisotropy parameters. Our results open a new route to design and develop a more efficient skyrmion memory, where information is coded as a skyrmion equilibrium size. The simulation approach based on the build-in Mumax function frozen spins is able to estimate the minimum energy path between two Néel skyrmions with different radii.

Computational Details

We performed finite-difference time-domain micromagnetic simulations with Mumax^3 solver[32] using a uniformly discretized grid with the cell size 0.5–1.0 nm × 0.5–1.0 nm × 0.6–4.2 nm. We used a set of parameters, which describes a multilayer thin film with a perpendicular magnetic anisotropy and DMI induced at the interfaces. We took the parameters measured for multilayer Pt/Co/Ir dot in Ref. [11]: saturation magnetization $M_s = 956$ kA m^{-1}, exchange stiffness $A = 10.0$ pJ m^{-1}, and perpendicular magnetic anisotropy $K_u = 0.717\,\mathrm{MJ\,m^{-2}}$. They are distributed uniformly in 0.6 nm thick Co layer. Ultrathin Pt/Co/Ir dot total thickness below 2.4 can be realized experimentally.[11,12] To keep magnetostatic interactions between the layers we used air-gap separation instead of the nonmagnetic spacers since the interlayer exchange was neglected. Total thickness of one repeat was 2.4nm. In order to simulate multilayer stacks we used finite periodic boundary conditions.[32] Magnetization non-uniformity through the thickness was neglected. To overcome staircase effects resulting from the calculation method, we used built-in Mumax function edge smooth.

The calculations of skyrmion size dependence on the DMI strength were performed by starting from an artificially nucleated skyrmion magnetic configuration, relaxing system and measuring the skyrmion radius (if skyrmion was stable). We increased the interfacial DMI, equilibrated the system at every DMI step and used the previous magnetization configuration as an initial state in the subsequent DMI increase step. Next, the same procedure was repeated decreasing the DMI strength, starting from a large radius skyrmion at maximum DMI value possible.

We used frozen spins technique to calculate the skyrmion magnetic energy exploiting the Mumax built-in frozen spin function. The edge of the skyrmion ($m_z = 0$, $m_r = 1$) is defined as a narrow ring around the center of the nanodot. Such condition facilitates a Néel skyrmion configuration with radius corresponding to the radius of the ring. The rest of the spins are free and relax to an energy minimum. This method does not assume any shape of the skyrmion profile, only its radius, in contrast with the semi-analytical approach.[14,21] When varying the ring radius we obtain the total skyrmion energy as a function of its radius, see Figure 3.

Acknowledgements

The project is financed by SASPRO Program. The research was supported by the People Program (Marie Curie Actions) European Union's FP7 under REA grant agreement No. 609427 (project WEST 1244/02/01) and further co-funded by the Slovak Academy of Sciences and the European Union Horizon 2020 Research and Innovation Program under Marie Sklodowska-Curie grant agreement No. 644348. The financial assistance from the National Science Center of Poland (MagnoWa DEC-2012/07/E/ST3/00538) is also acknowledged. K.G. acknowledges support by IKERBASQUE (the Basque Foundation for Science), the Spanish MINECO grants FIS2016-78591-C3-3-R and MAT2013-47078-C2-1-P. The simulations were partially performed at the Poznan Supercomputing and Networking Center (Grant No. 209) and supported by the National Scholarship Program of the Slovak Republic funded by the Ministry of Education, Science, Research, and Sport of the Slovak Republic.

Conflict of Interest

The authors declare no conflict of interest.

Keywords

bi-stability, magnetostatic interactions, nanodots, Néel skyrmion, skyrmions

Received: August 4, 2017
Revised: August 30, 2017

---

[1] I. Dzyaloshinsky, *J. Phys. Chem. Solids* **1958**, *4*, 241.
[2] T. Moriya, *Phys. Rev.* **1960**, *120*, 91.
[3] A. Fert, P. M. Levy, *Phys. Rev. Lett.* **1980**, *44*, 1538.
[4] A. Crépieux, C. Lacroix, *J. Magn. Magn. Mater.* **1998**, *182*, 341.
[5] A. O. Leonov, T. L. Monchesky, N. Romming, A. Kubetzka, A. N. Bogdanov, R. Wiesendanger, *New J. Phys.* **2016**, *18*, 1.
[6] M. Beg, R. Carey, W. Wang, D. Cortés-Ortuño, M. Vousden, M. A. Bisotti, M. Albert, D. Chernyshenko, O. Hovorka, R. L. Stamps, H. Fangohr, *Sci. Rep.* **2015**, *5*, 17137.
[7] G. Yu, P. Upadhyaya, Q. Shao, H. Wu, G. Yin, X. Li, C. He, W. Jiang, X. Han, P. K. Amiri, K. L. Wang, *Nano Lett.* **2017**, *17*, 261.
[8] A. Fert, V. Cros, J. Sampaio, *Nat. Nanotechnol.* **2013**, *8*, 152.
[9] N. S. Kiselev, a. N. Bogdanov, R. Schäfer, U. K. Rößler, *J. Phys. D: Appl. Phys.* **2011**, *44*, 392001.
[10] M. Mruczkiewicz, M. Krawczyk, K. Y. Guslienko, *Phys. Rev. B* **2017**, *95*, 094414.
[11] C. Moreau-Luchaire, C. Moutais, N. Reyren, J. Sampaio, C. A. F. Vaz, N. Van Horne, K. Bouzehouane, K. Garcia, C. Deranlot, P. Warnicke, P. Wohlhüter, J. M. George, M. Weigand, J. Raabe, V. Cros, A. Fert, *Nat. Nanotechnol.* **2016**, *11*, 444.
[12] S. D. Pollard, J. A. Garlow, J. Yu, Z. Wang, Y. Zhu, H. Yang, *Nat. Commun.* **2017**, *8*, 14761.
[13] O. Boulle, J. Vogel, H. Yang, S. Pizzini, D. d. S. Chaves, A. Locatelli, T. O. M. A. Sala, L. D. Buda-Prejbeanu, O. Klein, M. Belmeguenai, Y. Roussigné, A. Stashkevich, S. M. Chérif, L. Aballe, M. Foerster, M. Chshiev, S. Auffret, I. M. Miron, G. Gaudin, *Nat. Nanotechnol.* **2016**, *11*, 449.
[14] F. Büttner, I. Lemesh, G. S. D. Beach, arXiv:1704.08489, **2017**. https://arxiv.org/abs/1704.08489
[15] A. Bogdanov, A. Hubert, *J. Magn. Magn. Mater.* **1994**, *138*, 255.
[16] A. Fert, N. Reyren, V. Cros, *Nat. Rev. Mater.* **2017**, *2*, 17031.
[17] H. Du, W. Ning, M. Tian, Y. Zhang, *Phys. Rev. B* **2013**, *87*, 14401.
[18] H. Du, W. W. Ning, M. Tian, Y. Zhang, *EPL (Europhys. Lett.)* **2013**, *101*, 37001.
[19] S. Rohart, A. Thiaville, *Phys. Rev. B* **2013**, *88*, 184422.
[20] C. Moutafis, S. Komineas, C. A. F. Vaz, J. A. C. Bland, T. Shima, T. Seki, K. Takanashi, *Phys. Rev. B* **2007**, *76*, 104426.
[21] K. Y. Guslienko, *IEEE Magn. Lett.* **2015**, *6*, 4000104.
[22] K. Zeissler, M. Mruczkiewicz, S. Finizio, J. Raabe, P. M. Shepley, A. V. Sadovnikov, S. A. Nikitov, K. Fallon, S. McFadzean, S. McVitie, T. A. Moore, G. Burnell, C. H. Marrows, arXiv:1706.01065, **2017**. https://arxiv.org/abs/1706.01065
[23] M. A. Castro, S. Allende, *J. Magn. Magn. Mater.* **2016**, *417*, 344.
[24] A. O. Leonov, U. K. Rößler, M. Mostovoy, EPJ Web of Conferences *75*, 05002 (**2013**).
[25] R. Tomasello, E. Martinez, R. Zivieri, L. Torres, M. Carpentieri, G. Finocchio, *Sci. Rep.* **2014**, *4*, 6784.
[26] X. Yu, N. Kanazawa, W. Zhang, T. Nagai, T. Hara, K. Kimoto, Y. Matsui, Y. Onose, Y. Tokura, *Nat. Commun.* **2012**, *3*, 988.
[27] N. Vidal-Silva, A. Riveros, J. Escrig, *J. Magn. Magn. Mater.* **2017**, *443*, 116.
[28] W. Koshibae, N. Nagaosa, *Nat. Commun.* **2016**, *7*, 10542.
[29] K. Y. Guslienko, Z. V. Gareeva, *J. Magn. Magn. Mater.* **2017**, *442*, 176.
[30] J. Sampaio, V. Cros, S. Rohart, A. Thiaville, A. Fert, *Nat. Nanotechnol.* **2013**, *8*, 839.
[31] A. B. Butenko, A. A. Leonov, A. N. Bogdanov, U. K. Rößler, *Phys. Rev. B* **2009**, *80*, 1.
[32] A. Vansteenkiste, B. V. De Wiele, *J. Magn. Magn. Mater.* **2011**, *323*, 2585.

4.5 Formation of Néel type skyrmions in antidot lattice with perpendicular magnetic anisotropy

4.5.1 Introduction

In the paper, we present a method for the capture of nanometer sized magnetic skyrmions in an antidot lattice. Antidot lattices have been proposed as possible mediums for ultrahigh data storage devices, where the information bit would be trapped between two consecutive antidots. In particular, we have combined skyrmions with the antidot lattices to answer few of the key challenges related to skyrmions like reproducible generation, stabilisation and confinement of skyrmions at room temperature. Here, we have demonstrated the formation of Néel type magnetic skyrmions in the antidot lattice. We present the capture of nanometer sized skyrmions in antidot lattice using scanning transmission X ray microscopy (STXM). We observed that the formation of skyrmion within the antidot lattice depends on the geometrical property of the lattice, like lattice constant of the array. In particular, below a certain lattice constant, the magnetic skyrmions no longer form within the antidot lattice. It is also shown in both experiment and micromagnetic simulations that the basic criterion for the formation of skyrmions is an open end in the labyrinth domain structure.

In this publication, Author has performed solely all of the numerical simulations based on the Mumax3 software, analysed the obtained numerical and partially with Dr Susmita Saha experimental results. He prepared all the figures and significantly contributed to the manuscript writing and manuscript evaluation. Moreover he prepared the supplementary materials (videos).

Number of Ministerial points: 140.
Impact Factor: 3.736

Formation of Néel-type skyrmions in an antidot lattice with perpendicular magnetic anisotropy

S. Saha,[1,2,*] M. Zelent,[3,†] S. Finizio,[2] M. Mruczkiewicz,[4] S. Tacchi,[5] A. K. Suszka,[1,2] S. Wintz,[2,6] N. S. Bingham,[1,2,7]
J. Raabe,[2] M. Krawczyk,[4] and L. J. Heyderman[1,2]
[1]*Laboratory for Mesoscopic Systems, Department of Materials, ETH Zurich, 8093 Zurich, Switzerland*
[2]*Paul Scherrer Institut, 5232 Villigen PSI, Switzerland*
[3]*Faculty of Physics, Adam Mickiewicz University in Poznan, Umultowska 85, Poznan PL-61-614, Poland*
[4]*Institute of Electrical Engineering, Slovak Academy of Sciences, Dubravska Cesta 9, SK-841-04 Bratislava, Slovakia*
[5]*Istituto Officina dei Materiali del CNR (CNR-IOM), Sede Secondaria di Perugia, c/o Dipartimento di Fisica e Geologia, Università di Perugia, I-06123 Perugia, Italy*
[6]*Helmholtz-Zentrum Dresden-Rossendorf, 01328 Dresden, Germany*
[7]*Department of Applied Physics, Yale University, New Haven, Connecticut 06511, USA*

(Received 27 May 2019; revised manuscript received 30 September 2019; published 25 October 2019)

Magnetic skyrmions are particlelike chiral spin textures found in magnetic films with out-of-plane anisotropy and are considered to be potential candidates as information carriers in next generation data storage devices. Despite intense research into the nature of skyrmions and their dynamic properties, there are several key challenges that still need to be addressed. In particular, the outstanding issues are the reproducible generation, stabilization, and confinement of skyrmions at room temperature. Here, we present a method for the capture of magnetic skyrmions in an array of defects in the form of an antidot lattice. We find that inhomogeneity in the total effective field produced by the antidot lattice is important for the formation of skyrmions which are mainly stabilized by the dipolar interaction. With micromagnetic simulations and scanning transmission x-ray microscopy we elucidate that the formation of skyrmions within the antidot lattice depends on the lattice constant and that, below a certain lattice constant, the skyrmion formation is suppressed. Based on our results we propose that, by varying the lattice constant, we can modify the probability of skyrmion formation in different parts of a sample by specific patterning. This provides another platform for experimental investigations of skyrmions and skyrmion-based devices.

DOI: 10.1103/PhysRevB.100.144435

I. INTRODUCTION

In materials exhibiting perpendicular magnetic anisotropy (PMA), noncollinear spin textures can be stabilized in weak magnetic fields or even at remanence. In particular, labyrinth domains can shrink to form isolated magnetic skyrmions [1,2], which are topologically nontrivial stable spin textures characterized by a nonzero winding number with topological charge [3]. The antisymmetric exchange interaction, known as the Dzyaloshinskii-Moriya interaction (DMI) [4], which can arise due to large spin-orbit coupling in the presence of broken inversion symmetry in the material, helps to stabilize the chiral magnetic skyrmions. For asymmetric heavy-metal/ferromagnet/heavy-metal heterostructures, the inversion symmetry is broken by using different layers above and below the ferromagnetic layer, giving rise to an interfacial DMI.

The Hamiltonian describing the DMI between two atomic spins $\mathbf{S}_i$ and $\mathbf{S}_j$ can be expressed as $\hat{\mathcal{H}}_{\mathrm{DM}} = -\mathbf{D}_{\mathrm{DM}} \cdot (\mathbf{S}_i \times \mathbf{S}_j)$, where $\mathbf{D}_{\mathrm{DM}}$ is the Dzyaloshinskii-Moriya vector. The direction of the DM vector is defined by the type of DMI in the material. For interfacial DMI, the orientation of the DM vector leads to the stabilization of Néel-type magnetic skyrmions [5], whereas the lack of structural inversion symmetry in bulk materials [6,7] (e.g., B20 materials) leads to the stabilization of Bloch-type magnetic skyrmions [8]. In addition, skyrmions can also be stabilized via the dipolar interaction in systems with small or no DMI [9–11]. The magnetic domain structure stabilized in magnetic layers and multilayer stacks depends on the properties of the magnetic film and magnetic history of the sample, with the final spin configuration of the material determined by the ratio of the uniaxial anisotropy K_{u} to the demagnetization energy, the thickness of magnetic layer d, the strength of the DMI, and the number of layers present in the superlattice. By changing the orientation of the external magnetic field, one can obtain different domain structures during magnetization reversal, such as stripe, labyrinth, nonchiral bubble domains and, in some cases, skyrmions [12,13].

Additionally, the magnetic properties of a film can be influenced via patterning. For example, magnonic crystals [14,15], which are spatially modulated magnetic thin films, form well-defined spin wave band structures [16] due to their periodicity. One common example of magnonic crystals is a ferromagnetic antidot lattice [17–19] consisting of periodically arranged holes in a ferromagnetic thin film. Antidot lattices have been proposed as a medium for data storage devices, where the information bit would be trapped between two consecutive antidots [20,21]. In addition, antidot lattices patterned in magnetic multilayers with high PMA have been

---

[*] Corresponding author: susmita.saha@psi.ch (Experiments).

[†] Corresponding author: mateusz.zelent@gmail.com (Simulations).

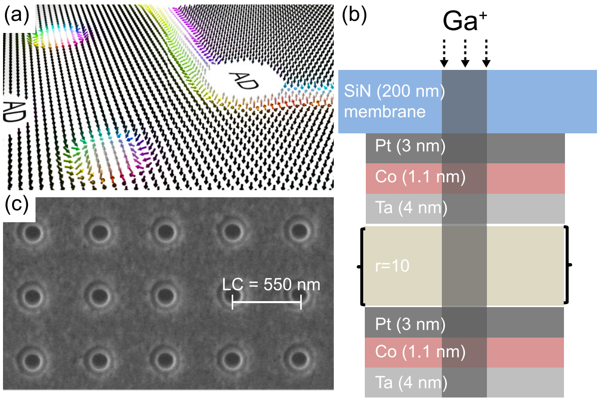

FIG. 1. (a) Visualization of the 3D spin orientation for skyrmions inside the antidot lattice in an applied magnetic field of -35 mT taken from micromagnetic simulations. (b) Schematic of the multilayer stack with an antidot fabricated using focused Ga ion beam milling (FIB). (c) Scanning electron microscope image of the antidot lattice with antidot diameter $d = 250$ nm and lattice constant LC $=$ 550 nm patterned in the $[\mathrm{Pt/Co/Ta}]_{12}$ film.

considered as a candidates for perpendicular percolated media [22], which constitutes an alternative approach to conventional bit patterned media. Antidots can also be employed to modify the intrinsic anisotropy of the system [23]. With regard to skyrmions, it has been shown that the edge of a magnetic element as well as defects [24] can repel the skyrmions. In an antidot lattice, the skyrmions are repelled from the edges of the holes, which helps to confine the skyrmions to the saddle-point region [25]. It has also been shown that pinning sites can accelerate skyrmion motion [24]. An antidot lattice can also give rise to a periodic potential similar to that of an array of pinning sites and therefore could also be used to control current driven skyrmion motion. However, a complete understanding of the influence of an antidot lattice on skyrmion formation during magnetization reversal is still required.

Here, we elucidate the skyrmion formation process in an antidot lattice using both experiment and micromagnetic simulation. In particular, the introduction of holes in an antidot lattice leads to inhomogeneity in the effective field, which has an impact on the formation of the skyrmions. Experimentally, we have fabricated antidot lattices with various lattice constants in a multilayer stack exhibiting both PMA and interfacial DMI (see Fig. 1). Imaging the skyrmions using scanning transmission x-ray microscopy (STXM), we observe that the skyrmions are created from a labyrinth domain pattern on application of a magnetic field. Additionally, we have shown that we can increase or decrease the probability of skyrmion formation by simply varying the lattice constant of the antidot array. From micromagnetic simulations, we have identified the role of the inhomogeneous effective field in the formation of skyrmions in an antidot lattice.

II. SAMPLE FABRICATION

Multilayer films of $[\mathrm{Pt}\ (3\ \mathrm{nm})/\mathrm{Co}\ (1.1\ \mathrm{nm})/\mathrm{Ta}\ (4\ \mathrm{nm})]_{12}$ were deposited on 200-nm-thick x-ray transparent $\mathrm{Si_3N_4}$ were deposited using DC magnetron sputtering (AJA International sputter system) with a confocal sputter up geometry at a base pressure of 2×10^{-8} Torr. The deposition of all of the layers was performed at a 3 mTorr Ar partial pressure. The antidot lattice was then patterned with focused ion beam milling (FIB) using a focused 30 kV $\mathrm{Ga^+}$ beam [Fig. 1(b)] with a beam current of 10 pA and a Gaussian spot size of 13 nm. Not only does the incident $\mathrm{Ga^+}$ ion beam modify the magnetic properties of the film, but also the scattered $\mathrm{Ga^+}$ ions, resulting in a lateral distribution of the deposited dose. To reduce the effect of the scattered ions, the ion milling was carried out from the back of the membrane. In this case, the $\mathrm{Si_3N_4}$ membrane absorbs most of the scattered $\mathrm{Ga^+}$ ions. Two different types of antidot lattices were fabricated with a hole (antidot) diameter d of 250 nm and lattice constant (LC) of 550 and 1000 nm. A scanning electron micrograph of one of the patterned antidot lattices is shown in Fig. 1(c).

III. MAGNETIC CHARACTERIZATION

The magnetic properties of the sputtered films were determined using various techniques. From the out-of-plane hysteresis loop, measured using a superconducting quantum interference device vibrating sample magnetometer (SQUID-VSM; Quantum Design MPMS3) and shown in Fig. 2(a), the saturation magnetization, M_s, was found to be $\approx 0.771 \times 10^6$ A/m and the saturation magnetic field ≈ 40 mT. The interfacial DMI of the system was determined by measuring the nonreciprocal spin wave dispersion using Brillouin light scattering (BLS). The presence of the interfacial DMI induces a frequency difference, Δf, between oppositely propagating Damon-Eshbach modes. This exhibits a linear dependence on the spin wave vector k and is proportional to the effective DMI constant $\mathbf{D}_{\mathrm{DM}}$, according to the following relation:

$$\Delta f = \frac{2\gamma \mathbf{D}_{\mathrm{DM}}}{\pi M_s} k, \tag{1}$$

where γ is the gyromagnetic ratio. The spin wave nonreciprocity, Δf, was determined by measuring the frequency difference between the Stokes (negative frequencies) and anti-Stokes (positive frequencies) peaks in the BLS spectra, which correspond to spin waves propagating in the opposite directions [26].

BLS measurements were carried out by focusing a monochromatic laser ($\lambda = 532$ nm) on the sample surface and analyzing the backscattered light by a Sandercock-type $(3 + 3)$ pass tandem Fabry-Perot interferometer. An in-plane magnetic field, sufficiently large to saturate the magnetization in the film plane, was applied along the direction perpendicular to the wave vector of the spin waves. Due to the photon-magnon conservation law of momentum in the scattering process, the magnitude of the wave vector is linked to the incidence angle of light θ, by the relation $k = 4\pi \sin\theta/\lambda$. For our measurements, Δf is measured as a function of k for an applied bias magnetic field, B, of 0.9 and -0.9 T. k was varied from 0 to 2×10^7 rad/m and a linear behavior is observed [Fig. 2(b)]. Note that, upon reversing the direction of the applied magnetic field, Δf changes sign due to the reversal of the spin wave propagation direction. The effective DMI

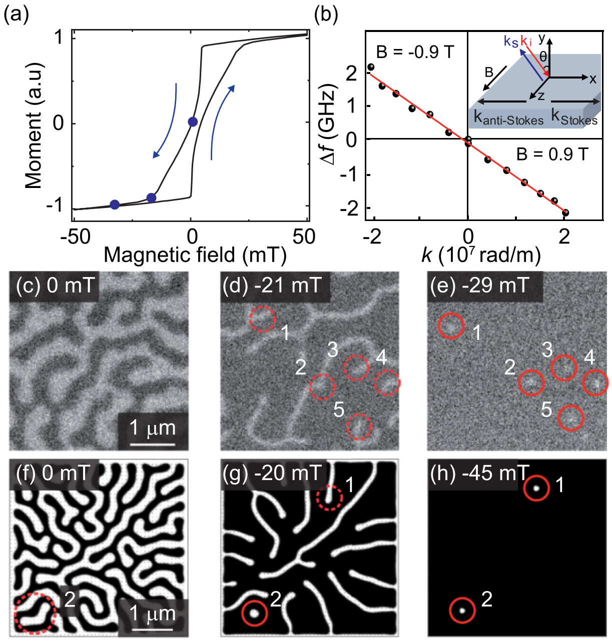

FIG. 2. (a) Out-of-plane hysteresis loop of the $[\mathrm{Pt/Co/Ta}]_{12}$ film. (b) The frequency asymmetry (Δf) extracted from the BLS measurement of the $[\mathrm{Pt/Co/Ta}]_{12}$ film for an in-plane applied bias magnetic field of 0.9 and −0.9 T. Black dots are the experimental results, while the red solid line is the linear fit to the experimental data. Δf is the difference between the frequency of the Stokes and the anti-Stokes peaks present in the BLS spectra. A schematic of the experimental configuration is shown in the inset. (c)–(e) XMCD-STXM images of magnetic states in the multilayer film at three different magnetic fields indicated with blue points on the hysteresis loop in (a). (f)–(h) Simulated images of similar magnetic configurations in the multilayer film. In all images, the dark and bright contrast corresponds to domains with magnetization pointing up and down, respectively. The skyrmions are indicated by solid red circles and the domain ends from which the skyrmions are formed are indicated by dashed red circles.

red solid line in Fig. 2(b)] to the experimental data based on Eq. (1). The value of DMI, $\mathbf{D}_{\mathrm{DM}} = -0.78 \pm 0.02\ \mathrm{mJ/m^2}$, was determined using the gyromagnetic ratio $\gamma = 194$ GHz/T and the measured value of M_{s}. The value of the DMI is sufficient to support the formation of Néel skyrmions. Moreover, the negative value of $\mathbf{D}_{\mathrm{DM}}$ indicates that left-handed chirality is favored in this material system.

The magnetic configuration of the antidot lattices was imaged using STXM at the PolLux endstation of the Swiss Light Source [27]. Circularly polarized photons are tuned to the L_3 absorption edge of Co (778 eV) and are focused onto a 25-nm spot on the sample using a diffractive Fresnel zone plate with an outermost zone width of ≈25 nm. Magnetic contrast was obtained through the x-ray magnetic circular dichroism (XMCD) effect and by illuminating the sample at normal incidence with respect to the surface. A selection of XMCD images of the magnetic states in a continuous $[\mathrm{Pt/Co/Ta}]_{12}$ multilayer film acquired under different applied out-of-plane acquisition of the images, the following field initialization protocol was applied; the sample was saturated with a 100 mT out-of-plane magnetic field, which was then reduced to 6 mT. After the field initialization, a demagnetized sample with labyrinth domains was observed. Then the magnetic field was reduced to zero and a reversed field was applied in increasing steps. As the magnetic field is increased up to the reverse saturation field, the width of the labyrinth domains with magnetization pointing antiparallel to the applied field is reduced from a value of ≈200 ± 35 nm at −6 mT to ≈150 ± 35 nm upon their collapse into several isolated skyrmions at −23 mT. Close inspection reveals that the skyrmions form at the end of the domains. These skyrmions eventually annihilate at an applied magnetic field of ≈−38 mT.

IV. MICROMAGNETIC SIMULATIONS OF SKYRMION FORMATION

The skyrmion formation process in a thin film and antidot lattices are simulated using MUMAX3 [28–30]. For the simulation, we have used periodic boundary conditions along the out-of-plane axis with six repetitions in both the negative and positive z directions [31]. The simulations were performed for a finite $4.4\,\mu\mathrm{m} \times 4.4\,\mu\mathrm{m}$ film using a uniformly discretized grid with a cell size of 2.0 nm × 2.0 nm × 1.1 nm, where the thickness of the cell of 1.1 nm corresponds to the thickness of the magnetic layer in the real sample. For the simulations, we employed the experimentally measured values of M_{s} and DMI reported in Sec. III. Furthermore, an exchange constant of $A = 1 \times 10^{-11}$ J/m and a PMA of $K_{\mathrm{u}} = 3.45 \times 10^5\ \mathrm{J/m^3}$, taken from the literature [32], were used in the simulations. In order to mimic the polycrystalline nature of the sample, a Voronoi tessellation was added in the micromagnetic simulations where, to each grain, a slightly different perpendicular magnetic anisotropy was assigned, drawn randomly from a normal distribution centered about a mean value with a standard deviation of 10%. The variation in the anisotropy is required to reproduce the experimental observations with the simulations, with high anisotropy grains acting as nucleation sites that facilitate sykrmion formation [33].

For continuous thin films, the ratio of the width of domains with magnetization pointing down (in black) to the width of domains with magnetization pointing up (in white) is controlled by the Zeeman energy, the size and morphology of the black and white domains are controlled by the anisotropy and domain wall energy, and the chirality is determined by the DMI. The simulations of the continuous thin film [Figs. 2(f) and 2(g)] exhibit a good qualitative agreement with the experimental images shown in Figs. 2(c)–2(e). In the simulations, a labyrinth domain pattern is formed at zero magnetic field [Fig. 2(f)]. As the magnetic field is increased, the labyrinth domains collapse into individual skyrmions [Figs. 2(d) and 2(e)]. The skyrmions are formed at the end of the white domains in both the experiment and the simulation. However, in the simulations, the magnetic skyrmions were created at a larger magnetic field than that in the experiment. These observed discrepancies between the micromagnetic simulations and the experimental data can be explained by the fact that the simulations were performed at 0 K, neglecting any thermal

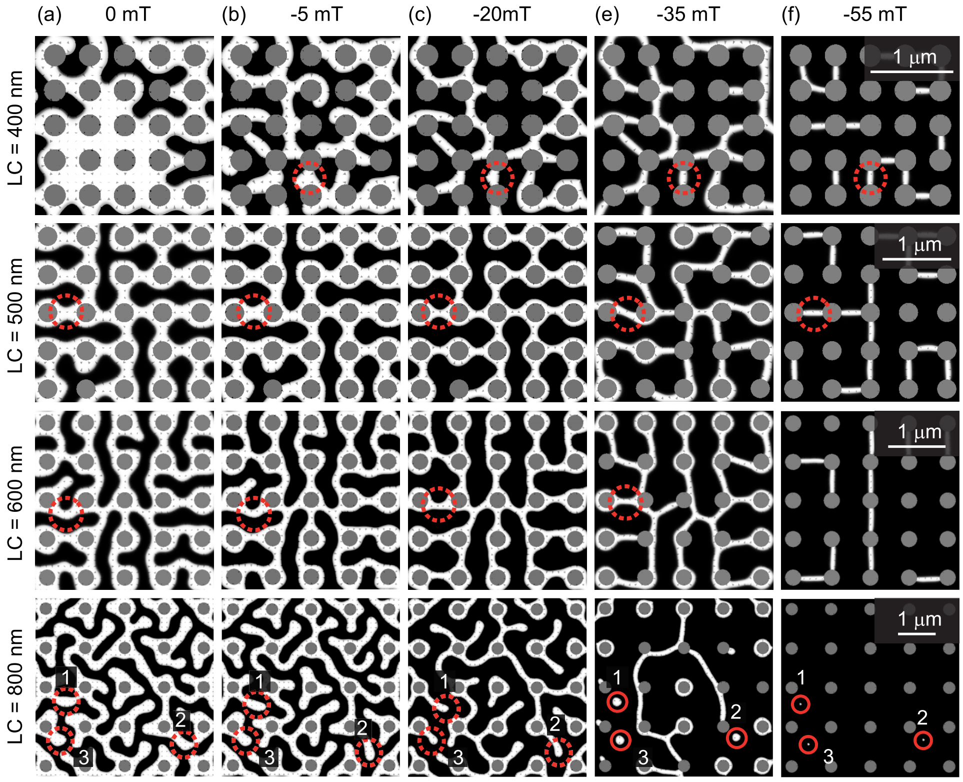

FIG. 3. Simulated images of the evolution of the magnetic configuration in antidot lattices with different lattice constants on increasing the magnetic field. The dark and bright contrast corresponds to domains with magnetization pointing up and down, respectively. Pinned domains are indicated by red dashed circles and the skyrmions are marked with circles with red solid lines.

In order to provide insight into the skyrmion stabilization and their capture in the antidot lattices, micromagnetic simulations were systematically performed for lattice constants of 400, 500, 600, and 800 nm. The evolution of the domain patterns on increasing the applied magnetic field is shown in Fig. 3 .

In general, during the magnetization reversal of the antidot lattice, reverse domains (in black) penetrate into the antidot lattice through the channels between the holes. The penetration of the black domains is hindered by the pinning field associated with the antidots, and white domains are pinned around the holes. For the more compact lattices (LC = 400, 500, and 600 nm), the labyrinth domain pattern is significantly modified and the details of the magnetization reversal strongly depend on the lattice constant. At 0 mT [Fig. 3(a)] the black domains have penetrated into the antidot lattice for the larger lattice constants, whereas for LC = 400 nm, most of the lattice is still in a saturated state.

A higher magnetic field is then required for the black domains to penetrate into the LC = 400 nm lattice and, due to the lack of space between the antidots, the white domains do not completely surround the holes. For all three lattice constants, the white domains often remain pinned at two neighboring holes on increasing the magnetic field, forming straight narrow domains between them, examples of which are indicated by red dotted circles in Fig. 3 for LC = 400, 500, and 600 nm. With further increase of the magnetic sections between the antidots and eventually vanish at a higher magnetic field. As a result, for these compact lattices, the formation of the skyrmions is hindered due to strong pinning of the domains at the holes in the antidot lattice, shown in the Supplemental Material [36].

For sufficiently large lattice constant, LC = 800 nm, a partial labyrinth domain pattern is observed at 0 mT. In this case, some of the domains are directly connected between two neighboring holes [see, e.g., dashed circles labeled 1 and 2 in Fig. 3(a)] and some form open domain ends [see dashed circle labeled 3 in Fig. 3(a)]. As the applied magnetic field is increased, the connecting domains detach from the holes, forming open domain ends as indicated by the dashed circles labeled 1 and 2 in Fig. 3. With further increase of the applied magnetic field, these open domain ends in the antidot lattice eventually shrink to form magnetic skyrmions indicated by red solid circles in Figs. 3(e) and 3(f). The size of the skyrmions also decreases with the further increase of the magnetic field [compare, e.g., skyrmions in Figs. 3(e) and 3(f), and see Supplemental Material for LC = 800 nm [37]]. The detailed evolution of the three-dimensional (3D) magnetization configuration on increasing the applied magnetic field for LC = 400 and 800 nm is shown in the Supplemental Material [38,39].

In order to understand the magnetization reversal process and the mechanism behind the skyrmion formation in the antidot lattice, we have extracted the spatial distribution of the

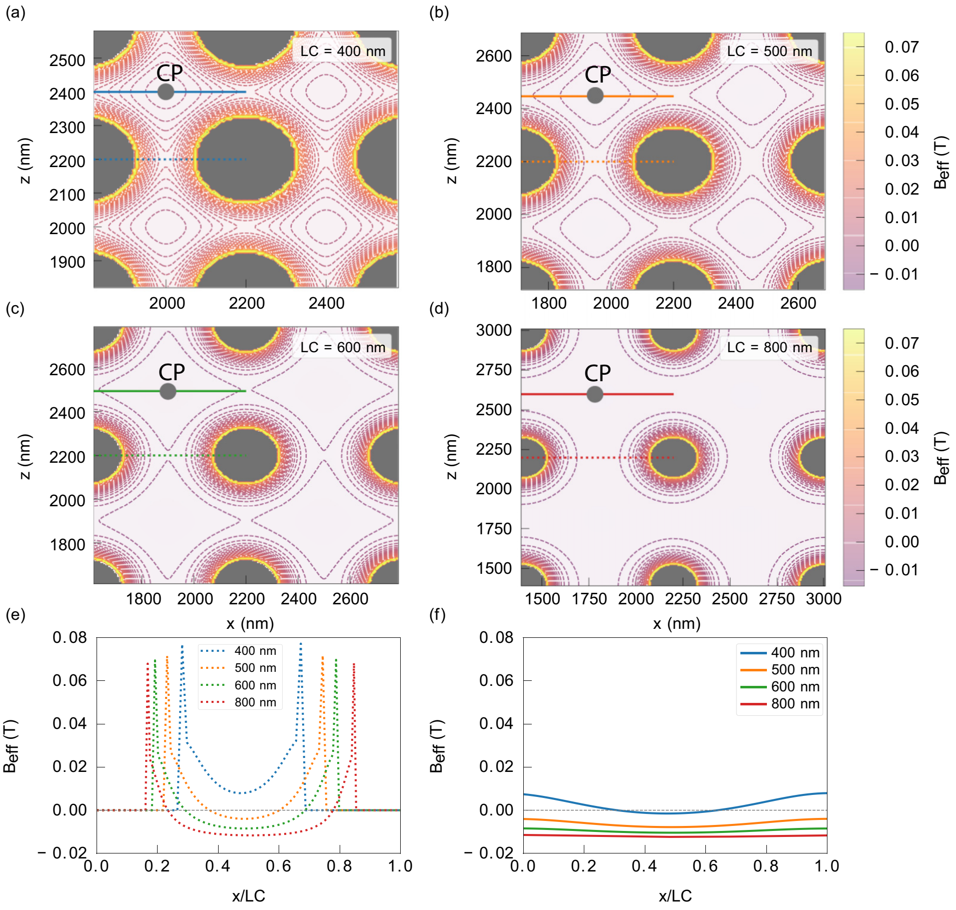

FIG. 4. (a)–(d) Contour plots of the simulated effective field distributions overlaid on the color map for the different lattices at 5 mT. The center point (CP), indicated by the gray dot, is the intersection of the diagonal lines connecting the centers of the antidots. (e), (f) Simulated effective field from different lattices obtained by taking a line scan across the two different regions marked by horizontal dashed and solid lines in Figs. 4(a)–4(d), respectively. Different line colors are used for the different lattices.

lattice constants at a field value of 5 mT so that the system is in a saturated state just before domain formation. The contributions to the effective magnetic field ($\boldsymbol{B}_{\text{eff}}$) are from the externally applied field ($\boldsymbol{B}_{\text{ext}}$), the magnetostatic field ($\boldsymbol{B}_{\text{demag}}$), the Heisenberg exchange field ($\boldsymbol{B}_{\text{exch}}$), the Dzyaloshinskii-Moriya exchange field ($\boldsymbol{B}_{\text{DM}}$), and the magnetocrystalline anisotropy ($\boldsymbol{B}_{\text{anis}}$) according to the following equation [29,40]:

$$\boldsymbol{B}_{\text{eff}} = \boldsymbol{B}_{\text{ext}} + \boldsymbol{B}_{\text{demag}} + \boldsymbol{B}_{\text{exch}} + \boldsymbol{B}_{\text{DM}} + \boldsymbol{B}_{\text{anis}}. \tag{2}$$

From Figs. 4(a)–4(d), it can be seen that the contour lines of the effective field are very dense around the holes and the line density between the holes decreases with increasing the lattice constant. The profile of effective field along the dashed and solid lines in Figs. 4(a)–4(d) are shown in Figs. 4(e) and 4(f), respectively. From this, it becomes clear that the effective field profile changes, in general decreasing and flattening with the increase of the lattice constant in both the regions. The reversal of the magnetization is facilitated or hindered, depending on whether the out-of-plane component of the

Although the variations in the effective field along the profiles is relatively small, it is sufficient to modify the domain patterns. In particular, in Fig. 4(e), it can be seen that the effective field has a high positive value close to the edges of the holes [41,42], which explains the pinning of the white domains around the holes. Additionally, the effective field is a minimum at the intersection of the diagonal lines connecting the antidots, labeled center point (CP), which explains the formation of black domains in the center point region, which is particularly noticeable in the antidot lattices with LC = 500 and 600 nm. The larger effective field in the region between neighboring holes supports the pinning of white domains forming a connection between the holes. For an antidot lattice with LC = 800 nm, the effective field in the channels between the holes [along the solid line in Fig. 4(d)] is almost uniform and, in order to achieve an equilibrium state, the system forms labyrinth domain patterns with open domain ends. As the external magnetic field is increased, the domain width changes to minimize the total energy of the system and, as shown in literature [43], the length of the domains will also decrease to minimize the total energy. During the contraction of the

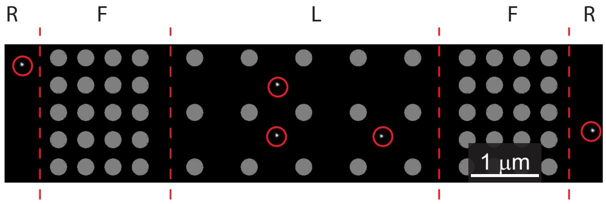

FIG. 5. Snapshot of a micromagnetic simulation showing the magnetic configuration of a composite structure combining two antidot lattices with LC = 800 and 400 nm with an unpatterned film at $H = -50$ mT. Symbols R, F, and L indicate three different regimes of the structure, where skyrmion formation is at random locations (R), forbidden (F), and localized at the center points in the effective magnetic field (L). For these simulations, the random distribution of the anisotropy of individual grains has not been included.

high anisotropy and, subsequently, a constriction forms that narrows until a skyrmion is formed. This mechanism of formation of skyrmion resembles the necking and detachment of a drop at the edge of a circular capillary tube [44]. We repeated the simulations several times for different distributions in the anisotropy field. The simulated results showed that, while the process of skyrmion formation is always the same, both the number of skyrmions and their position strongly depend on the anisotropy distribution. In general, for an antidot lattice with a uniform anisotropy, the probability of formation of the skyrmions is maximum at the CP, which has the lowest effective field.

In an unpatterned thin film, the skyrmions are spontaneously formed at random positions [45]. However, in our system, the antidot lattice increases the probability of skyrmion formation at a predefined position within the thin film. In order to demonstrate the control of the location of skyrmion formation, we have performed micromagnetic simulations of a composite structure combining a compact (LC = 400 nm) and a sparser (LC = 800 nm) antidot lattice together with an unpatterned thin film without a random distribution of anisotropy (Fig. 5). Here, we observe that the skyrmions form at random positions in the film indicated by R (random), whereas there is a high probability to form the skyrmions at the center points of the antidot lattice with moderate lattice constant indicated by L (localized). In the region with smaller lattice constant, the skyrmion formation is completely forbidden indicated by F (forbidden). Therefore, it is possible to have skyrmion formation in a selected region of a thin film by fabricating antidot lattice with tailored lattice constants. This concept could be used as a magnetic field induced skyrmion generator for skyrmion-based devices such as skyrmion race track memories, where repeated generation of a skyrmion in a particular location is needed. The skyrmions could then be transferred into other parts of the system, even in the regions where their formation is forbidden, using a spin-polarized current [46].

V. EXPERIMENTAL OBSERVATIONS

Following the micromagnetic simulations, we performed experiments on two samples patterned into antidot lattices with different lattice constants, LC = 550 and 1000 nm. The XMCD-STXM images of the magnetic configurations in the antidot lattices are shown in Figs. 6(a)–6(h). As for the experiments on the continuous $[\mathrm{Pt/Co/Ta}]_{12}$ films, we first performed a field initialization protocol, decreasing the field from 100 mT to zero and then increasing the magnetic field in reverse direction. For the antidot lattice with LC = 550 nm, the labyrinth domains form connections between the antidots on increasing the magnetic field as indicated by red dashed ellipses in Figs. 6(b)–6(d), which prevents the formation of skyrmions. In contrast, for LC = 1000 nm, initially the labyrinth domains directly connect two neighboring antidots as indicated, for example, by red dashed circles labeled 1 and 2 in Figs. 6(e)–6(g). On increasing the magnetic field, the domains disconnect from one of the antidots creating an open domain end as indicated by the red dashed circles

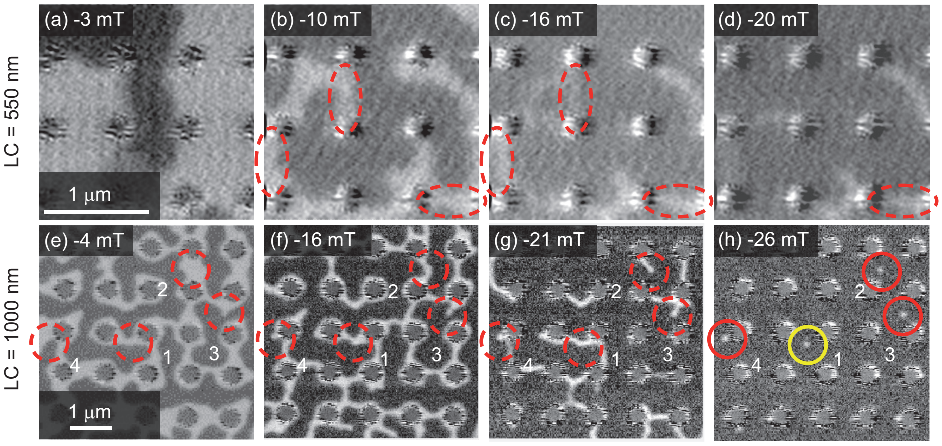

FIG. 6. XMCD-STXM images of the evolution of the magnetic configuration in the antidot lattices with magnetic field for anitdot lattices with (a)–(d) LC = 550 nm and (e)–(h) LC = 1000 nm. The dark and bright contrast corresponds to magnetic domains with magnetization pointing up and down, respectively. The skyrmions are indicated by solid circles and the domains from which the skyrmions are formed are

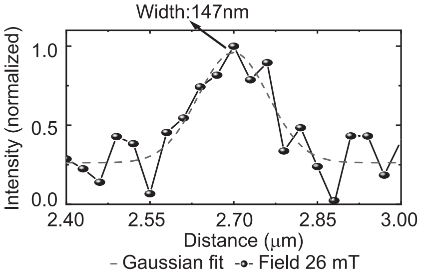

FIG. 7. Line profile of the magnetic contrast across the skyrmion marked with a yellow solid circle in Fig. 6(h). The profile is fitted with a Gaussian curve and has a full width half maximum of 147 nm.

labeled 2, 3, and 4 in Fig. 6(g). The domains with open ends progressively shrink down in width and length until they collapse into isolated magnetic skyrmions indicated by red and yellow solid circles in Fig. 6(h). This experimental observation that skyrmions only form for larger lattice constants is consistent with the results of the micromagnetic simulations. In particular, we note that the mechanism for the skyrmion formation, which occurs at domain ends that only appear for large lattice constants, is observed in both the experiment and simulation.

The domains marked by red dashed circles in Fig. 6 collapse into isolated skyrmions at an applied field of about -22 mT. The diameter of one of the skyrmions [indicated by the yellow circle in Fig. 6(h)] was determined to be 147 ± 35 nm (see Fig. 7). This is comparable with the simulated skyrmion size, which decreases from 200 to 100 nm as the field is increased from -35 to -55 mT although, in the experiment, no significant change in the skyrmion size on increasing the magnetic field could be seen. The skyrmions finally annihilate at a higher applied field and, on repeating the initialization protocol and increasing the field, we observed that the magnetic skyrmions can be repeatedly created in the antidot lattice. With regard to the skyrmion size, DMI leads to stabilized nanometer-sized skyrmions, whereas the larger sized skyrmions are mostly stabilized by the dipolar interaction [47,48]. In our case, the size of the observed skyrmions indicates that they are mostly stabilized by the dipolar interaction but the effect of DMI cannot be ignored.

VI. DISCUSSION

In summary, we have fabricated magnetic antidot lattices with LC = 550 and 1000 nm in a multilayered $[\mathrm{Pt/Co/Ta}]_{12}$ multilayer film with perpendicular magnetic anisotropy and DMI, and have imaged the evolution of the magnetic configuration in the presence of an applied magnetic field with scanning transmission x-ray microscopy. Our experimental results correspond to the predictions obtained with micromagnetic simulations. Not only do we observe the formation of Néel skyrmions for the sample with larger lattice constant (LC = 1000 nm), but also that the size of the skyrmions is comparable with the predictions of the micromagnetic simulations. With both experiment and simulations, we elucidate the lattice. In particular, the skyrmions are created at unconnected domain ends, which are necessary for the formation of the skyrmions in the antidot lattices.

Our micromagnetic simulations confirmed the existence of two distinct regimes, one characterized by small lattice constant LC $\leqslant$ 600 nm that suppresses the formation of skyrmions, while skyrmions are formed for an antidot lattice with LC $\geqslant$ 800 nm in the second regime. We showed that the introduction of the holes in a thin magnetic film modifies the spatial distribution of the effective magnetic field, which has a profound influence on the formation of the skyrmions. In particular, the skyrmion formation only occurs at the large lattice constants. In our experimental system, which has random variation of the local anisotropy, the skyrmions form in regions with high anisotropy. However, for an antidot lattice where random variation of the anisotropy is excluded, the skyrmions are formed at the center points of the antidot lattice, where the effective field is a minimum. This property can be exploited to design patterns in magnetic thin films to create skyrmions at predefined locations, while suppressing their formation in other regions.

Recently, it has been reported that, in the presence of a spin-polarized current, the skyrmion trajectory is modified by the defects [24,46]. These defects behave as a series of potential barriers for the skyrmions and interact with the skyrmions to modify their trajectory. The array of artificial defects introduced in the form of an antidot lattice can also be used to modify the skyrmion trajectory in the presence of a spin-polarized current. In addition, the potential barriers created by the antidot lattice can be varied by changing the lattice constant of the system.

In conclusion, our demonstration of the role of the effective field in an antidot lattice in the formation of skyrmions is a significant step towards reproducible generation and confinement of stable skyrmions at room temperature. This possibility to control skyrmions is of interest for data storage [8,49,50], reconfigurable skyrmion-based magnonic devices [51], and skyrmion-based race track memory [3].

The data that support this study are available via the Zenodo repository [52].

ACKNOWLEDGMENTS

We would like to acknowledge Dr. P. Derlet, Staff Scientist at PSI, for his valuable scientific inputs. XMCD-STXM measurements were performed at the PolLux endstation installed at the X07DA beamline of the Swiss Light Source, Paul Scherrer Institute, Switzerland. We thank Dr. E. Müller and A. Weber for sample fabrication. S.S. acknowledges support from an ETH Zurich Post-Doctoral fellowship and Marie Curie actions for People COFUND program (Grant No. FEL-11 16-1). M.M. acknowledges funding from the EU FP7 SASPRO Programme (REA Grant Agreement No. 609427, project WEST 1244/02/01) with further cofunding by the Slovak Academy of Sciences. A.K.S. acknowledges funding from the European Community's Seventh Framework Program (FP7/2007-2013) under Grant No. 290605 (COFUND: PSI-FELLOW). M.Z. and M.K. acknowledge funding from

Polish Ministry of Science and Higher Education resources for science in 2017-2019 (W28/H2020/2017), National Science Centre of Poland Grant No. 2017/27/N/ST3/00419, and Adam Mickiewicz University Foundation. The simulations were partially performed at the Poznan Supercomputing and Networking Center (Grant No. 398). S.F. acknowledges funding from the EU Horizon 2020 project MagicSky (Grant No. 665095). The PolLux end-station was financed by the German Ministerium für Bildung und Forschung (BMBF) through Contracts No. 05KS4WE1/6 and No. 05KS7WE1. S.T. acknowledges financial support by the European Metrology Programme for Innovation and Research (EMPIR), under Grant Agreement No. 17FUN08 TOPS.

---

[1] U. K. Rößler, A. N. Bogdanov, and C. Pfleiderer, Spontaneous skyrmion ground states in magnetic metals, Nature (London) **442**, 797 (2006).

[2] A. Fert, V. Cros, and J. Sampaio, Skyrmions on the track, Nat. Nanotechnol. **8**, 152 (2013).

[3] S. Zhang, A. A. Baker, S. Komineas, and T. Hesjedal, Topological computation based on direct magnetic logic communication, Sci. Rep. **5**, 15773 (2015).

[4] O. Boulle, J. Vogel, H. Yang, S. Pizzini, D. de Souza Chaves, A. Locatelli, T. O. Menteş, A. Sala, L. D. Buda-Prejbeanu, O. Klein, M. Belmeguenai, Y. Roussigné, A. Stashkevich, S. M. Chérif, L. Aballe, M. Foerster, M. Chshiev, S. Auffret, I. M. Miron, and G. Gaudin, Room-temperature chiral magnetic skyrmions in ultrathin magnetic nanostructures, Nat. Nanotechnol. **11**, 449 (2016).

[5] G. Chen, J. Zhu, A. Quesada, J. Li, A. T. N'Diaye, Y. Huo, T. P. Ma, Y. Chen, H. Y. Kwon, C. Won, Z. Q. Qiu, A. K. Schmid, and Y. Z. Wu, Novel Chiral Magnetic Domain Wall Structure in Fe/Ni/Cu(001) Films, Phys. Rev. Lett. **110**, 177204 (2013).

[6] N. Nagaosa and Y. Tokura, Topological properties and dynamics of magnetic skyrmions, Nat. Nanotechnol. **8**, 899 (2013).

[7] E. Turgut, H. Paik, K. Nguyen, D. A. Muller, D. G. Schlom, and G. D. Fuchs, Engineering Dzyaloshinskii-Moriya interaction in B20 thin-film chiral magnets, Phys. Rev. Mater. **2**, 074404 (2018).

[8] A. Fert, N. Reyren, and V. Cros, Magnetic skyrmions: Advances in physics and potential applications, Nat. Rev. Mater. **2**, 17031 (2017).

[9] A. Hrabec, J. Sampaio, M. Belmeguenai, I. Gross, R. Weil, S. M. Chérif, A. Stashkevich, V. Jacques, A. Thiaville, and S. Rohart, Current-induced skyrmion generation and dynamics in symmetric bilayers, Nat. Commun. **8**, 15765 (2017).

[10] M. Zelent, J. Tóbik, M. Krawczyk, K. Y. Guslienko, and M. Mruczkiewicz, Bi-stability of magnetic skyrmions in ultrathin multilayer nanodots induced by magnetostatic interaction, Phys. Status Solidi RRL **11**, 1700259 (2017).

[11] S. Finizio, S. Wintz, D. Bracher, E. Kirk, A. S. Semisalova, J. Förster, K. Zeissler, T. Weßels, M. Weigand, K. Lenz, A. Kleibert, and J. Raabe, Thick permalloy films for the imaging of spin texture dynamics in perpendicularly magnetized systems, Phys. Rev. B **98**, 104415 (2018).

[12] K.-O. Ngand D. Vanderbilt, Stability of periodic domain structures in a two-dimensional dipolar model, Phys. Rev. B **52**, 2177 (1995).

[13] J. H. Han, J. Zang, Z. Yang, J.-H. Park, and N. Nagaosa, Skyrmion lattice in a two-dimensional chiral magnet, Phys. Rev. B **82**, 094429 (2010).

[14] M. Krawczyk and D. Grundler, Review and prospects of magnonic crystals and devices with reprogrammable band

[15] P. Malagò, L. Giovannini, R. Zivieri, P. Gruszecki, and M. Krawczyk, Spin-wave dynamics in permalloy/cobalt magnonic crystals in the presence of a nonmagnetic spacer, Phys. Rev. B **92**, 064416 (2015).

[16] A. V. Chumak, V. I. Vasyuchka, A. A. Serga, and B. Hillebrands, Magnon Spintronics, Nat. Phys. **11**, 453 (2015).

[17] S. Pal, J. W. Klos, K. Das, O. Hellwig, P. Gruszecki, M. Krawczyk, and A. Barman, Optically induced spin wave dynamics in $[Co/Pd]_8$ antidot lattices with perpendicular magnetic anisotropy, Appl. Phys. Lett. **105**, 162408 (2014).

[18] N. Tahir, M. Zelent, R. Gieniusz, M. Krawczyk, A. Maziewski, T. Wojciechowski, J. Ding, and A. O. Adeyeye, Magnetization reversal mechanism in patterned (square to wave-like) Py antidot lattices, J. Phys. D **50**, 025004 (2017).

[19] M. Zelent, N. Tahir, R. Gieniusz, J. W. Kłos, T. Wojciechowski, U. Guzowska, A. Maziewski, J. Ding, A. O. Adeyeye, and M. Krawczyk, Geometrical complexity of the antidots unit cell effect on the spin wave excitations spectra, J. Phys. D **50**, 185003 (2017).

[20] R. P. Cowburn, A. O. Adeyeye, and J. A. C. Bland, Magnetic domain formation in lithographically defined antidot Permalloy arrays, Appl. Phys. Lett. **70**, 2309 (1997).

[21] Z. K. Wang, H. S. Lim, V. L. Zhang, J. L. Goh, S. C. Ng, M. H. Kuok, H. L. Su, and S. L. Tang, Collective spin waves in high-density two-dimensional arrays of FeCo nanowires, Nano Lett. **6**, 1083 (2006).

[22] D. Suess, J. Fidler, K. Porath, T. Schrefl, and D. Weller, Micromagnetic study of pinning behavior in percolated media, J. Appl. Phys. **99**, 08CG905 (2006).

[23] A. Y. Toporov, R. M. Langford, and A. K. Petford-Long, Lorentz transmission electron microscopy of focused ion beam patterned magnetic antidot arrays, Appl. Phys. Lett. **77**, 3063 (2000).

[24] C. J. O. Reichhardt, D. Ray, and C. J. O. Reichhardt, Quantized transport for a skyrmion moving on a two-dimensional periodic substrate, Phys. Rev. B **91**, 104426 (2015).

[25] A. I. Marchenko and V. N. Krivoruchko, Skyrmion-like bubbles and stripes in a thin ferromagnetic film with lattice of antidots, J. Magn. Magn. Mater. **377**, 153 (2015).

[26] S. Tacchi, R. E. Troncoso, M. Ahlberg, G. Gubbiotti, M. Madami, J. Åkerman, and P. Landeros, Interfacial Dzyaloshinskii-Moriya Interaction in Pt/CoFeB Films: Effect of the Heavy-Metal Thickness, Phys. Rev. Lett. **118**, 147201 (2017).

[27] J. Raabe, G. Tzvetkov, U. Flechsig, M. Böge, A. Jaggi, B. Sarafimov, M. G. C. Vernooij, T. Huthwelker, H. Ade, D. Kilcoyne, T. Tyliszczak, R. H. Fink, and C. Quitmann, PolLux: A new facility for soft x-ray spectromicroscopy at the Swiss Light Source, Rev. Sci. Instrum. **79**, 113704

[28] A. Vansteenkiste and B. Van de Wiele, MUMAX: A new high-performance micromagnetic simulation tool, J. Magn. Magn. Mater. **323**, 2585 (2011).

[29] A. Vansteenkiste, J. Leliaert, M. Dvornik, M. Helsen, F. Garcia-Sanchez, and B. Van Waeyenberge, The design and verification of MUMAX3, AIP Adv. **4**, 107133 (2014).

[30] J. Leliaert, B. Van de Wiele, A. Vansteenkiste, L. Laurson, G. Durin, L. Dupré, and B. Van Waeyenberge, Current-driven domain wall mobility in polycrystalline Permalloy nanowires: A numerical study, J. Appl. Phys. **115**, 233903 (2014).

[31] S. Woo, K. Litzius, B. Krüger, M.-Y. Im, L. Caretta, K. Richter, M. Mann, A. Krone, R. M. Reeve, M. Weigand, P. Agrawal, I. Lemesh, M.-A. Mawass, P. Fischer, M. Kläui, and G. S. D. Beach, Observation of room-temperature magnetic skyrmions and their current-driven dynamics in ultrathin metallic ferromagnets, Nat. Mater. **15**, 501 (2016).

[32] R. L. Stoop and P. Tierno, Clogging and jamming of colloidal monolayers driven across disordered landscapes, Commun. Phys. **1**, 68 (2018).

[33] X. Yu, M. Mostovoy, Y. Tokunaga, W. Zhang, K. Kimoto, Y. Matsui, Y. Kaneko, N. Nagaosa, and Y. Tokura, Magnetic stripes and skyrmions with helicity reversals, Proc. Natl. Acad. Sci. USA **109**, 8856 (2012).

[34] D. Suess, L. Breth, J. Lee, M. Fuger, C. Vogler, F. Bruckner, B. Bergmair, T. Huber, J. Fidler, and T. Schrefl, Calculation of coercivity of magnetic nanostructures at finite temperatures, Phys. Rev. B **84**, 224421 (2011).

[35] M. P. Sharrock, Time dependence of switching fields in magnetic recording media (invited), J. Appl. Phys. **76**, 6413 (1994).

[36] See Supplemental Material at http://link.aps.org/supplemental/10.1103/PhysRevB.100.144435 for the evaluation of two-dimensional (2D) magnetization configuration on increasing the applied magnetic field for LC = 400 nm.

[37] See Supplemental Material at http://link.aps.org/supplemental/10.1103/PhysRevB.100.144435 for the evaluation of 2D magnetization configuration on increasing the applied magnetic field for LC = 800 nm.

[38] See Supplemental Material at http://link.aps.org/supplemental/10.1103/PhysRevB.100.144435 for the evaluation of 3D magnetization configuration on increasing the applied magnetic field for LC = 400 nm.

[39] See Supplemental Material at http://link.aps.org/supplemental/10.1103/PhysRevB.100.144435 for the evaluation of 3D magnetization configuration on increasing the applied magnetic field for LC = 800 nm.

[40] J. Leliaert, M. Dvornik, J. Mulkers, J. De Clercq, M. V. Milošević, and B. Van Waeyenberge, Fast micromagnetic simulations on GPU—Recent advances made with MUMAX3, J. Phys. D **51**, 123002 (2018).

[41] J. W. Kłos, D. Kumar, J. Romero-Vivas, H. Fangohr, M. Franchin, M. Krawczyk, and A. Barman, Effect of magnetization pinning on the spectrum of spin waves in magnonic antidot waveguides, Phys. Rev. B **86**, 184433 (2012).

[42] V. V. Kruglyak, C. S. Davies, V. S. Tkachenko, O. Y. Gorobets, Y. I. Gorobets, and A. N. Kuchko, Formation of the band spectrum of spin waves in 1D magnonic crystals with different types of interfacial boundary conditions, J. Phys. D **50**, 094003 (2017).

[43] R. Wolfe, *Applied Solid State Science. Volume 1: Advances in Materials and Device Research* (Elsevier Science, Amsterdam, 2013).

[44] D. F. Zhang and H. A. Stone, Drop formation in viscous flows at a vertical capillary tube, Phys. Fluids **9**, 2234 (1997).

[45] J. Brandão, D. A. Dugato, R. L. Seeger, J. C. Denardin, T. J. A. Mori, and J. C. Cezar, Observation of magnetic skyrmions in unpatterned symmetric multilayers at room temperature and zero magnetic field, Sci. Rep. **9**, 4144 (2019).

[46] D. Suess, C. Vogler, F. Bruckner, P. Heistracher, F. Slanovc, and C. Abert, Spin torque efficiency and analytic error rate estimates of skyrmion racetrack memory, Sci. Rep. **9**, 4827 (2019).

[47] A. Bernand-Mantel, L. Camosi, A. Wartelle, N. Rougemaille, M. Darques, and L. Ranno, The skyrmion-bubble transition in a ferromagnetic thin film, SciPost Phys. **4**, 027 (2018).

[48] F. Büttner, I. Lemesh, and G. S. Beach, Theory of isolated magnetic skyrmions: From fundamentals to room temperature applications, Sci. Rep. **8**, 4464 (2018).

[49] K. Wang, L. Qian, S.-C. Ying, G. Xiao, and X. Wu, Controlled modification of skyrmion information in a three-terminal racetrack memory, Nanoscale **11**, 6952 (2019).

[50] Y. Liu, N. Lei, C. Wang, X. Zhang, W. Kang, D. Zhu, Y. Zhou, X. Liu, Y. Zhang, and W. Zhao, Voltage-driven high-speed skyrmion motion in a skyrmion-shift device, Phys. Rev. Appl. **11**, 014004 (2019).

[51] M. Mruczkiewicz, P. Gruszecki, M. Zelent, and M. Krawczyk, Collective dynamical skyrmion excitations in a magnonic crystal, Phys. Rev. B **93**, 174429 (2016).

[52] S. Saha and M. Zelent, Formation of Néel type skyrmions in an antidot lattice with perpendicular magnetic anisotropy (Version 1.0), https://doi.org/10.5281/zenodo.3478883 (2019).

4.6 Edge localization of spin waves in antidot multilayers with perpendicular magnetic anisotropy (under review in Phys. Rev. B)

4.6.1 Introduction

In the paper, we presented results regarding the spin-wave dynamics in nanoscale antidot lattices based on Co/Pd multilayers with perpendicular magnetic anisotropy. In collaboration with prof. Anjan Barman group from Kolkata, we combined time-resolved magneto-optical Kerr effect measurements with micromagnetic simulations to demonstrate that the variation of the antidot shape introduces significant change in the spin-wave spectra, especially in the lower frequency range. By performing micromagnetic simulations, we found that additional peaks observed in the measured spectra are related to narrow shell regions around the antidots, where the magnetic anisotropy is reduced due to the Ga^+ ion irradiation during the focused ion beam milling process of the antidot fabrication.

In this publication, the Author has performed all of the numerical simulations in collaboration with bachelor student Radek Szwierz based on the Mumax3 software. He has been participated in the analysis and discussion of the results and has prepared Figures 1, 3, 5, 6, 7. Moreover, he took part in the manuscript writing and been involved in the manuscript evaluation.

Number of Ministerial points: 140.
Impact Factor: 3.736

Edge localization of spin waves in antidot multilayers with perpendicular magnetic anisotropy

S. Pan[1*], S. Mondal[1*], M. Zelent[2], R. Szwierz[2], S. Pal[1], O. Hellwig[3,4], M. Krawczyk[2], and A. Barman[1]
[1]Department of Condensed Matter Physics and Material Sciences, S. N. Bose National Centre for Basic Sciences, Block JD, Sector III, Salt Lake, Kolkata 700 106, India
[2]Faculty of Physics, Adam Mickiewicz University, Umultowska 85, 61-614 Poznań, Poland
[3]Institute of Physics, Chemnitz University of Technology, Reichenhainer Straße 70, D-09107 Chemnitz, Germany
[4]Institute of Ion Beam Physics and Materials Research, Helmholtz-Zentrum Dresden-Rossendorf, 01328 Dresden, Germany
Email: krawczyk@amu.edu.pl

Abstract

We study the spin-wave dynamics in nanoscale antidot lattices based on Co/Pd multilayers with perpendicular magnetic anisotropy. Using time-resolved magneto-optical Kerr effect measurements we demonstrate that the variation of the antidot shape introduces significant change in the spin-wave spectra, especially in the lower frequency range. By employing micromagnetic simulations we show that additional peaks observed in the measured spectra are related to narrow shell regions around the antidots, where the magnetic anisotropy is reduced due to the Ga^+ ion irradiation during the focused ion beam milling process of the antidot fabrication. The results point at new possibilities for exploitation of localized spin waves in out-of-plane magnetized thin films, which are easily tunable and suitable for magnonics applications.

I. Introduction

Spin-wave (SW) dynamics in antidot lattices (ADLs), i.e., ferromagnetic thin films with a regular two-dimensional array of holes, was extensively studied during the past decade[1,2,3,4,5]. The investigations were focused on soft ferromagnetic materials with in-plane magnetization. In this case, the properties of SWs controlled by the pattern are additionally affected by the demagnetizing field, which introduces an inhomogeneous potential for SWs.[6] In particular, at the edges of antidots the demagnetizing field decreases the internal magnetic field creating favorable conditions for SW localization.[7] The effects of ordered arrays, inhomogeneous demagnetizing field, edge modes, and configurational magnetic anisotropy in the in-plane magnetized ADL make the spectra quite complex[8,9,10] with rich physics,[11,12] but difficult for practical exploitation in magnonic devices.

In thin films with out-of-plane magnetization the forward volume SW dispersion relation is isotropic, offering better prospect for direct translation of various ideas from photonics into magnonics.[13,14,15] Moreover, a full magnonic band gap has been theoretically predicted,[16] and a fast SW guiding along a defect in perpendicularly magnetized ADL was experimentally demonstrated.[17] However, to saturate a ferromagnetic film in the out-of-plane direction, an external magnetic field exceeding its demagnetizing field is required. Ferromagnetic thin films and multilayers with perpendicular magnetic anisotropy (PMA) allow to avoid this difficulty. Ferromagnetic thin films with PMA have already found applications in magnetic recording.

However, they are rarely explored in magnonics even though they have shown some promising potential[18].

PMA originates at the interface of ferromagnetic (FM) metals (like Co, Fe) and heavy metals (HM) (like Pt, Pd) and it decreases sharply with the increase in the layer thicknesses. FM/HM multilayers can cause a cumulative increase in PMA as well as provide sufficiently large FM layer thickness for convenient detection of its magnetic response. Interestingly, the FM/HM multilayers with structural inversion asymmetry have become a recent focus of the physics community due to the emergence of interfacial Dzyaloshinskii-Moriya interaction, which helps to stabilize chiral magnetization textures and introduces SW non-reciprocity.[19]

Here, we have investigated the SW excitations in ADLs carved into Co/Pd multilayers with PMA using time-resolved magneto-optical Kerr effect (TR-MOKE) microscopy. We study antidots arranged in a square lattice with four different shapes of antidots. We have observed very rich SW spectra which depend strongly on the antidot's shape. To explain the experimental results we had to assume a region around the antidot (shell) with reduced PMA which may occur due to the focused ion beam (FIB) milling during patterning of the antidots.[20] Consequently, the demagnetizing field aligns the magnetization around the antidots in the film plane forming an in-plane domain structure. The shape of the antidot determines the domain structure and thus also determines the SW spectra. The proposed scenario is confirmed in micromagnetic simulations.

The paper is organized as follows. In the next section (Sec. II) we have defined the ADL structure, describe the fabrication and measurement techniques, and the computational approach used in the numerical simulations. In Sec. III, we describe the experimental data and support them with numerical results. The summary and possible usefulness of our findings are discussed in the last section (Sec. IV).

II. Structure and methods

The [Co(0.75 nm)/Pd(0.9 nm)]$_8$ ML structures (shown in Fig. 1) were deposited by dc magnetron sputtering using a confocal sputter up geometry with the targets tilted and arranged in a circle around a center target (Pd) [21, 22]. The substrate, which rotates during deposition at 3 Hz, is at the focal point of the targets. The base pressure of the deposition chamber was 2 × 10^{-8} mbar and the deposition was performed at 4 μbar of Ar pressure at room temperature. The ADLs are fabricated by focused ion beam (FIB) milling of the Co/Pd ML using liquid Ga^+ ion at 30 kV voltage and 20 pA beam current, which produces a spot size of about 10 nm. For creating the ADLs, first we create a pattern of antidots having desired shape on the ML sample. In our case, the four following shapes were investigated: triangles (T), squares (S), diamonds (Di) and circles (C), all arranged in a square lattice with slight differences between orthogonal lattice vectors, as indicated in the scanning electron microscope (SEM) images in Fig. 2(a). Subsequently, the material is milled out by exposing the patterned part to the Ga^+ ion beam source. Each pattern covers an area of 8 × 8 μm^2. The initial milling is done by using a raster scan of the focused ion beam in a single pass, which is followed by cleaning the residual materials from the ADLs in multipass (about 200 passes). The measured values of the lattice constant a_1 and a_2 along the x and y axis, respectively, the size of the antidots D (which corresponds to the side length in T, S or Di antidots and diameter for C antidots) from the SEM images are shown in Fig. 2(a). For the four samples, the values of the structural parameters of the four ADLs are shown in Table 1.

Table 1: Structural parameters of four different ADLs as obtained from the SEM images.

Sample	D(nm)	a_1(nm)	a_2(nm)	Filling Fraction
Circle (C)	209	496	502	0.86
Square (S)	175	460	472	0.86
Triangle (T)	185	490	450	0.93
Diamond (Di)	190	484	510	0.85

All structures have similar filling fractions defined as a ratio of the ferromagnet area to the area of the unit cell S_{Py}/a_1a_2.

The magnetization dynamics of the ADLs were measured by a custom-built TR-MOKE microscope in a two-colour optical pump-probe geometry [23]. The second harmonic ($\lambda = 400$ nm, spot size ~ 1 µm, fluence = 18 mJ cm^{-2}) of a Ti-sapphire oscillator laser was used to excite the dynamics, whereas the time delayed fundamental laser ($\lambda = 800$ nm, spot size ~ 800 nm, and fluence 2.5 mJ cm^{-2}) was used to probe the dynamics. The two beams were made collinear before being incident on the sample through a single microscope objective with numerical aperture of 0.65. A piezo-electric scanning *x-y-z* stage is used to locate the pump and the probe beams at the central region of each array during the measurement. The back-reflected probe beam is collected by the same microscope objective and is analyzed to measure the polar Kerr rotation by an optical bridge detector as a function of the time-delay between the pump and probe beams. A bias magnetic field ($H = 2.23$ kOe) is applied at a small angle (~ 10°) to the surface normal of the sample.

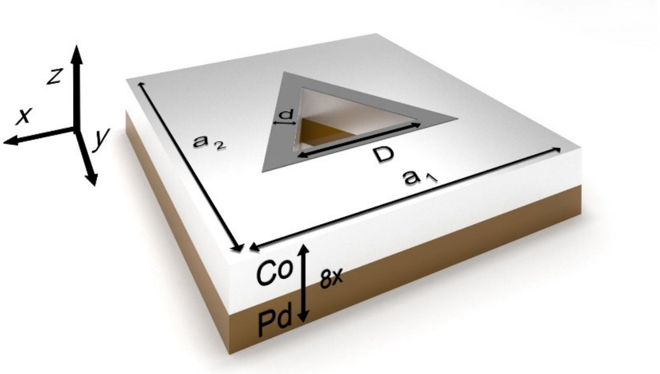

Fig. 1. A schematic of the multilayered ADL structure composed of Co and Pd layers under investigation and the definition of the coordinate system used throughout the paper. Here the antidot has a triangle shape with side length D and the shell with width d around it with reduced PMA is marked by the grey color. a_1 and a_2 are the x and y lattice constants of the antidot array, respectively.

To interpret the experimental results we performed micromagnetic simulations.[24] We assumed homogeneous material across the thickness with the effective parameters taken from the literature,[21] $K_u = 4.5 \text{ x } 10^5$ J/m^3, $M_S = 0.81 \text{ x } 10^6$ A/m, exchange constant $A = 1.3 \text{ x } 10^{-11}$ J/m, and gyromagnetic ratio $\gamma = 187 \text{ x } 10^9$ rad GHz/T. The damping was neglected in the simulations. The simulations have been performed for the unit cell with dimensions obtained from the SEM images after applying periodic boundary condition along the *x*- and *y*-axis. The discretization for all structures was fixed to 1 x 1 x 4.4 nm^3.

The stabilization of the magnetization configuration was obtained in the following steps. We assumed an uniform shell with constant width and shape corresponding to the shape of the respective antidots, where the magnetic anisotropy was reduced to zero. The initial magnetization of each cell was set to a random magnetization, except the shell, where the orientation of the magnetization was forced into either a vortex state, or alternatively into a head-to-head and tail-to-tail domain wall state in the shell around the antidot. In the following step the system was relaxed at magnetic field equal to 2.23 kOe. To excite SWs we use a microwave magnetic field h_{mf} directed along the *x* axis. h_{mf} was uniform in each unit cell with the shape of the sinc function in the time domain with cutting frequency f_c = 25 GHz and amplitude 15 Oe. The assumed conditions are close to the detection of SWs with TR-MOKE, where the width of the probe beam is larger than the unit cell.

Results

Time-resolved traces from the TR-MOKE measurements are presented in Fig. 2(b), while their fast Fourier transformed (FFT) spectra are presented in Fig. 2(c). The vertical dashed line indicates the frequency (10.6 GHz) of the SW measured from the unpatterned ML film. In ADLs, the most intense peak (marked as '1') changes only slightly with the change in the antidot's shape (10.30, 10.80, 10.13 and 10.80 GHz for C, S, T and Di, respectively), but the number and position of the peaks with lower intensity vary significantly. For the C-antidot there are two peaks relatively close to each other at 8.25 and 10.30 GHz. For the S-antidot also only two peaks (7.25 and 10.80 GHz, marked as 3 and 2, respectively) appear. However, for the T-antidot three clear peaks appear, two with smaller intensity at 2.58 and 7.73 GHz, and an intense peak at 10.13 GHz. The richest spectra is measured for the Di antidot, which consists of a set of five peaks (5.15, 6.70, 8.25, 9.28 and 10.82 GHz) with varying intensities, out of which two peaks have comparable intensity.

To elucidate the type and origin of the measured SW excitations we have performed micromagnetic simulations in samples with dimensions as extracted from the SEM images in Fig. 2(a) at an applied magnetic field of 2.23 kOe. For all four ADLs we obtained a single peak spectrum with only slight changes of the peak position between ADLs with different antidot shape (10.21, 10.24, 10.21 GHz for C, S and D, respectively). The spatial distribution of the SW amplitude extracted from the micromagnetic simulations reveals the fundamental mode, i.e., the mode with the in-phase magnetization oscillations in the entire sample. The slight variation of the fundamental mode frequency with the variation in the antidot shape is reasonable, considering that the ferromagnetic material occupies about 85% of the area, independent of the structure. However, these simulation results do not explain the experimental spectra in Fig. 2(c). This indicates the presence of a missing factor crucial for the observed multi-mode SW excitations, which has not been included in the simulation.

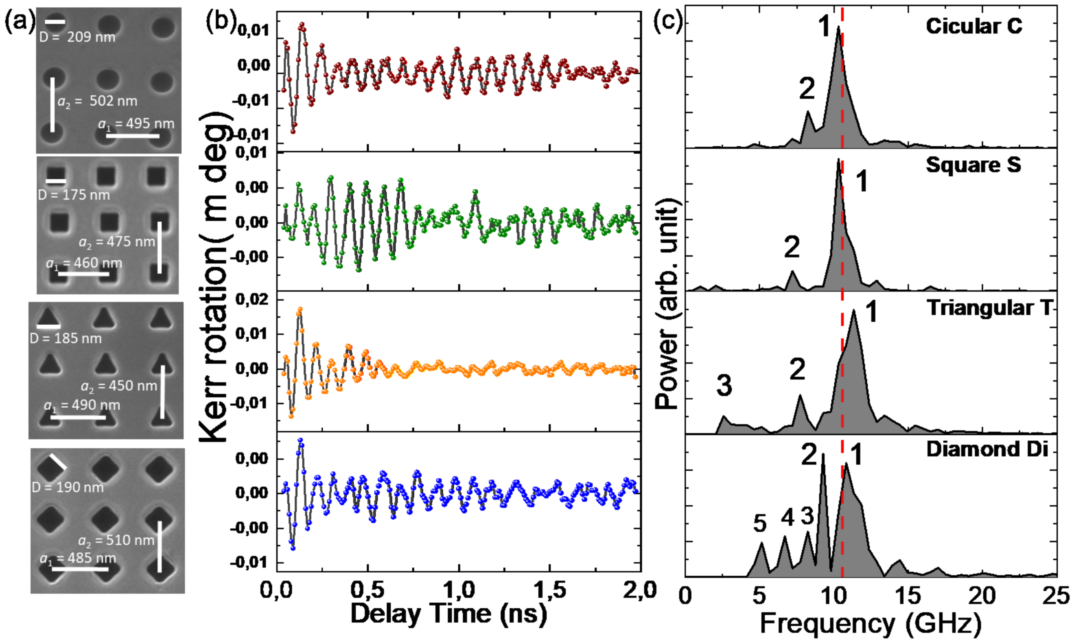

Fig. 2. (a) The SEM images of the four types of ADLs investigated in the paper. (b) TR-MOKE signal after subtracting a bi-exponential background and (c) its FFT spectra at $H = 2.23$ kOe for ADLs with different shapes of the antidots: circular C, square S, triangles T and diamond Di. The vertical red-dashed line points at the SW in the plain ML film.

The presence of additional peaks below the frequency of the fundamental mode points at the lowering of magnetic anisotropy or saturation magnetization, as both these two factors can decrease the frequency of SWs. A previous study indicated[21] that these two magnetic properties near the antidot edges in PMA multilayers can be strongly affected during the fabrication process. Indeed, in the literature we have found confirmation that light ion irradiation can affect the magnetic properties in PMA multilayers. In ref. [25] the decrease of PMA due to interface roughening and alloy formation caused by ion irradiation in Co/Pt ML systems has been demonstrated. The FIB irradiation has also been used to control the magnetic anisotropy in multilayers with PMA.[26,27] In our case, during the process of ion milling of the Co/Pd MLs for the creation of the antidots some scattered ions may have penetrated through the sidewalls of the antidots, causing a degradation of the magnetic properties over a narrow rim-like region around the antidots. These rim-like region around the antidots (shells) cover a small fraction of the ADL area. For instance, a shell with width, $d = 10$ nm around a C-type antidot will constitute only 3.2% of the ML area. The interesting question is, whether the MOKE signal from such a small area collected during TR-MOKE measurement can have significant intensity as compared to the fundamental mode occupying over 80% of the surface area? To check this, we performed simulations with $K_u = 0$ in the $d = 10$ nm wide shell, while keeping other parameters unchanged.

The results are shown in Fig. 3. The SW spectra [Fig. 3(a)] is very close to the TR-MOKE result presented in Fig. 2(b). There are two intense peaks, one with higher intensity at 10.2 GHz (marked as ii, close to the resonance peak in the plain ML), the other one (i) at 8.3 GHz. Other peaks of smaller intensity also appear, but as they were not detected in the measurements they will not be analyzed here. The ground state magnetic configuration in the unit cell is shown in Fig. 3(b), where the white color means the out-of-plane magnetization, and the color indicates orientation of the magnetization in the film plane. It becomes clear, that lack of the PMA in the shell region allows the demagnetizing field to align the magnetization into an in-plane closure domain structure (like a vortex) around the antidots. The extracted amplitude profiles and phase of SWs shown in Fig. 3(c-f) demonstrate, that the low frequency mode (i) has its amplitude concentrated in the area of the decreased anisotropy, known as the edge SW mode. The mode (ii) at 10.2 GHz has its amplitude spreading over the whole area, but with an out-of-phase contribution from the magnetization precession in the shell. Importantly, magnetization precession in the shell generates much larger amplitude of the dynamical out-of-plane component of the magnetization than the magnetization in other part of the ML which is normal to the film plane or slightly tilted from this direction. As the TR-MOKE signal is proportional to the out-of-plane component of the dynamic magnetization (polar MOKE geometry), the peak related to the SW edge mode appears with significant intensity as compared to the intensity of the fundamental mode. Moreover, the collective response of the fundamental mode in the measurements is additionally decreased due to the negative contribution of the out-of-phase

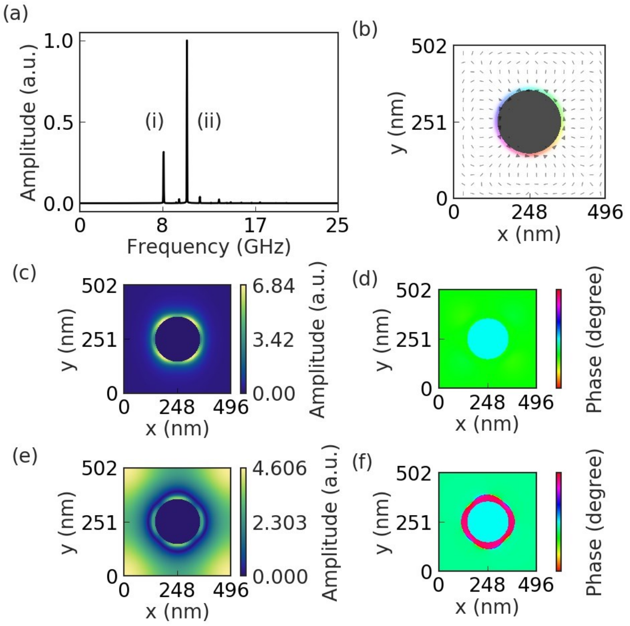

Fig. 3. (a) The simulated spectra of SWs in the C antidot with the zero PMA value in the shell of 10 nm width around the antidot, with $H = 2.23$ kOe. (b) The static configuration of the magnetization stabilized in the structure. (c, e) The amplitude of the out of plane component of the dynamical part of the magnetization, and (d, f) the phase of high intensity SWs at 8.3 and 10.2 GHz, indicated as i and ii in (a), respectively.

oscillations in the shells, bringing the fundamental mode intensity level close to the edge mode intensity level.

To clarify the influence of the relative intensities of the edge and fundamental SW modes, we performed simulations for different *d* values for the sample C. We found a nonlinear dependence (Fig. 4) and observed a mode crossover of the two most intense peaks with increasing *d*. At small *d*, the higher frequency peak appears with higher intensity, while for larger *d* intensity becomes higher in the lower frequency mode, the crossover occurs at $d \approx 12$ nm. Interestingly, we do not observe a crossing of the frequency peaks in Fig. 4, rather an anti-crossing is observed, which indicates a hybridization of the edge and fundamental mode, justifying the mixed mode profile in Fig. 3(e). We need to stress, that the interaction between these modes depends on many parameters, including the profile of the anisotropy increase from the antidot edge and the variation of other magnetic parameters in the shell, which could not be experimentally measured. Consequently, the study of these dependences are out of the scope of this paper.

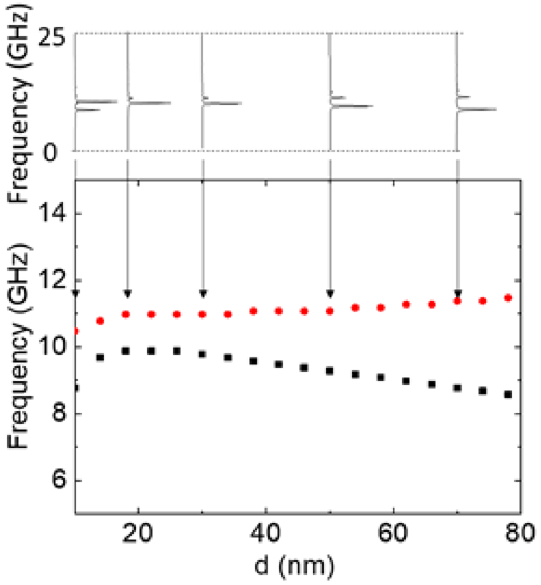

Fig. 4. Simulated spectra (top panel) and the frequency of the most intense modes (bottom panel) as a function of the width of the shell *d* around the antidots in the sample C.

The numerical spectra for the S, T and Di samples with 10 nm shell having zero PMA, together with the static magnetization configurations, and selected SW profiles are shown in Fig. 5. Similar to the C antidots, the static magnetization forms closure domains in the shells, aligned tangentially to the antidot edges. Due to different shapes, their magnetization configurations are different: for the S and Di there are four domains along the antidot edges with four domain walls at the vertices of the square. For T there are 3 domains separated by domain walls.

The calculated spectrum for the S-antidot has two resonant peaks of high intensity at 8.33 GHz (i) and 10.54 GHz (iii), along with a number of peaks having smaller intensity [Fig. 5(a)]. The spectrum is very close to the experimental result shown in Fig. 2(c). The lower frequency mode [8.33 GHz in Fig. 5(a)] (i) has an amplitude in the shell with maximum at the vortices of the square antidot. The most intense peak (iii) is the fundamental mode, while the modes of low intensity at 9.64 and 9.8 GHz (ii) are the excitations with the amplitude concentrated in the domains along the antidot side walls. A qualitative agreement between the simulated and the experimental results [Fig. 2(c)] is obtained also for the T-antidot structure [Fig. 5(b)]. There are two moderately intense resonant peaks at 6.95 GHz (i) and 7.32 GHz, two very weak peaks around 8.8 GHz, one reasonably intense peak at 9.7 GHz (ii) all of which are well separated from the most intense fundamental mode at 10.21 GHz (iii). According to the calculated profiles the two SWs of lowest frequency have amplitude concentrated in the domain walls at the vertices (like the mode (i) at 6.95 GHz with the amplitude at the top vertex shown in the inset). The modes at 8.8 and 9.73 (ii) GHz are concentrated in the domains along the triangle antidot sides. We checked that an increase in d from 10 to 20 nm results in the low frequency modes shifting toward the fundamental mode, which makes the spectra even closer to the experimental one. Interestingly, in Ref. [28] three-peak SW spectra were detected for the in-plane magnetized isolated triangular rings made of Py. Although the width of the rings (380 nm) was almost 40 times more than the shell assumed in our ADLs, the spectra and the mode profiles are qualitatively very similar.

The spectra for Di-ADL is shown in Fig. 5(c). The most intense peak (iii) related to the fundamental mode is at 10.41 GHz. The mode of lowest frequency (i) is at 7.37 GHz and it corresponds to the vertex excitation. The low intensity mode (ii) at 8.6 GHz is a SW in the domains of the shell. Overall the spectrum of Di-ADL is similar to the S-ADL spectra. Because, the shape of the antidots in both structures are almost the same, the differences between the S and Di spectra can be related to the effects of interaction between different antidots in the lattice. This suggests collective dynamics, not only of the fundamental mode, but also of the edge SW modes. Nevertheless, the simulated spectrum of Di-ADL structure does not match with the experimental spectrum shown in Fig. 2(c), where 5 resonant modes are clearly visible. An increase of shell width in the simulation changes the relative intensities of the two modes, essentially retaining the two peak spectra, as can be observed in Fig. 6(a) for a Di-ADL structure with $d = 20$ nm.

To underpin the origin of the discrepancies between the experimental and the simulated spectra for the Di-ADL type, we revisit the ground state magnetization configuration and the SW spectra measured in ring structures of square, diamond and rectangular shapes made of soft ferromagnetic materials.[29,30,31] Those reports state that the closure domain is a magnetic ground state configuration, but at remanence other magnetic patterns can also form. The latter include configurations with the head-to-head and tail-to-tail domain walls trapped in the vertices of the shells around the antidots. The change in the magnetic configuration is manifested in the variation of the SW spectra. Apart from having much smaller width of the shells assumed in our ADLs as compared with the reported nanorings (tens of times narrower), different magnetic configurations realized in the shells probably lead to an increase in the number of the SW modes in our ADLs. Indeed, during measurements we do not control the magnetization alignment in the shells, closure domain or configurations with the head-to-head and tail-to-tail domain walls at the vertexes can be stabilized at remanence or at small magnetic field. In Fig. 6(b), we show the SW spectra for Di-ADL with $d = 20$ nm shell, with one head-to-head and tail-to-tail domain walls in opposite vertexes of the diamond. Interestingly, this spectra is different from the spectra in Fig. 6(a). In Fig. 6(b), there are additional resonant modes at 6.2 GHz (i) and above 9.6 GHz (ii), with amplitude concentrated at vertices with head-to-head and tail-to-tail domain walls, and in the domains respectively, making this spectra closer to the experimental spectra.

The difference between experimental and numerical results can be related also to the tilted external magnetic field form the surface normal orientation. For homogeneous ML and ADLs, this has a minor effect. However, in the shell with the in-plane closure domain structure, the magnetic field orientation breaks the domain symmetry which can result in increasing number of modes. This scenario found confirmation in the results of micromagnetic simulations presented in Fig. 6(c), where the SW spectra for the Di-ADL structure with the magnetic field tilted by 10° from the surface normal direction towards the *x*-axis is presented. The closure domain structure was relaxed in the shell and we found a number of low intensity resonances at lower frequencies (below 9 GHz). The mode (i) of the largest intensity at 10.2 GHz, shown in the inset of Fig. 6(c), can be considered as a fundamental mode hybridized with the asymmetric edge mode, whose amplitude is concentrated in the domains with and without nodal lines along the opposite antidot edges. Also the other simplifications made in our model can result in discrepancies between simulation and experimental results. As mentioned above, in the real sample the value of anisotropy and saturation magnetization may vary continuously, while in the simulation these quantities are assumed constant. However, these properties could not be experimentally detected so far, and hence further experimental and theoretical investigations are necessary to clarify the validity and relative contributions of the proposed effects.

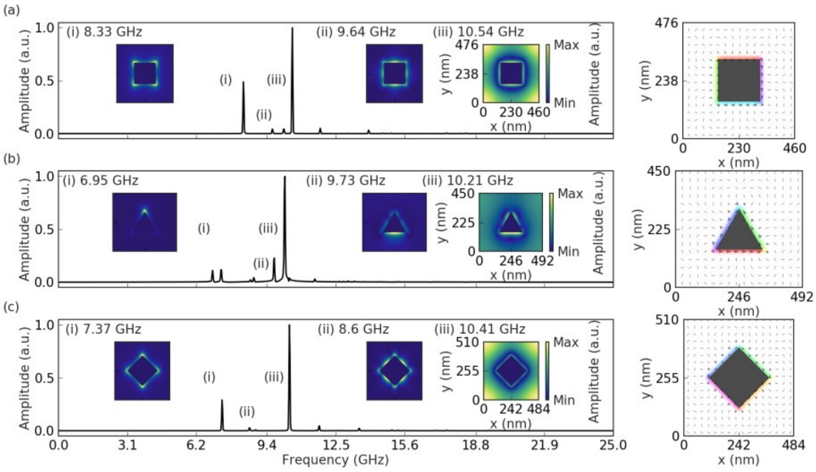

Fig. 5. Simulated SW spectra for the S-, T- and Di-ADL structure with $d = 10$ nm with the respective static magnetization configurations and the profiles of the most intense lines in the spectra. The out of plane magnetic field $H = 2.23$ kOe was used.

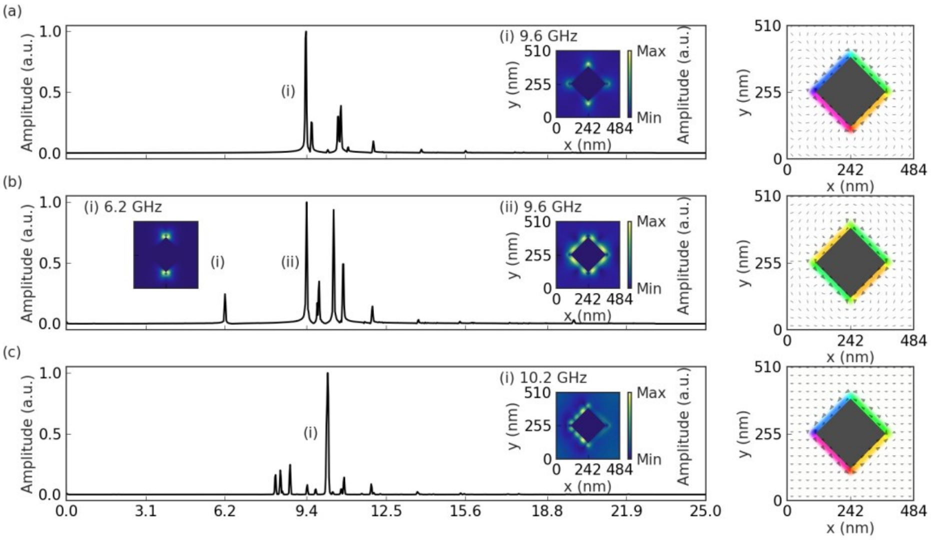

Fig. 6. The spectra for the Di-ADL structure with the shell of the $d = 20$ nm width. (a) The magnetization in the shell forms the closure domain structure, and (b) the head-to-head and tail-to-tail domain walls are present in the bottom and top of the shell. (c) The static magnetic field has been tilted by 10° from the normal direction towards the *x* axis, the magnetization in the shell form the closure domain structure. In simulations the magnetic field of 2.23 Oe was assumed.

Conclusions

We have investigated experimentally the SW excitations in ADLs based on Co/Pd multilayers having PMA with antidots of different shapes using TR-MOKE microscope. With the aid of micromagnetic simulations we propose that the emergence of narrow (~10 nm wide) shells with reduced PMA around the antidots are responsible for the observed lower frequency peaks below the fundamental mode frequency, in the SW spectra. The shells with reduced PMA are probably formed due to Ga^+ ion irradiation during the patterning process. In those shells the magnetization stabilizes in the film plane, contributing strongly to the measured TR-MOKE signal, which is proportional to the out of plane component of the dynamical magnetization. The different magnetization states in the shells form suitable conditions for formation of different kinds of edge localized SW modes.

We speculate, that the magnetization in the shells around the antidots of the triangle, square and diamond shapes can stabilize in different configurations at remanence, similar to the isolated rings with respective shapes, but having larger width and made of the soft ferromagnetic materials. The variety of the magnetization states in the shells gives opportunity for further exploitation of the edge localized SW spectra, which can be controlled by the magnetization configuration. This can be achieved by developing protocols of the remagnetization with the in-plane component of the external magnetic field, like in the case of the isolated rings based on soft ferromagnetic materials of circular, triangle, square and diamond shapes. [32,33,34] Furthermore, the role of interactions between the edge localized SW excitations, and other types of SWs present in ADL, open the prospect for exploiting collective dynamics in these new kinds of ADLs.

Acknowledgements: AB acknowledges S. N. Bose National Centre for Basic Sciences for funding (grant no.: SNB/AB/18-19/211). SM acknowledges DST for INSPIRE fellowship (award number: IF140998). MZ acknowledges support from National Science Center of Poland grant no UMO-2017/27/N/ST3/00419. The simulations were partially performed at the Poznan Supercomputing and Networking Center (Grant No. 398).

References

* SP and SM contributed equally to the paper.

---

[1] S. Tacchi, P. Gruszecki, M. Madami, G. Carlotti, J. W. Kłos, M. Krawczyk, A. Adeyeye, and G. Gubbiotti, Sci. Rep 5, 10367 (2015).

[2] S. Neusser, G. Duerr, H. G. Bauer, S. Tacchi, M. Madami, G. Woltersdorf, G. Gubbiotti, C. H. Back, and D. Grundler, Phys. Rev. Lett. **105**, 067208 (2010).

[3] B. Lenk, H. Ulrichs, F. Garbs, and M. Münzenberg, Phys. Rep. **507**, 107 (2011).

[4] M. Mansurova, J. von der Haar, J. Panke, J. Walowski, H. Ulrichs, and M. Münzenberg, J. . Phys.: Condens. Matter **29**, 214001 (2017).

[5] S. Mamica, X. Zhou, A. Adeyeye, M. Krawczyk, and G. Gubbiotti, Phys. Rev. B **98**, 054405 (2018).

[6] R. Mandal, P. Laha, K. Das, S. Saha, S. Barman, A. K. Raychaudhuri, and A. Barman, Appl. Phys. Lett. **103**, 262410 (2013).

[7] C.-L. Hu, R. Magaraggia, H.-Y. Yuan, C. S. Chang, M. Kostylev, D. Tripathy, A. O. Adeyeye, and R. L. Stamps, Appl. Phys. Lett. **98**, 262508 (2011).

[8] R. Zivieri, S. Tacchi, F. Montoncello, L. Giovannini, F. Nizzoli, M. Madami, G. Gubbiotti, G. Carlotti, S. Neusser, G. Duerr, and D. Grundler, Phys. Rev. B **85**, 012403 (2012).

[9] M. Zelent, N. Tahir, R. Gieniusz, J. W. Kłos, T. Wojciechowski, U. Guzowska, A. Maziewski, J. Ding, A. O. Adeyeye, and M. Krawczyk, J. Phys D: Appl. Phys. **50**, 185003 (2017).

[10] M. Krawczyk, S. Mamica, M. Mruczkiewicz, J. W. Klos, S. Tacchi, M. Madami, G. Gubbiotti, G. Duerr, and D. Grundler, J. Phys. D: Appl. Phys. **46**, 495003 (2013).

[11] S. Neusser, G. Duerr, S. Tacchi, M. Madami, M.L. Sokolovskyy, G. Gubbiotti, M. Krawczyk, and D. Grundler, Phys. Rev. B **84**, 094454 (2011);

[12] S. Choudhury, S. Majumder, S. Barman, Y. Otani, and A. Barman, Phys. Rev. Applied **10**, 064044 (2018).

[13] R. Bali, M. Kostylev, D. Tripathy, A. O. Adeyeye, and S. Samarin, Phys. Rev. B **85**, 104414 (2012).

[14] M. Zelent, M. Mailyan, V. Vashistha, P. Gruszecki, O.Y. Gorobet, Y.I. Gorobets, and M. Krawczyk, SWs collimation using flat metasurface, (to be published).

[15] P. Gruszecki, J. Romero-Vivas, Yu. S. Dadoenkova, N. N. Dadoenkova, I. L. Lyubchanskii, K. Guslienko, and M. Krawczyk, Phys. Rev. B **92**, 054427 (2015).

[16] T. Schwarze, R. Huber, G. Duerr, and D. Grundler, Phys. Rev. B **85**, 134448 (2012).

[17] T. Schwarze and D. Grundler, Appl. Phys. Lett. **102**, 222412 (2013).

[18] S. Klingler, P. Pirro, T. Brächer, B. Leven, B. Hillebrands, and A. V. Chumak, Appl. Phys. Lett. 106, 212406 (2015).

[19] H. Bouloussa, J. Yu, Y. Roussigné, M. Belmeguenai, A. Stashkevitch, H. Yang, and S. M. Chérif, J. Phys. D: Appl. Phys. **51**, 225005 (2018).

[20] S. Pal, J. W. Klos, K. Das, O. Hellwig, P. Gruszecki, M. Krawczyk, and A. Barman, Appl. Phys. Lett. **105**, 162408 (2014).

[21] S. Pal, B. Rana, O. Hellwig, T. Thomson, and A. Barman, Appl. Phys. Lett. **98**, 082501 (2011).

---

[22] O. Hellwig, T. Hauet, T. Thomson, E. Dobisz, J. D. Risner-Jamtgaard, D. Yaney, B. D. Terris, and E. E. Fullerton, Appl. Phys. Lett. **95**, 232505 (2009).

[23] B. Rana and A. Barman, SPIN 3, 1330001 (2013).

[24] A. Vansteenkiste, J. Leliaert, M. Dvornik, M. Helsen, F. Garcia-Sanchez, and B. Van Waeyenberge, AIP Advances **4**, 107133 (2014).

[25] T. Devolder, Phys. Rev. B **62**, 5794 (2000).

[26] A. Aziz, S. J. Bending, H. G. Roberts, S. Crampin, P. J. Heard, and C. H. Marrows, Phys. Rev. Lett. **97**, 206602 (2006).

[27] J. Fassbender and J McCord, J. Magn. Magn. Mater. **320**, 579 (2008).

[28] J. Ding, M. Kostylev, and A. O. Adeyeye, Appl. Phys. Lett. **100**, 062401 (2012).

[29] C. Banerjee, S. Saha, S. Barman, O. Rousseau, Y.C. Otani, and A. Barman, J. Appl. Phys. **116**, 163912 (2014).

[30] X. Zhu, P. Grütter, V. Metlushko, and B. Ilic, J. Appl. Phys. **93**, 7059 (2003).

[31] P. Vavassori, M. Grimsditch, V. Novosad, V. Metlushko, and B. Ilic, J. Appl. Phys. **93**, 7900 (2003).

[32] A. Imr, E. Varga, L. Ji, B. Ilic, V.Metlushko, G. Csaba, A. Orlov, G. H. Bernstein, and W. Porod, IEEE Trans. Magn. **42**, 3641 (2001).

[33] G. Bordignon, T. Fischbacher, M. Franchin, J. P. Zimmermann, P. A. J. de Groot, and Hans Fangohr, J. Appl. Phys. **103**, 07D932 (2008).

[34] M. D. Mascaro, H. S. Körner, C. Nam, B. G. Ng, and C. A. Ross, Appl. Phys. Lett. **98**, 252506 (2011).

Chapter 5

Important papers, but not included to the main topic of the thesis

5.1 Spin wave collimation using a flat metasurface

5.1.1 Introduction

In the manuscript, we demonstrated numerically a new idea for local control of the spin-wave phase delay. We proposed the few atomic layers thick interface between lateral sides of the two ferromagnetic films to control the spin-wave phase and use this finding to construct a flat metasurface for spin waves. The phase delay is controlled by the strength of the RKKY interlayer exchange coupling between the films, which depends on the interface width. We combine the phase-shift dependency along with the interface achieved by variation of the interface width with the lens equation to show the operation of the metalens for spin waves numerically. We concluded that these mechanisms of the magnetisation coupling between ferromagnets could also be exploited for designing magnonic metasurfaces and metalenses.

In this publication, all numerical simulations presented in this work were performed solely by the author of this thesis, while analytical calculations were performed in collaboration with dr Marina Mailyan. He also prepared all the figures and significantly contributed to the manuscript writing and manuscript evaluation.

Number of Ministerial points: 140.
Impact Factor: 6.970

Nanoscale

PAPER

View Article Online
View Journal | View Issue

Cite this: *Nanoscale*, 2019, **11**, 9743

Received 28th December 2018,
Accepted 19th April 2019

DOI: 10.1039/c8nr10484k

rsc.li/nanoscale

Spin wave collimation using a flat metasurface†

M. Zelent, *[a] M. Mailyan, [b] V. Vashistha, [a] P. Gruszecki, [a] O. Y. Gorobets, [b] Y. I. Gorobets [b,c] and M. Krawczyk [a]

In this paper, we show that the phase shift of spin waves propagating in the plane of the film can be controlled by a metasurface formed by an ultra-narrow non-magnetic spacer separating edges of the two thin ferromagnetic films. For this purpose, we exploit the strength of the exchange coupling of the RKKY type between the films which allows tuning the phase of the transmitted spin waves in the wide range of angles [$-\pi/2$; $\pi/2$]. We combined the phase-shift dependency along the interface with the lens equation to demonstrate numerically the metalens for spin waves.

Introduction

Spin waves (SWs) are promising data carriers for future logic devices, information processing and communication with low energy consumption, relatively high and flexible frequency operation, possible miniaturization down to the nanoscale,[1–4] and possible exploitation of unique wave phenomena.[5–8] However, still basic units, such as SW generators and detectors, SW waveguides, SW amplifiers or SW modulators, have to be further developed to demonstrate their useful performance.[9] Control of the phase of propagating SWs is expected to be one of the key elements in future magnonics, like it is in microwave technology, electronics, and photonics. To fulfill the requirements of miniaturization, the expected magnonic component shall be small, ideally shorter than the wavelength. An interesting idea to fulfill this condition comes from photonics, where ultra-thin slabs of sub-wavelength thickness, called metasurfaces (MSs), have been introduced. They promise valuable advantages in controlling the waves by spatial manipulation of the wavefront characteristics.

The MS concept is based on the phase gradient introduced by the specially arranged tiny elements of a sub-wavelength size as compared with the wavelength λ of the incident wave.[10] In optics, these tiny phase-shifting elements are mostly designed from metallic materials or dielectric resonators. They rely on subwavelength gratings, resonators, and waveguides, and they introduce geometric phase differences to tune the phase of the reflected or transmitted wave. Their working principle is well described with the generalized Snell's law[11] which takes into account an inhomogeneous phase change in the two-dimensional plane of the MS. Such structures are widely investigated for application to steer propagation of electromagnetic waves.[12–14] Originally designed at radiowave frequencies for radar and space communications,[15] MSs have been implemented to design many new planner devices at infrared and optical frequencies, such as an ultra-thin lens, vortex plates, polarization converters, color filters or holograms.[15–21]

In this paper, we propose a new concept of the MS for SWs based on the ultra-narrow interface between two thin ferromagnetic films. The working principle behind the proposed magnonic MS is based on the interlayer exchange coupling between magnetic films, which can be mediated by a non-magnetic metallic spacer between the edges of the films and had essentially the same physical origin as the Ruderman–Kittel–Kasuya–Yosida (RKKY) interaction. We showed analytically and numerically that such an ultra-narrow interface, of the width up to a few atomic planes, can effectively change the phase of the reflected and transmitted SWs having tens of nanometers wavelength. In particular, we demonstrate the magnonic MS allowing to focus the plane SWs in an arbitrary located focal point in the plane of the ferromagnetic film. It is a new approach with respect to the already demonstrated concepts of SW lenses basing the classical optic rules to focus the wave.[22–24]

Analytical model

Let's consider the system of two semi-infinite ferromagnetic thin films separated by an ultra-narrow interface along the y-axis with the uniform static external magnetic field $\mathbf{H}_0$ paral-

---

[a] *Faculty of Physics, Adam Mickiewicz University in Poznan, ul. Uniwersytetu Poznańskiego 2, Poznań, 61-614, Poland. E-mail: mateusz.zelent@amu.edu.pl*

[b] *Faculty of Physics and Mathematics, National Technical University of Ukraine "Igor Sikorsky Kyiv Polytechnic Institute", 37 Peremogy ave., 03056 Kyiv, Ukraine*

[c] *Institute of Magnetism, National Academy of Sciences of Ukraine, 36-b Vernadskogo st, 03142 Kyiv, Ukraine*

† Electronic supplementary information (ESI) available. See DOI: 10.1039/C8NR10484K

5.2 Spin-wave phase inverter upon a single nanodefect

5.2.1 Introduction

We study the spin wave (SW) transmission through Co-Fe-based waveguides by all-electrical spin-wave spectroscopy in the frequency range 1 - 20 GHz. Five Co-Fe waveguides were fabricated. One of them was left as-deposited for reference purposes, while a 120 nm-wide nanogroove was milled by FIB in the middle of each of four other waveguides. A vector network analyzer (VNA) was used to apply a radiofrequency signal to conventional coplanar waveguide one (CPW1) and detect the SW transmission at CPW2. Increasing the nanogroove depth from 0 to 35 nm and the in-plane bias magnetic field strength from 0 to 2.3 kOe, we have been able to continuously tune the spin-wave phase shift from 0 to π without a significant suppression of the SW transmission, see Fig. 3. Micromagnetic simulations revealed that the modification of magnetization under the groove due to implantation of Ga ions should be taken into account to explain such a large phase shift.

In this publication, all of the numerical simulations in Mumax3 has been performed solely by the author of this thesis. Author have been participated in the analysis and discussion of the results and in figure number 6 preparation. Moreover, he took part in the manuscript writing and been involved in the manuscript evaluation.

Number of Ministerial points: 200.
Impact Factor: 8.097

Spin-Wave Phase Inverter upon a Single Nanodefect

Oleksandr V. Dobrovolskiy,*[†,#] Roland Sachser,[†] Sergey A. Bunyaev,[‡] David Navas,[‡]
Volodymyr M. Bevz,[§,#] Mateusz Zelent,[‖] Wojciech Śmigaj,[⊥] Justyna Rychły,[‖] Maciej Krawczyk,[‖]
Ruslan V. Vovk,[§,#] Michael Huth,[†] and Gleb N. Kakazei[‡]

[†]Physikalisches Institut, Goethe University, 60438 Frankfurt am Main, Germany
[‡]IFIMUP-IN/Departamento de Física e AstronomiaUniversity of Porto, 4169-007 Porto, Portugal
[§]ICST Faculty, Ukrainian State University of Railway Transport, 61050 Kharkiv, Ukraine
[‖]Faculty of Physics, Adam Mickiewicz University in Poznań, Poznań 61-712, Poland
[⊥]Synopsys Northern Europe Ltd., Bradninch Hall, Castle Street, EX4 3PL Exeter, U.K.
[#]Physics Department, V. Karazin National University, 61077 Kharkiv, Ukraine

ABSTRACT: Local modification of magnetic properties of nanoelements is a key to design future-generation magnonic devices in which information is carried and processed via spin waves. One of the biggest challenges here is to fabricate simple and miniature phase-controlling elements with broad tunability. Here, we successfully realize such spin-wave phase shifters upon a single nanogroove milled by a focused ion beam in a Co−Fe microsized magnonic waveguide. By varying the groove depth and the in-plane bias magnetic field, we continuously tune the spin-wave phase and experimentally evidence a complete phase inversion. The microscopic mechanism of the phase shift is based on the combined action of the nanogroove as a geometrical defect and the lower spin-wave group velocity in the waveguide under the groove where the magnetization is reduced due to the incorporation of Ga ions during the ion-beam milling. The proposed phase shifter can easily be on-chip integrated with spin-wave logic gates and other magnonic devices. Our findings are crucial for designing nanomagnonic circuits and for the development of spin-wave nano-optics.

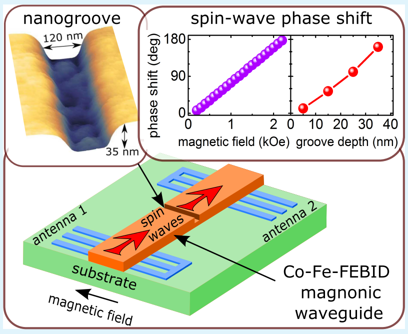

KEYWORDS: *nanomagnonics, spin waves, phase shift, focused electron beam-induced deposition, focused ion-beam milling*

INTRODUCTION

Spin waves, and their quanta magnons, can be used for carrying and processing of information without net transfer of electric charge.[1−3] Featuring low dissipation, magnonic devices based on spin-wave logic gates are being actively developed to expand the functionality of next-generation nanoelectronics and information processing. For instance, prototypes of a spin-wave-based NOT gate,[4] a majority gate[5] as well as exclusive-not-OR and not-AND gates based on a Mach−Zehnder-type interferometer[6] have been demonstrated experimentally. In these, logic information is encoded in the phase of spin waves, such that logic “0” corresponds to a certain phase $\phi^{(0)}$, whereas logic “1” is represented by the phase of $\phi^{(1)} = \phi^{(0)} + \pi$.[5] Spin-wave phase-setting elements are therefore important for magnonic information processing. Furthermore, the interest in tailoring the spin-wave phase in magnonics is urged by the implementation of concepts originating from optics. Here, the aim is to achieve steering of spin waves in conjunction with the miniaturization of a device while maintaining its high-frequency operation.[7] The emerging domain of spin-wave nano-optics[8] requires the generation and manipulation of spin-wave beams in the microwave frequency range, thus enabling realization of spin-wave fibers[9] and exploitation of refraction and reflection effects.[10−13]

The propagation of spin waves through areas with changed magnetization has been widely exploited in magnonic crystals.[14,15] In such crystals, which are media with periodically varying magnetic characteristics, spin waves exhibit rejection bands where the spin-wave propagation is prohibited. Under proper conditions, individual building blocks of magnonic crystals allow for control of the spin-wave amplitude and phase.[16] In particular, it was shown both experimentally and by numerical simulations that spin waves propagating in a magnetic film can pass through a region of a magnetic field inhomogeneity[17] or a mechanical gap.[18] Furthermore, spin waves were predicted to change their phase when passing through a magnetic domain wall in different branches of a ring[19] or when a local spin-polarized current is applied to a ferromagnetic stripe.[20] Due to experimental challenges, these approaches have not been realized so far. Further systems suggested as spin-wave phase shifters include magnetic dot arrays with a chessboard antiferromagnetic ground state,[21] multiferroic structures,[22] application of polarized light pulses,[23] electric fields,[24] nanomagnets,[25] and increasing signal power.[26]

Received: February 13, 2019
Accepted: April 22, 2019
Published: April 22, 2019

Chapter 6

Summary

6.1 Research presented in thesis

Magnonics is a relatively new field of physics which explores spin-wave phenomena on the nanoscale. It can be regarded as a magnetic analogue of electronics, photonics, phononics or plasmonics, with spin waves acting as information carriers, i.e. playing the same role as electrons, electromagnetic waves, acoustic waves or plasmon waves in electronic, photonic, phononic and plasmonic materials, respectively. Most of the effects characteristic for waves of the other types, including propagation, reflection, refraction, interference and focusing effects, have already been proved to occur for spin waves as well.

Taking into account above, the main aim of the thesis was to explore theoretically new concepts for modelling the magnetisation texture and spin-wave spectra of magnonic nanostructures and to acquire the knowledge necessary to understand new phenomena in magnonics and the physics of magnonic crystals. To realise this goal and to find answers for the questions of this thesis, the results of micromagnetic simulations and experimental measurements (in collaboration with experimental groups) have been presented. These were all performed to understand how geometry, magnetic parameters, the anisotropy of dipolar interactions, the coexistence of short-range (exchange) interactions and long-range (dipolar) interactions, external magnetic field influence on static and dynamic properties of magnetisation in complex nanostructures. Although complex magnetic textures have been studied theoretically and experimentally for over several decades, this complexity of phenomena, that have to be considered, is still challenging, and there are still many aspects that have not been fully described. The papers included in this thesis contribute to this field of research, creating new opportunities for further development of magnonics.

The results of the research are presented as the collection of the papers, which is preceded by Chapters 1-3, in which the background of the research is presented. In section 4.2 the equilibrium magnetic states and magnetization reversal processes of three different type of ADLs based on permalloy thin films with increased complexity of the unit cell: simple square ADL, bi-component ADL (with two antidots of different sizes int he unit cell) and wave-like ADL (formed by introducing the air gaps between smaller and larger antidots) were presented. These structures were governed by the interplay between anisotropy, the shape of antidots and lattice symmetry. We showed that, the direction of the external magnetic fiend or even small change in ADL pattern can significantly change the magnetisation reversal process. Furthermore we have found found the formation of regular 360° domain walls. Experimental results were interpreted and reproduced by micromagnetic simulations.

In section 4.3 the analysis and interpretation of the experimental data and numerical calculations concerning spin wave dynamics in three types of ADLs (the same as in section 4.2) were presented. The studies of ferromagnetic resonances spectra and dispersion relations obtained by Brillouin light scattering were performed. The results of the measurements were interpreted with the aid of the micromagnetic simulations and the plane wave method calculations. We found that the sensitivity of the FMR spectra on the orientation of the magnetic field is strongly dependent on the minor changes of the antidot pattern in the unit cell, even if the unit cell preserves the same symmetry. Authors showed, that the dispersion relations of SWs are significantly affected by the modification of the antidot pattern in the unit cell, even if this modification covers less than a few percents of the unit cell. Thus, the Authors found an answer for the first question of the thesis.

In section 4.4, the simulations of magnetic skyrmion stability in ultrathin magnetic multilayer nanodots with interfacial Dzyaloshinskii–Moriya exchange interaction were presented. In particular the influence of the magnetostatic interaction in circular multilayer nanodots on the stability. Authors show, that the skyrmions can be stabilised due to two different mechanisms, leading to the existence of two equivalent energetically possible skyrmions states in the same nanodot. Furthermore, the Authors showed that the skyrmion size could be switched by a magnetic field pulse. Thus the Author has found an answer for the second question of the thesis .

In section 4.5 a method for the nucleation and capture of magnetic skyrmions in an array of antidot lattice during the remagnetisation process were presented. The role of inhomogeneity in the total effective field produced by the antidot lattice has been presented as an important factor for the formation of skyrmions. The study was performed experimentally and numerically. With this the answer for the third question has been found .

In section 4.6 the spin wave excitations in ADLs based on Co/Pd multilayers having perpendicular magnetic anisotropy with antidots of different shape were studied using experimental and numerical methods. The impact for spin wave spectrum of the shell around the holes with reduced anisotropy were discussed.

Chapter 5 contains two papers with a significant Author contribution, but not related to the main topic of his thesis. In first paper of this chapter Author presents a new concept of the phase-shifting interface for spin waves based on the ultra-narrow interface between two thin ferromagnetic films based on the interlayer exchange coupling between magnetic films. The Author has also shown the concept of focusing the spin waves in thin cobalt film by ultra-narrow flat phase-shifting metasurface. The second paper shows the realisation of the tunable spin waves phase shifter upon a single nanogroove milled by a focused ion beam in a Co-Fe micro sized magnonic waveguide. Authors showed experimentally and numerically a technique whereby increasing the groove depth and the in-plane biasing magnetic field, they have continuously tuned the spin-wave phase. These results are the first step for the experimental implementation of the spin waves lens.

To summarise, the Author has demonstrated through the set of systematic investigations that the static and dynamic properties of the magnetization in ferromagnetic structures can be tuned by fabrication processes like magnetic parameters, geometry and nano structuralization. Changing even one of them leads to the creation of new and interesting properties. As a whole, this thesis demonstrates that non-uniformities in a magnetic configuration can be used to host skyrmions, excite and steer spin waves. The experimental and numerical results discussed in Chapter 4 collectively reveal that non-uniformities in either the magnetization and / or effective field give rise to a corresponding spatially-varying frequency of resonance. The Author shows that the micromagnetic simulations were successfully used to predict or understand the experimental measurements. Thus micromagnetic simulations are an essential tool for the exploration of magnetic systems on nanoscale. The results of this thesis hints to the few possible routes for the future investigations of the magnetization static and dynamics in micro and nanostructured ferromagnetic structures.

6.2 Outlook

One of the important parts of the field of magnonics still occupies investigations of isolated skyrmions and magnonic crystals. In the near future, Author aims to combine magnetic skyrmions, magnonic crystals and spin ways approaching applications in logic and microwave communication systems operating at microwave frequencies on the nm length scale. He wants to study the coupling between isolated skyrmions in nanodots with propagating spin-waves. He will focus on the study of magnetostatic and exchange interactions between multilayered nanodots and a ferromagnetic waveguide. He expects that skyrmion stabilised in the nanodots will influence the magnetisation in the waveguide. As a result, the spin waves will excite the skyrmions, and in the reversal process, skyrmion oscillations will excite propagating spin waves. Author's preliminary results show also that the ring shape patterning of the nanodot surface allows for enhancing stability and increase probability for nucleation of the skyrmions in remagnetisation process. The Author also plans to work on the experimental realisation of the metalens for spin waves by changing the groove thickness along with the interface.

6.3 Conference presentations

6.3.1 Oral presentations

This list of the 10 most important oral presentations:

1. **Magnonics 2019**

   Spin wave collimation using flat metasurface ,

   Carovigno, Italy, 28.07-01.08.2019

2. **Sol-SkyMag 2019**

   Formation and driving of Néel type skyrmion in magnonic antidote lattices ,

   San Sebastian, Spain, 24-28.06.2019

3. **NanoTech Poland 2018 and 1st Symposium on Polydopamine**

   Spin wave focusing interface between two ferromagnetic films as a magnonic metasurface.,

   Poznań, 06-09.06.2018

4. **DPG-Frühjahrstagung (DPG Spring Meeting) and EPS-CMD27**

   Bi-stable skyrmion states in Pt/Co/Ir multilayer nanodots as a switchable memory cell ,

   Berlin, Germany, 11.03.2018

5. **Konferencja użytkowników KDM 2018**

   Symulacje mikromagnetyczne struktur magnonicznych ,

   Poznań, 6-7.06.2018

6. **13th Interregional Workshop on Advanced Nanomaterials 2017**

   Bi-stable magnetic skyrmion states in Pt/Co/Au multilayer nanodots. ,

   Poznań, 15-16.11.2017

7. **Sol-SkyMag 2017**

   Bi-stable magnetic skyrmion states in Pt / Co / Au multilayer nanodots ,

   San Sebastian, 21.06.2017

8. **NanoTech Poland 2017 International Conference and Exhibition**

   Skyrmions in Pt/Co/Au multilayer nanodots ,

   Poznań, 23-24.05.2017

9. **Konferencja użytkowników KDM 2017**

   Symulacje mikromagnetyczne układów magnonicznych ,

   Poznań, 23-24.05.2017

10. **Konferencja użytkowników KDM 2016**

    Symulacje mikromagnetyczne układów magnonicznych przy wykorzystaniu kart graficznych,

    Poznań, 27-28.06.2016

In summary Author presented 16 times the oral speech, during abroad and local conferences. Additionally, around next 14 presentations given by co-Authors.

6.3.2 Poster presentations

This list of the 10 most important poster presentations:

1. **Magnonics 2019**

   Spin-wave phase inverter upon a single nanodefect,

   2'nd place best poster award,

   Carovigno, Italy, 28.07-01.08.2019

2. **DPG-Frühjahrstagung (DPG Spring Meeting) and EPS-CMD27**

   Phase-modulated Fresnel zone plate for spin waves in bulk and thin-film geometry,

   Berlin, Germany, 13.03.2018

3. **Magnonics 2018**

   Spin-wave phase inverter upon a single nano-groove

   Kiev, Ukraine, 21.09.2018

4. **Nano-Magnonics workshop 2018**

   Design of a spin-wave flat lens with phase-dependent interface between two ferromagnetic thin films,

   Kaiserslautern, Germany, 19-21.01.2018

5. **NanoTech Poland 2018 & 1st Symposium on Polydopamine**

   Magnetostatic interactions in bi-component one-dimensional magnonic crystals,

   Poznań, Poland, 6-9.06.2018

6. **2018 IEEE International conference on microwave magnetics**

   Spin wave propagation through anisotropic interface between antiferromagnetically coupled ferrimagnets,

   Exeter, England, 25-28.06.2018

7. **Sol-SkyMag 2017**

   Dynamics of spin waves in ferromagnet thin film with an antidot,

   San Sebastian, Spain, 21.06.2017

8. **The European Conference PHYSICS OF MAGNETISM 2017 (PM'17)**

   Hysteresis behaviour of skyrmions in Pt/Co/Au multilayer nanodots,

   Poznań, Poland, 27.06.2017

9. **The Joint European Magnetic Symposia 2016**

   Spin wave dynamics in antidot Py lattices of complex geometries,

   Glasgow, England, 21.08.2016

10. **MANA 2016 - Micromagnetics: Analysis, Numerics, Applications**

    Investigation of magnetization reversal in periodic arrays of wave-like Py nanostructures

    Viena, Austria, 18-19.02.2016

    In summary Author presented 25 times the poster presentations, during abroad and local conferences.

6.3.3 Conference awards, grants, and scholarships

1. **Poster presentation – 2'nd place best poster award Magnonics 2019**

   Spin-wave phase inverter upon a single nanodefect ,

   Carovigno, Italy, 28.07 – 01.08.2019

2. **NCN Preludium 14, Grant No. 2017/27/N/ST3/00419**

   Study of the bi-stable magnetic skyrmions in ultrathin nanodots.

   01.06.2018 – 01.06.2020

3. **Master's scholarship as part of the Team Symphony – TEAM/2011-8/4/styp14**

   Scholarship received as part of a grant project coordinated by prof. dr hab. Andrzej Maziewski.

   01.11.2014 – 30.06.2015.

4. **Internship scholarship as part of the competition organised by the National Scholarship Program of the Slovak Republic**

   10.10.2016 – 10.11.2016

5. **Internship scholarship as part of the competition organised by the National Scholarship Program of the Slovak Republic**

   10.04.2018 – 10.05.2018

6. **UAM Fundation Schoolarship in 2018 for the best PhD students**

7. **Dr. Jan Kulczyk Scholarship in 2018 for the best PhD students**

8. **The best PhD students scholarship on Faculty of Physics, UAM in 2016, 2017, 2018**

6.4 Conference organisation

1. Adam Mickiewicz University, Poznań / Trzebaw

   18 – 21.11.2016

   XV Ogólnopolska Konferencja Kół Naukowych Fizyków

   Role: main organizer.

2. Adam Mickiewicz University, Poznań / Trzebaw

   2 – 7.07.2017

   Workshop MagIC 2017 – Magnetism, Interactions and Complexity: a multifunctional aspects of spin wave dynamics

   Role: main organiser.

3. Poznań and the Institute of Molecular Physics, Polish Academy of Science and Adam Mickiewicz University, Poznań

   26 – 30.06.2017

   The European Conference PHYSICS OF MAGNETISM 2017 (PM'17)

   Role: volunteer, information display system developer.

4. National Technical University of Ukraine (KPI), Kyiv, Ukraine and Adam Mickiewicz University, Kijev, Ukraine

   17 – 21.09 2018

   3rd International Advanced School on Magnonics 2018

   Role: main organizer.

6.5 Scientific visits

1. One month internship in the abroad institute "Institute of Magnetism, National Academy of Sciences of Ukraine" in Kiev, Ukraine. The internship took place from 02.09.2018 to 26.09.2018.

   During internship Author worked on the calculations and paper preparation entitled "Ultrathin spin wave phase shifting metasurface". As a result of this collaboration, Author implemented the concept of using RKKY coupling to design a meta-surface for spin waves.

2. A month internship in a abroad center in Bratislava, at the Institute of Electrical Engineering, Slovak Academy of Sciences. The internship took place from 10.04.2018 to 10.05.2018.

   During internship, Author performed micromagnetic simulations of complex thin-film systems, in which he observed skyrmion nucleation in the process of magnetising the system. He prepared a manuscript entitled "Skyrmion Confinement and Controlled Motion in Magnonic Antidot Lattices" was written.

3. One month internship in the abroad institute "Institute of Magnetism, National Academy of Sciences of Ukraine" in Kiev, Ukraine. The internship took place from 22.08.2017 to 07.09.2017.

   During this intership Author performed calculations on RKKY coupling induced on the interface of two ferromagnetics to design a meta surface capable of focusing spin waves.

4. A month internship in a foreign center in Bratislava, at the Institute of Electrical Engineering, Slovak Academy of Sciences. The internship took place from 10.10.2016 to 10.11.2016.

   During internship, Author gain knowledge in the field of skyrmion computational methods, and also began research on researching bi-stable skyrmions in nanopots. The effect of the internship was research that was published in paper entitled 'Bi-Stability of Magnetic Skyrmions in Ultrathin Multilayer Nanodots Induced by Magnetostatic Interaction', Physica status solidi (RRL) - Rapid Research Letters 11 (10), 1700259 (2017).

5. Internship in the abroad institute "Institute of Magnetism, National Academy of Sciences of Ukraine" in Kiev, Ukraine. The internship took place from 13.07.2016 to 14.08.2016.

   During internship Author started joint project with prof. Oksana Gorobets to investigate an analytical model of RKKY interactions between two ferromagnets.

Alphabetical Index